

Thesis for Doctor of Philosophy

**Anisotropy of Charpy Properties in
Linepipe Steels**

Joo, Min Sung (주 민 성)

Department of Ferrous Technology

(Computational Metallurgy)

Graduate Institute of Ferrous Technology

Pohang University of Science and Technology

2012

Anisotropy of Charpy Properties in Linepipe Steels

2012

Min Sung Joo

Linepipe강의 Charpy특성 이방성

**Anisotropy of Charpy Properties in
Linepipe Steels**

Anisotropy of Charpy Properties in Linepipe Steels

by

Joo, Min Sung
Department of Ferrous Technology
(Computational Metallurgy)
Graduate Institute of Ferrous Technology
Pohang University of Science and Technology

A thesis submitted to the faculty of Pohang University of Science and Technology in partial fulfillments of the requirements for the degree of Doctor of Philosophy in the Graduate Institute of Ferrous Technology (Computational Metallurgy)

Pohang, Korea
12 April 2012

Approved by

Prof. Bhadeshia, H. K. D. H.

Prof. Suh, Dong-Woo

Major Advisor

Co-Advisor

Anisotropy of Charpy Properties in Linepipe Steels

Joo, Min Sung

This dissertation is submitted for the degree of Doctor of Philosophy at the Graduate Institute of Ferrous Technology of Pohang University of Science and Technology. The research reported herein was approved by the committee of Thesis Appraisal

12 April 2012

Thesis Review Committee

Chairman: Prof. Bhadeshia, H. K. D. H.	(Signature)
Member: Dr. Im, Young-Roc	(Signature)
Member: Prof. Kim, Han Soo	(Signature)
Member: Prof. Lee, Chong Soo	(Signature)
Member: Prof. Suh, Dong-Woo	(Signature)

Preface

This dissertation is submitted for the degree of Doctor of Philosophy at Pohang University of Science and Technology. The research reported herein was conducted under the supervision of Professor H. K. D. H. Bhadeshia, Professor of the Computational Metallurgy in the Graduate Institute of Ferrous Technology, Pohang University of Science and Technology and Professor of the Department of Materials Science and Metallurgy, University of Cambridge, between September 2008 and April 2012.

Except where acknowledgement and references are made to previous work, this work is, to the best of my knowledge, original. Neither this, nor any substantially similar dissertation has been, or is being, submitted for any degree, diploma or other qualification at any other university or institution. This dissertation does not exceed the word limit of 60,000 words.

Some of the work described herein has been published:

Joo, M. S., Suh, D.-W., Bae, J.-H. and Bhadeshia, H. K. D. H.: Anisotropy of Charpy Properties in API-X80 Steels. *Poster session of 2010 Fall Conference of KIMM*, Changwon, Korea, Nov. 4–5, 2010.

Joo, M. S., Suh, D.-W., Bae, J.-H. and Bhadeshia, H. K. D. H.: Influence of Delamination and Crystallography on Anisotropy of Charpy toughness in API-X80 steel. *Materials Science & Engineering A*, vol. 546, pp. 314–322, 2012.

Joo, M. S., Suh, D.-W., Bae, J.-H. and Bhadeshia, H. K. D. H.: An Experiment to Separate the Effect of Texture on Anisotropy of Pipeline Steel. *Submitted*, 2012.

Joo, M. S., Suh, D.-W. and Bhadeshia, H. K. D. H.: Mechanical Anisotropy in Steels for Pipelines. *To be submitted*, 2012.

Min Sung Joo

April, 2012

DFT Joo, Min Sung
20081020 Anisotropy of Charpy Properties in Linepipe Steels
Department of Ferrous Technology (Computational Metallurgy)
2012, 246p
Advisor: Prof. Bhadeshia, H. K. D. H. and Prof. Suh, D.-W.
Text in English

Abstract

Pipes can be manufactured by welding spirals of hot-rolled linepipe steels. This process has a cost advantage relative to one in which the steel is seam welded after bending into a tubular shape. Even though properties such as the Charpy toughness and strength meet minimum specifications, the existence of anisotropy can compromise, for example, the stability of the pipe to buckling. In the case of spiral pipes, the least tough Charpy orientation also happens to coincide with the circumferential direction which experiences the largest stress.

The aim of the work presented in this thesis was to examine the possible factors of the anisotropy of Charpy properties in the hot-rolled linepipe steels. Six alloys of grade API-X70 and X80 have been investigated. Regardless of their different chemical compositions and processing variables, all the steels show similar anisotropy features; the ductile-to-brittle transition temperature is highest for the Charpy specimens machined in a diagonal direction relative to the rolling direction. It is known that orientation-dependent properties in linepipe steels correlate with inclusions, microstructural anisotropy and unfavourable crystallographic texture. In the present study, the occurrence of delamination and preferential alignment of {100}

ferrite cleavage planes are found to be key factors in determining the observed anisotropy in Charpy properties. Delamination is related to the presence of banding in hot-rolled steels, and the additional plasticity it entails during the process of fracture leads to an effective increase in toughness. As a consequence, the toughness is worst when the Charpy specimen is machined at 45° to the rolling direction because the extent of delamination at that orientation is minimal.

The crystallographic texture also leads to a greater propensity of $\{100\}$ ferrite planes parallel to the fracture surface for the 45° orientation, leading to a further decrease in toughness. Even though delamination was avoided since microstructural banding was eliminated after a quenching heat treatment, the crystallographic texture was retained due to the texture memory effect so that anisotropic mechanical properties resisted.

This implies that the anisotropy in hot-rolled steel is the essence of the problem because the microstructural banding and the typical rolling and transformation textures, $\{112\}\langle 110\rangle$ and $\{001\}\langle 110\rangle$ of ferrite, cannot be avoided in hot-rolled steels.

Contents

PREFACE.....	I
ABSTRACT	III
CONTENTS	V
NOMENCLATURE AND ABBREVIATIONS.....	IX
CHAPTER I. INTRODUCTION.....	1
CHAPTER II. LITERATURE REVIEW	3
2.1. Austenite to Ferrite Phase Transformation.....	3
2.2. Linepipe Steels.....	5
2.2.1. Characteristics of linepipe steels.....	6
2.2.2. Microstructure of linepipe steels.....	8
2.2.3. Constituents of linepipe steels.....	11
2.2.4. The control of microstructure.....	18
2.3. Fracture Mechanisms	22
2.3.1. The general theory of brittle fracture.....	25
2.3.2. The energy release rate.....	29
2.3.3. Ductile to brittle transition.....	32
2.3.4. Toughness.....	33
2.3.5. Delamination.....	38
2.4. Toughness Anisotropy.....	40
2.4.1. Inclusions	41
2.4.2. Microstructural anisotropy	47

2.4.3. Crystallographic texture.....	53
III. EXPERIMENTAL	57
3.1. Sample Preparation	57
3.2. Mechanical Tests	59
3.2.1. Tensile	59
3.2.2. Charpy	59
3.2.3. Hardness.....	61
3.3. Microstructural Observations	62
3.3.1. Metallography	62
3.3.2. Optical and scanning electron microscopy.....	62
3.3.3. Transmission electron microscopy.....	63
3.3.4. Energy dispersive X–ray spectroscopy and electron back–scattered diffraction..	63
3.3.5. X–ray diffraction	63
3.4. Metallurgical Experiments.....	65
3.4.1. Heat treatment.....	65
3.4.2. Computer simulation	65
IV. ANISOTROPY OF LINEPIPE STEELS	67
4.1. Microstructures.....	67
4.2. Mechanical Properties.....	84
4.2.1. Tensile	84
4.2.2. Charpy	85
4.3. Inclusions	87
4.4. Fractography	91
4.5. Grain Boundary Density	105

4.6. Crystallographic Texture	107
4.7. Summary.....	114
V. DELAMINATION AND CRYSTALLOGRAPHIC TEXTURE	115
5.1. Additional Orientation of Charpy Specimen	115
5.2. Quenching Heat Treatment.....	124
VI. DIFFERENT ROLLING PROCESSES IN API_X70 STEELS	134
6.1. Microstructures.....	134
6.2. Charpy Properties	145
6.3. Grain Boundary Density	147
6.4. Fracture Surfaces.....	148
6.5. Crystallographic Texture.....	153
6.6. Summary.....	159
VII. CONCLUDING REMARKS	160
7.1. Anisotropy indices for the steels.....	160
7.2. Summary and Future Work	168
REFERENCES	171
Appendix A. Chemical Compositions for Linepipe Steels.....	193
A.1. API X65.....	193

A.2.	API X70.....	196
A.3.	API X80.....	199
	References.....	201
Appendix B. Fundamentals of Crystallography and Texture.....		214
B.1.	Orientation of crystallites.....	214
B.2.	Texture.....	221
B.3.	Summary.....	227
	References.....	227
Appendix C. RANDOM_ORIENTATION		228
Appendix D. Change of Microstructure in X80_A Steel.....		239
	References.....	246
ACKNOWLEDGEMENT		A
CURRICULUM VITAE		B

Nomenclature and Abbreviations

δ_t	crack tip opening displacement
γ_p	plastic work per unit area
γ_s	surface energy per unit area
ν	Poisson's ratio
μ	shear modulus of the material
σ	applied stress
σ_c	critical stress
σ_{dislo}	dislocation strengthening stress
σ_f	fracture stress
σ_l	lattice friction stress
σ_{ppt}	precipitation strengthening stress
σ_{ss}	solid solution strengthening stress
σ_{tex}	texture strengthening stress
σ_y	yield stress
ρ_{GB}	density of grain boundary
a_0	atomic distance
c	the half of initial crack length
d	grain size
k_y	constant for yield stress
E	Young's modulus of the material
E_{kin}	kinetic energy

G	energy release rate
K	stress intensity factor
K_c	critical stress intensity factor
K_{Ic}	fracture toughness
L_{GB}	length of grain boundary
R	force of crack resistance
U_e	total elastic energy
U_s	total surface energy
α	ferrite
α_b	bainite
α_{lb}	lower bainite
α_{ub}	upper bainite
α'	martensite
γ	austenite
δ	delta ferrite
θ	cementite
A_{c1}	temperature at which γ begins to form during heating at a specified rate
A_{c3}	temperature at which transformation of α to γ is completed during heating at a specified rate

A_{c4}	temperature at which γ transforms to δ during heating at a specified rate
A_{e1}	lower temperature limit of the equilibrium $\alpha + \gamma$ phase field
A_{e3}	upper temperature limit of the equilibrium $\alpha + \gamma$ phase field
A_{e4}	temperature of phase changes between γ and δ at the equilibrium transformation
A_{r1}	temperature at which transformation of γ to α or α plus θ is completed during cooling at a specified rate
A_{r3}	temperature at which γ begins to transform to α during cooling at a specified rate
A_{r4}	temperature at which δ transforms to γ during cooling at a specified rate
B_s	temperature at which transformation of γ to α_b starts during cooling
B_f	temperature at which transformation of γ to α_b is substantially completed
M_s	temperature at which transformation of γ to α' starts during cooling
M_f	temperature at which transformation of γ to α' is substantially completed
API	American Petroleum Institute
ASTM	American Society for Testing and Materials

BCC	Body–Centred Cubic
CT	Coiling Temperature
CTOD	Crack Tip Opening Displacement
CVN	Charpy V Notch
DBTT	Ductile–to–Brittle Transition Temperature
DD	Diagonal Direction
EBS	Electron Back–Scattered Diffraction
ED	Extrusion Direction
EDS	Energy Dispersive X–Ray Spectroscopy
FCC	Face–Centred Cubic
FESEM	Field–Emission Scanning Electron Microscopy
FETEM	Field–Emission Transmission Electron Microscopy
FRT	Finish Rolling Temperature
GOS	Grain Orientation Spread
HAZ	Heat Affected Zone
HIC	Hydrogen–Induced Cracking
M/A	Martensite–Austenite constituent
MAP	Materials Algorithms Project
MTDATA	Metallurgical and Thermochemical Databank
ND	Normal Direction
ODF	Orientation Distribution Function
ODS	Oxide Dispersion Strengthened
OM	Optical Microscopy

RA	Retained Austenite
RD	Rolling Direction
RH	Rheinstahl and Heraeus
SCC	Stress–Corrosion Cracking
SCT	Start Cooling Temperature
SD	Short transverse Direction
SEM	Scanning Electron Microscopy
STEM	Scanning Transmission Electron Microscopy
TD	Transverse Direction
TE	Total Elongation
TEM	Transmission Electron Microscopy
TEMP	Temperature
TMP	Thermo–Mechanical Processing
UE	Uniform Elongation
UTS	Ultimate Tensile Strength
XRD	X–Ray Diffraction
YS	Yield Strength

Chapter I. Introduction

Linepipe steels have for many decades been in demand but are becoming vital because there is an expansion in the need to transport fossil fuels over large distances and in dire environments. There are many essential properties for linepipe steels. They need to be weldable, possess a low yield to ultimate tensile strength ratio for safe design, and suitable strength and toughness for transporting fluids at high pressures. It is necessary for the steel to resist hydrogen-induced cracking and sulphide stress-corrosion cracking because low-grade petroleum wells contain hydrogen sulphide.

In order to lower the cost of construction, it is desirable to replace expensive thick plates by cheaper, hot-rolled spiral-welded pipes. But, large-calibre spiral-welded pipes have not been exploited fully due to their anisotropy of mechanical properties and decrease in strength after pipe forming [Seo *et al.*, 2007; Kim and Bae, 2008]. The anisotropy of toughness is a particular problem, with toughness depending on the orientation relative to the rolling direction. The latter is of course the circumferential direction of spiral-welded pipe, which normally experiences the highest load (hoop stress), would have weakest toughness and strength than other orientations [Kim and Bae, 2008]. This increases the chances of fracture [Kang *et al.*, 2004; Stalheim *et al.*, 2007]. It is the purpose of the present work to understand the orientation dependence of the Charpy energy.

The orientation dependence of toughness is a well-known phenomenon for hot-rolled steels [Fegredo, 1975; Ray *et al.*, 1995]. There have been many attempts to

understand and control the toughness anisotropy. Three factors have emerged from previous research, the non-uniform distribution of inclusions with various sizes and shapes, microstructural anisotropy due to banding and crystallographic texture. The current research is an attempt to describe primarily the X80 grade of API linepipe steel and its mechanical properties, particularly the toughness at the temperatures below -20 °C.

Chapter II. Literature Review

2.1. Austenite to Ferrite Phase Transformation

The different forms of ferrite (α) that form during the solid-state transfer of austenite (γ) in steels can be categorised into reconstructive or displacive. The former transformation involves the redistribution of atoms between parent and product phase by a process of diffusion. Atoms are thermally activated to undergo random jumps across the transformation interface in a manner which minimises strain energy. Any resulting shape deformation is due to the change in density accompanying transformation. Therefore, reconstructive transformation may not occur at low temperatures where atomic mobility is limited. Allotriomorphic ferrite, idiomorphic ferrite [Dubé *et al.*, 1958; Bhadeshia, 1985] and pearlite [Sorby, 1886; Ridley, 1984; Howell, 1998] belong to this class of transformation.

During displacive transformation, the atoms move less than an interatomic distance and preserve positional relationships with respect to their neighbours. The deformation from the parent crystal lattice to that of the product results in the formation of thin plates because this is the shape which minimises strain energy. Normally, an invariant-plane strain shape deformation with a large shear component results. So the transformation can occur at low temperatures because the diffusion of substitutional elements is not necessary. Widmanstätten ferrite [Watson and McDougall, 1973], bainite [Ko and Cottrell, 1952; Srinivasan and Wayman, 1968; Swallow and Bhadeshia, 1996], acicular ferrite [Strangwood and Bhadeshia, 1987; Babu and Bhadeshia, 1992] and martensite [Greninger and Troiano, 1940;

Bowles and MacKenzie, 1954; Wechsler *et al.*, 1953] are in the displacive category. The scheme is summarised in Fig. 2.1. The term “paraequilibrium” means that the carbon can be partitioned but the substitutional atoms do not diffuse, so the ratio of the substitutional to iron atoms is unchanged by transformation [Bhadeshia, 2001].

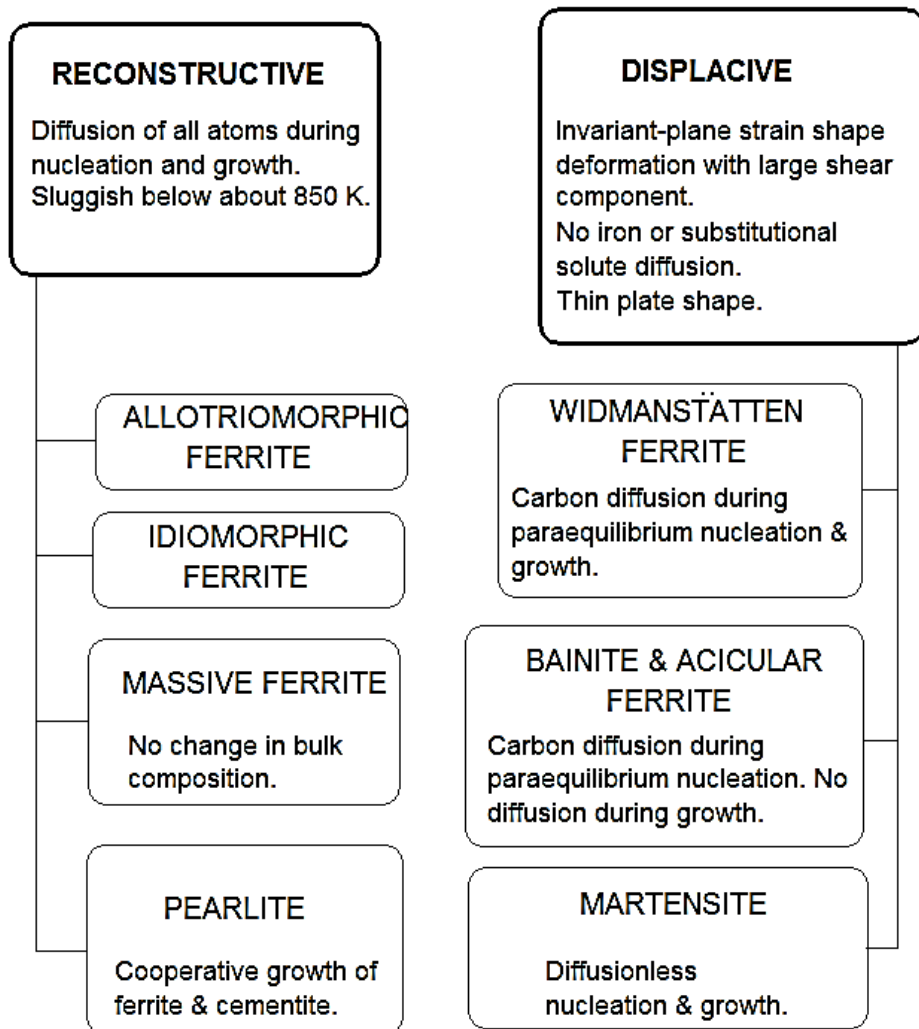


Figure 2.1. Summary of the variety of phases generated by the decomposition of austenite. Courtesy of H. K. D. H. Bhadeshia [Bhadeshia, 2001].

2.2. Linepipe Steels

Linepipe steels are used mostly for the economic transmission of crude oil and natural gas from regions in which the fuels are mined, to those where they are utilised to generate energy. Table 2.1 summarises the enormous level of linepipe construction that is currently in progress.

Table 2.1. High strength linepipe projects over the period 2007–2012 [Liessem *et al.*, 2008]. The X100 grade is at a trial stage.

Region	Length (km)	Grade
North America	11,000	X80/X100
Russia	2,000	X80
China	8,000	X80
Europe	500	X80

There are many technical challenges for linepipe steels. These include a need for homogeneous microstructure and properties, weldability, a low yield to ultimate strength ratio with safe design, and obviously, a high level of toughness. Indeed, the quality required is likely to be much more demanding as pipe engineering enters the era of difficult environments, whether these are in the deep oceans of Brazil or in the freezing climates of Siberia and Alaska. Fortunately, the steel makers have developed an excellent combination of required strength and toughness steels for the pipe by optimizing technologies such as microalloying and thermo–mechanical processing. The strength not only helps transmit fluids at higher pressures, but can

achieve better design when the weight can be reduced in the context of pipes which have to hang from an ocean–surface collection vessel. The toughness helps mitigate disasters, particularly the long–range propagation of high–velocity cracks [Kim, 1983; Fairchild *et al.*, 2002; Corbett *et al.*, 2004]. Low–grade petroleum wells contain much sour gas (H_2S), so the steels particularly need to resist hydrogen–induced cracking (HIC) and stress–corrosion cracking (SCC). Further issues arise because significant changes occur in mechanical properties after pipe–forming, such as the change of yield strength, a decrease in impact toughness due to the work hardening and so on [Seo *et al.*, 2007; Kim and Bae, 2008]. These and other requirements needed to ensure integrity during service are well–known and to a large extent understood and incorporated into practice, both via specifications and detailed analysis.

2.2.1. Characteristics of linepipe steels

The grade designation of linepipe steel follows the standards of the American Petroleum Institute (API). The designation is categorised by the yield strength expressed in megagrams per square inch, for example X42, X60, and so on. The yield strength can be described by a modified Hall–Petch equation [Hall, 1951; Petch, 1953].

$$\sigma_y = \sigma_i + \sigma_{ss} + \sigma_{ppt} + \sigma_{dislo} + \sigma_{tex} + k_y d^{-1/2} \quad (2-1)$$

- σ_i : lattice friction stress
- σ_{ss} : solid solution strengthening stress
- σ_{ppt} : precipitation strengthening stress
- σ_{dislo} : dislocation strengthening stress
- σ_{tex} : texture strengthening stress
- k_y : constant
- d : ferrite grain size

Recently, X60, X70 and X80 grades have seen wide application, although even stronger alloys such as X100 have yet to be full commercialised. Table 2.2 shows the standard for X65 ~ X80 [API Recommended Practice, 1996], but it can be modified by the demands of customers or the conditions in which the steels will be used. Normally, the steels contain other alloying elements such as nickel, molybdenum, copper, aluminium, *etc.* to control the mechanical properties required. Beyond the high strength and elongation values listed in Table 2.2, the low-temperature toughness may be improved by grain refining and reducing the carbon concentration. The latter can be particularly helpful in enhancing weldability. HIC and SCC resistance can be improved by reducing impurity concentrations through the control of non-metallic inclusions in the steel. The actual chemical compositions of the X65, X70 and X80 steels are listed in Appendix A.

2.2.2. Microstructure of linepipe steels

The microstructures of linepipe steels are complicated because of the nature of alloying and processing. This is in contrast to the equiaxed ferritic microstructures of conventionally hot-rolled steels. Linepipe steel microstructures can be divided essentially into the following fundamental phases [Kim, 1983]:

1. Allotriomorphic ferrite – pearlite steels.
2. Acicular ferrite or bainitic steels.
3. Multi-phase steels.

Ferrite–pearlite steel, which has 0.1 ~ 0.2 wt% carbon and micro alloying elements such as niobium, titanium and vanadium for strength hardening, is used to make steel less strong than the X70 grade. Usually it shows the banding of pearlite–rich and ferrite–rich area. It was developed at 1950s but still widely used with improvements resulting from better controlled rolling technologies. Acicular ferrite steel has also been available for some time but this microstructure can now be produced economically in low carbon (0.02 ~ 0.08 wt% C) steel due to the development of the RH (Rheinstahl and Heraeus) refining process. This involves degassing and stirring of the melt using argon injection into a vacuum vessel in order to reduce the non–metallic inclusions. This process is used to make steels mechanically superior to the X70 grade [Wilson, 1965]. Multiphase steel has bainite, martensite, retained austenite and carbonitride in the ferrite matrix. It is used to

make alloys exceeding the specifications of the X100 grade. Fig. 2.2 shows a summary of linepipe steels with alloying elements according to the microstructure and thermo–mechanical processes [Sage, 1981].

Table 2.2. The specification API 5L.

(a) The regulation of chemical composition (Ladle, wt%).

Grade	Carbon	Manganese	Phosphorus	Sulphur	Niobium	Vanadium
X65	≤ 0.26	≤ 1.40	≤ 0.04	≤ 0.05	≥ 0.005	≥ 0.005
X70	≤ 0.23	≤ 1.60	≤ 0.04	≤ 0.05	–	–
X80	≤ 0.18	≤ 1.80	≤ 0.03	≤ 0.018	–	–

(According to the demands of customer, other alloying elements can be added.)

(b) Mechanical properties.

Grade	Yield strength (MPa)	Tensile strength (MPa)	Yield ratio (%)	Elongation (%, 50.8 mm of gauge length)
X65	≥ 448	≥ 530	≤ 90	$e = 625,000 \times \frac{A^{0.2}}{U^{0.9}}$
X70	≥ 482	≥ 565	≤ 90	
X80	≥ 551	620 ~ 827	≤ 93	

e : minimum elongation in 50.80 mm of gauge length in percent to nearest 1/2 percent.

A : cross–sectional area of the tensile specimen in mm² based on specified outside diameter or nominal specimen width and specified wall thickness rounded to the nearest 6.5 mm² or 484 mm².

U : specified minimum ultimate tensile strength (MPa).

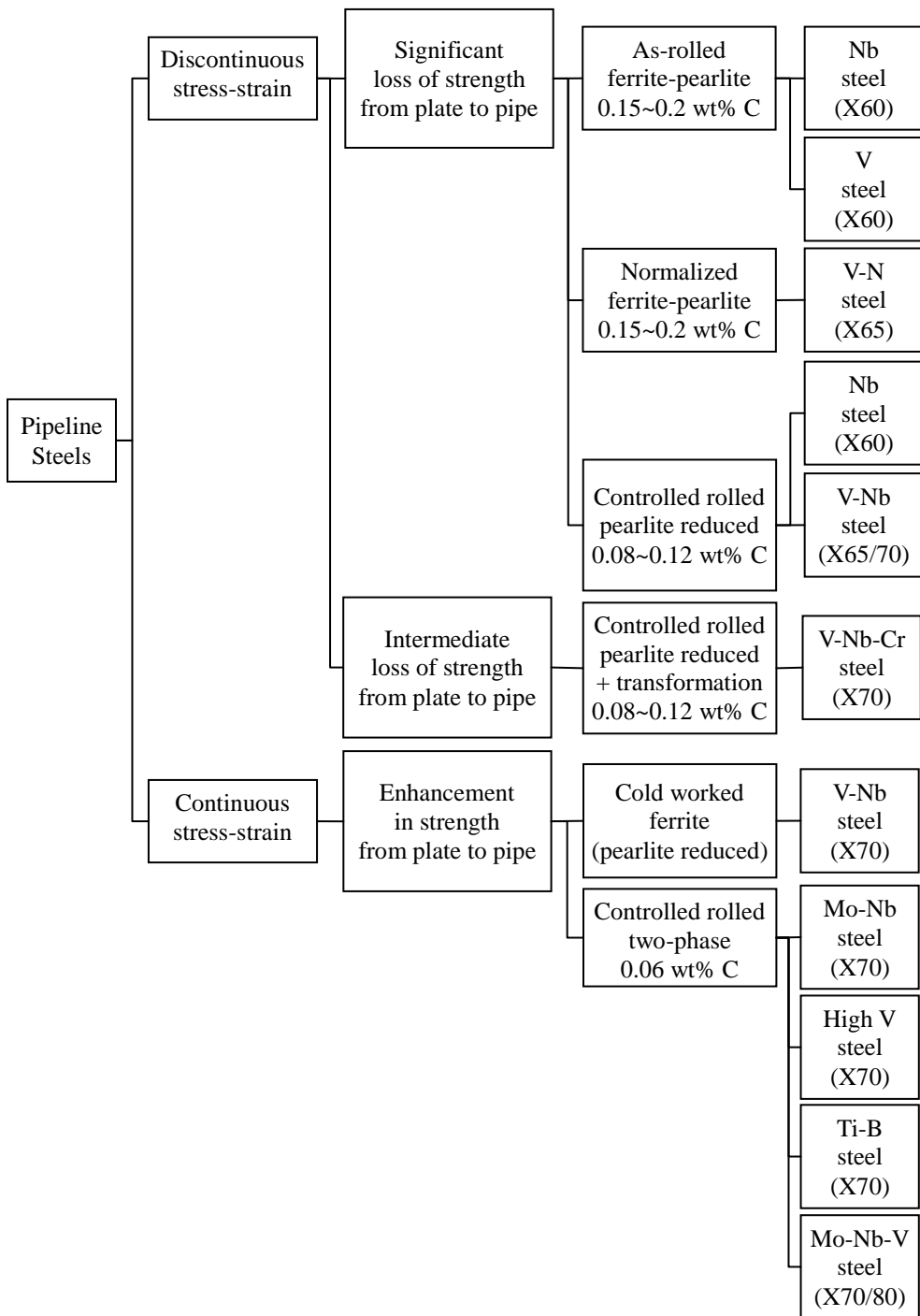


Figure 2.2. Summary of Steel pipes in production for high strength steel linepipes in Europe, the Americas and Japan. Adapted from [Sage, 1981].

2.2.3. Constituents of linepipe steels

Allotriomorphic ferrite

The allotriomorphic ferrite (also loosely referred to as proeutectoid ferrite, grain boundary ferrite or polygonal ferrite) [Bhadeshia, 1985] is the first phase to transform from austenite on cooling over the whole range of composition and temperature. It starts to transform just below the A_{r3} temperature and is characterized by low dislocation densities and the absence of substructure. An allotriomorph means that it has a shape which does not reflect its internal crystalline symmetry. It nucleates at γ/γ grain boundaries and grows along those boundaries by a reconstructive transformation. Their growth is not restricted by austenite grain boundaries. The growth of allotriomorphic ferrite is determined by the transfer of substitutional atoms across γ/α boundaries and of carbon atoms by diffusion. The allotriomorphic ferrite has a coherent orientation with one of the adjacent austenite grains, but a chance with any other adjacent austenite grain orientation. Therefore, it may be crystallographically faceted on one side but with a curved boundary on other faces [Bhadeshia and Honeycombe, 2006].

Pearlite

Pearlite is a lamellar mixture of ferrite and iron carbide (cementite) where a pearlite colony is a bicrystal of cementite (θ) and α , growing at a common front with the γ . The growth follows reconstructive transformation, so the rate may be controlled by

the diffusivity of the relevant atoms. The structure resembles the iridescence of a pearl, hence the name was given as pearlite [Sorby, 1886; Ridley, 1984; Howell, 1998].

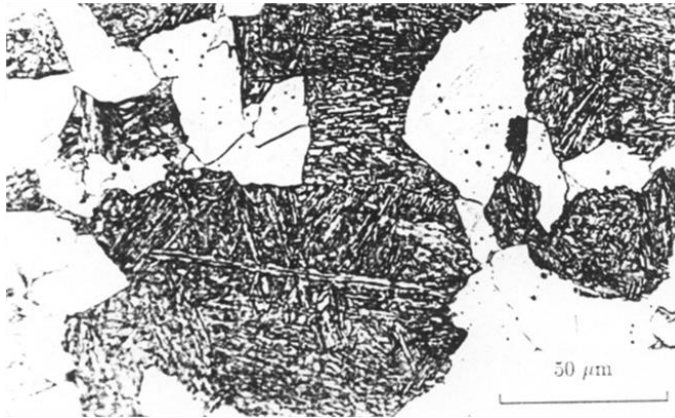


Figure 2.3. Optical micrograph of weld metal, with the martensite after quenching process and the allotriomorphic ferrite (white area) all along the austenite grain boundaries. Courtesy of S. S. Babu [Babu, 1991].

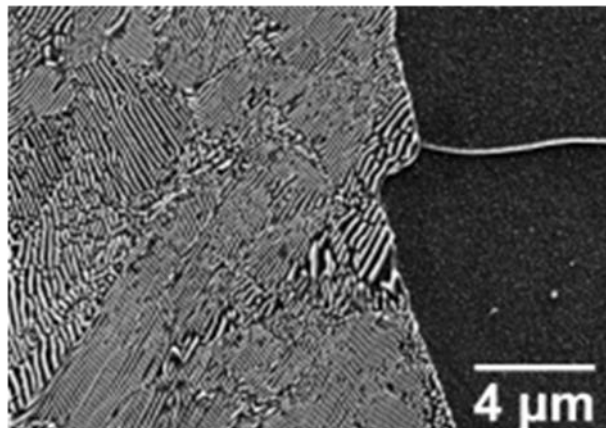


Figure 2.4. SEM micrograph of medium carbon steel with pearlite. Reproduced from [Yi, 2010] with permission from Elsevier.

Bainitic ferrite

Bainite (α_b) is a non-lamellar structure of ferrite, with or without carbides. During bainitic transformation, ferrite grows first, and precipitation of carbides can follow. The ferrite is in the form of clusters of thin platelets, called sub-units, and the aggregates of plates are called sheaves. It follows a displacive transformation mechanism, with an accompanying invariant-plane strain shape deformation with a large shear component and occurs without the partitioning of substitutional alloying elements. Bainite can be obtained by isothermal transformation at all temperatures where the formation of pearlite and allotriomorphic ferrite is sluggish, and also at temperatures below that at which martensite occurs. There are two morphological variants in steel, upper and lower bainite. Upper bainite (α_{ub}), which forms at relatively high temperatures, consists of sheaves or groups of parallel ferrite crystals, in the form of laths or plates, with discontinuous interlath cementite particles. In contrast, lower bainite (α_{lb}) is characterised by ferrite plates which contain fine carbides at angles around 55° to 60° to the long axis of the ferrite. Upper bainite is obtained if the time taken for the carbon diffusion process is smaller than that required for the precipitation of carbides in the bainitic ferrite. So normally the upper bainite does not contain carbides in the ferrite when lower bainite is conventionally classified that it is in the form of ferrite with carbides being present inside the ferrite [Bhadeshia, 2001].

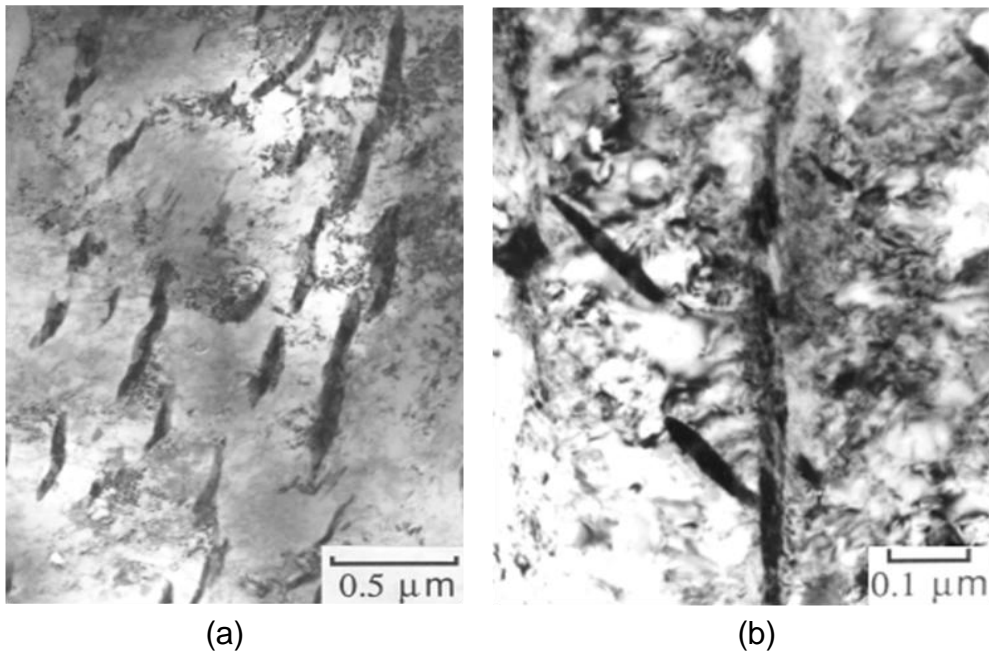


Figure 2.5. The images of bainite. (a) Distribution of cementite particles between the ferrite platelets in upper bainite (AISI 4340 steel). (b) Lower bainite obtained by isothermal transformation for a short time period (435 °C, 10 min) in Fe–0.3C–4.08Cr wt%. Courtesy of H. K. D. H. Bhadeshia [Bhadeshia, 2001].

Acicular ferrite

Acicular ferrite can be classified as bainitic ferrite since the transformation mechanism and the forming temperature of acicular ferrite are similar to that of bainitic ferrite. By inoculating molten steel with controlled additions of non-metallic particles, bainite can be nucleated intragranularly on the inclusions, *i.e.* the plates of bainite nucleate heterogeneously on the inclusions and radiate in many

different directions from the nucleation sites. This intragranularly nucleated bainite is called “acicular ferrite” [Bhadeshia and Honeycombe, 2006]. The major difference between bainite and acicular ferrite comes from the morphology of their microstructures because the former nucleates at austenite grain surfaces and hence grows in the form of sheaves of parallel platelets when the latter nucleates on the inclusions and has much more disorganized microstructure with adjacent platelets pointing in different directions. Therefore, the microstructure of acicular ferrite is described as chaotic with a larger ability to deflect cracks. Therefore, it is believed that the acicular ferrite is beneficial to the mechanical properties since it has fine grains and can retard the propagation of crack efficiently. The term “acicular” means shaped and pointed like a needle, but acicular ferrite has, in three dimensions, the shape of the thin lenticular plate, of which the aspect ratio in a random section is about 0.1 [Bhadeshia, 2001]. It should be emphasised that this definition of acicular ferrite is for intragranularly nucleated bainite, which is found in weld metals. It is not clear whether the so-called acicular ferrite in linepipe steels is intragranularly nucleated [Ito and Nakanishi, 1976; Abson and Pargeter, 1986; Bhadeshia, 1992].

Martensite

Martensite formation follows a displacive transformation mechanism, so it forms by a deformation of the austenite lattice without any diffusion of atoms. The carbon, in solid solution in the austenite, cannot diffuse out when martensitic transformation occurs, so it can be a hard phase as the carbon is formed into solid solution in

martensite. The martensite structure usually contains a high density dislocations and has a specific orientation relationship with the parent austenite. The morphology is thin plate or lath-like to minimize the strain energy associated with the shape deformation. Normally, the martensite reaction takes place athermally in steels [Bhadeshia and Honeycombe, 2006].

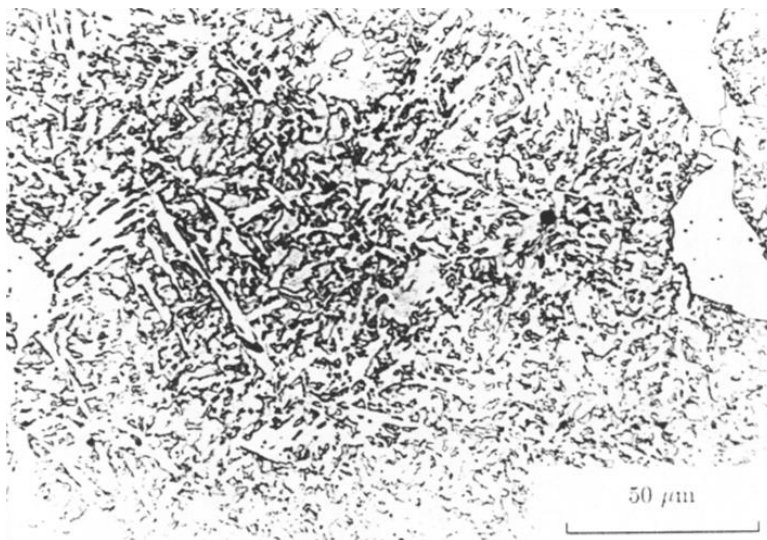


Figure 2.6. Microstructure of allotropic ferrite and acicular ferrite. Courtesy of S. S. Babu [Babu, 1991].

Retained austenite

Retained austenite is that remaining untransformed at ambient temperature [Bhadeshia, 1979].

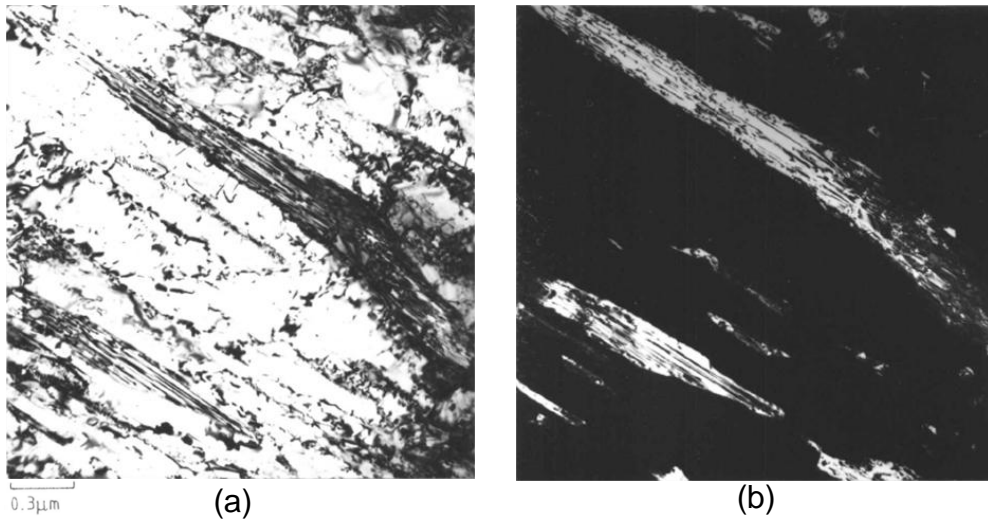


Figure 2.7. The images of martensite and retained austenite. (a) Bright field image of martensite and retained austenite in a high alloy steel. (b) Corresponding dark field image of retained austenite. Courtesy of H. K. D. H. Bhadeshia [Bhadeshia, 1979].



Figure 2.8. Light microscopy image of the heat-affected zone of C-Mn steel in welding, the carbides are black, the M/A constituents white, and the ferrite gray. Reproduced from [Alé *et al.*, 1996] with permission from Elsevier.

Martensite–austenite constituent

When ferrite is transformed from austenite on cooling, the remaining austenite is enriched in carbon due to the lower solubility of carbon in ferrite relative to austenite and becomes stable, and finally, a part of this austenite decomposes into ferrite and carbide. If the cooling is sufficiently rapid, the decomposition does not happen. Instead, the remaining austenite transforms into lath and twin martensite at lower temperatures, and a small amount of austenite is retained. This is the so-called martensite–austenite constituent (M/A), which is an unresolvable mixture of martensite and austenite when using optical microscopy [Ikawa *et al.*, 1980; Alé *et al.*, 1996].

2.2.4. The control of microstructure

The strength and toughness of the linepipe steel can be enhanced by controlling the ferrite grain size. Alloying often enhances the mechanical properties of the linepipe steel by controlling the microstructure as thermo–mechanical processing (TMP) does.

Thermo–Mechanical Processing

TMP, such as controlled rolling and accelerated cooling, can enhance the various mechanical properties such as strength, toughness, yield ratio, corrosion resistance and weldability. Steels can have typical ferrite–pearlite microstructure by just air

cooling. However, TMP can make the steels have the microstructure such as ferrite/“acicular” ferrite, ferrite/bainite and so on without pearlite by the rapid cooling over the $-10\text{ }^{\circ}\text{C s}^{-1}$ and controlled rolling. Furthermore, ductile-to-brittle transition temperature (DBTT) can be lowered by the grain refinement with TMP [Hyzak and Bernstein, 1976; Kim, 1983; Tamura *et al.*, 1988; Kim *et al.*, 2002].

Accelerated cooling greatly enhances the strength. If the cooling rate is slow, and as a consequence the ferrite transformation occurs at a high temperature, then the structure obtained will be coarse. In contrast, accelerated cooling enhances the nucleation of ferrite since transformation temperature is suppressed to greater undercoolings. In addition, the growth or coalescence of ferrite will be retarded due to the low transformation temperature. Therefore, it is possible to obtain finer grains of ferrite [Tanaka, 1984].

Fig. 2.9 shows the process of microstructural change due to controlled rolling and cooling [Kim, 2002]. The rolling condition can be divided into three categories, γ recrystallisation region, γ non-recrystallisation region and $\alpha + \gamma$ region as the temperature decreases. In recrystallisation region, the grain of austenite will undergoes heating and deformation, therefore the grains will be refined by recrystallisation but in this case, the grain size of ferrite will be larger due to grain growth after cooling. However, in the non-recrystallisation region, the austenite grains have a deformed shape consistent with rolling (often referred to as a pancaked shape). The pancaked grains contain deformation-induced defects such as dislocations, and deformation bands, so ferrite nucleation is possible not only at the austenite grain boundaries but also with the grain. Pancaking is useful to achieve

grain refinement in the final product. Deformation in the $\alpha + \gamma$ region, leaves the austenite in a plastically deformed state, and any ferrite that forms may also contain a defect substructure. After cooling, the deformed austenite forms equiaxed ferrite and the deformed ferrite is left as subgrains.

Alloying

Alloying elements can enhance the mechanical properties of steels. Solute elements such as Nb, V, Ti and Mo will be precipitated in the form of carbides or nitrides. If the formation of undesirable coarse precipitates is abandoned, then the fine dispersion of particles can retard the grain boundary motion by pinning effects, which promote the stability of a fine microstructure [Hillert, 1965]. Moreover, the alloying elements can elevate the recrystallisation temperature, enabling a reduction in grain size by controlled rolling.

However, the segregation of the alloying elements such as manganese can result in the banding of ferrite and pearlite in the steels. It is reported that such steel exhibits anisotropy of impact toughness [Matrosova and Polyakov, 1976; Wilson *et al.*, 1975] and can be more susceptible to hydrogen-induced cracking [Lyons and Plisga, 2005] by the banding than an alloy which is homogeneous.

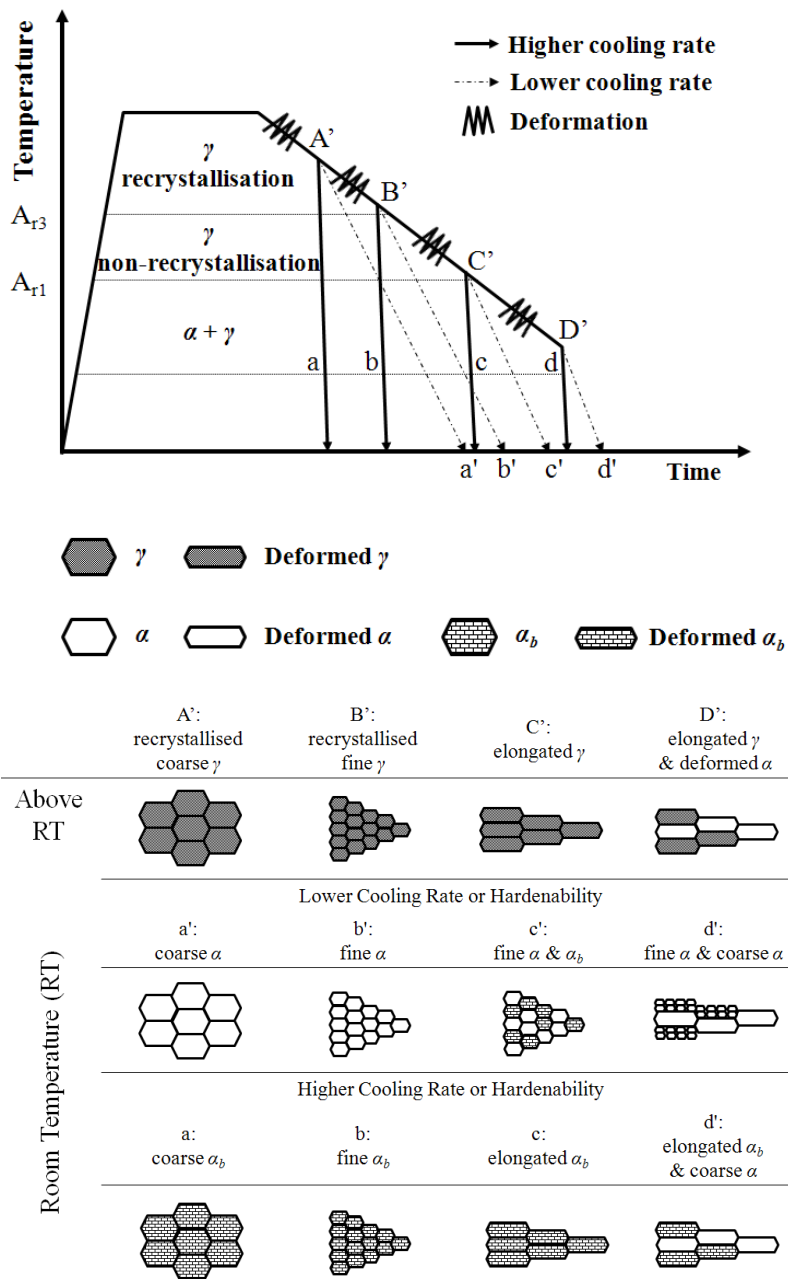


Figure 2.9. Schematic illustration of the structural changes during the three stages of the controlled-rolling and cooling processes. Adapted from [Kim, 2002].

2.3. Fracture Mechanisms

Fracture toughness is a property which describes the ability of a material containing a crack to resist fracture. It is defined in terms of the work of fracture, and as a material parameter is the critical stress intensity at which a sharp crack becomes unstable, denoted K_{IC} and with units of $\text{MPa}\sqrt{\text{m}}$. Fig. 2.10 shows schematically the fracture toughness of body-centred cubic (BCC) metals as a function of temperature [Kameda, 1986].

Fracture can be discussed in terms of ductile and brittle processes. Ductile fracture is associated with considerable plasticity prior to failure. It is slow and generally results from shear deformation and the formation and coalescence of voids. In contrast, brittle fracture involves the rapid propagation of cracks with minimal, highly localised plasticity. The “ductile to brittle transition” occurs as the test temperature is reduced and plastic flow becomes more difficult relative to cleavage, and is a feature of materials with a flow stress that is sensitive to temperature. Because the cleavage stress is insensitive to temperature, the flow stress becomes greater than that required for cleavage at low temperatures, and hence the material becomes brittle. All BCC metals show a marked temperature dependence of the yield stress. Plastic flow in BCC crystal structure of iron becomes particularly difficult at low temperatures because the core of the dislocations is anisotropic, leading to a large Peierls barrier, which eventually it needs higher stress to move dislocations [Bhadeshia and Honeycombe, 2006].

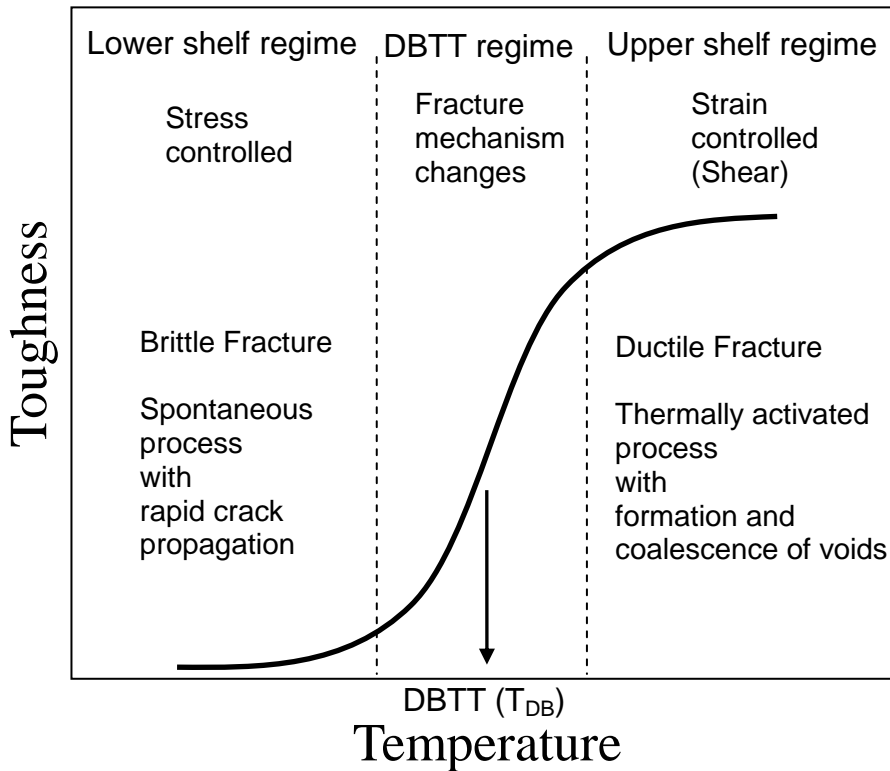


Figure 2.10. Schematic illustration of fracture toughness of BCC metals as a function of temperature. Adapted from [Kameda, 1986].

Thus, operating temperature and strain rate have a marked effect on its fracture mechanism. Fig. 2.11 shows that a reduction in temperature and an increase in strain rate generally results in a marked increase in the yield stress of the material. The effect on the cleavage stress may or may not be pronounced [Meguid, 1989]. However, the fracture stress will increase with a reduction in temperature and an increase in the strain rate [Grimpe *et al.*, 1999]. Therefore, in certain conditions such as low temperature and high strain rate, brittle fracture can be happen below

the yield stress.

Brittle fracture at low temperatures came to prominence from the Liberty ships. In 1943, during World War II, many Liberty ships which encountered the cold area between Siberia and Alaska were broken due to the flaws caused by welding, local stress concentration on the edge part and the low toughness of materials used [Meguid, 1989]. After this, design of engineering structures has been done assuming the existence of internal cracks in steels and considering strength, ductility and toughness.

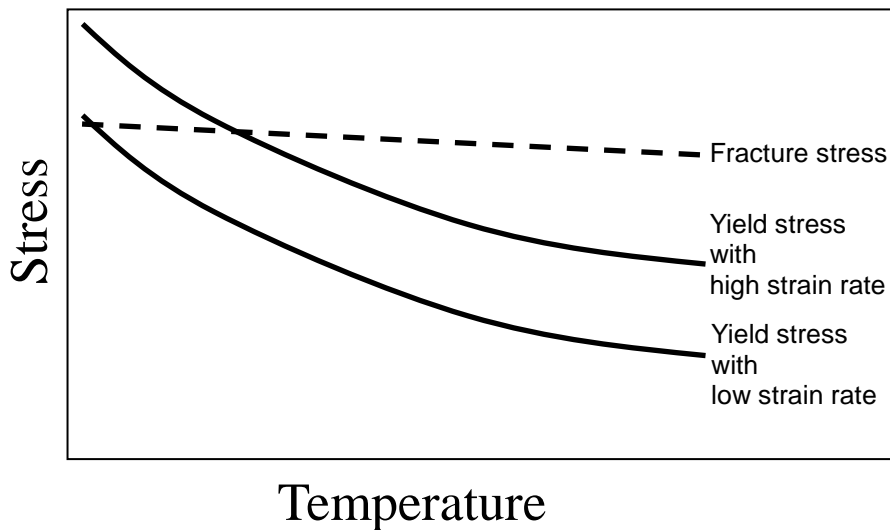


Figure 2.11. Schematic illustration of effect of temperature and strain rate upon yield and fracture stresses. Adapted from [Meguid, 1989].

2.3.1. The general theory of brittle fracture

The theoretical stress for fracture is calculated assuming no flaw in the material. This means that the fracture stress corresponds to the breaking of atomic bonds in the perfect material:

$$\sigma_c = \left[\frac{EU_s}{a_0} \right]^{\frac{1}{2}} \quad (2-2)$$

σ_c : critical stress E : Young's modulus

a_0 : atomic distance U_s : surface energy of crack per unit area

From equation 2-2, the theoretical fracture stress is about E/π (about 70,000 MPa).

However, the observed values are lower by a factor of $10^3 \sim 10^4$. In order to describe this difference, Griffith considered the condition needed for the propagation of a pre-existing crack of length $2c$ in a brittle solid. If a sharp crack already exists in the material, it can propagate when the elastic energy released is more than that to form the crack surface during crack propagation [Griffith, 1921].

When the applied stress σ is high enough, the crack which has primarily length of $2c$, will propagate and release stored elastic energy. This total elastic energy U_e is:

$$U_e = -\frac{\pi\sigma^2c^2}{E} \quad (2-3)$$

c : the half of initial crack length σ : applied stress

The negative sign means that it is released energy.

And, the crack creates two new crack surfaces with total surface energy U_s during propagation as:

$$U_s = +4c\gamma_s \quad (2-4)$$

where γ_s is surface energy per unit area, and the positive sign means that there is absorption of energy.

The total energy of difference is

$$\Delta U = U_e + U_s = -\frac{\pi\sigma^2 c^2}{E} + 4c\gamma_s \quad (2-5)$$

If $\Delta U < 0$ then the crack can propagate.

Under the plane-stress conditions, equilibrium is when the rate of energy release with crack length is zero:

$$\frac{dU}{dc} = \frac{d(U_e + U_s)}{dc} = 0 \quad (2-6)$$

$$\therefore \left(-\frac{2\pi c\sigma^2}{E} + 4\gamma_s \right) = 0 \quad (2-7)$$

The fracture stress needed for crack propagation, σ_f , is therefore:

$$\sigma_f = \left[\frac{2E\gamma_s}{\pi c} \right]^{\frac{1}{2}} \quad (2-8)$$

This equation is well fitted for a perfectly elastic material such as glass and MoO, not however, for metals. Plastic deformation is involved in the creation of crack surfaces [Orowan, 1955], especially, at the root of the crack which is consequently blunted. The crack therefore requires greater energy needed to propagate than simply the creation of flat surfaces. Thus, a modified Griffith equation was introduced to capture plastic work per unit area, γ_p :

$$\sigma_f = \left[\frac{E(2\gamma_s + \gamma_p)}{\pi c} \right]^{\frac{1}{2}} \quad (2-9)$$

It has been found that γ_p ($= 10^2 \sim 10^3 \text{ J m}^{-2}$) $\gg \gamma_s$ ($= 1 \sim 2 \text{ J m}^{-2}$), thus equation 2-9 becomes:

$$\sigma_f = \left[\frac{E\gamma_p}{\pi c} \right]^{\frac{1}{2}} \quad (2-10)$$

The critical crack length can be predicted by the criterion that if $\sigma(\pi c)^{1/2}$ is larger than $E\gamma_p$, then growth occurs.

The local stress field at the crack tip is characterized usually by a parameter K , stress intensity factor, which reaches a critical value K_c when propagation takes place:

$$K = \sigma\sqrt{\pi c} \quad (2-11)$$

$$K_c = \sigma_f\sqrt{\pi c} \quad (2-12)$$

In the case of crack opening mode, K_c will be:

$$K_{Ic} = \sqrt{EG_{Ic}}; \text{ plane stress condition} \quad (2-13)$$

$$K_{Ic} = \left(\frac{EG_{Ic}}{\pi(1-\nu^2)} \right)^{\frac{1}{2}}; \text{ plane strain condition} \quad (2-14)$$

where G_{Ic} is the critical release rate of strain energy in the mode I loading (opening).

K_{Ic} is regarded usually as the fracture toughness of the steel, a material parameter.

It can be obtained from tests on notched specimens. Many attempts have been made to obtain the relationship between the fracture toughness and absorbed impact

energy in Charpy tests. Barson and Rolfe, and Sailors and Corten suggested the equations which relates K_{Ic} and absorbed impact energy of Charpy V Notch (CVN) test, at the ductile-to-brittle transition temperature [Anderson, 1955] :

$$\frac{K_{Ic}^2}{E} = 2(\text{CVN})^{\frac{3}{2}}; \text{ Barson and Rolfe} \quad (2-15)$$

$$\frac{K_{Ic}^2}{E} = 8(\text{CVN})^{\frac{3}{2}}; \text{ Sailors and Corten} \quad (2-16)$$

K_I is often related to the crack tip opening displacement (CTOD), δ_t , which is the relative movement of the two faces when a plastic zone at the crack-tip enables the faces to move apart at the crack-tip. CTOD is referred to the stress and defect size by an equation of the form:

$$\delta_t = \frac{K_I^2}{\sigma_y E} \quad (2-17)$$

where σ_y is a yield stress in uniaxial tensile test.

In ferrite steel, the macroscopic crack causes local stress concentration and deformation, while the microscopic crack may be nucleated at the carbides, inclusions and secondary phases. Once the microcrack is formed, it propagates into the ferrite grains in the form of cleavage fracture when a sufficiently large shear stress is applied. Essentially, the size and distribution of carbides are the most important factor. If the carbide particles are spherical, then the fracture strength is:

$$\sigma_f = \left[\frac{\pi E \gamma_p}{2c_0} \right]^{\frac{1}{2}} \quad (2-18)$$

where c_0 is the carbide diameter.

In contrast, in bainitic and martensitic steels, lath structures with intervening low

angle boundaries are formed in packets with larger misorientation packet-boundaries [Bhadeshia, 2001]. In these structures, the packet width is the most important factor for cleavage crack propagation, thus the fracture strength is:

$$\sigma_f = \left[\frac{4E\gamma_p}{(1 - \nu^2)d_p} \right]^{\frac{1}{2}} \quad (2-19)$$

where d_p is packet width [Bhadeshia and Honeycombe, 2006].

The creation of a cleavage crack does not mean that fracture necessarily occurs. If the crack cannot be grown just after nucleation, the tip may become blunted by deformation and associated dislocation motion, in which case of the crack may not propagate. Even if a crack grows, its propagation can be arrested if the applied stress is suddenly becomes lower than that for fracture. Fracture toughness is governed not by the creation of a crack but by its propagation.

2.3.2. The energy release rate

The release rate is often denoted by G and represents the amount of energy per unit area of the crack growth. That is supplied by the elastic energy in the body and by the loading system in creating the new fracture surface area. In terms of the stress intensity factor K , there is an Irwin relationship, for plane stress and plane strain conditions:

$$G = \frac{K^2}{E} ; \text{ plane stress condition} \quad (2-20)$$

$$G = \frac{(1 - \nu^2)}{E} K^2 ; \text{ plane strain condition} \quad (2-21)$$

where ν is the Poisson's ratio.

The total energy release rate in combined mode cracking can be obtained by adding from the different modes, I is for opening or tensile mode, II is for sliding mode and III is for tearing mode [Parton, 1992]:

$$G = G_I + G_{II} + G_{III} = \frac{1 - \nu^2}{E} \left(K_I^2 + K_{II}^2 + \frac{K_{III}^2}{1 - \nu} \right) \quad (2-22)$$

where G_I , G_{II} and G_{III} are the energy release rates for modes I, II and III respectively, K_I , K_{II} and K_{III} are the stress intensity factors for modes I, II and III respectively.

Fracture instability happens when the energy release rate G is larger than the force needed to resist crack propagation. Any excess is converted into kinetic energy which governs the speed of the crack propagation. The total amount of kinetic energy for a crack growth is:

$$E_{kin} = (G - R)dA \quad (2-23)$$

E_{kin} : kinetic energy R : force of crack resistance

with three assumptions; the crack propagation takes place under constant stress, the elastic energy release rate G does not depend on the speed of crack propagation and the crack growth resistance R of material is constant. The crack resistance is a function of the plastic behaviour and fracture characteristics of the material at the crack tip. It is dependent upon strain rate. At the tip of a crack moving at high velocity, the strain rates are very high and it is expected that the material behaves in

a more brittle manner at high crack speeds. The force of crack resistance is independent of crack length under plane strain condition. But, for plane stress condition, the crack resistance can vary with the amount of crack growth. When the crack starts propagating, a further increase of the stress is required to maintain growth.

In stable crack growth, G is equal to R . The crack growth rate as a function of an increase in crack size is shown in Fig. 2.12, where c is the crack size, c_c is the critical crack size, \dot{c} is crack growth rate and v_s is the velocity of sound. In a ductile material, the energy required for crack growth is the same as the amount of work for formation of a new plastic zone at the tip of the advancing crack, plus the work required for initiation, growth and coalescence of microvoids [Broek, 1982].

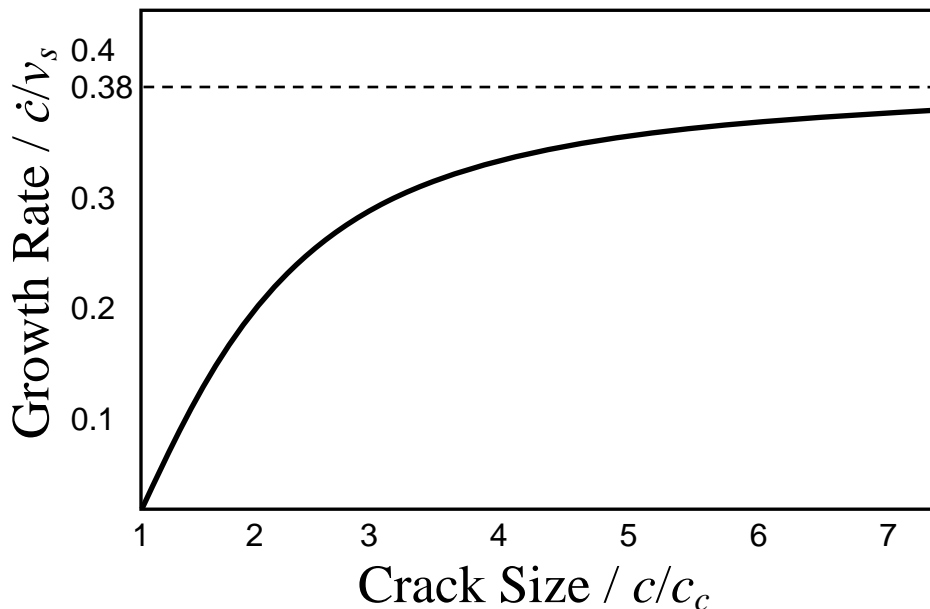


Figure 2.12. A graph for the increase of growth rate with crack size. Adapted from [Broek, 1982].

2.3.3. Ductile to brittle transition

The “ductile-to-brittle transition” is well known for its complicated nature *per se* because it is the region where fracture mechanisms “compete”. Pickering made a linear regression model to predict the “ductile-to-brittle transition temperature” (DBTT) as a function of chemical composition, strength and grain size as follows [Pickering and Gladman, 1963]:

$$T = f(\text{composition}) + g(\text{strength}) - 11.5d^{-1/2} \quad (2-24)$$

T : DBTT / °C f : function of chemical composition

d : grain size / μm g : function of strength

This model was simple but still useful because of the variables considered, *i.e.* composition, strength and grain size. To improve on this requires other features to be considered, such as microstructural parameters like carbide morphology and precipitation hardening, the effective grain size and texture, thermally activated growth processes of tensile mode I and shear mode II cracks, *etc.* [Mintz *et al.*, 1979; Bhattacharjee *et al.*; 2004, Baczynski *et al.*, 1999; Kameda, 1986]. Numerical models have been suggested to introduce fracture mechanism [Gurson, 1975, 1977; Ritchie *et al.*, 1973; Tvergaard and Needleman, 1984, 2000]. Recently, the non-linear models have been proposed using various modelling method such as statistical modelling, fuzzy modelling and network modelling, trying to capture the full complexity of influencing factors quantitatively [Oldfield, 1975; Beremin, 1983; Todinov, 1999; Chen *et al.*, 2004; Moskovic, 1997].

2.3.4. Toughness

The Charpy V notch impact test is the most common empirical method to evaluate the toughness of steels. However, it is hard to analyse because many factors can influence toughness such as grain size, alloying elements, processing parameters, texture and work of fracture. Nevertheless, many researchers have tried to discover quantitative relationships, linear or non-linear, between the Charpy impact energy and potential influencing factors [Chen *et al.*, 2004].

Grain size

As shown in Fig. 2.13, the grain refinement enhances both the fracture and yield strength [Low, 1954]. The relationship between grain size and fracture strength was introduced by work of Cottrell [1958]:

$$\sigma_f = \sigma_y + \Delta\sigma \geq \frac{C\mu\gamma_s}{k_y} d^{-1/2} \quad (2-25)$$

where σ_f is the fracture strength, σ_y is the yield strength, $\Delta\sigma$ is the increase in yield strength from work-hardening beyond the yield point, C is a constant related to stress state and average ratio of normal to shear stress on the slip plane, μ is the shear modulus, γ_s is the surface energy, k_y is the Hall-Petch slope, and d is the grain size.

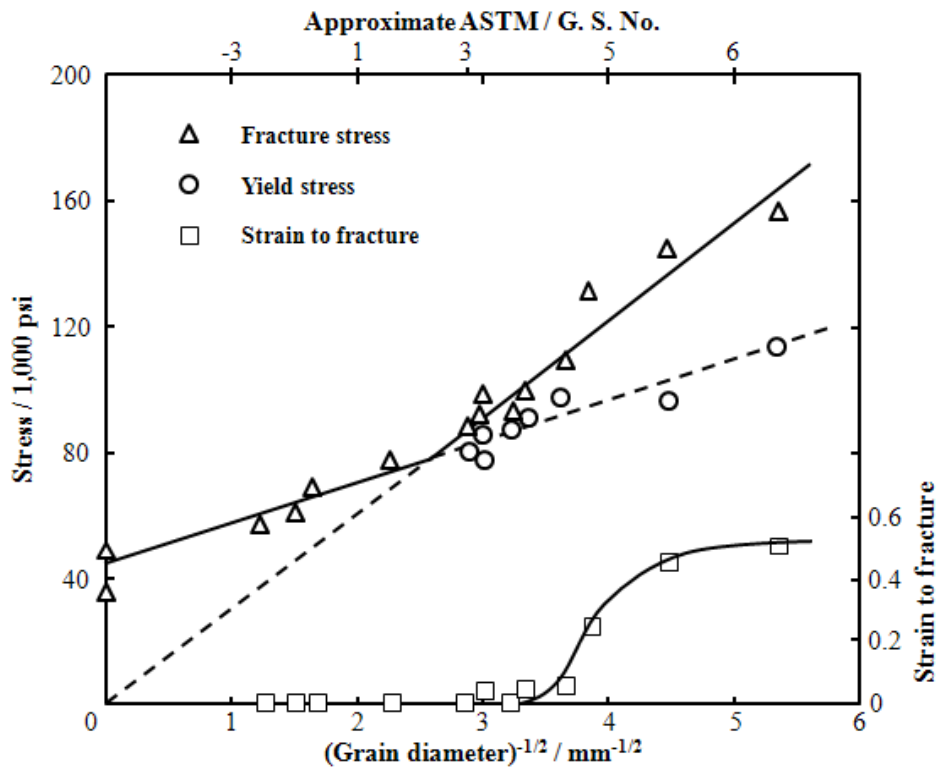


Figure 2.13. Effect of grain size on the yield and fracture stresses for low carbon steel tested in tension at $-196\text{ }^{\circ}\text{C}$. Data from [Low, 1954].

The grain size d is not always the metallographically measured grain size [Gourgues *et al.*, 2000]. Because some clusters of crystals tend to form with little deviation in crystallographic orientation at the boundaries between the individual grains within the collection, such clusters define a crystallographic grain size as opposed to the conventional size. This means that cleavage cracks can propagate without much deviation across these regions with similar crystal orientation, whose size then corresponds to that of the brittle fracture facet. Therefore, it can be defined by the distance across which crack propagates coherently through the $\{100\}$ plane

in BCC and is called effective grain size. In ferrite–pearlite steel, it is well known that the cleavage path is associated with the metallographic grain size. However, in bainitic or martensitic steels, it can correspond to the prior austenite grain size although this is not universally agreed. The effective grain size for those steels can be the packet size defined as the distance between two nearest high–angle boundaries [Naylor and Krahe, 1975; Naylor, 1979; Gourgues *et al.*, 2000; Qiao and Argon, 2003; Bhadeshia, 2001]. A cluster of neighbouring grains sharing a similar orientation, is called the “crystallographic grain” [Pickering, 1967]. The determination of effective grain size requires an assumption of boundary misorientation, for example some values have been taken arbitrarily to be 15° and 18° for the bainitic steels [Kim *et al.*, 2000] and 12° for the thermomechanical controlled rolled steels [Bhattacharjee, 2004]. A better procedure would be to relate the misorientation required to arrest or deflect cracks to the cleavage–fracture facet size.

The crystallographic grain size can vary with depth within a steel plate [Bhattacharjee *et al.*, 2003; 2004] or at positions where the pipe is welded [Yan *et al.*, 2010; Gürgör *et al.*, 2010] because the deformation during hot–rolling is not uniform as a function of depth [Zhu *et al.*, 2007]. Therefore, it is natural that there should exist a corresponding difference in the texture and hence the crystallographic grain size. Thus, a larger crystallographic grain size just below the surface leads to a relatively poor toughness when compared with measurements made at the plate centre where the similarly oriented grain clusters are finer [Bhattacharjee *et al.*, 2003].

Alloying elements and processing variables

Carbon is an important factor in determining toughness, for example, carbide particles can be detrimental to toughness as shown in Fig. 2.14. Large carbides in particular provide crack initiation sites, although fine carbides help improve toughness if they help refine the structure, for example through microalloying. Nitrogen is generally considered to be detrimental to toughness but it has various interactions with other alloying elements. Phosphorus and molybdenum can be detrimental elements because they raise the transition temperature while chromium has little effect [Dieter, 1988].

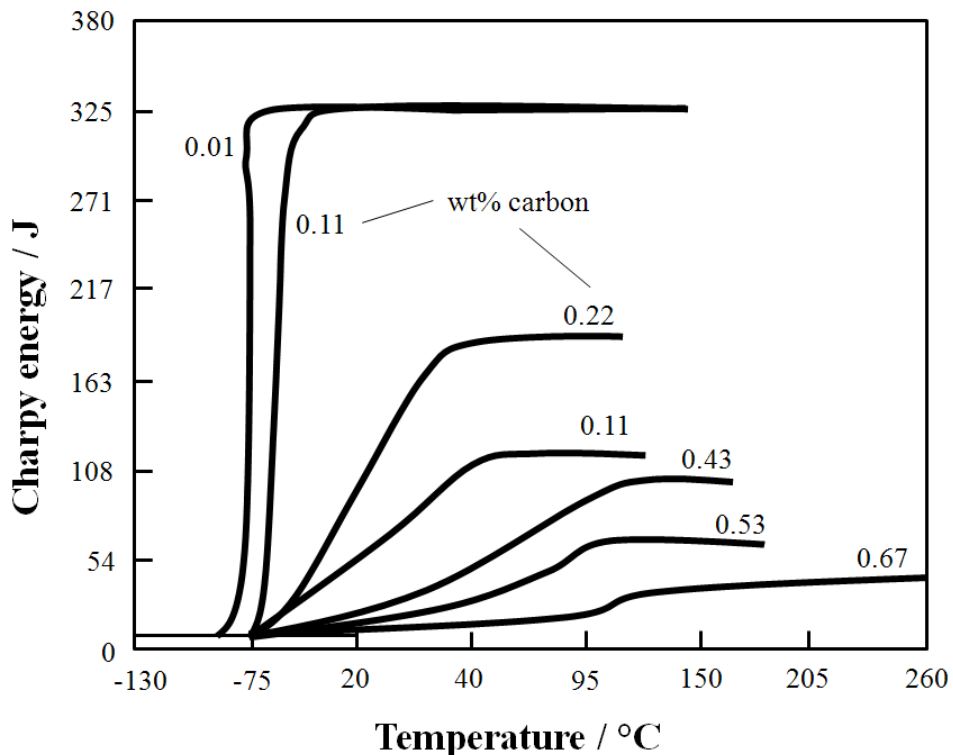


Figure 2.14. The effect of carbon contents on the toughness in plain carbon steels. Data from [Rinebolt and Harris, 1951].

Oxygen can be an embrittling element since it reduces the surface energy of a crack or more commonly, through brittle oxide inclusions. Manganese can be beneficial to toughness if it leads to a reduction in the thickness of grain boundary carbides and redistributes them to intragranular sites. However, over a certain amount, manganese can increase the transition temperature again if it promotes martensite [Stoloff, 1969]. Nickel helps alter the Peierls stress leading to solid solution softening [Spitzig and Leslie, 1971; Gerberich *et al.*, 1981]. Silicon is detrimental for toughness since it reduces the surface energy for cleavage but there are contradictory results [François and Pineau, 2002; Dieter, 1988].

Niobium and titanium can be beneficial to the toughness because they can grain refine while vanadium has little effect [Klassen *et al.*, 1986; Tsunekage *et al.*, 2001]. Titanium below a certain amount is helpful to increase the fraction of acicular ferrite [Beidokhti *et al.*, 2008]. Sulphur is generally considered to be detrimental to the toughness but there are contradictory results with respect to grain refinement [Tsunekage *et al.*, 2001]. With the addition of copper or boron, the toughness can be decreased due to the increase of effective grain size [Shin *et al.*, 2009a].

A low finish-rolling temperature (FRT) can lead a high cleavage fracture stress due to its fine ferrite grain size by heavy deformation but there is an exceptional case to be considered that the elongated ferrite, *i.e.*, banded structure, can provide a continuous path for the cleavage fracture if the fracture surface is parallel to the rolling plane [Sun and Boyd, 2000]. Tempering helps enhance the toughness with decreasing the strength [Merabi and Mintz, 1997]

Texture

The toughness of the rolled steels must depend on texture since the distribution of {100} planes is important in cleavage fracture [Cottrell, 1958; Morrison, 1976; Tyson *et al.*, 1973]. Ductile fracture occurs by the nucleation and coalescence of microvoids [Broek, 1982] which is associated with slip processes. {110}<111> is the main slip system of the body-centred cubic (BCC). So the volume fraction of grains with {110} planes parallel to the notch plane can have an influence. {112} and {123} planes are also associated with slip in BCC crystals, but their interpretation is not clear [Dieter, 1988; Baczynski, 1999; Ju *et al.*, 2007].

2.3.5. Delamination

Delamination has been observed in high-strength low alloy steels [Schofield *et al.*, 1974; Baldi and Buzzichelli, 1978; Dabkowski *et al.*, 1976; Deardo, 1977], in ferritic stainless steels [Mintz, 1980; Chao, 1978], ausformed alloys [McEvily and Bush, 1962], marformed steels [Ray and Basu, 1985] and low carbon steels [Bramfitt and Marder, 1977; Shin *et al.*, 2009b]. It is shown in Fig. 2.15. It arises from weakness parallel to the rolling plane of the steel, because hot-rolling is terminated at temperatures within the $\alpha + \gamma$ phase field, texture, inclusion alignment on the rolling plane, intergranular failure along prior austenite boundaries, segregation of phosphorus and sulphur and any aspect that leads to anisotropy [Bourell, 1983; Tamura *et al.*, 1988].

Delamination is regarded macroscopically as brittle fracture behaviour which is

concerned with a decrease of upper shelf energy in Charpy tests [Brozzo and Buzzichelli, 1976; Verdeja *et al.*, 2003]. However, Song *et al.* proposed that delamination can something reduce the DBTT [Song *et al.*, 2005]. So-called delamination toughening has long been known to lead to improved toughness in a wide variety of materials, for example in ceramics [Clegg *et al.*, 1990], carbon [Sakai *et al.*, 1986], and fine-grained steels [Kimura *et al.*, 2008, 2010; Inoue *et al.*, 2010; Mintz *et al.*, 2007]. In particular, delaminations that form parallel to the plate surface can lead to a reduction in the impact transition temperature [Maina *et al.*, 2011] although excessive fissuring can compromise the upper shelf energy of Charpy tests [Mintz *et al.*, 2008].

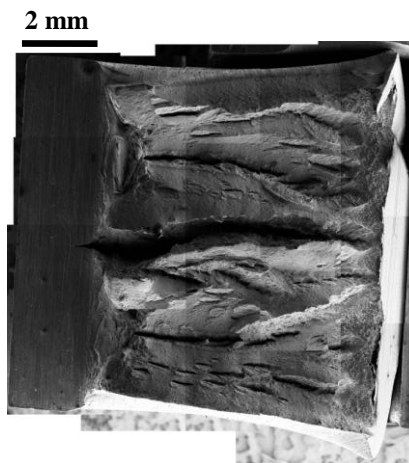


Figure 2.15. Fracture normal to the length of the Charpy notch is a “split” or “delamination” which influences the impact energy measured.

2.4. Toughness Anisotropy

The orientation dependence of toughness is a well-known phenomenon for hot-rolled steels in general [Fegredo, 1975; Ray *et al.*, 1995]. Fig. 2.16 shows the effect of specimen orientation on the Charpy transition-temperature curves of a rolled plate [Mintz *et al.*, 1976; Dieter, 1988]. As will be seen later, there is also considerable work in the context of pipeline steels. There are three particular factors which are emphasized in discussing toughness anisotropy: non-uniform distribution in the size and shape of inclusions, microstructural anisotropy due to banding or elongated grain structure, and crystallographic texture.

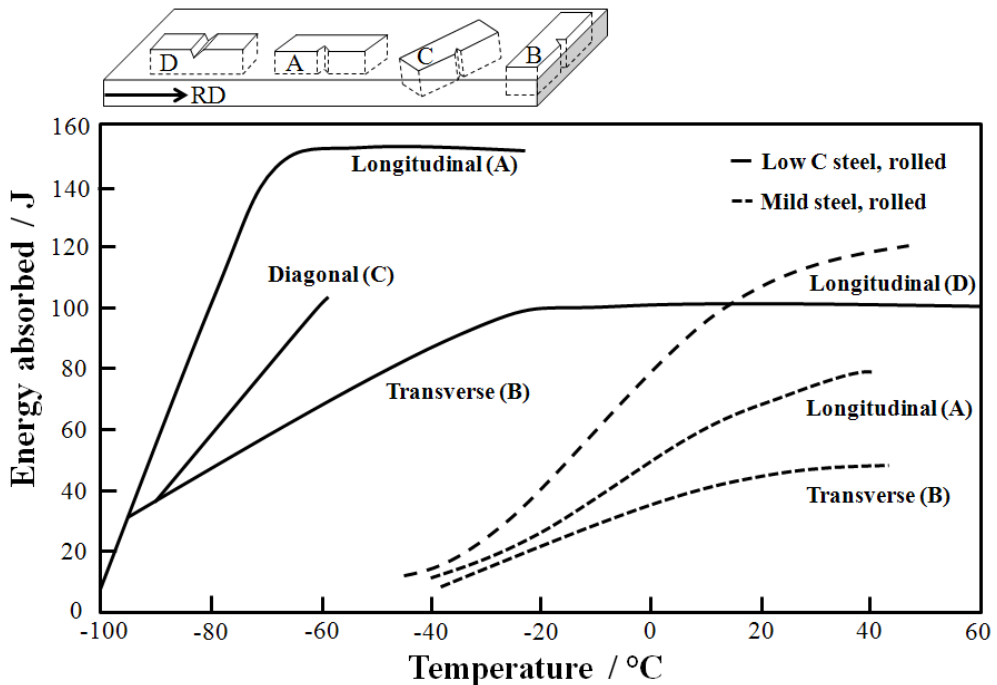


Figure 2.16. Effect of specimen orientation of Charpy transition-temperature curves of a rolled plate. Data from [Mintz *et al.*, 1976; Dieter, 1988].

2.4.1. Inclusions

Inclusions influence anisotropy because they often are associated with the initial solidification process and any solidification-induced chemical segregation; others may precipitate in the austenite at high temperatures prior to the hot deformation that the cast steel is subjected to. Common inclusions include the manganese sulphides, silicates and alumina and combinations of oxides depending on the particular steelmaking route, and the hot deformation needed to shape the steel has the effect of orienting these phases along the principal plastic-strain directions. Some phases such as manganese sulphides and silicate can deform along with the steel and hence become elongated, whereas others fragment and form stringers along these same directions [Sims, 1959; Baker and Cameron, 1972]. The inclusions can as a consequence, lead to a variety of anisotropies, particularly with respect to tensile elongation, bend properties, fracture mode and fracture toughness. The toughness in cases where the Charpy notch is in the rolling direction, is found to be much lower than when it is normal to that orientation [Hodge *et al.*, 1959; Kramer *et al.*, 1987; Burnos *et al.*, 1988; Wilkowski *et al.*, 1991; Mohan *et al.*, 1995a]. It is the directionality of MnS inclusions that is found responsible for the orientation dependence of toughness on the forging reduction ratio [Harada *et al.*, 1987]. A typical microstructure of ferritic grains, pearlite bands and shape of flattened MnS is illustrated in Fig. 2.17 [Benzerga *et al.*, 2004].

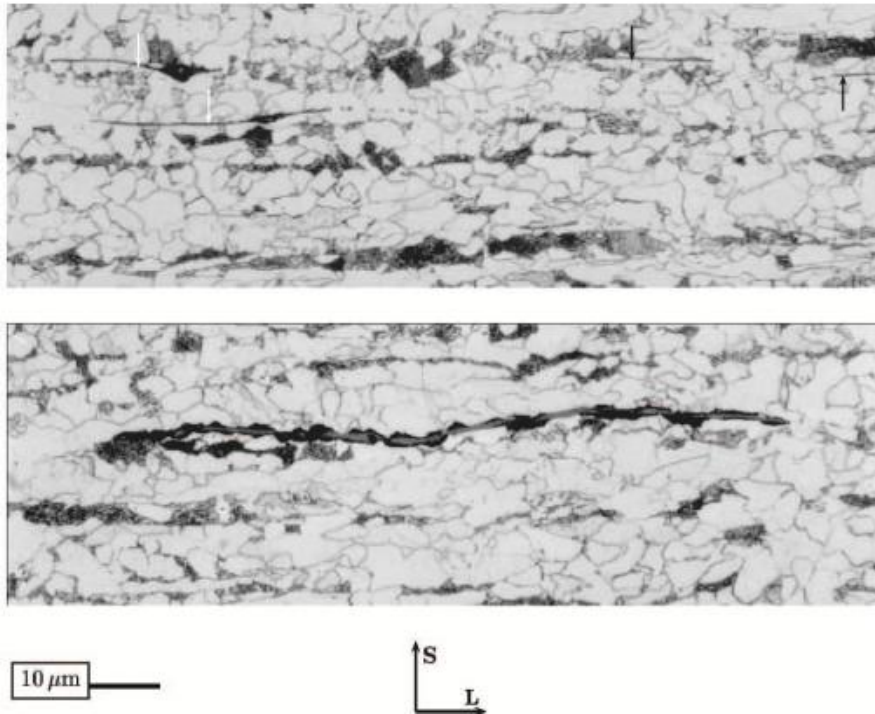


Figure 2.17. Steel microstructure consisting of ferritic grains, pearlite bands and shape of flattened MnS (arrows) and mixed oxide–MnS (white arrows) both in ferrite in upper image and crushed MnS in pearlite in lower image. ‘S’ and ‘L’ stand for the short transverse and longitudinal directions respectively. Reproduced from [Benzerga *et al.*, 2004] with permission from Elsevier.

Fig. 2.18 illustrates the impact energy values for two steels with different sulphur contents. The interesting observation is that the degree of anisotropy is less for the higher sulphur steel. This is because the sulphides in the low–sulphur alloy were relatively more elongated [Mohan *et al.*, 1995b]. These observations also emphasize the role of inclusions in nucleating and linking voids, since the data illustrated all

represent the ductile mode of failure, so that the observed anisotropy is a direct consequence of the shape of the inclusions. It is important to note also that the sulphides may not be uniformly distributed within the steel in which case correlations of properties with the average concentration become less certain [Medinskaya *et al.*, 1981].

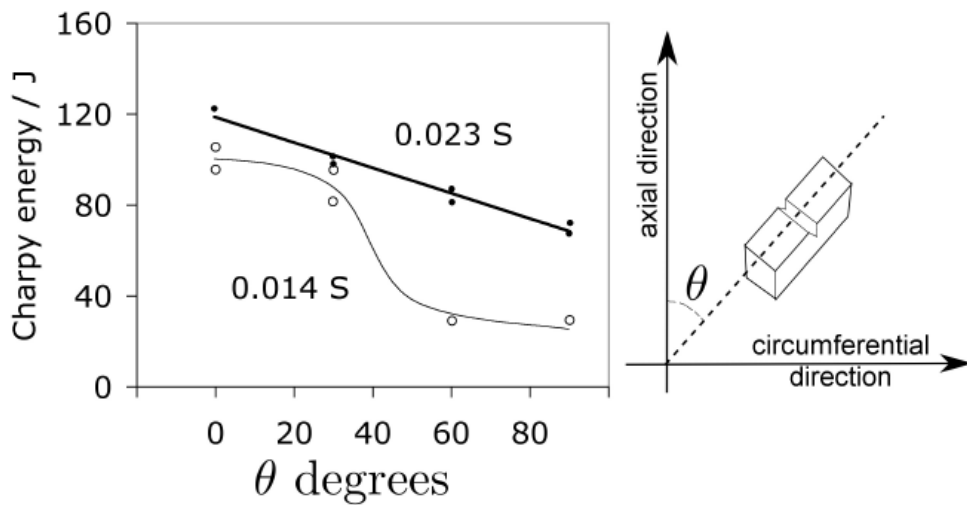


Figure 2.18. Charpy energy as a function of orientation and sulphur content (wt%). The tests were arranged so that all of the samples undergo ductile failure. Courtesy of H. K. D. H. Bhadeshia [Bhadeshia, 2011]. Data for A106 grade B steel pipe, from [Mohan *et al.*, 1995b].

Nonmetallic inclusions influence properties by nucleating cleavage or voids. It is often the case that the inclusions serve to concentrate stress so that adjacent, and more brittle cementite particles can initiate cleavage [Baker *et al.*, 1986]. This is

because inclusions like MnS can lose cohesion with the matrix before the onset of cleavage. The resulting hole provides the greatest stress concentration at the tip of an elongated inclusion, so that loading normal to the plane of the inclusion leads to poor toughness, in contrast to the case where the principal loading is parallel to the long axis, when the stress concentration due to decohesion is of minor importance. This of course, leads to anisotropy of toughness [Baker *et al.*, 1986]. The anisotropy can be reduced by using lower rolling reductions [Tomita, 1990] so that the inclusions themselves have smaller aspect ratios (length divided by thickness).

Inclusions are not simply a problem of pipelines or anisotropy, and many methods have been introduced over time to control the shape and size of non-metallic particles, particularly the manganese sulphides. The most obvious is to reduce the concentration of sulphides but anisotropic toughness persists even when the concentration is much less than 0.01 wt% [Hodge *et al.*, 1959; Matrosov and Polyakov, 1976]. Presumably, as emphasised in [Mohan *et al.*, 1995b], it is the shape of the particles that plays the major role in the orientation dependence of properties. Cross-rolling can mitigate the effects of manganese sulphide even when the sulphur concentration is as large as 0.06 wt% [Hodge *et al.*, 1959], but the method is not practical for most pipelines where the steel plate has to be long in one direction. The addition of cerium, zirconium or titanium helps reduce the plasticity of MnS, thus modifying the inclusion shape into a more spheroidal form [Matrosov and Polyakov, 1976].

Imai and co-workers did some interesting experiments in which the steel was heat-treated in a variety of ways to modify the manganese sulphide layers present in the

hot-rolled state (Fig. 2.19) [Imai *et al.*, 1982; 1985]. Although the anisotropy in mechanical properties decreased when the layers were broken up into spherical particles, it was not completely eliminated when the sulphur concentration exceeded about 0.01 wt%. This is because at high concentrations, the spheroidised particles remained aligned as strings (Fig. 2.19e). Similar observations have been reported in the context of bearing steels subjected to rolling-contact fatigue, where strings of non-metallic particles aligned normal to the contact surface are much more harmful than those parallel to that surface [Courbon *et al.*, 2003], and there is a strong dependence of life on the length of these strings of inclusions [Eckel *et al.*, 1999]. The role of inclusions in promoting the orientation dependence of toughness also is a function of the steel microstructure; a large fraction of pearlite reduces anisotropy by becoming the primary source for void initiation [Imai *et al.*, 1982].

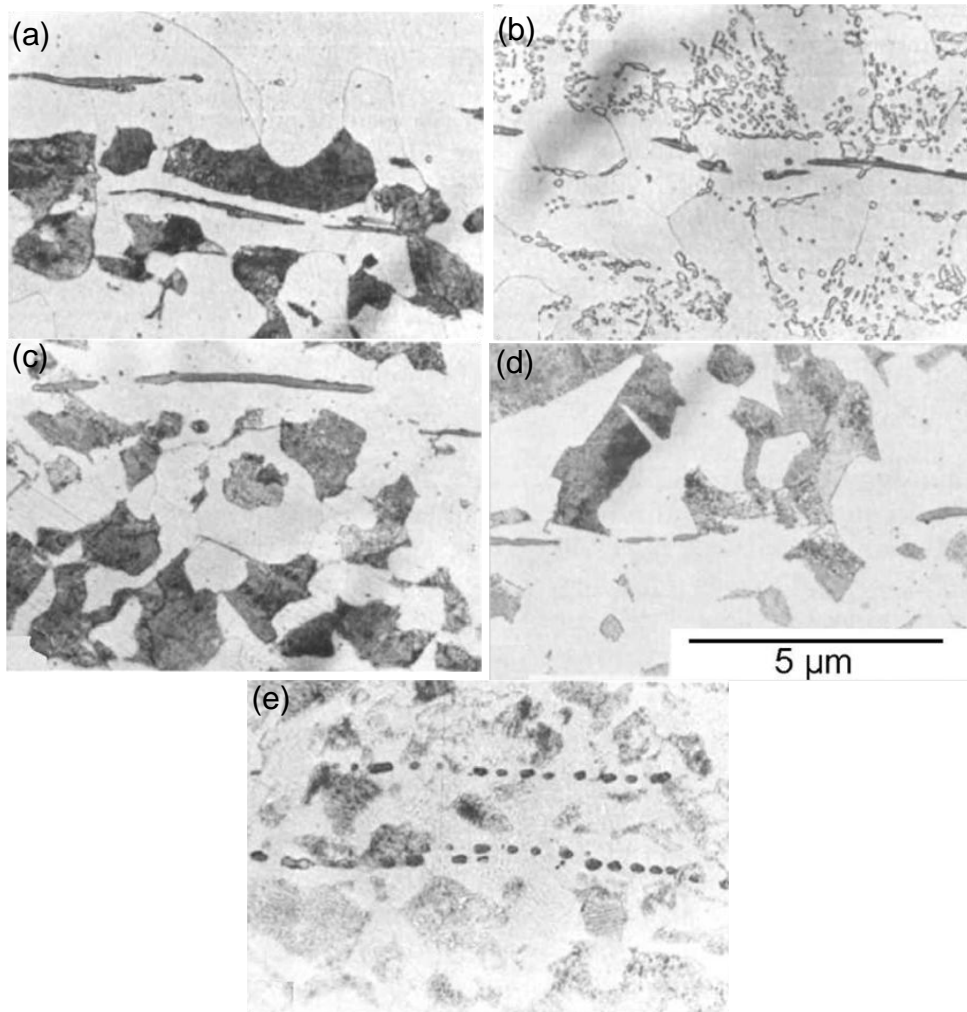


Figure 2.19. Fe-0.36C-0.22Si-0.73Mn-0.02P-0.025S wt%. (a) As-received hot-rolled condition. (b) Following spheroidisation heat-treatment involving dwell and cycling between 750 and 690 °C followed by furnace cooling. (c) Austenitisation at 950 °C for 1h followed by air cooling. (d) Homogenisation at 1300 °C for 1h followed by furnace cooling. (e) Homogenisation at 1300 °C for 4 h followed by furnace cooling. Reproduced from [Imai *et al.*, 1982] with permission from Elsevier.

2.4.2. Microstructural anisotropy

A typical microstructure in a hot-rolled low-alloy steel is illustrated in Fig. 2.20a [Tau *et al.*, 1993; Korda *et al.*, 2006]. There are planar patches of pearlite parallel to the rolling plane. Microstructural banding is often more pronounced in sections containing the rolling direction than in those containing the transverse direction [Thomson and Howell, 1992; Chae *et al.*, 2000]. Such banding is known to be responsible for the orientation dependence of properties [Matrosov and Polyakov, 1976; Wilson *et al.*, 1975], and homogenisation to mitigate the banding reduces anisotropy [Garwood, 1984].

Banding occurs primarily because of the segregation of solutes in the last regions of the liquid to solidify during the cooling of steel from the molten state. The low-alloy steels which exhibit banding typically begin solidification as δ -ferrite so that elements such as manganese, silicon, phosphorus and sulphur are partitioned into the interdendritic regions which then solidify with a higher than average concentration of these solutes. Subsequent deformation, for example by hot-rolling, causes these regions to spread out as bands. The segregation of concern is of substitutional solutes such as manganese (Fig. 2.20b). Carbon also segregates during solidification but it diffuses rapidly as the steel cools through the austenite phase field until its chemical potential becomes uniform. The silicon concentration, which is not illustrated in Fig. 2.20b, was also found to be in phase with the pearlite bands. Although silicon is a ferrite stabiliser, its influence on the transformation in typical steels of interest here is much smaller than that of manganese.

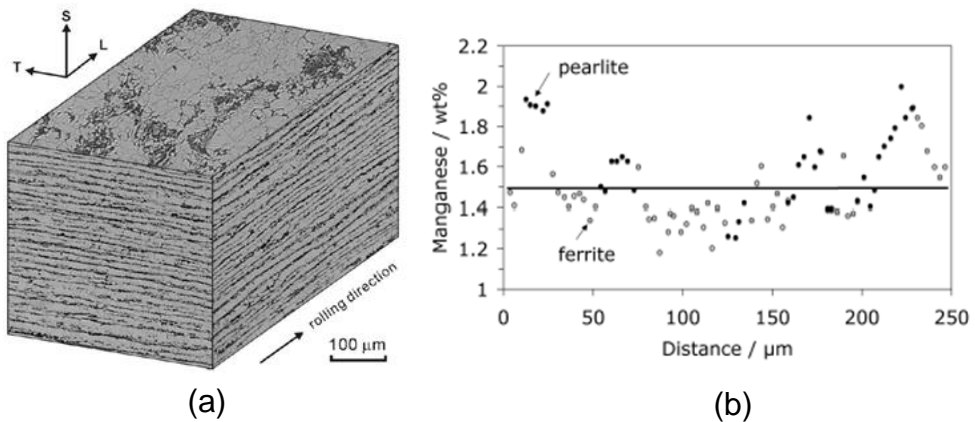


Figure 2.20. (a) Banding in hot-rolled ferrite-pearlite steel, Fe-0.15C-0.16Si-1.07Mn wt%. 'S', 'T' and 'L' stand for the short transverse, transverse and longitudinal directions respectively, in the rolling frame of reference. Reproduced from [Korda *et al.*, 2006] with permission from Elsevier. (b) The location of pearlite relative to the manganese concentration. Courtesy of H. K. D. H. Bhadeshia [Bhadeshia, 2011]. Data from [Thomson and Howell, 1992]

The ferrite-pearlite banding evident in Fig. 2.20a occurs when the regions which are depleted in austenite-stabilising elements decompose into ferrite, before the transformation can occur in other areas [Jaczak *et al.*, 1956]. As a result, carbon is partitioned into the adjacent substitutional-solute rich austenite, which ultimately becomes the pearlite. The microstructural banding therefore correlates with the segregation pattern and the correlation becomes more pronounced when the microstructure is generated by slow cooling. This is because larger cooling rates are

associated with greater undercoolings, which permit ferrite to form even in manganese-enriched regions.

A reduction in the carbon concentration also helps make the steel more isotropic because it is the partitioning of carbon into the manganese-rich regions that leads to the formation of pearlite bands [Matrosov and Polyakov, 1976].

The development of microstructural banding is illustrated in Fig. 2.21. As pointed out previously, the highly mobile carbon homogenises during cooling through the austenite phase field. However, there are gentle variations which occur in concert with the manganese, as the carbon maintains a uniform chemical potential in the austenite. Manganese lowers the activity of carbon and hence the manganese-rich regions are associated with a somewhat higher carbon concentration [Kirkaldy *et al.*, 1962]. The dependence of the spatial distribution of carbon on that of substitutional solute in austenite was originally thought to be the cause of banding [Jaczak *et al.*, 1956]. Bastien, however, considered the banding to be due to the substitutional solutes and Kirkaldy *et al.* later showed that this is indeed the dominant effect [Bastien, 1957; Kirkaldy *et al.*, 1962].

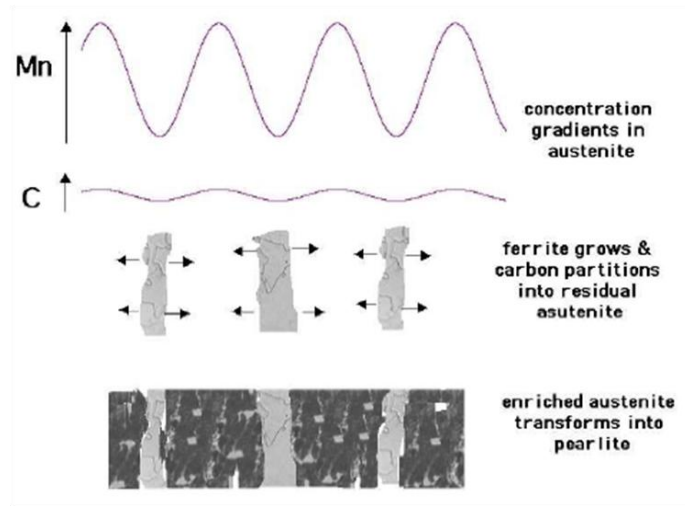


Figure 2.21. An illustration of the common mechanism of banding [Bhadeshia, 2010, 2011]. Note that banding has irregularities so it is not entirely an accurate reflection of the chemical segregation pattern [Thomson and Howell, 1992]. Courtesy of H. K. D. H. Bhadeshia.

An alternative mechanism is found in steels containing relatively large sulphur concentrations [Kirkaldy *et al.*, 1963]. Manganese sulphides then precipitate in the regions containing a large average concentration of manganese. As a consequence, the manganese is bound in the sulphide which is surrounded by a manganese-depleted zone where ferrite forms. The ferrite partitions carbon into the adjacent zones which have a low average concentration of manganese, which transform into pearlite. The position of the ferrite bands is thus shifted into locations where the average Mn concentration is large, but where the Mn is tied up as sulphides (Fig. 2.22).

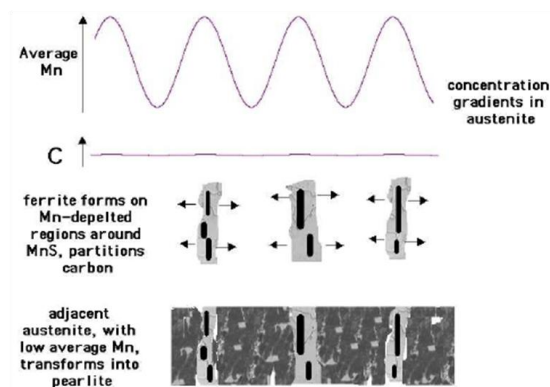


Figure 2.22. The mechanism of banding in steels containing substantial quantities of manganese sulphides [Bhadeshia, 2010, 2011]. Courtesy of H. K. D. H. Bhadeshia.

Other kinds of microstructural anisotropy also have been shown to correlate with toughness in pipeline steels. Fig. 2.23 shows the case for the X80 grade pipeline steel where the minimum in Charpy toughness in the ductile–brittle transition temperature range corresponds to the smallest fraction of lower bainite on the fracture plane. Also the study suggested that the non–uniform grain shape is related to the anisotropy of the Charpy toughness [Petrov *et al.*, 2007a, 2007b]. One difficulty with this interpretation is that the fraction should be independent of the plane of section provided that the number of measurements made is statistically meaningful. It is also not clear why the minimum correlates with the smallest lineal intercept since a finer microstructural scale should lead to better toughness. As pointed out by Garcia *et al.*, the real explanation in the context of the X80 steels is

likely to be a complex combination of microstructure and crystallographic texture; the latter aspect is discussed in the next section [Garcia *et al.*, 2007]. Kichkina *et al.* also discussed in ferrite–bainite microstructure that the bainite morphology oriented predominantly in the intermediate direction to the rolling direction, such as 50°, is needed to be considered for anisotropy of toughness in API–X70 steel, since the density of grain boundaries and interphase boundaries in that direction are minimum which is corresponding to the minimal obstacles of crack propagation [Kichkina *et al.*, 2011]. Sun and Boyd investigated the effect of processing parameter on anisotropy of cleavage fracture stress in microalloyed linepipe steel. The anisotropy of fracture stress increases with decreasing FRT above non–recrystallisation temperature of austenite and the factor for anisotropy was determined from microstructural anisotropy such as elongated grain and banding [Sun and Boyd, 2000]. Some early study also suggests that an elongated grain structure, for example that generated by warm–rolling with a low finish–rolling temperature, has been shown to cause variations in the impact properties according to direction relative to the elongated structure [Mintz *et al.*, 1978]. Okuda *et al.* also reported that the DBTT in longitudinal direction is lower than transverse direction due to elongated grain in the extruded oxide dispersion strengthened (ODS) ferritic steels [Okuda *et al.*, 2009].

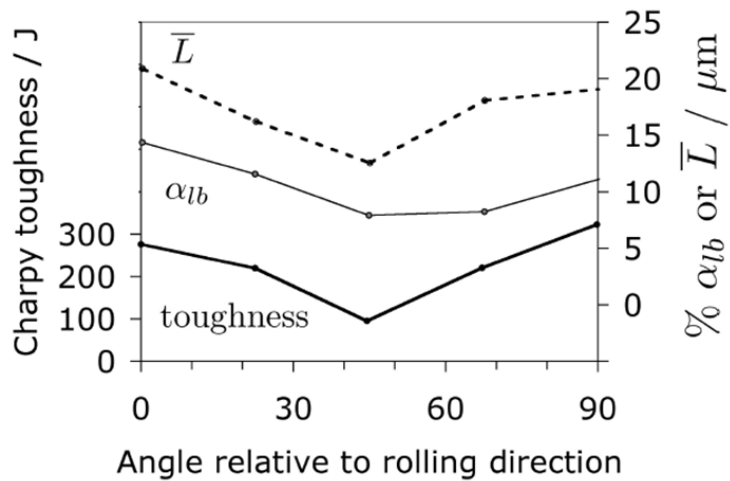


Figure 2.23. The Charpy toughness at $-60\text{ }^{\circ}\text{C}$, percentage of lower bainite (α_{lb}) and mean lineal intercept (\bar{L}) as a function of the angle in degrees, relative to the rolling direction. Courtesy of H. K. D. H. Bhadeshia [Bhadeshia, 2011]. Data for X80 pipeline steel adapted from [Petrov *et al.*, 2007b]

2.4.3. Crystallographic texture

Texture implies a non-random distribution of crystal orientations and clearly must influence the isotropy of a polycrystalline material. Kotrechko *et al.* investigated the effect of texture on the anisotropy of the cleavage stress of metals by theoretical calculation. It shows that the non-uniform distribution of crystallographic planes is the main reason for the cleavage-stress anisotropy in the textured polycrystals [Kotrechko *et al.*, 2004]. Mintz *et al.* investigated the influence of texture on the impact properties of controlled rolled steels, and suggested that the role of texture

on the directionality of impact properties is small and largely on ductile fracture [Mintz *et al.*, 1976]. Inagaki and co-workers focused on controlled rolled high strength steel with several textured specimens of different chemical compositions. It showed that $\{100\}_\alpha$ cleavage plane is related qualitatively to the anisotropy of toughness. In particular, it pointed out that anisotropy of toughness is induced with the $\{113\}$ texture, which is placed between $\{110\}$ and $\{112\}$ planes, parallel to the rolling plane. Thus, the impact transition temperature peaked in the intermediate directions such as 45° to the rolling direction, and correlated this to the texture which favoured cleavage [Inagaki *et al.*, 1975]. Bourell and Sherby also discussed the effect of strong $\{001\}\langle 110\rangle$ texture component corresponding to lower Charpy energy of diagonal specimens than that of longitudinal specimens at various test temperatures in warm-rolled low carbon steel [Bourell and Sherby, 1983].

The plates used in the manufacture of pipeline steels are thermo-mechanically processed and hence are textured. Baczynski *et al.* showed that components of the macroscopic texture can be correlated with the observed anisotropy of impact toughness in niobium-microalloyed steels. It is well known that in the ductile fracture region corresponding to relatively high test temperatures, the distribution of $\{110\}_\alpha$ and $\{112\}_\alpha$ slip planes has a greater influence on toughness than that of the $\{100\}_\alpha$ cleavage planes. The toughness anisotropy associated with ductile fracture correlates with the $\{112\}\langle \bar{1}10\rangle_\alpha$ component, and for cleavage fracture with the $\{001\}\langle 110\rangle_\alpha$ and $\{110\}\langle 001\rangle_\alpha$ components if they exist [Baczynski *et al.*, 1999]. Ju *et al.* also reported that the anisotropy of toughness at room temperature might be related to the distribution of $\{110\}_\alpha$ planes as a function of angle relative to the

circumferential direction in API-X65 linepipe steel [Ju *et al.*, 2007].

It has been suggested that the partial splitting or delamination of Charpy specimens during macroscopically ductile fracture, following an impact test, is related to separation on $\{100\}_\alpha$ cleavage planes [Verdeja *et al.*, 2003]. Such a split is suggested to lead to a decrease in toughness in the upper shelf regime, and in a reduction in the ductile–brittle impact transition temperature. This does not seem correct; a decrease in DBTT is an increase in toughness, and the evidence has not been presented well to support this notion, and since the split is not parallel to the plane containing the notch, it could be argued that an improvement in toughness may follow due to the additional work of fracture at the split. However, if the separation occurs in the 100% ductile range then the impact energy decreases [Verdeja *et al.*, 2003], but if it takes place at low temperatures then the enhancement of toughness is observed as mentioned in the previous section [Song *et al.*, 2005].

Mechanical anisotropy depends on many factors other than texture, so it is not surprising that there are studies which reach the conclusion that crystallography has little or no role to play in determining the orientation dependence of properties. Mintz *et al.*, found no indication of texture having any influence on the anisotropy of impact toughness in the transition temperature especially when the grain structure itself is directional, so the microstructural anisotropy is severe [Mintz *et al.*, 1978]. Fegredo *et al.* found no significant relationship between toughness and the macroscopic texture in low-carbon steels containing 0.002–0.007 wt% sulphur, produced using different rolling temperatures [Fegredo *et al.*, 1985]. Microstructural anisotropy and elongated sulphides seemed to have the strongest influence. Kasada

et al. investigated the effect of texture and microstructure on the mechanical anisotropy in hot-extruded bar of oxide dispersion strengthened (ODS) ferritic steels with {110} textured along the extrusion direction (ED) parallel to the rolling direction (RD), and the toughness anisotropy was induced by the combined effect of elongated grains and small particles along ED, not by texture [Kasada *et al.*, 2011]. Garcia *et al.* reported that both microscopic and macroscopic textures had negligible influence on the anisotropy of properties in X80 steel, the main cause being associated with an uneven distribution of carbide-rich microstructural constituents [Garcia *et al.*, 2007]. Pyshmintsev *et al.* also reported that the modern X80 linepipe tends to show no clear correlation between the {100} planes and ductile fracture parallel to the rolling plane [Pyshmintsev *et al.*, 2012]

III. Experimental

3.1. Sample Preparation

The steels used in the present study were two API-X80 steels and four API-X70 steels. Their chemical compositions and processing parameters are shown in Tables 3.1 and 3.2 respectively. All the conditions meet the API 5L specification for linepipe steels [API Recommended Practice, 1996].

The slabs were subjected to austenitisation between 1100 and 1180 °C to dissolve all the alloying elements and to minimize grain size of recrystallised austenite. These were followed by severe rolling to obtain fine grain size for all the steels [Tamura *et al.*, 1988; Suh *et al.*, 2008]. X80_A, X80_B and X70_A have different compositions but similar processing variables; rolling was finished and cooling was started above A_{r3} , in order to investigate the effect of composition on the toughness anisotropy. In contrast, X70_B, X70_C and X70_D have same compositions but different processing variables; rolling was finished and cooling was started above A_{r3} for X70_B, rolling was finished above A_{r3} but cooling was started between A_{r1} and A_{r3} for X70_C, and rolling was finished and cooling was started between A_{r1} and A_{r3} for X70_D, in order to investigate the effect of processing variables on the orientation dependence of toughness.

The orientations of the specimens were determined as L, D and T having the long axes of the test specimens inclined at 0°, 45° and 90° respectively to the rolling direction (RD).

Table 3.1. Chemical compositions of the target steels (wt%).

Steels	C	Mn	Si	P+S	Nb+Ni+Mo	Ti+Al	V+Cr+Cu	N
X80_A	< 0.08	< 2.0	0.21	< 0.013	< 0.8	0.03		< 0.0036
X80_B	< 0.06	< 2.0	0.31		< 0.5	0.02	0.30	
X70_A	< 0.08	< 1.7	0.25		< 0.4	0.03	0.15	
X70_B	< 0.07	< 1.7	0.25		< 0.7	0.05	0.20	
X70_C	< 0.07	< 1.7	0.25		< 0.7	0.05	0.20	
X70_D	< 0.07	< 1.7	0.25		< 0.7	0.05	0.20	

Table 3.2. Processing parameters of the target steels.

Steels	Reheating	Cooling			Final
	Temp. (°C)	SCT* (°C)	FRT* (°C)	CT* (°C)	Thickness (mm)
X80_A	1100 ~ 1180	Above A _{r3}	Above Ar ₃	< 550	18
X80_B	1100 ~ 1180	Above A _{r3}	Above Ar ₃	< 550	18
X70_A	1100 ~ 1180	Above A _{r3}	Above Ar ₃	< 550	18
X70_B	1100 ~ 1180	Above A _{r3}	Above Ar ₃	< 550	21.6
X70_C	1100 ~ 1180	Between A _{r1} and A _{r3}	Above Ar ₃	< 550	21.6
X70_D	1100 ~ 1180	Above A _{r1}	Between A _{r1} and A _{r3}	< 550	21.6

* SCT, FRT and CT stand for start cooling temperature, finish rolling temperature and coiling temperature respectively.

3.2. Mechanical Tests

3.2.1. Tensile

The tensile specimens were machined according to the flat-test specimen ASTM E8 standard. The geometry with dimensions and the orientation are illustrated in Fig. 3.1. The experiments were conducted on a Zwick/Roell Z100 tensile machine at room temperature, using a crosshead speed of 3.6 mm min^{-1} (strain rate approximation 0.001 s^{-1}) with full-sized sheet type test coupons each with a gauge length of 2 inch.

3.2.2. Charpy

The Charpy specimens were machined according to the ASTM A370 standard. Charpy V-notched specimens $10 \times 10 \times 55 \text{ mm}$ in size, each with a 2 mm-deep V-notch, were used in tests conducted between ambient temperature to $-100 \text{ }^\circ\text{C}$. The experiments were performed on a Zwick/Roell BRA307204 Charpy impact machine of maximum recordable impact energy of 750 J. The test temperature was controlled using a K-type thermocouple attached to the specimen. Fig. 3.2a shows the conventionally specified orientations of the Charpy specimen relative to the steel processing directions, with L-T, T-L and D-D designations, in which the first letter represents the sample direction and the second the impact direction. The notches in this case are all normal to the plate. Fig. 3.2b shows additional specified orientations of the Charpy specimen but with the notches parallel to the plate, with

L–S, T–S and D–S. Here, S stands for short transverse direction parallel to the plate normal. Note that the planes on which fracture occurs are the same for the conventional and additional orientations in Fig. 3.2, but the difference comes from the direction of impact during the Charpy test. The DBTT was determined from the Charpy curve as the temperature corresponding to the half value of the upper shelf energy.

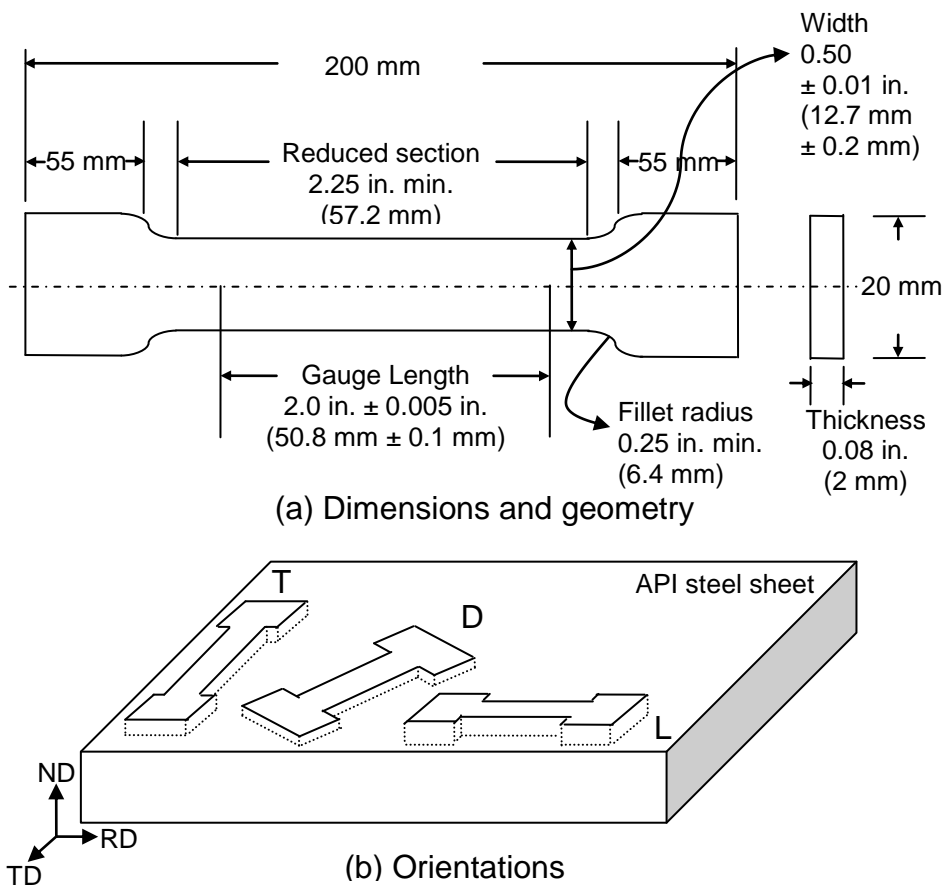


Figure 3.1. Tensile specimens. (a) Dimensions and geometry, (b) orientations. L, D and T stand for longitudinal, diagonal and transverse respectively.

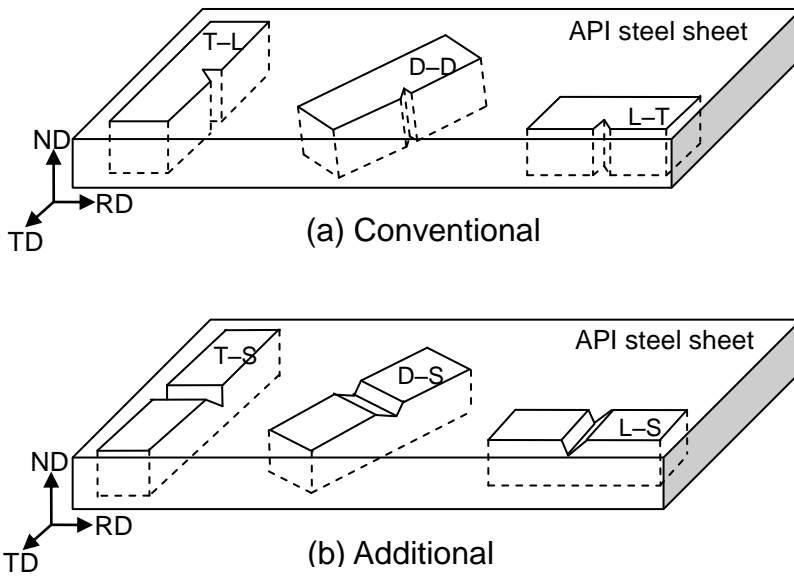


Figure 3.2. Charpy specimens. (a) Conventional, (b) additional orientations. L, D, T and S stand for longitudinal, diagonal, transverse and short transverse respectively.

3.2.3. Hardness

The hardness tests were carried out in two ways, macroscopic tests using a Wilson Wolpert 430/450-SVD tester with a load of 10 kgf, dwell time of 10 s and magnification of x100. The other was micro-hardness using a Future-Tech FM-700 tester with a load of 50 gf, dwell time of 10 s and magnification of x500 to characterise specific microstructural constituents.

3.3. Microstructural Observations

3.3.1. Metallography

Most of the observations of microstructure and crystallographic texture were carried out on 4 surfaces, which are the RD–TD surface and the surfaces parallel to the fracture surfaces of L–T, D–D and T–L in conventional Charpy specimens. The surfaces metallographically prepared, but the details vary and will be mentioned in context.

3.3.2. Optical and scanning electron microscopy

Micrographs were taken at random locations of the designated 4 surfaces in all the steels investigated using a LEICA DM4000M optical microscopy (OM) and a Carl Zeiss Ultra 55 field–emission scanning electron microscopy (FESEM). The samples were prepared using standard methods. The surfaces were ground using 200–grit silicon carbide paper and mechanically polished with diamond paste of 0.1 μm . The samples were etched using either 2% nital solution (2 ml nitric acid with 98 ml methanol) to observe ferrite grain boundaries, or colour tint etching (4% picral mixed with few drops of concentrated hydrochloric acid and 10% aqueous sodium metabisulfite solution) for multiphase steels to determine the fractions of phases with image processing [De *et al.*, 2003].

3.3.3. Transmission electron microscopy

For transmission electron microscopy (TEM), thin foil samples were prepared from 80~90 μm and 3 mm diameter discs, which were electro-polished in 5% perchloric acid with 95% acetic acid at 15 $^{\circ}\text{C}$. The experiments were carried out on a JEOL JEM 2100F field-emission transmission electron microscopy (FETEM).

3.3.4. Energy dispersive X-ray spectroscopy and electron back-scattered diffraction

For orientation imaging with crystallographic information using electron back-scattered diffraction (EBSD), and for inclusion detection using energy dispersive X-ray spectroscopy (EDS), samples were mechanically polished with colloidal silica in the final polishing stage. Orientation images were taken at an operating voltage of 20 kV, a working distance of 20 mm and a tilt angle of 70° . Data were collected using a step size of 0.2 μm at a magnification of $\times 2000$. Using EBSD, microtexture data can be obtained in finer scale compared with X-ray diffraction (XRD) which yields overall texture. The data were analysed using TSL OIM 5 software.

3.3.5. X-ray diffraction

The specimens were machined to 12×10 mm with thickness of 2 mm, and finish-polished using 6 μm diamond paste for X-ray diffraction. The orientation

distribution function (ODF) of the specimen was measured using a Bruker D8 Advance X-ray diffraction equipment with Co K_{α} radiation. The orientation distribution of the (110), (200), (211) and (311) poles were used for ODF calculations.

3.4. Metallurgical Experiments

3.4.1. Heat treatment

A simple heat treatment was conducted to investigate the effects of microstructure and texture on toughness anisotropy in X80_A steel. The specimen was heated from room temperature in a furnace at $1\text{ }^{\circ}\text{C s}^{-1}$ and kept for 10 min at $890\text{ }^{\circ}\text{C}$, followed by water quenching to room temperature. It should be noted that the A_{e3} temperature was calculated as $840\text{ }^{\circ}\text{C}$ using the metallurgical and thermochemical databank (MTDATA) and the TCFE4 database [NPL, 2006]. The annealing temperature was chosen as $890\text{ }^{\circ}\text{C}$ to minimize the prior austenite grain size and to suppress austenite grain growth as much as possible in order to retain the texture memory effect [Demura *et al.*, 2007; Lischewski *et al.*, 2008]. Before the heat treatment, several dilatometric experiments in different temperatures were carried out to take account the possibility of change in microstructure. For dilatometric experiments, samples were machined cylinders 3 mm diameter and 10 mm length, and the experiments were performed on a BAHR DIL805 dilatometer.

3.4.2. Computer simulation

A computer program was created to simulate the number of grains having specific orientations when the set of generated grains satisfied the distribution of misorientation angles for a randomly textured polycrystalline sample [Mackenzie, 1958]. A hypothetical fraction of randomly oriented 10,000 grains was calculated in

order to compare to actual fractions in the investigated steels. The source code of the program is listed in Appendix C to the materials algorithms project (MAP) standard [MAP].

IV. Anisotropy of Linepipe Steels

4.1. Microstructures

Fig. 4.1 shows the optical micrographs of X80_A steel etched with a 2% nital solution. The micrographs indicate a mixed microstructure of fine products along with what appears to be coarse grained ferrite, which looks like banding. The black dots could be pearlite or small quantities of martensite & retained austenite [Ikawa *et al.*, 1980] or carbides, but cannot clearly be identified in this stage.

Figs 4.2 and 4.3 show optical micrographs with the colour tint etching. Here, straw-coloured martensite-austenite constituents (M/A) was revealed in everywhere (white arrows in Fig. 4.3). Fine grained area was more severely etched than coarse grained area. Since picral attacks carbides, it might be from the uneven distribution of carbides between them.

The presence of the allotriomorphic ferrite was established using scanning electron microscopy with diffraction facilities; allotriomorphic ferrite is the product of diffusional transformation and hence the grains that grow are relatively free from dislocations. As a consequence, individual grains have little spread in crystallographic orientation. Fig. 4.4 shows regions in which this spread is less than 1.5° , which is regarded as threshold value of grain orientation spread in recrystallised grains [Mitsche *et al.*, 2006], with boundaries identified when the orientation difference is greater than 15° .

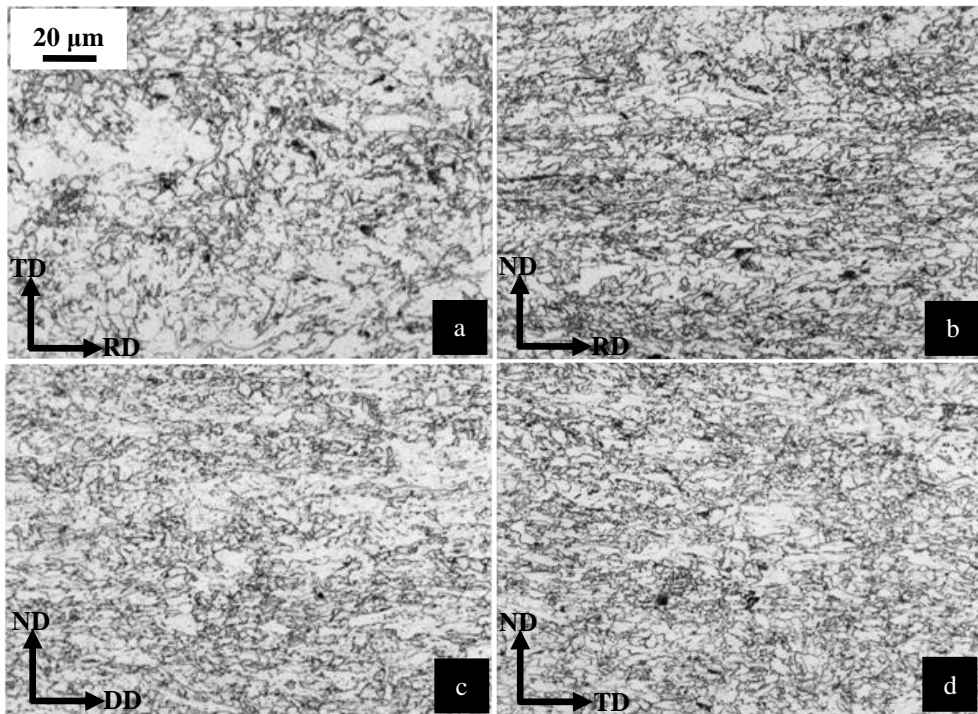


Figure 4.1. Optical micrographs in X80_A steel: Surface normal to (a) ND, (b) TD, (c) DD and RD. 2% nital etched. RD, TD, ND and DD stand for rolling direction, transverse direction, normal direction and diagonal direction respectively.

The remainder of the structure is too fine to resolve, but transmission electron microscopy suggests that it is some form of plate-like, heavily dislocated structure in the coarse grained region, probably bainite given that X80_A steel is cooled continuously, Fig. 4.5. In fine grained region, aggregate of ferrite plates with a significant dislocation density was also observed.

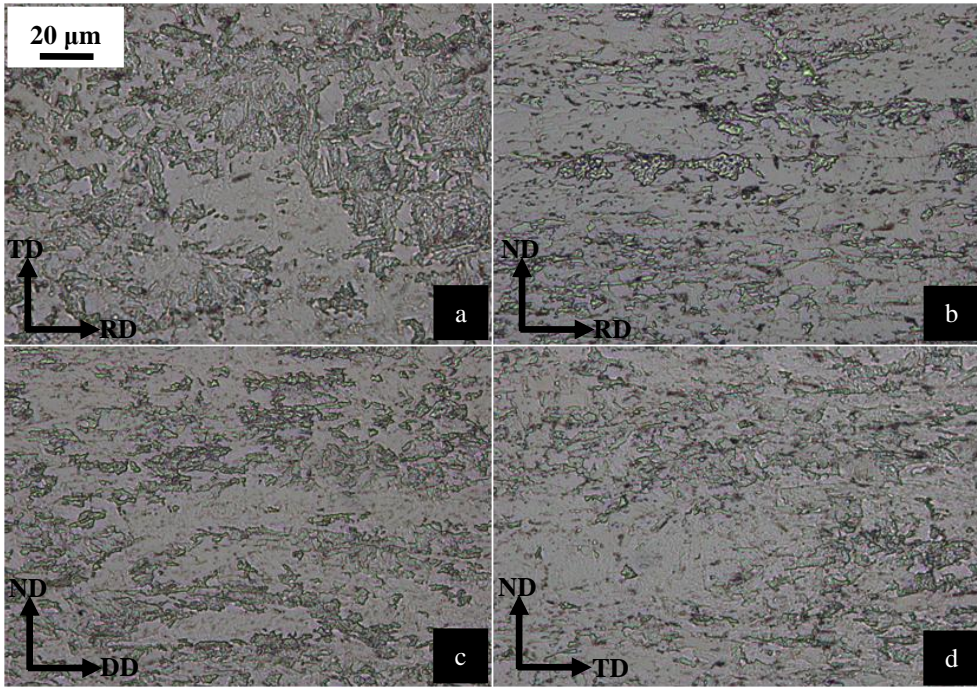


Figure 4.2. Optical micrographs in X80_A steel: Surface normal to (a) ND, (b) TD, (c) DD and RD. Colour tint etched.

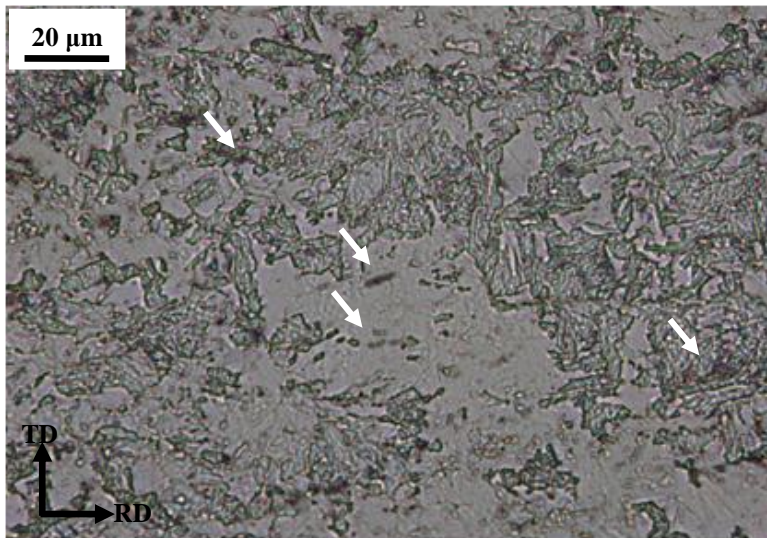


Figure 4.3. Optical micrographs of surface normal to ND in X80_A steel. Colour tint etched. White arrows indicate straw-coloured M/A.

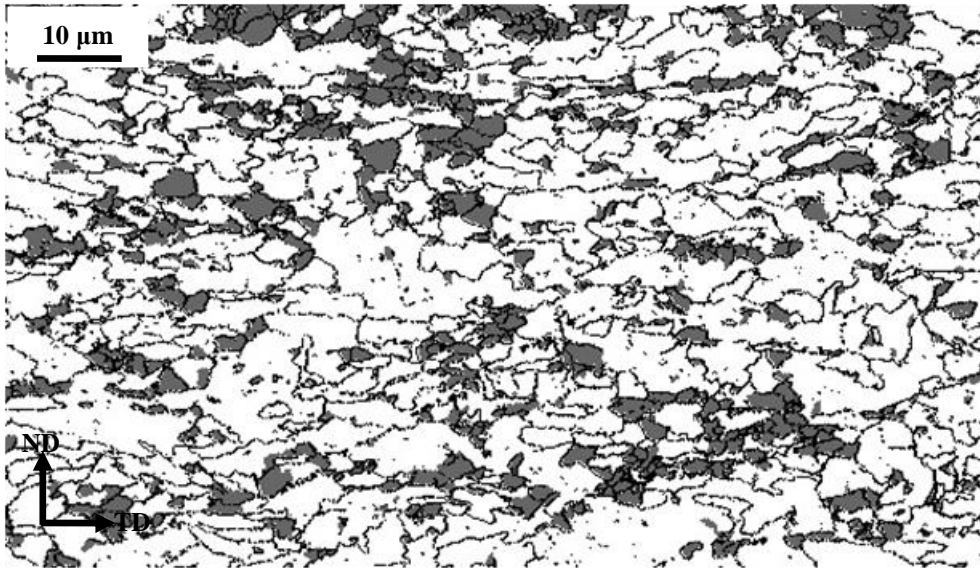


Figure 4.4. Map of grain orientation spread in X80_A with the value less than 1.5° in a grain with boundaries identified using the criterion that the orientation difference is greater than 15° .

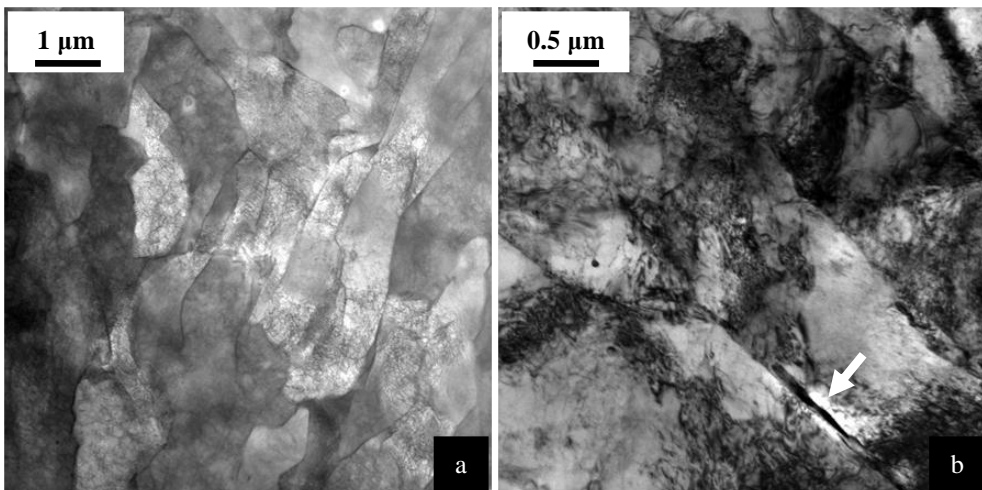


Figure 4.5. The TEM micrographs of the X80_A steel: (a) STEM micrograph of coarse grained region, (b) TEM micrograph of acicular type in fine grained region with cementite precipitation indicated by the white arrow.

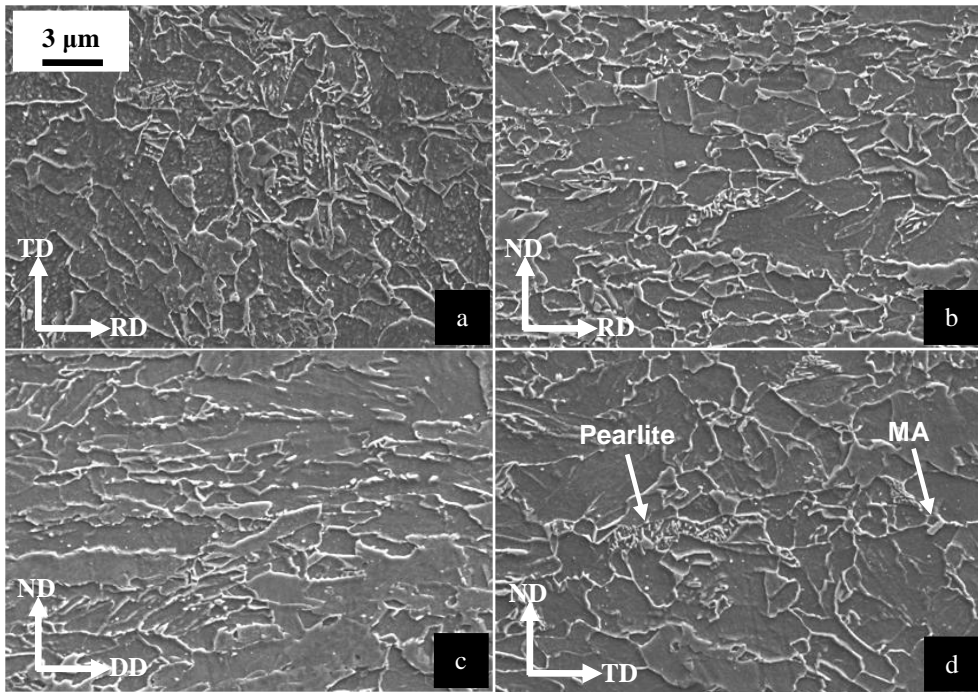


Figure 4.6. SEM micrographs in X80_A steel: Surface normal to (a) ND, (b) TD, (c) DD and RD. 2% nital etched.

There is evidence of some cementite precipitation, as shown by the arrow in Fig. 4.5b. Cementite associated with pearlite and the M/A phase, can be seen in the regions thought to be bainitic as shown in Fig. 4.6, but their fractions are very small. As mentioned previously, Figs 4.1 and 4.2 show signs of banding due to the existence of chemical segregation inherited from the solidification stage and spread into layers by the rolling deformation. Manganese is known to play a prominent role in the development of bands because the transformation to allotriomorphic ferrite occurs first in Mn-depleted regions so that the residual austenite becomes enriched

in carbon. The latter then transforms into pearlite or harder phases such as bainite depending on the rate of cooling experienced by the steel.

In summary, the microstructure of X80_A steel consists of bainitic ferrite, allotriomorphic ferrite, pearlite and martensite–austenite constituents. In particular, the bainitic ferrite can be categorised into two types; fine grained with carbides and carbide–free coarse grained regions. The hardness values in the fine and coarse microstructures are found to be approximately 266 ± 2 and 230 ± 3 HV, respectively, and the macroscopic hardness value was 220 ± 6 HV.

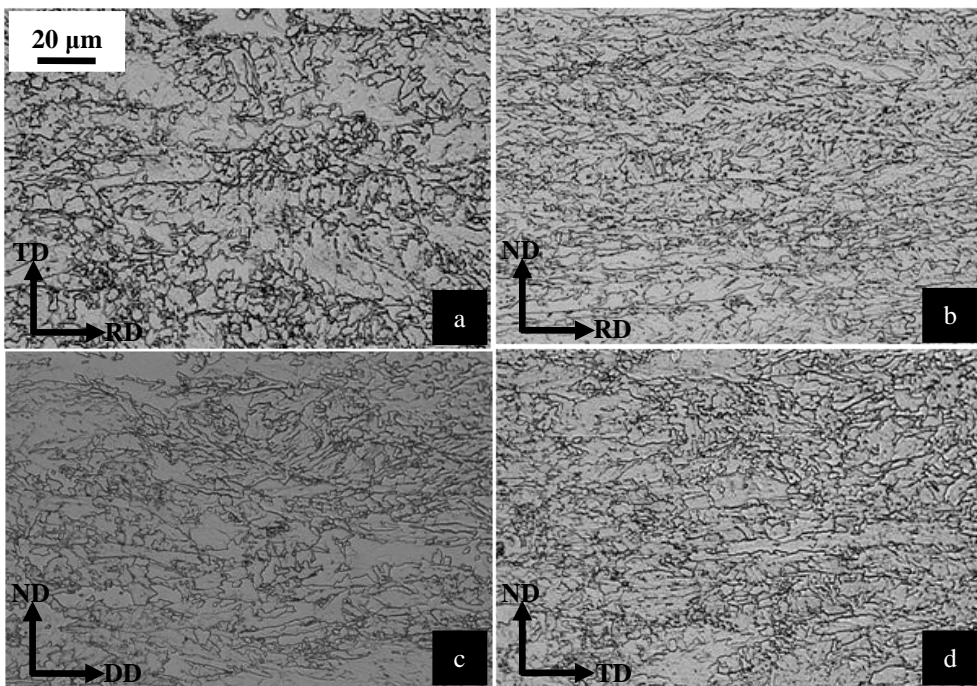


Figure 4.7. Optical micrographs in X80_B steel: Surface normal to (a) ND, (b) TD, (c) DD and RD. 2% nital etched.

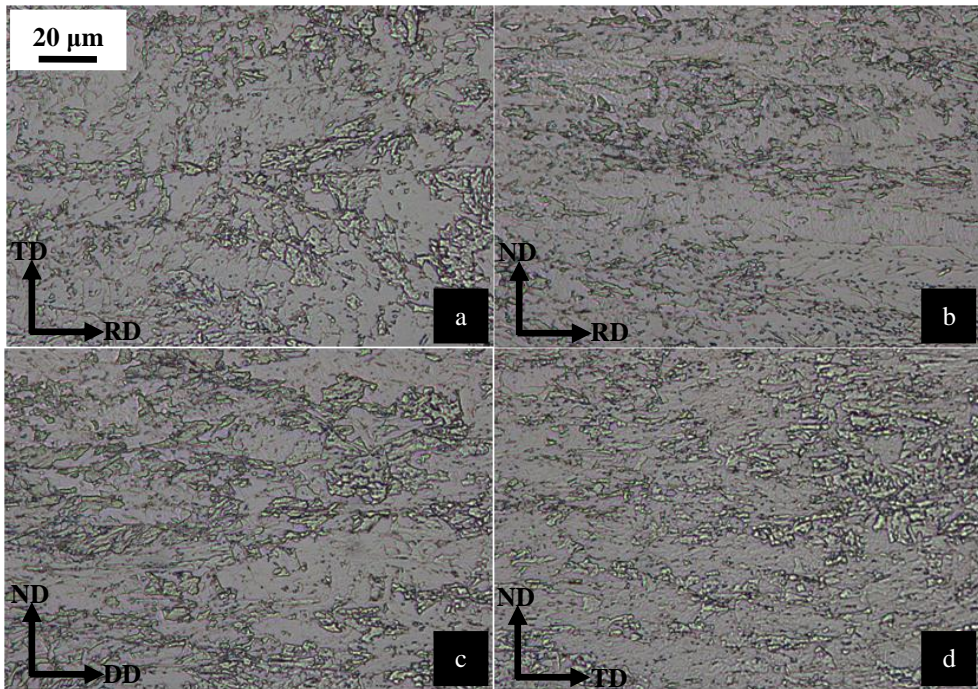


Figure 4.8. Optical micrographs in X80_B steel: Surface normal to (a) ND, (b) TD, (c) DD and RD. Colour tint etched.

Fig. 4.7 shows the optical micrographs of X80_B steel. The microstructure looks different with fewer precipitates than X80_A steel as shown in Fig. 4.1 since it has less carbon than X80_A steel. However, in colour tint etching as shown in Fig. 4.8, the microstructures appear similar with carbide-free coarse grained regions and carbide-containing finer regions with M/A. Further detail is illustrated in Figs 4.9 and 4.10. The hardness values in the fine and coarse microstructures are found to be 250 ± 4 and 221 ± 4 HV, respectively and the macroscopic hardness value was 241 ± 2 HV.

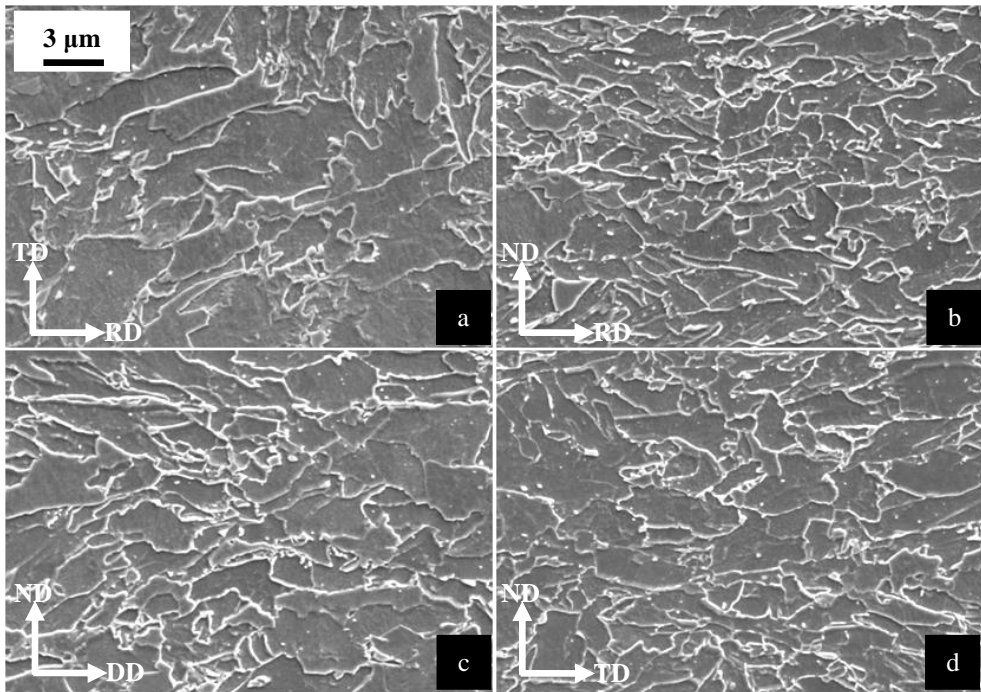


Figure 4.9. SEM micrographs in X80_B steel: Surface normal to (a) ND, (b) TD, (c) DD and RD. 2% nital etched.

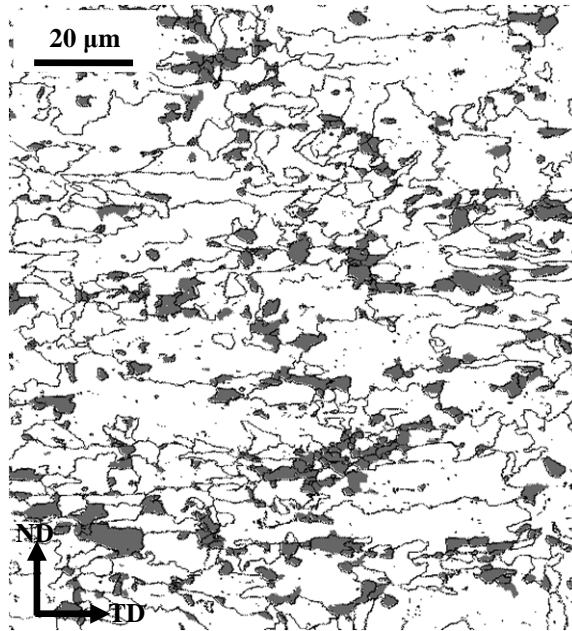


Figure 4.10. Map of grain orientation spread in X80_B with the value less than 1.5° in a grain with boundaries identified using the criterion that the orientation difference is greater than 15° .

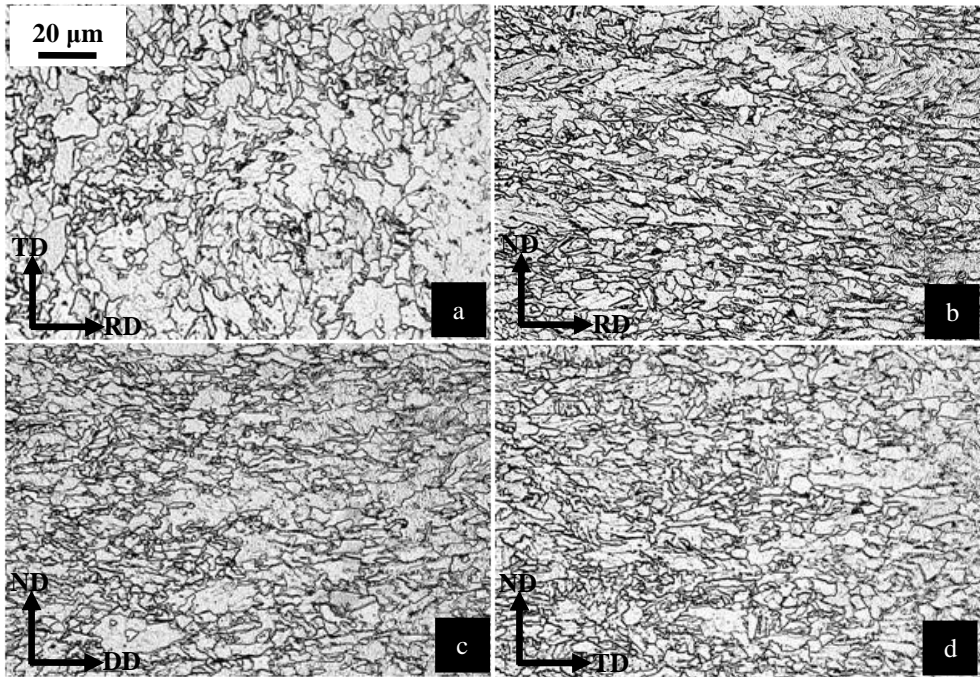


Figure 4.11. Optical micrographs in X70_A steel: Surface normal to (a) ND, (b) TD, (c) DD and RD. 2% nital etched.

Figs 4.11 and 4.12 represent X70_A steel with coarse and fine grained regions, and some banding containing M/A. Pearlite and allotriomorphic ferrite are apparent in Figs 4.13 and 4.14. There is a greater amount of pearlite than in X80_A steel, but fraction is still small. The hardness values in the fine and coarse microstructures are 256 ± 4 and 227 ± 5 HV, respectively, with a macroscopic hardness of 220 ± 4 HV.

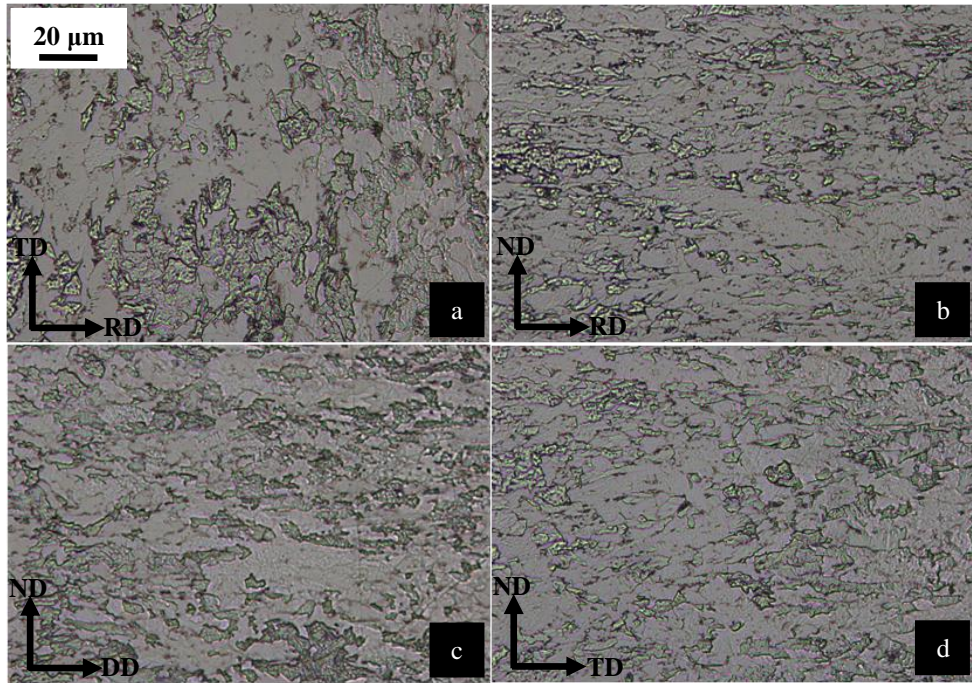


Figure 4.12. Optical micrographs in X70_A steel: Surface normal to (a) ND, (b) TD, (c) DD and RD. Colour tint etched.

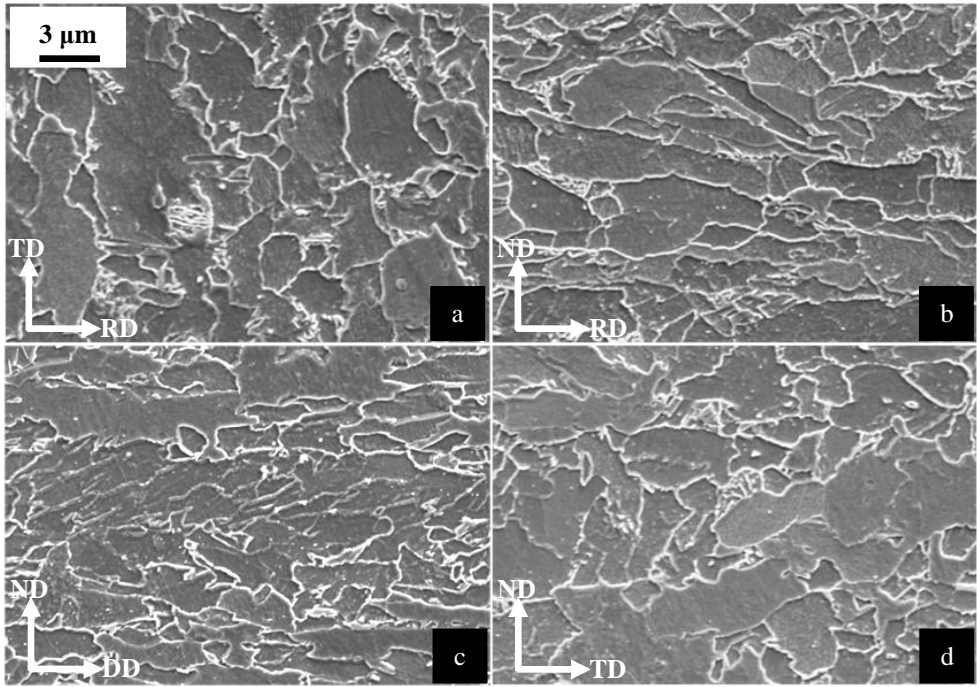


Figure 4.13. SEM micrographs in X70_A steel: Surface normal to (a) ND, (b) TD, (c) DD and RD. 2% nital etched.

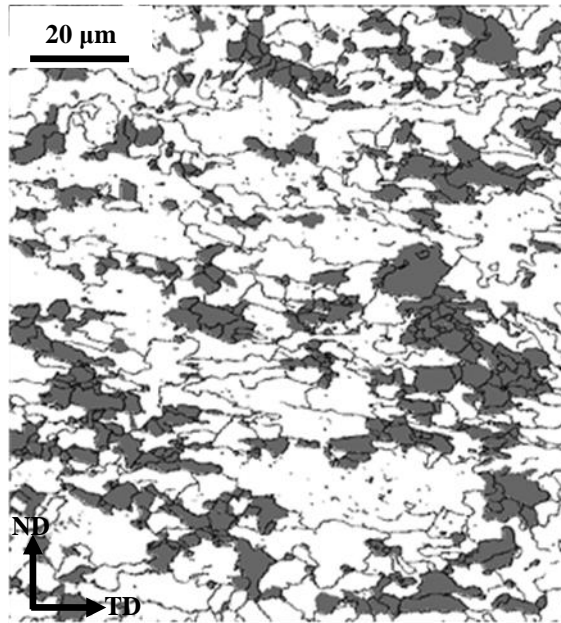


Figure 4.14. Map of grain orientation spread in X70_A with the value less than 1.5° in a grain with boundaries identified using the criterion that the orientation difference is greater than 15° .

X80_A, X80_B and X70_A steels have similar microstructures, containing allotriomorphic ferrite, coarse and fine grained bainite and M/A. X80_A and X70_A steels also contain a small amount of pearlite. Volume fractions measured using image processing are listed in Table 4.1, but it is not possible to distinguish between allotriomorphic and bainitic ferrite using this technique so the fraction of allotriomorphic ferrite was evaluated using EBSD experiments, and bainite regions result from the difference with the optical clarity. Table 4.2 shows that the steels have similar hardness with X70_A being somewhat softer due to its large

allotriomorphic ferrite content.

The metallographic and crystallographic grain sizes calculated as a function of misorientation in Table 4.3, and the difference is illustrated in Fig. 4.15, with showing banding clearly between fine and coarse grained ferrite.

The development of microstructure in linepipe steels can be explained as follows. The liquid steels solidify when an uneven distribution of manganese, leading to Mn banding during rolling in the austenitic state. Allotriomorphic ferrite starts to form at A_{r3} , with the partitioning of carbon into the residual austenite. On further cooling, the manganese-depleted residual austenite transforms into coarse grained bainite, with the enriched remainder then forming the fine bainite richer in carbides. Some austenite decomposes finally into martensite and some is retained, to form the so-called M/A phase. Fig. 4.16 illustrates the development of microstructure in linepipe steels.

Table 4.1. Volume fractions of phases.

Steels	Volume fractions of phases			
	Allotriomorphic	Fine grained	Coarse grained	Others
	ferrite	bainite	bainite	
X80_A	0.17 ± 0.02	0.35 ± 0.05	0.48 ± 0.05	M/A, Pearlite
X80_B	0.14 ± 0.01	0.35 ± 0.05	0.51 ± 0.05	M/A
X70_A	0.29 ± 0.07	0.25 ± 0.06	0.46 ± 0.06	M/A, Pearlite

Table 4.2. Hardness data.

Steels	Hardness (HV)		
	Macroscopic	Fine grained bainite	Coarse grained bainite
X80_A	241 ± 2	266 ± 2	221 ± 4
X80_B	241 ± 2	250 ± 4	221 ± 4
X70_A	220 ± 4	256 ± 4	227 ± 5

Table 4.3. Grain size data.

Steels	Metallographic grain size* (µm)	Crystallographic grain size* (µm)
X80_A	1.42 ± 1.36	10.32 ± 3.83
X80_B	1.38 ± 1.46	11.26 ± 4.19
X70_A	1.63 ± 1.48	9.13 ± 2.93

* Metallographic and crystallographic grain size with grain boundary misorientation $\geq 2^\circ$ and 15° respectively.

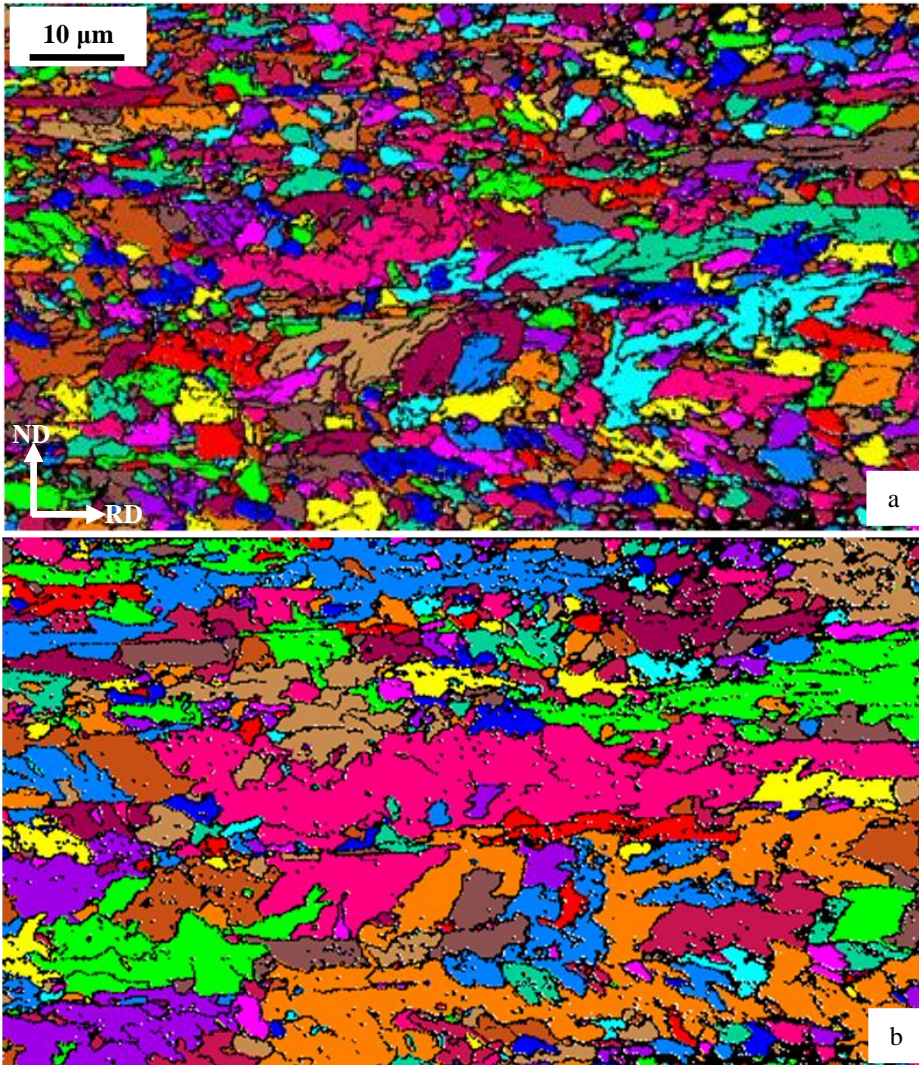


Figure 4.15. Grain maps of surface normal to TD in X80_A steel. The maps represent the difference in grain size between when grain boundary misorientation is greater than (a) 2° and (b) 15° . Black lines represent grain boundaries and each grain is highlighted in its own colour.

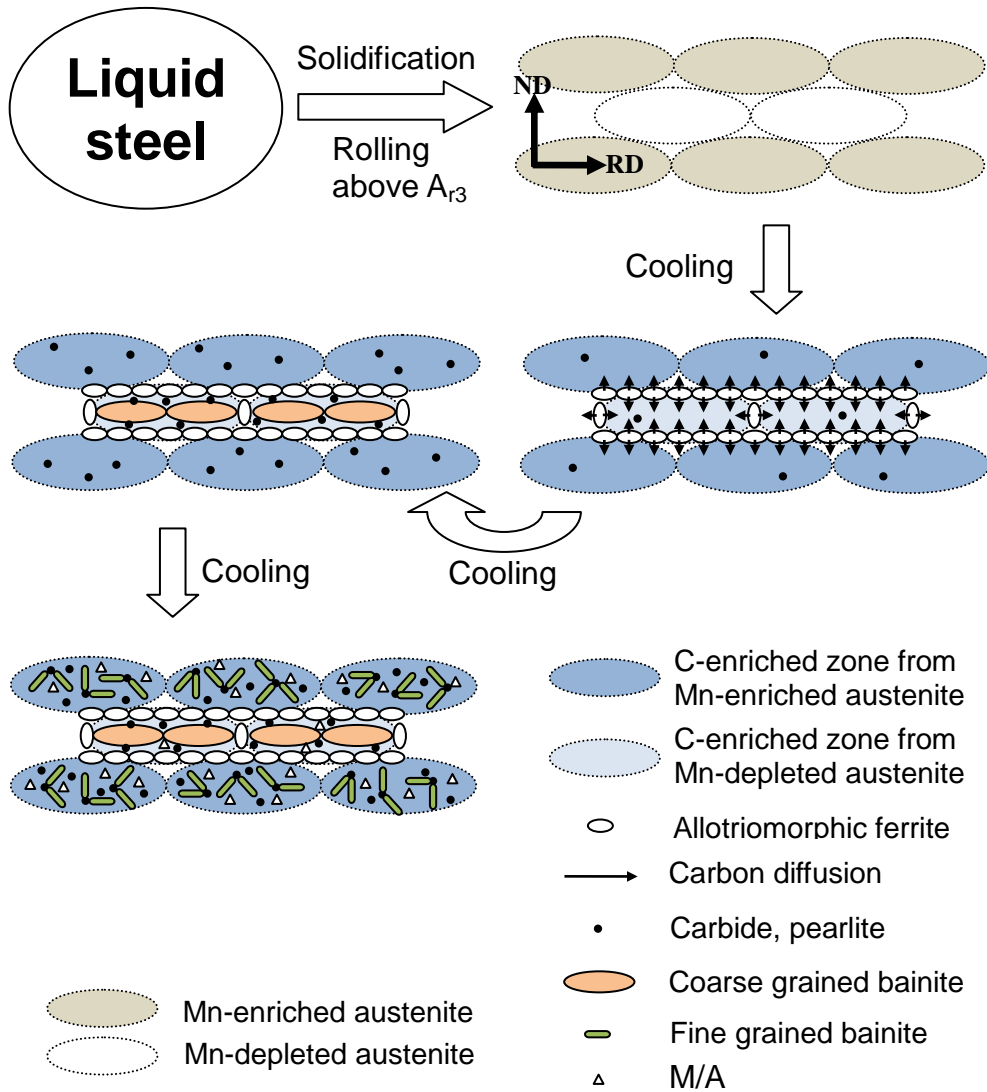


Figure 4.16. Schematic illustration of development of microstructure in linepipe steels.

4.2. Mechanical Properties

4.2.1. Tensile

The tensile properties measured as a function of sample orientation (Fig. 3.1b) are summarised in Table 4.4. All of the data meet the API 5L specification for linepipe steels [API Recommended Practice, 1996]. ‘T’ orientations show the highest strength whereas better elongations are observed along the ‘D’ orientations in all the steels, although the differences are rather small.

Table 4.4. Tensile properties of the investigated linepipe steels.

Steels	Orientations	YS* (MPa)	UTS* (MPa)	TE* (%)	UE* (%)
X80_A	T	634 ± 29	707 ± 16	14.7 ± 1.1	7.1 ± 1.4
	D	600 ± 35	663 ± 10	15.8 ± 1.9	7.7 ± 1.9
	L	602 ± 35	676 ± 4	13.0 ± 2.0	7.1 ± 1.7
X80_B	T	633 ± 8	722 ± 4	15.8 ± 0.7	8.6 ± 0.3
	D	582 ± 13	667 ± 6	19.7 ± 0.7	10.2 ± 0.3
	L	572 ± 9	691 ± 3	17.1 ± 0.9	10.1 ± 0.3
X70_A	T	581 ± 2	657 ± 5	17.1 ± 1.5	9.5 ± 0.4
	D	528 ± 2	608 ± 3	21.6 ± 0.5	10.4 ± 0.3
	L	528 ± 17	631 ± 5	15.4 ± 1.2	9.9 ± 0.2

* YS, UTS, TE and UE stand for yield strength, ultimate tensile strength, total elongation and uniform elongation respectively.

4.2.2. Charpy

Fig. 4.17 shows the changes of Charpy energy with temperature and test orientation for the conventional notch orientation (Fig. 3.2a) in X80_A steel. As might be expected, and consistent with the tensile test data, anisotropy is minimal when failure is in the ductile regime, or when the sample fails in a completely brittle manner during test at $-100\text{ }^{\circ}\text{C}$. In contrast, the orientation dependence of Charpy energy is marked in the ductile–brittle transition temperature range, with the D–D orientation faring worst. This might be expected given that Fig. 4.17a shows that the impact transition temperature itself is orientation–dependent. Note that it is unlikely that the small differences in strength noted in the data of Table 4.4 can be responsible for the observed anisotropy of Charpy properties [Kapp and Underwood, 1992]. X80_B and X70_A steels show similar tendencies but with the minima in toughness recorded at different test temperatures as shown in Figs 4.18 and 4.19.

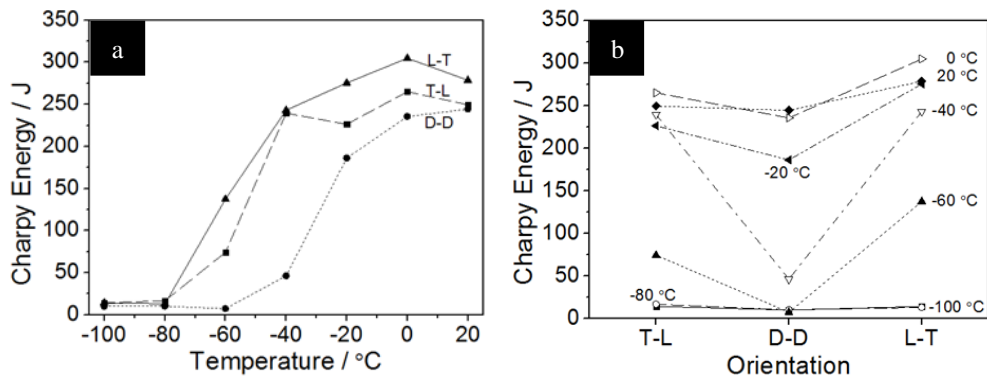


Figure 4.17. Charpy properties of X80_A: (a) the impact transition curve and (b) the anisotropy curve. The specimens have the conventional notch orientations.

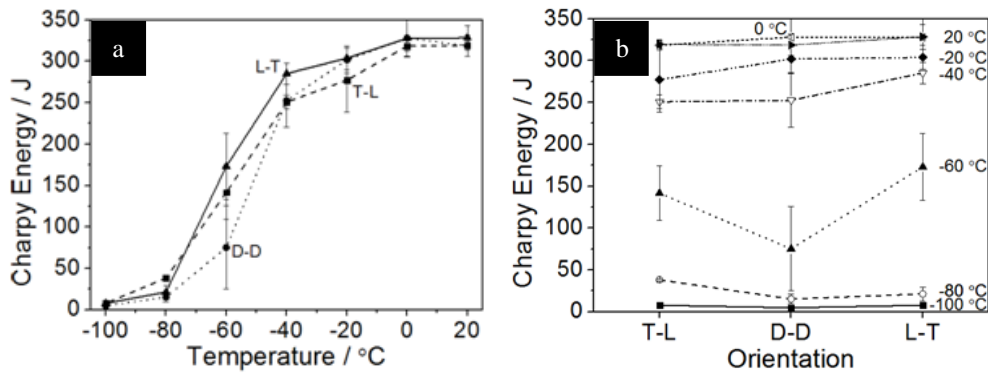


Figure 4.18. Charpy properties of X80_B: (a) the impact transition curve and (b) the anisotropy curve. The specimens have the conventional notch orientations.

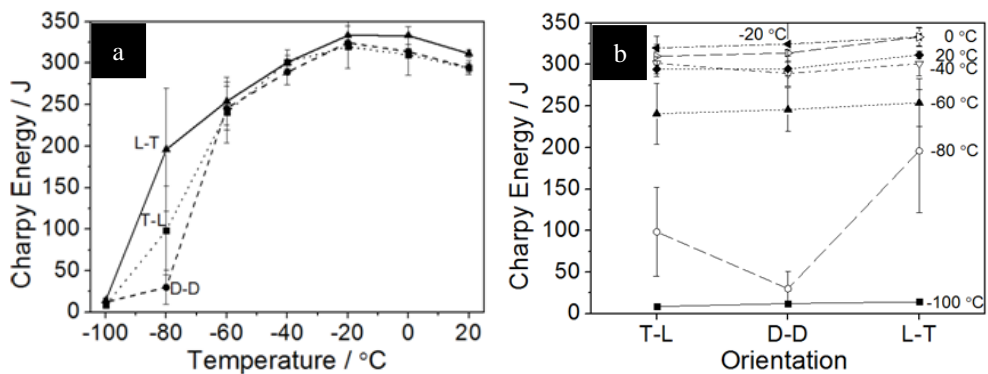


Figure 4.19. Charpy properties of X70_A: (a) the impact transition curve and (b) the anisotropy curve. The specimens have the conventional notch orientations.

4.3. Inclusions

In order to examine the ductile fracture behaviour, it is necessary to investigate inclusions. Figure 4.20 shows the result of EDS in X80_A steel. Clusters of complex oxide with calcium sulphides were found. If the inclusion has enough plasticity to be elongated in the rolling process then the interface between the inclusion and matrix can be an easy crack propagation path, leading to toughness anisotropy [Mohan, 1995a]. However, the inclusions are not elongated, compatible result with isotropic properties in the upper shelf regime of the Charpy curve (Fig. 4.17a).

X80_B and X70_A steels also have inclusions of spherical shape but of a different type as shown in Figs 4.21 and 4.22. In X80_B and X70_A steels, aluminium oxide with calcium sulphide was found. But this kind of inclusion lacks plasticity [Shackelford and Doremus, 2008], so it is unlikely to influence toughness anisotropy.

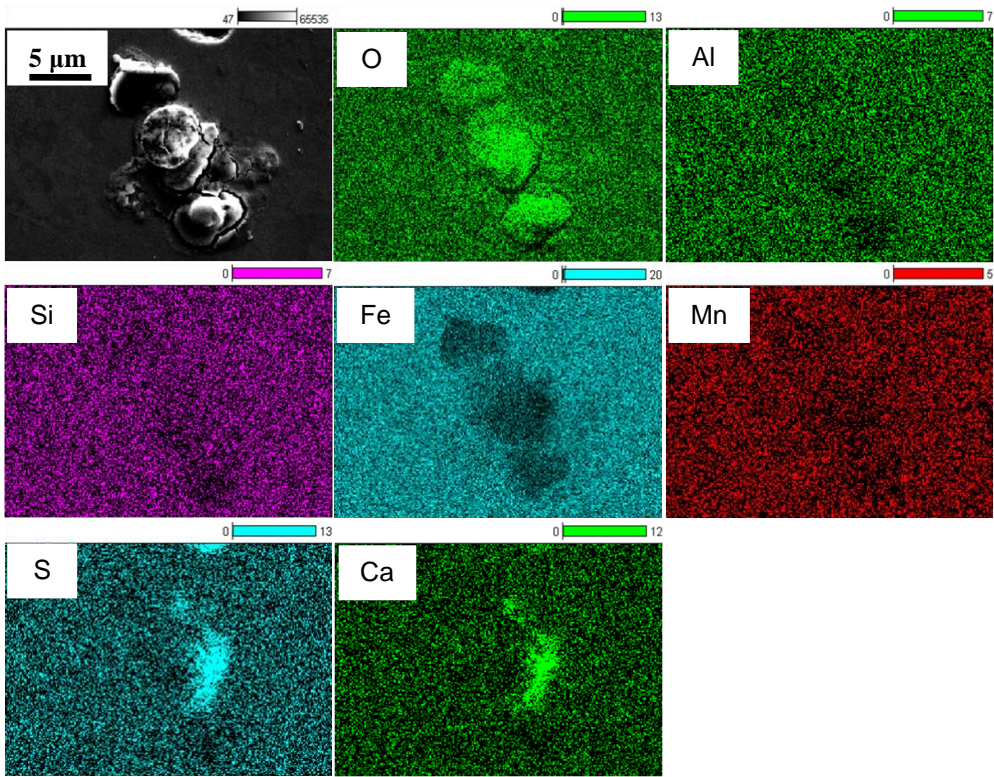


Figure 4.20. EDS result from X80_A steel.

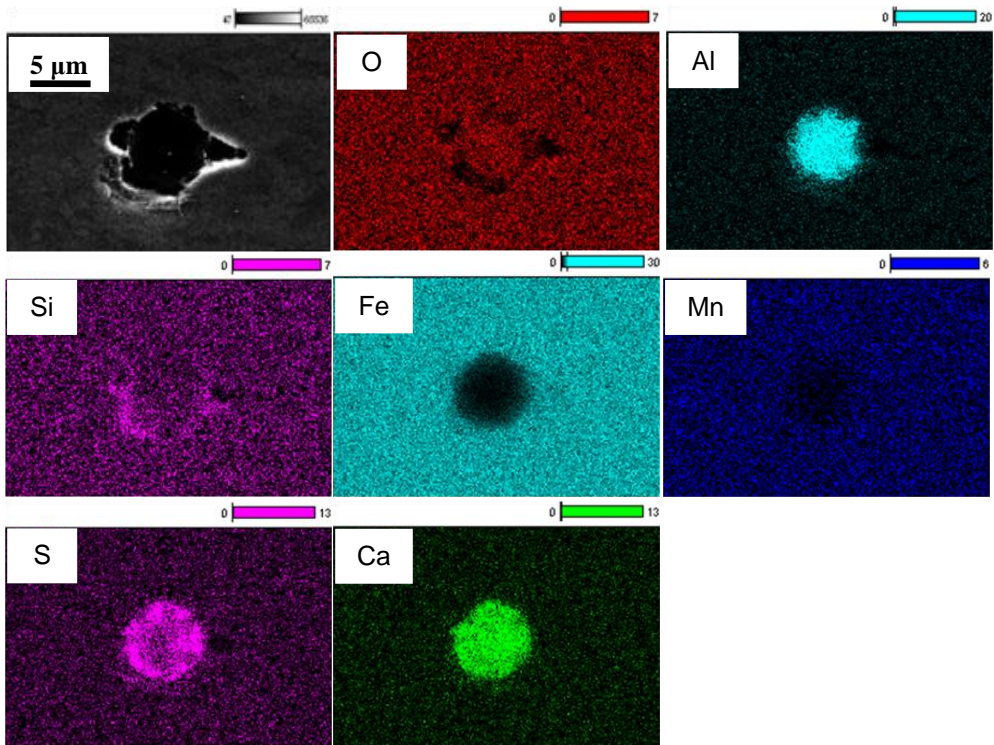


Figure 4.21. EDS result from X80_B steel.

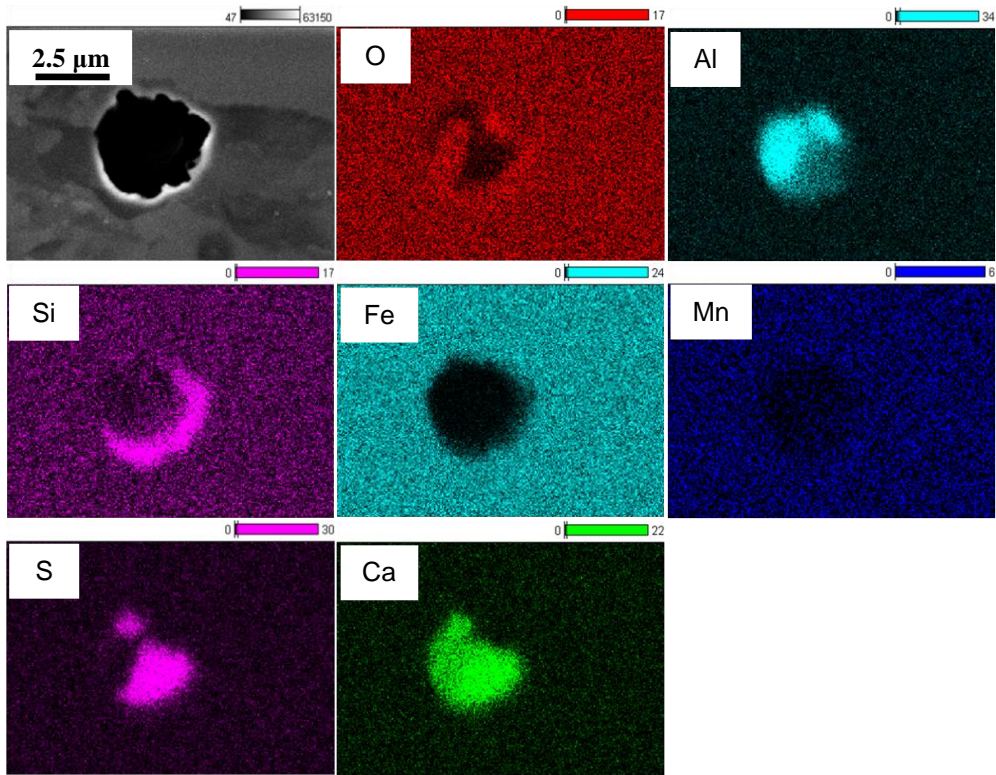


Figure 4.22. EDS result from X70_A steel.

4.4. Fractography

The fracture surfaces of Charpy specimens in X80_A steel are shown in Figs 4.23 and 4.24, showing brittle fracture becoming dominant as the test temperature is reduced. The cleavage facet size was measured as approximately up to 20 μm at $-100\text{ }^\circ\text{C}$ (Fig. 4.23c), which exceeds the average crystallographic grain size (Table 3). In Fig. 4.23, partial splitting of the Charpy specimen parallel to the rolling plane is observed in specimens with L–T and T–L orientations for $-20\text{ }^\circ\text{C}$ to $-60\text{ }^\circ\text{C}$ but with D–D orientation only for $-20\text{ }^\circ\text{C}$ (white arrows). This splitting is commonly referred to as “delamination”, attributed to weakness parallel to the rolling plane as a consequence of inclusion alignment or microstructural anisotropy.

Delamination in the ductile regime is reported to reduce the upper shelf energy because it is related with separation on $\{100\}$ cleavage planes [Schofield, 1974]. However, it can contribute to the toughness in the transition region when the split occurs on a plane not containing the notch [Song *et al.*, 2005]. From the variation in Charpy energy and the corresponding fracture surfaces shown in Figs 4.17 and 4.24, it is evident that the L–T and T–L orientations with higher impact energy in the ductile–brittle transition region always have the delaminations as a part of the fracture process. For the D–D orientation, the impact energy is comparable to those of other orientations at $-20\text{ }^\circ\text{C}$ where the delamination is a feature of all fracture surfaces, but the energy decreases sharply at lower temperatures in the absence of splitting. This indicates clearly a relationship between the observed Charpy–energy anisotropy and the occurrence of delamination at fracture surface. Furthermore, the

D orientation when compared with other directions has a slightly lower strength with slightly higher elongation in tensile tests. It is nevertheless more brittle, correlating with the absence of delamination in Charpy specimens tested in the brittle regime.

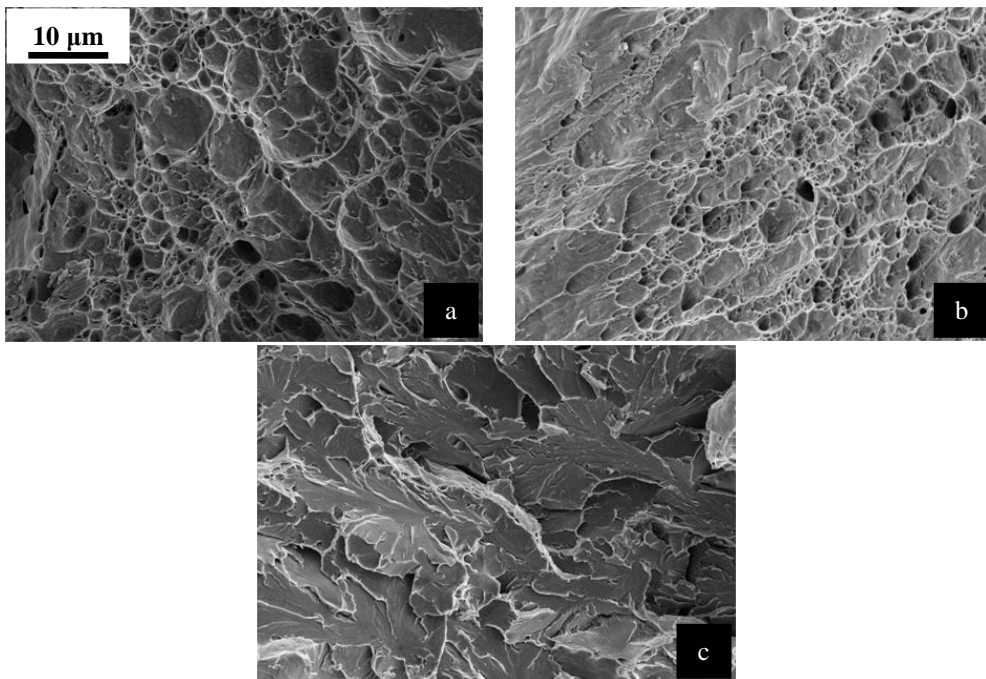


Figure 4.23. Fracture surfaces of L–T orientation specimen in X80_A steel at (a) room temperature, (b) -20 °C (c) -60 °C, and (d) -100 °C

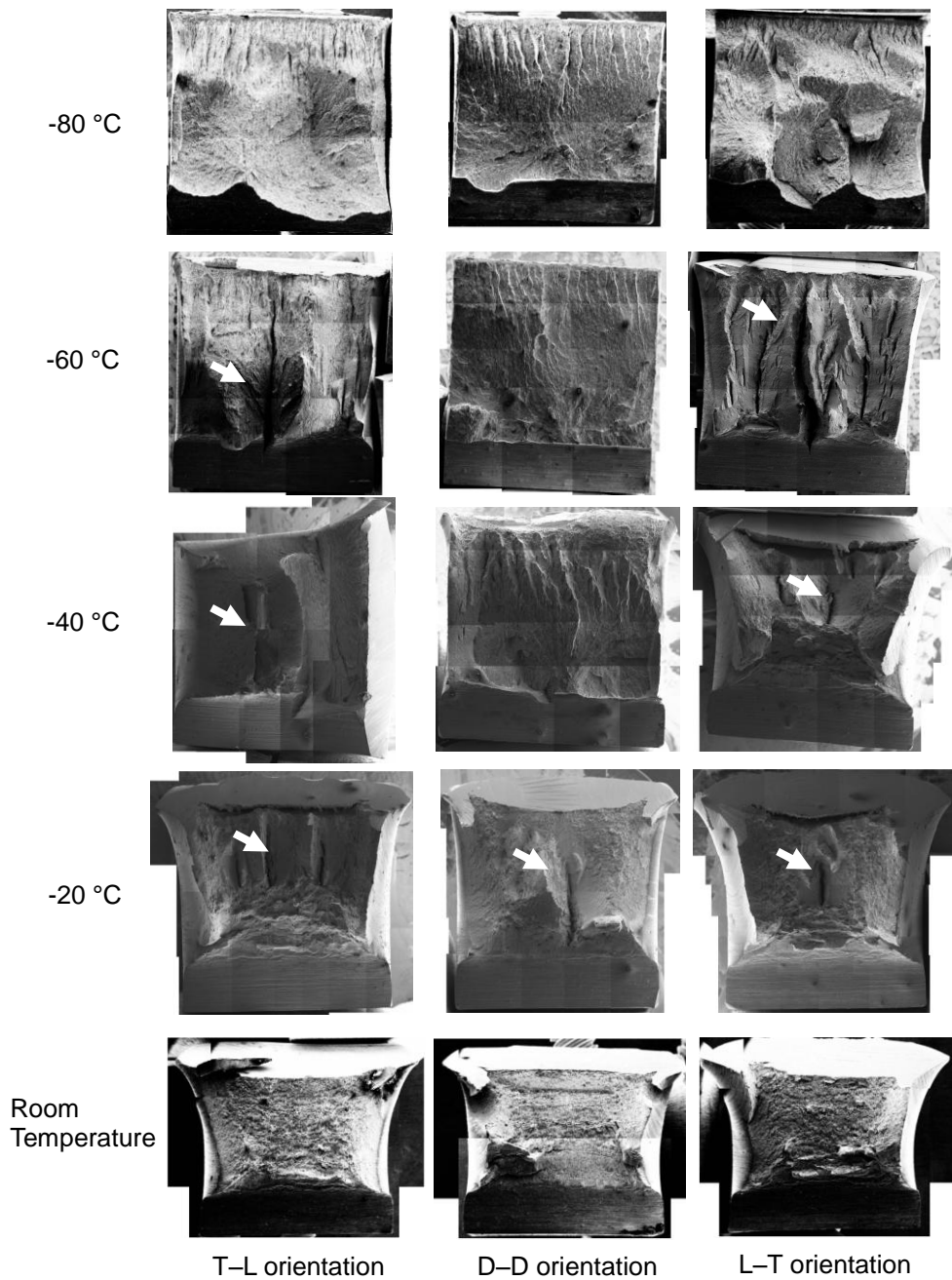


Figure 4.24. Fracture surfaces of Charpy specimens from room temperature to -80 °C of T-L, D-D and L-T orientations with delaminations indicated by white arrows in X80_A steel.

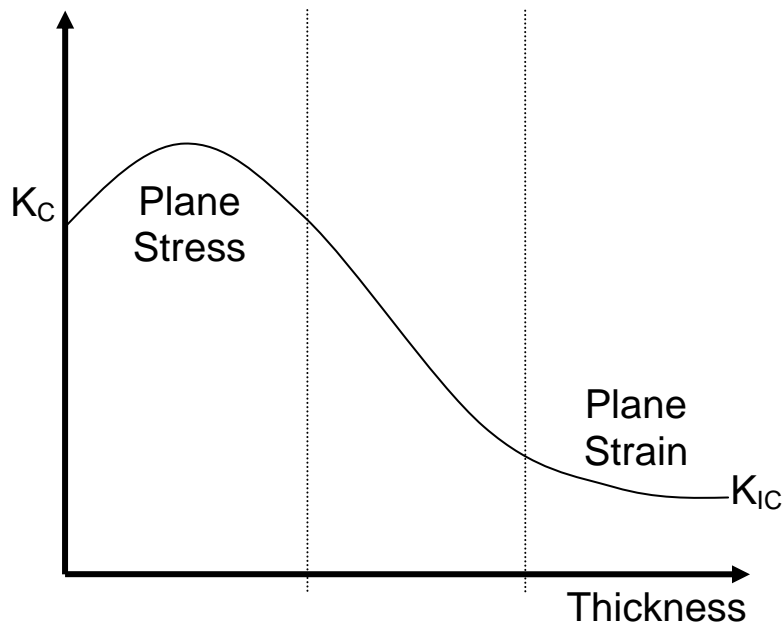


Figure 4.25. The change of the stress intensity factor as a function of sample thickness.

The role of delamination can be explained as follows. The classical curve representing the variation in fracture toughness as a function of sample thickness, *i.e.*, as a function of whether the sample is subjected to plane stress or plane strain conditions, is illustrated schematically in Fig. 4.25 [Meguid, 1989; Knott, 1973]. Delamination during Charpy testing will alter the stress state favourably, leading to an improved value of energy absorbed – in effect, producing additional shear lips which are characteristic features at the surfaces of non-delaminating samples [Song *et al.*, 2005]. It has been pointed out previously in a study of thickness effects [Guo *et al.*, 2002] that the occurrence of delamination reduces the out of plane constraint; this would in turn lead to an increase in the tendency for ductile fracture and hence

a higher impact energy in a Charpy test. This is irrespective of the fact that the fracture that leads to delamination is brittle (Figs 4.26 and 4.27), as long as it precedes the gross fracture of the sample.

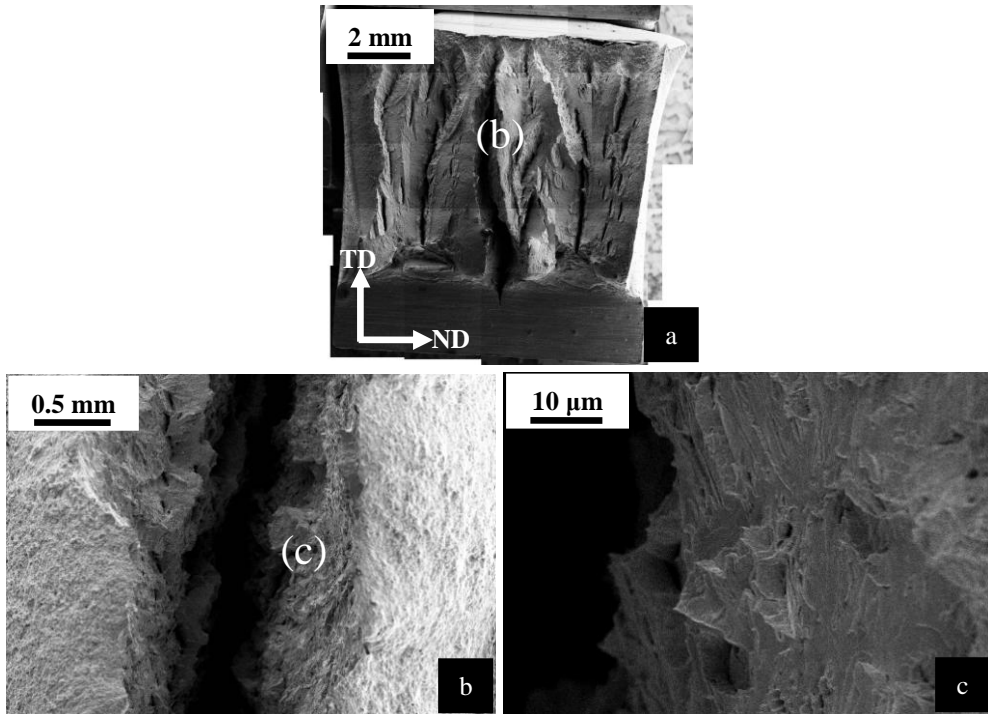


Figure 4.26. Micrographs of the fracture surfaces of the L–T orientation with delamination in X80_A steel, (a) fracture surface of the steel processed at -60 °C, (b) delamination, and (c) inside of the delamination.

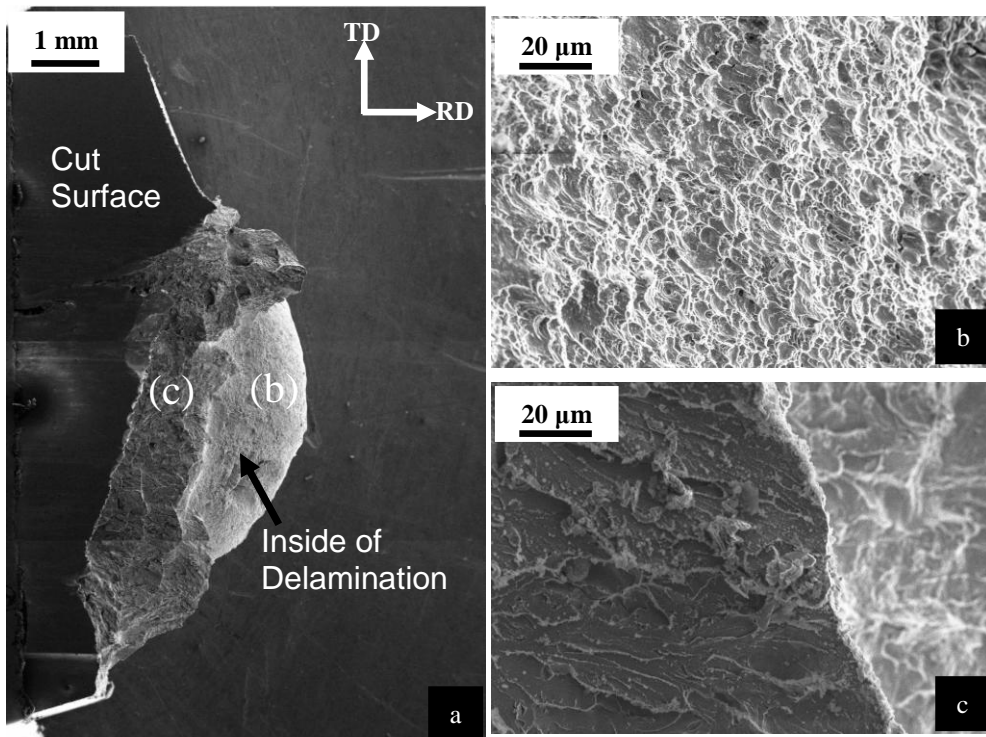


Figure 4.27. Side view of delamination of the L–T orientation processed at $-70\text{ }^{\circ}\text{C}$ in X80_A steel: (a) Side view of the delamination, (b) ductile fracture near the initiation part of the delamination and (c) brittle fracture of the end part of the delamination.

The occurrence of delamination might be attributed to crystallographic texture; cleavage delaminations are known to occur in warm-rolled steel and have been discussed in terms of texture [Bourell and Sherby, 1983]. Other causes include intergranular failure along prior austenite boundaries, segregation of P and S, anisotropy of microstructures, banding and aligned particles and inclusions [Tamura *et al.*, 1988; McEvily *et al.*, 1962; Shin *et al.*, 2009b]. Some of these factors can clearly contribute in the present context, but Fig. 4.28 indicates that microstructural

banding is an important culprit in X80–A steel. A close examination of the (arrowed) regions on either side of the separation in Fig. 8b shows that the delamination occurs between the relatively clean and coarse grained region, and on the opposite side, a refined region richer in the harder phases. This might be expected given the mechanical incompatibilities that must inevitable exist between the bands.

However, there also seems to be a significant difference in the crystallography of the regions on either side of the delamination. Fig. 4.29 shows orientation imaging around the delamination in the specimen with L–T orientation tested at -40°C in X80_A steel. The macroscopic texture is different in the coarser and refined bands, and this in turn must add to the mechanical incompatibilities. Also, the grain orientation spread in upper and lower regions separated by delamination shows a remarkable difference, meaning that the delamination occurs along the boundary between bands of fine and coarser structures.

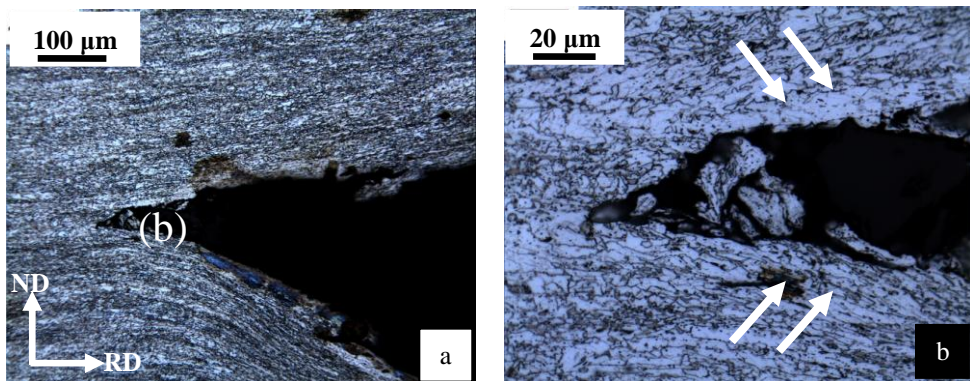


Figure 4.28. Delamination of the L–T orientation specimen processed at -40°C in X80_A steel.

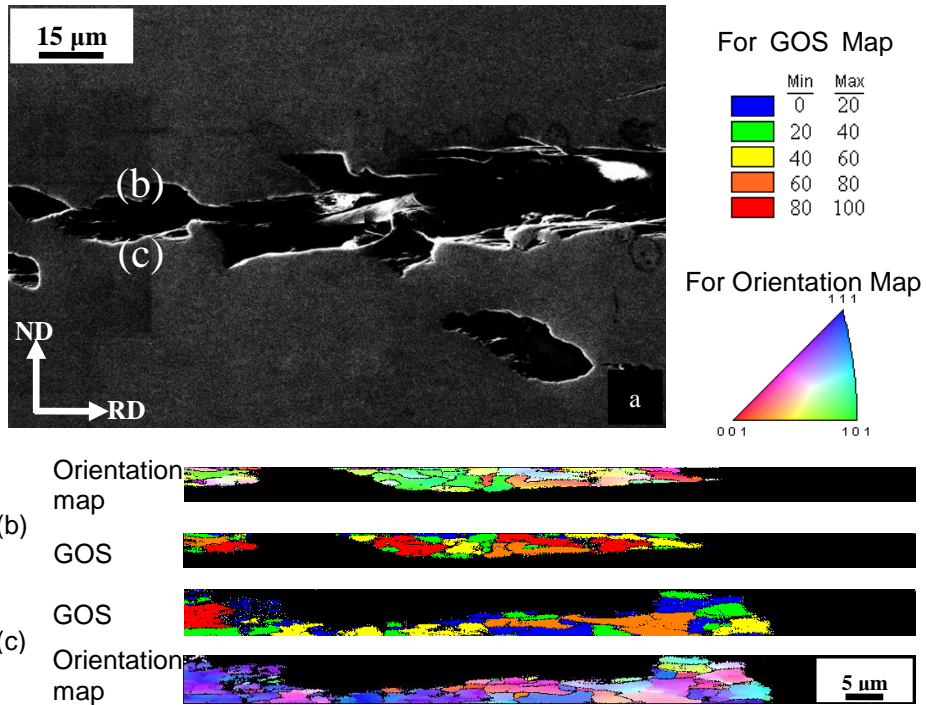


Figure 4.29. SEM image, orientation maps and grain orientation spread (GOS) maps for delamination in the L–T orientation specimen processed at $-40\text{ }^{\circ}\text{C}$ in X80_A steel.

Fig. 4.30 shows the fracture surfaces of Charpy specimens in X80_B steel. In the $-20\text{ }^{\circ}\text{C}$, $-40\text{ }^{\circ}\text{C}$ and $-60\text{ }^{\circ}\text{C}$, All the orientations show delamination and it is connected with the Charpy results that the anisotropy was relieved in X80_B steel at those temperatures compared to X80_A steel as shown in Figs 4.17 and 4.18. Since the delamination of D–D orientation specimen in X80_B steel was not developed well compared to other orientations at $-60\text{ }^{\circ}\text{C}$, the Charpy–energy anisotropy was highest at that temperature in X80_B steel. Similar to X80_A steel, the fracture

mode changes gradually from ductile to brittle as the test temperature is reduced, and the cleavage facet size was measured as approximately up to 25 μm at $-100\text{ }^\circ\text{C}$ (Fig. 4.31).

Even though the facet size and crystallographic grain size of X80_B steel is greater than those of the X80_A steel, the DBTT of X80_B steel is lower than that of X80_A steel. This comes from the higher upper shelf energy in X80_B steel than in X80_A steel, and it is associated with the presence of pearlite in X80_A steel. Fig. 4.32 shows the fracture surfaces in X80_A steel processed at $-40\text{ }^\circ\text{C}$ and $-60\text{ }^\circ\text{C}$. Vicinity of the pearlite, the crack holes are initiated as indicated by the black arrows in Fig. 4.32a. As expected, the fine grained region is more effective than the coarse grained region for toughness. Fig. 4.32b shows that the crack propagated through coarse grained ferrite and blocked by the fine grained ferrite. However, this cannot be the reason for difference in upper shelf energies since the fraction of each phase is similar between X80_A and X80_B steels.

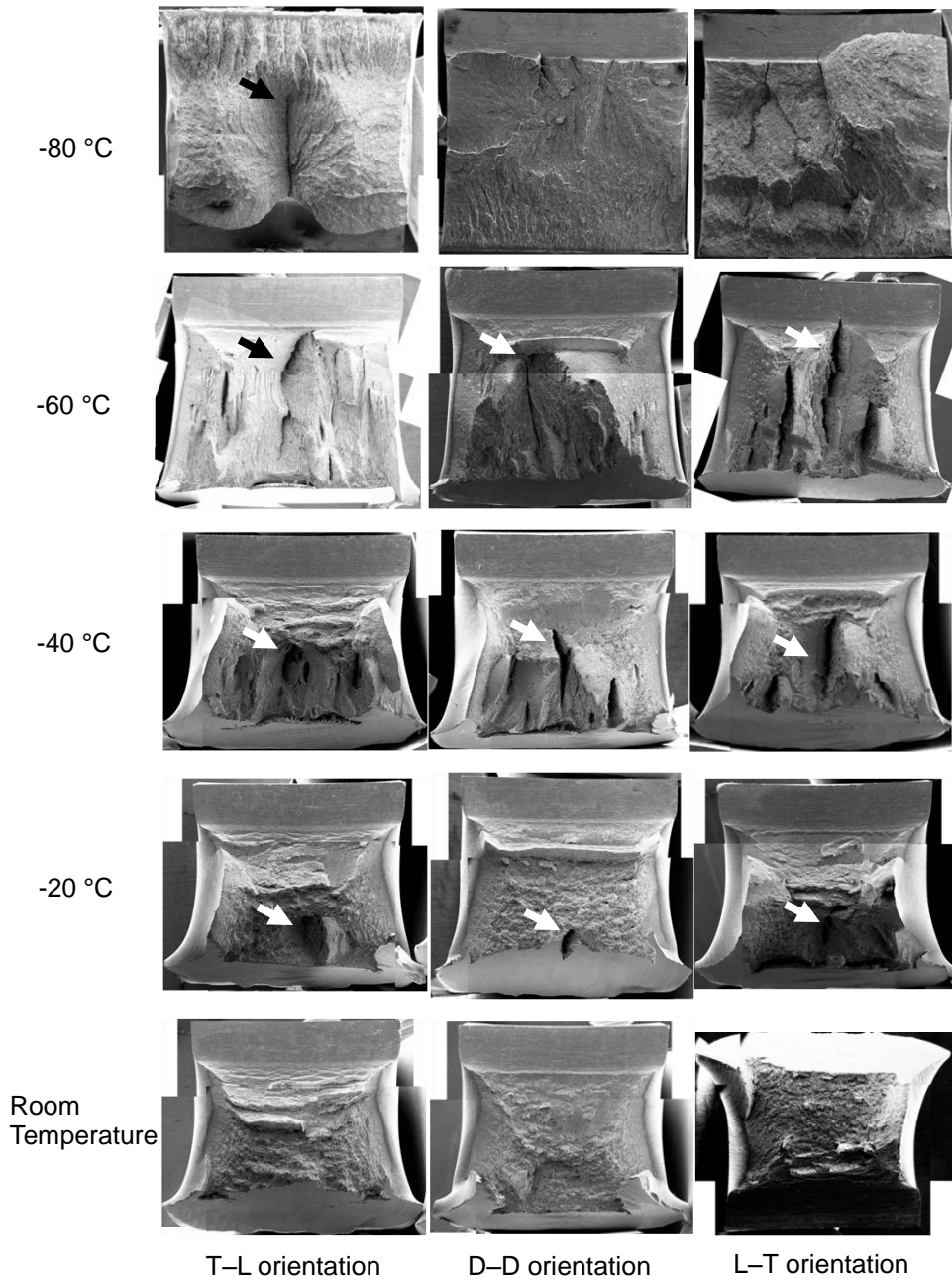


Figure 4.30. Fracture surfaces of Charpy specimens from room temperature to -80 °C of T-L, D-D and L-T orientations with delaminations indicated by black and white arrows in X80_B steel.

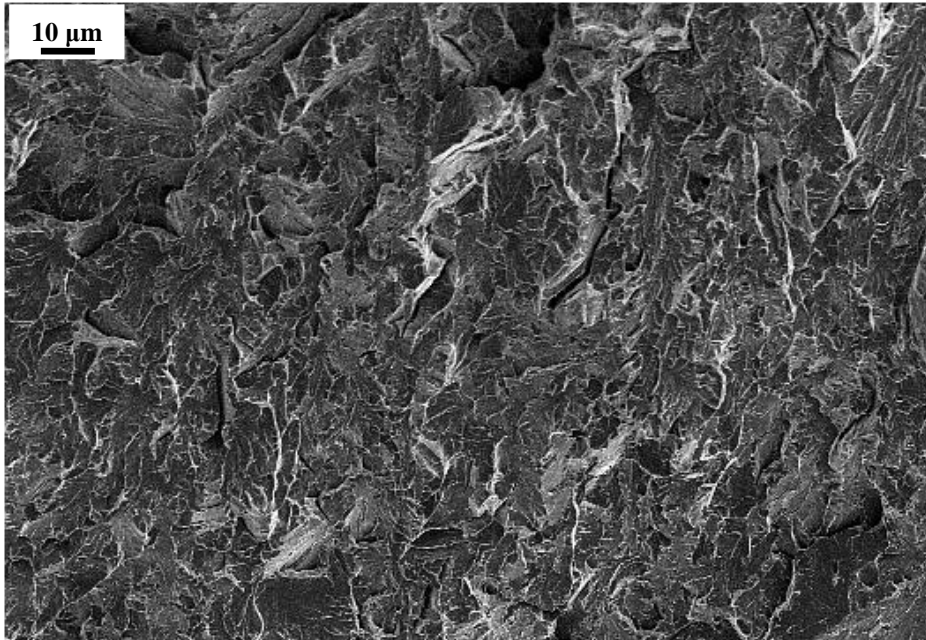


Figure 4.31. Fracture surfaces of L–T orientation specimen at -100 °C in X80_B steel.

Fig. 4.33 shows the fracture surfaces of Charpy specimens in X70_A steel. In the -80 °C, delaminations occurred except D–D orientation, and this can be associated with that the Charpy results shows the most severe anisotropy at that temperature as shown in Fig. 4.19. The delamination does not develop well in this steel; this might be due to the high fraction of allotriomorphic ferrite which may hinder the banding between fine and coarse grained regions. Without delamination, the Charpy energies are isotropic at -20 °C and -40 °C, Figs 4.19 and 4.32. The cleavage facet size was measured as approximately up to 15 μm at -100 °C (Fig. 4.34).

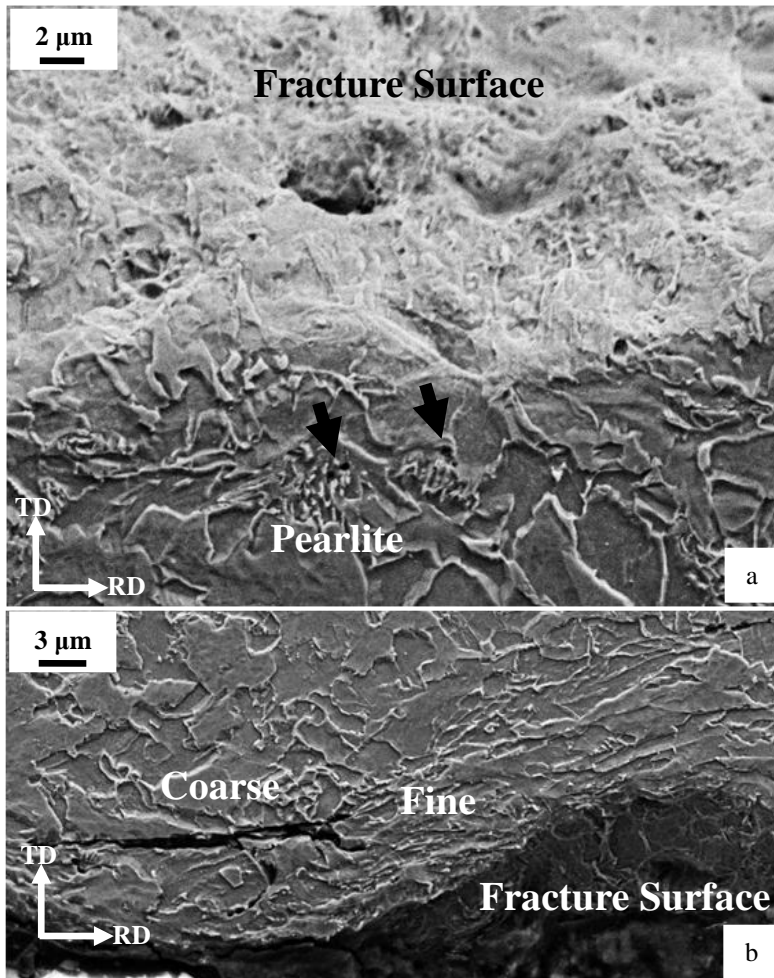


Figure 4.32. Fracture surfaces of the X80_A steel: (a) -40 °C and (b) -60 °C.

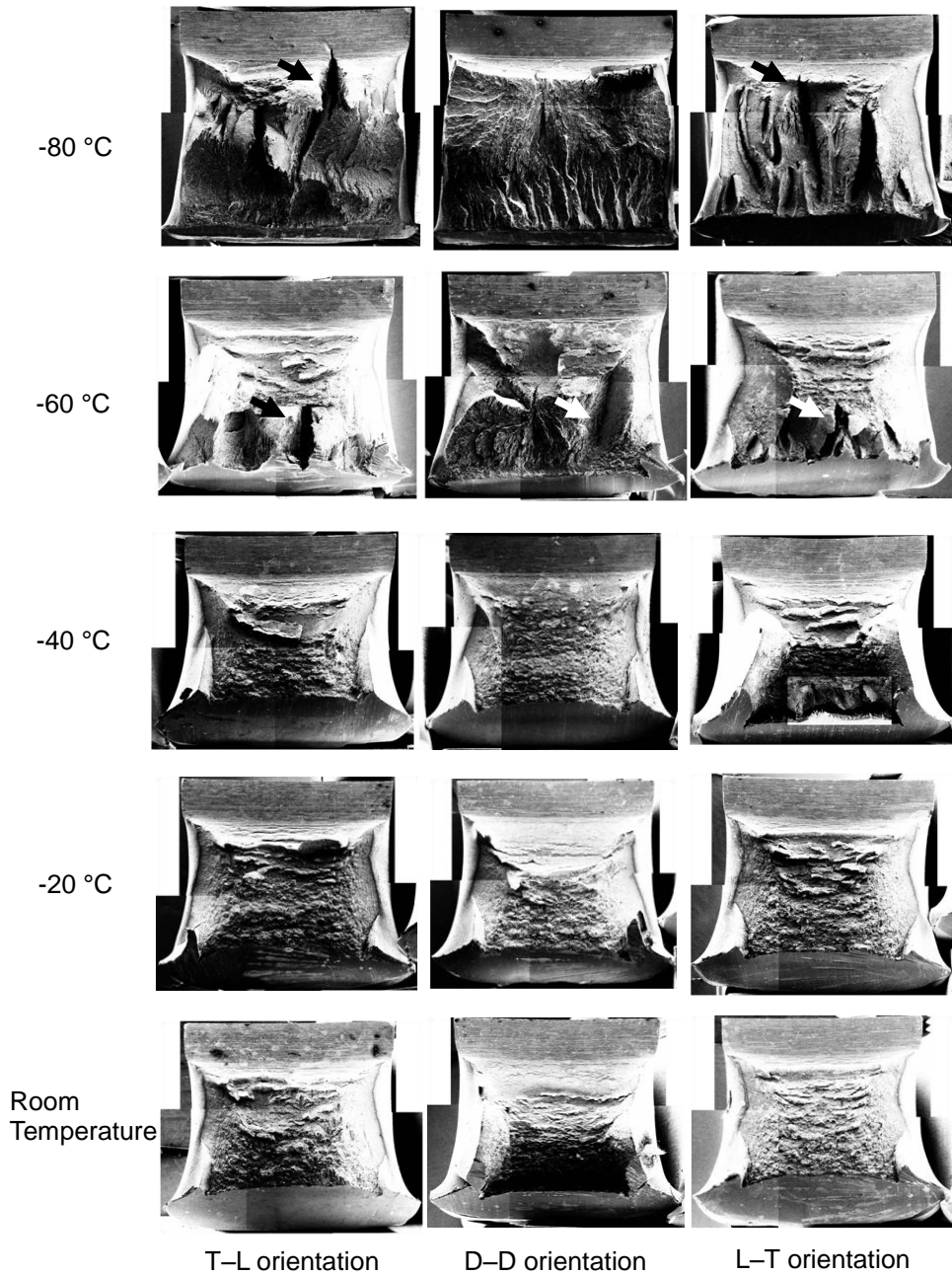


Figure 4.33. Fracture surfaces of Charpy specimens from room temperature to -80 °C of T-L, D-D and L-T orientations with delaminations indicated by black and white arrows in X70_A steel.

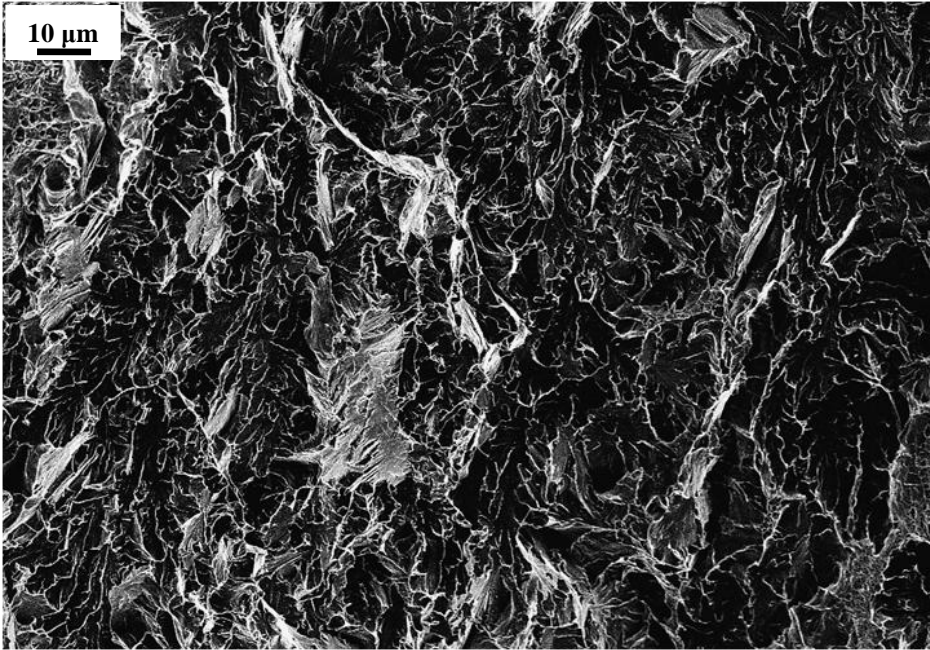


Figure 4.34. Fracture surfaces of L-T orientation specimen at -100 °C in X70_A steel.

4.5. Grain Boundary Density

It is well known that a cleavage crack can change its propagation direction when it meets an appropriate grain boundary [Hahn *et al.*, 1959]. Such deflection leads to higher fracture toughness and can modulate the ductile-to-brittle transition temperature. High angle grain boundaries provide the more effective resistance to such propagation [Qiao and Argon, 2003]. Low angle boundaries, such as lath boundaries, are less effective in this respect. [Naylor, 1979; Naylor and Krahe, 1975; Kim *et al.*, 2000]. Therefore, the density of grain boundaries ρ_{GB} on a plane parallel to the fracture surfaces of each orientation was calculated using EBSD analysis. The length of the grain boundaries L_{GB} (μm) was measured first, then divided with the observation area A (μm^2);

$$\rho_{GB} = L_{GB}/A, (\mu\text{m}^{-1}) \quad (4-1)$$

Fig. 4.35 shows ρ_{GB} for each fracture surface for low angle ($2^\circ \sim 15^\circ$), high angle ($15^\circ \sim 180^\circ$) and all boundaries ($2^\circ \sim 180^\circ$) in the investigated steels. It is evident that the density of high angle grain boundaries cannot explain the anisotropy in the DBTT region.

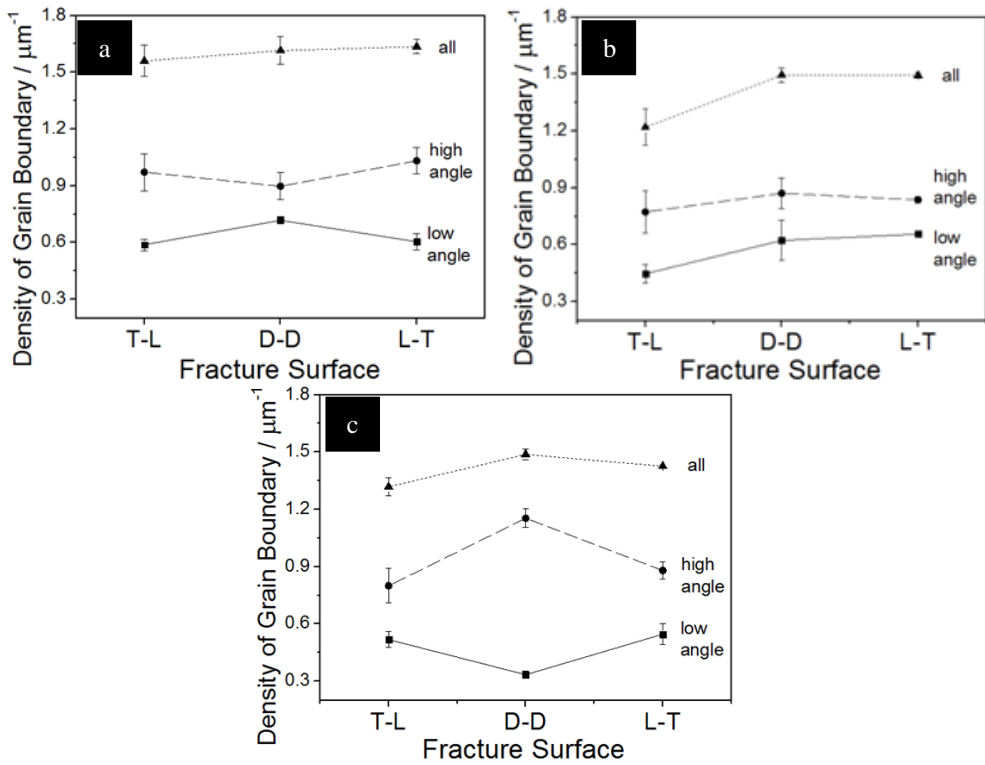


Figure 4.35. Density of grain boundaries: (a) X80_A, (b) X80_B and (c) X70_A, with low angle ($2^\circ\sim 15^\circ$), high angle ($15^\circ\sim 180^\circ$) and all boundaries ($2^\circ\sim 180^\circ$).

4.6. Crystallographic Texture

Figs 4.36 ~ 4.38 show that the ODFs of the investigated steel are similar. The texture is typical of hot-rolled steels since they underwent similar rolling process [Guillén, 1995]. It is also observed in (200) pole figures shown in Fig. 4.40, the numbers in pole figures indicates the intensity. As shown in Fig. 4.39, all the steel has strong $\{112\}\langle 110\rangle$ and $\{001\}\langle 110\rangle$ components. It should be noted that $\{112\}\langle 110\rangle$ is associated with good toughness at ambient temperature [Baczynski *et al.*, 1999] and the rotated cube texture of $\{001\}\langle 110\rangle$ conversely with low Charpy-energy of diagonal specimens than longitudinal specimens [Bourell and Sherby, 1983]. Therefore, it is necessary to investigate the distribution of $\{100\}$ planes in the investigated steels since high α intensity of $\{001\}\langle 110\rangle$ component can lead orientation dependence of Charpy-energy at low test temperatures.

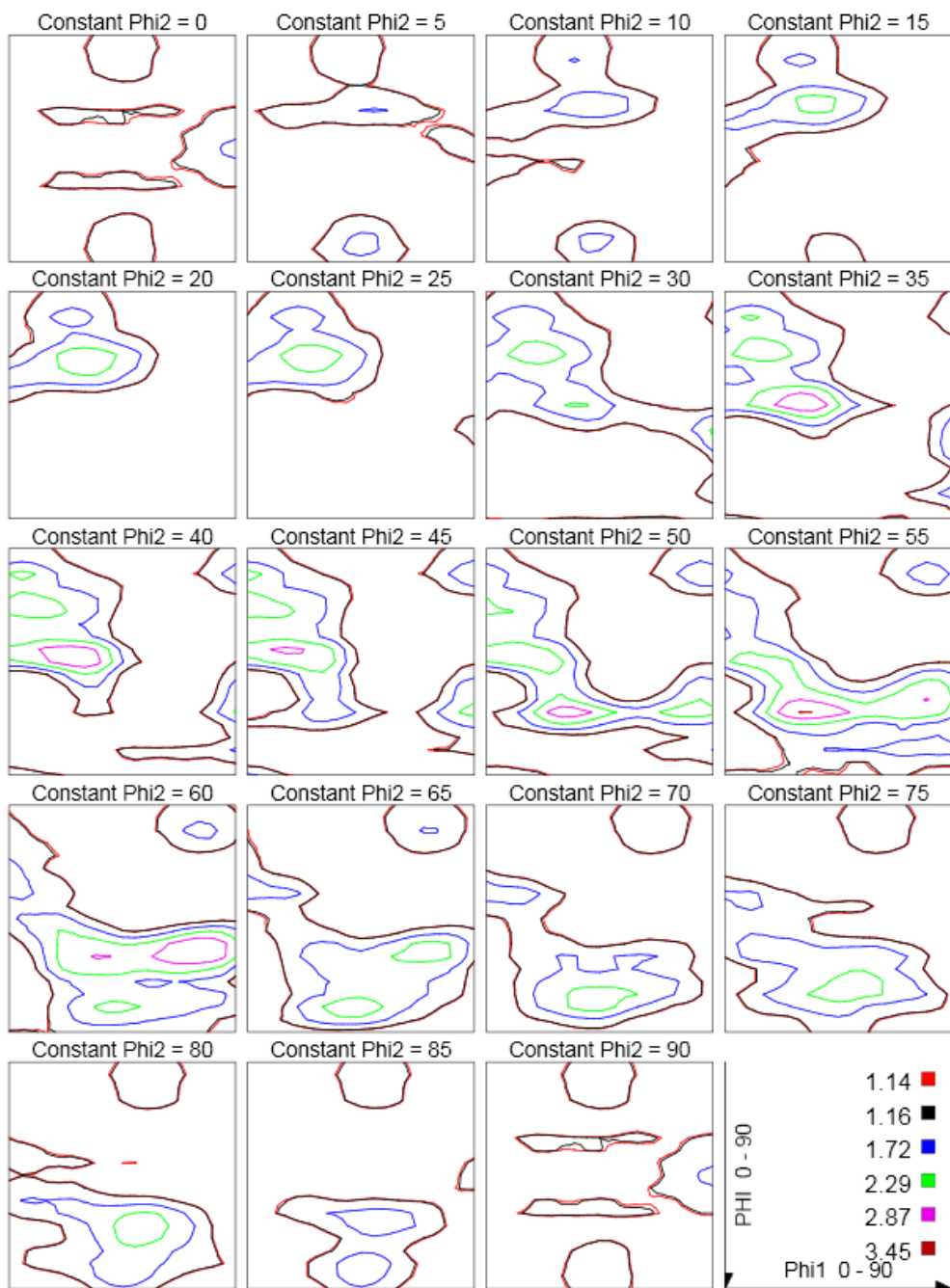


Figure 4.36. ODFs (φ_2 sections 0° to 45°, 5° intervals) of X80_A steel.

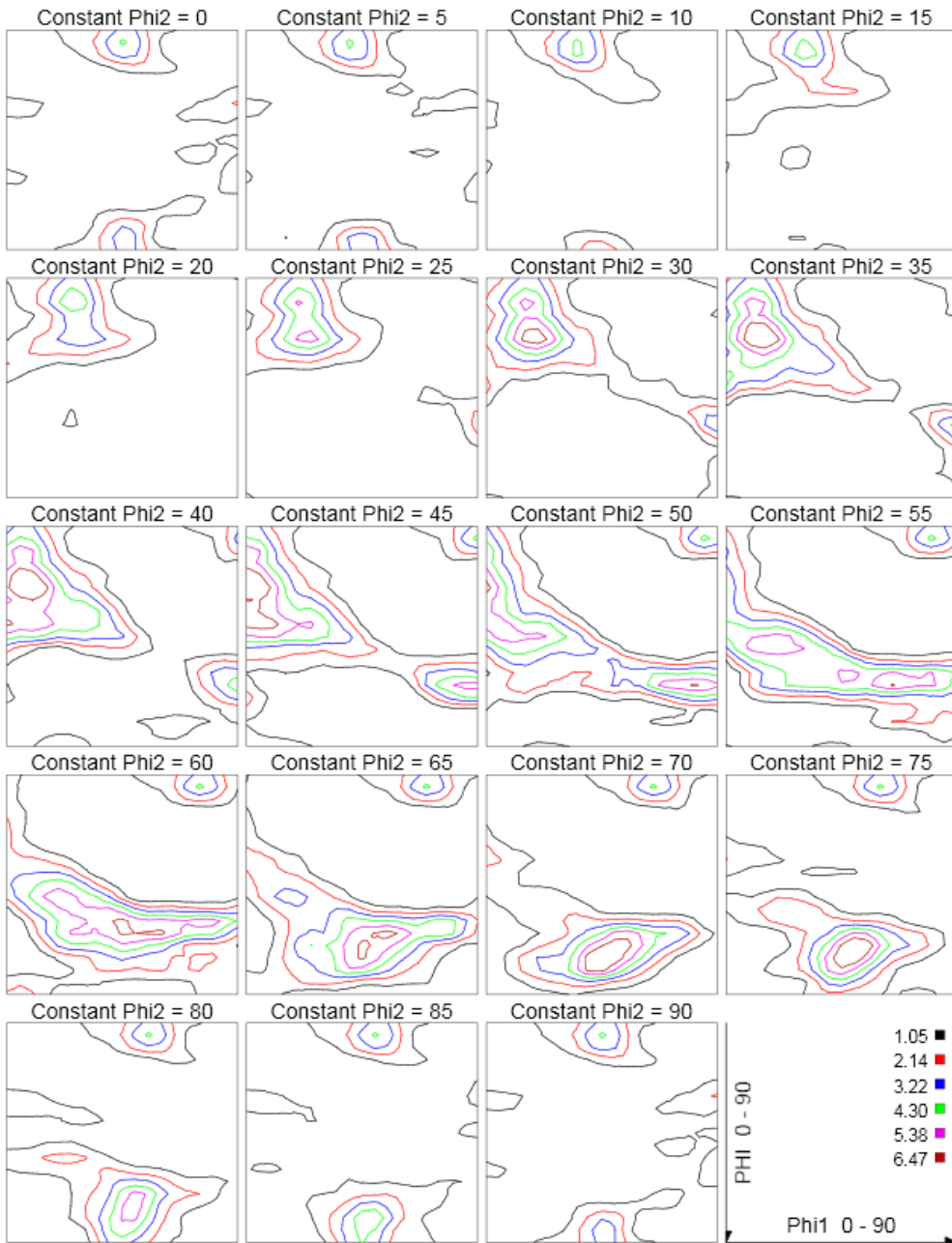


Figure 4.37. ODFs (ϕ_2 sections 0° to 45°, 5° intervals) of X80_B steel.

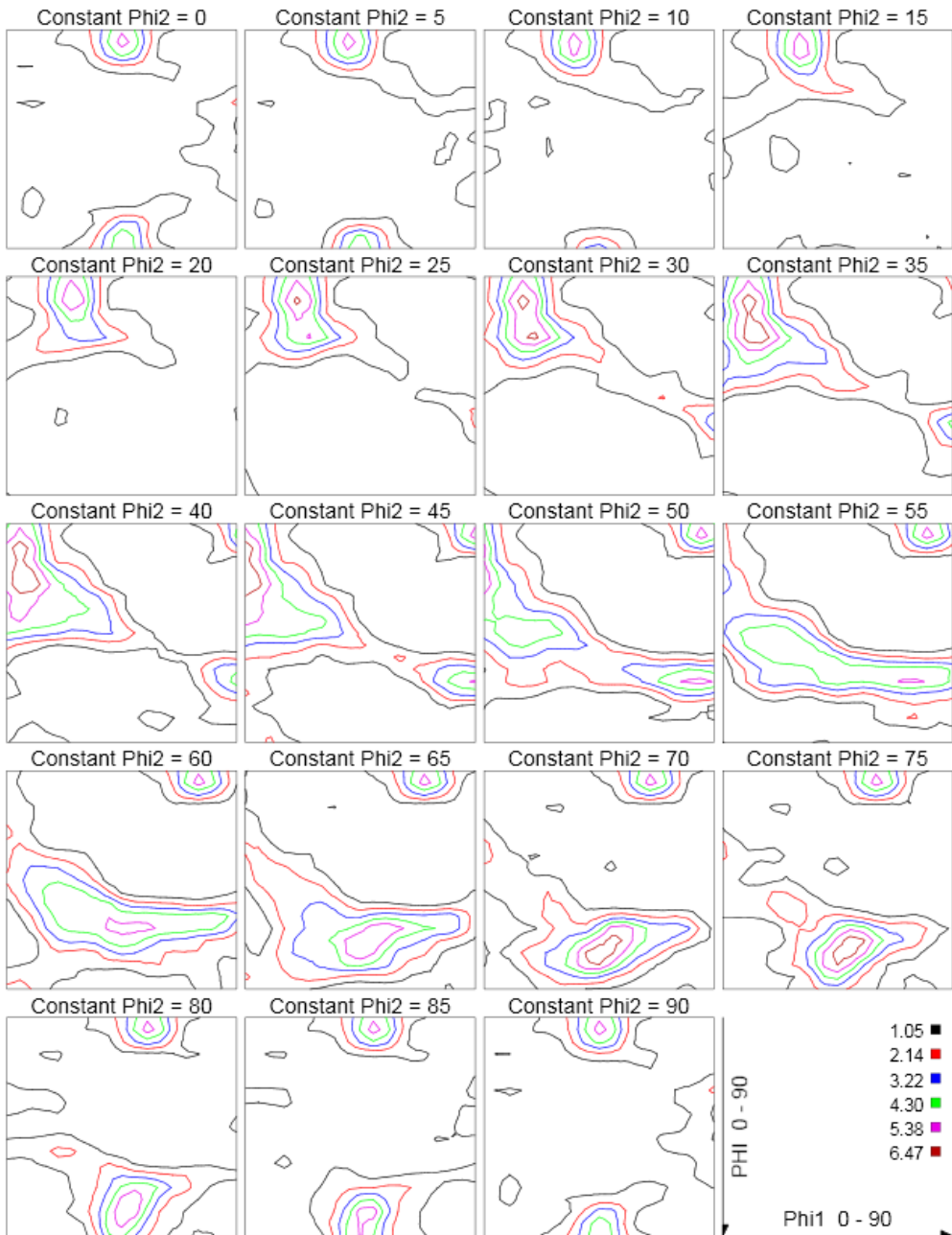


Figure 4.38. ODFs (ϕ_2 sections 0° to 45°, 5° intervals) of X70_A steel.

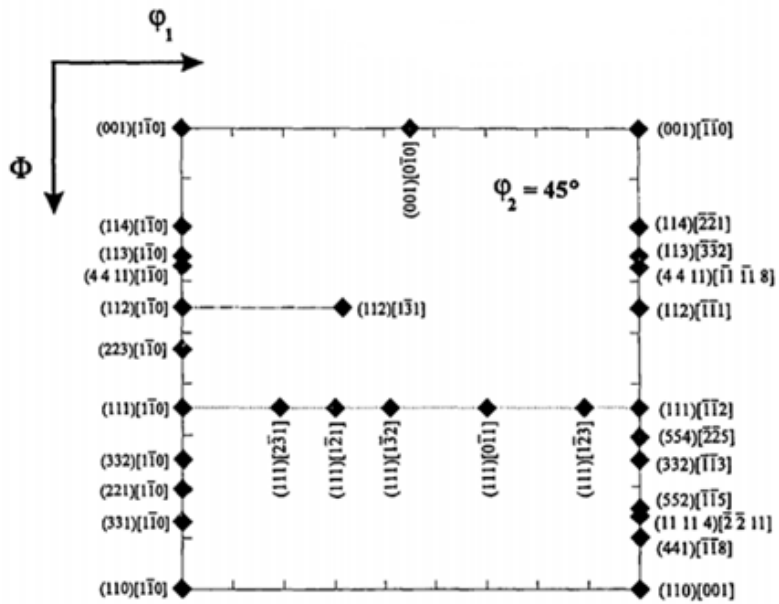


Figure 4.39. The $\varphi_2 = 45^\circ$ section of the ODF showing some important texture components in ferrite.

It is possible that a propensity of grains which have $\{100\}$ planes parallel to the fracture plane during Charpy testing can lead to brittle behaviour. Fig. 4.41 shows the estimated fraction of ferrite grains as a function of the angles 0° , 22.5° , 45° , 67.5° and 90° between the $\{100\}$ plane normal and the rolling direction obtained from the EBSD analysis with a tolerance angle of 11.25° . The tolerance angle was introduced to capture the ferrite grains as much as possible but avoiding overlap among grains in the calculations. Indeed, the fraction in Fig. 4.41 is balanced about 45° to RD, because of the symmetry of $\{100\}$ plane in cubic structure. Therefore, it is noted that the fractions at 0° , 90° to RD and at 22.5° , 67.5° to RD came from the same

grains measured. A hypothetical fraction of randomly oriented 10,000 grains was created in a computer simulation for comparison (Appendix C). The set of generated grains satisfied the distribution of misorientation angles for a randomly textured polycrystalline sample [Mackenzie, 1958].

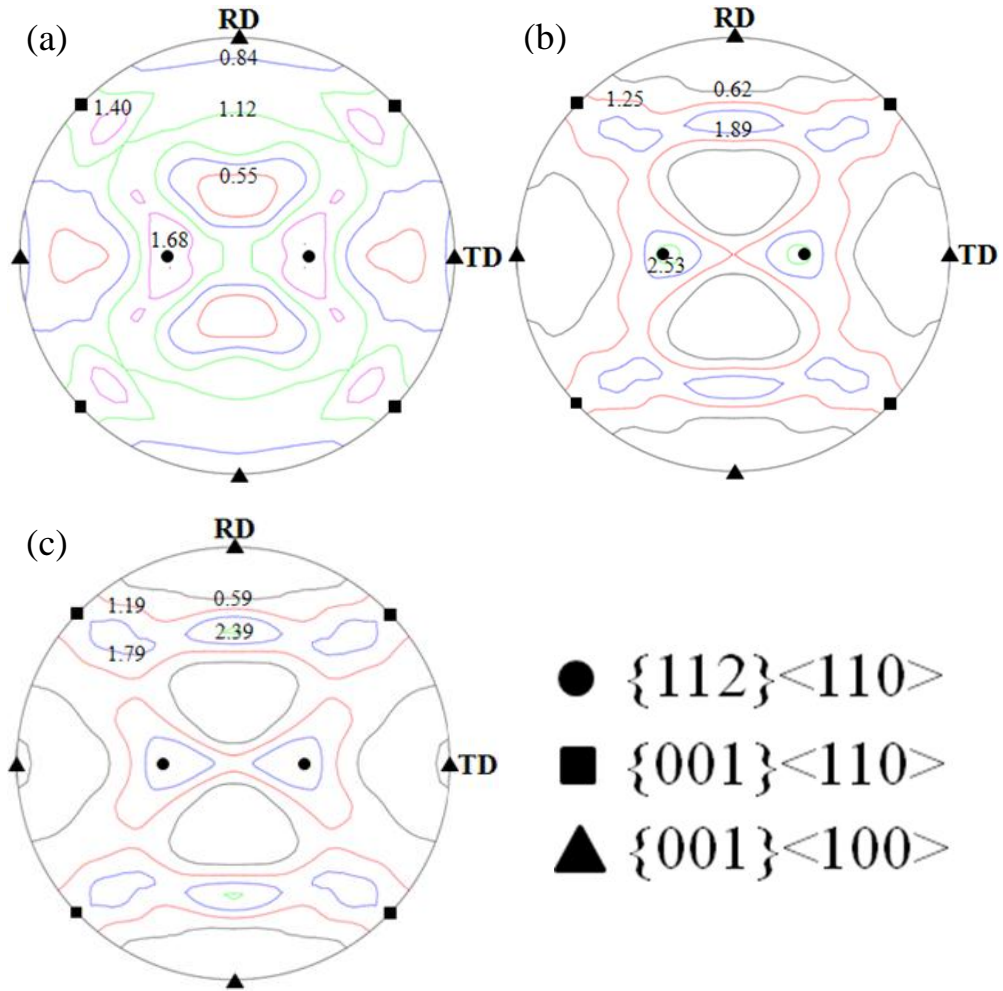


Figure 4.40. $\{200\}$ pole figure with intensity and some important texture components ($\{112\}\langle 110\rangle$, $\{001\}\langle 110\rangle$ and $\{001\}\langle 100\rangle$): (a) X80_A, (b) X80_B and (c) X70_A.

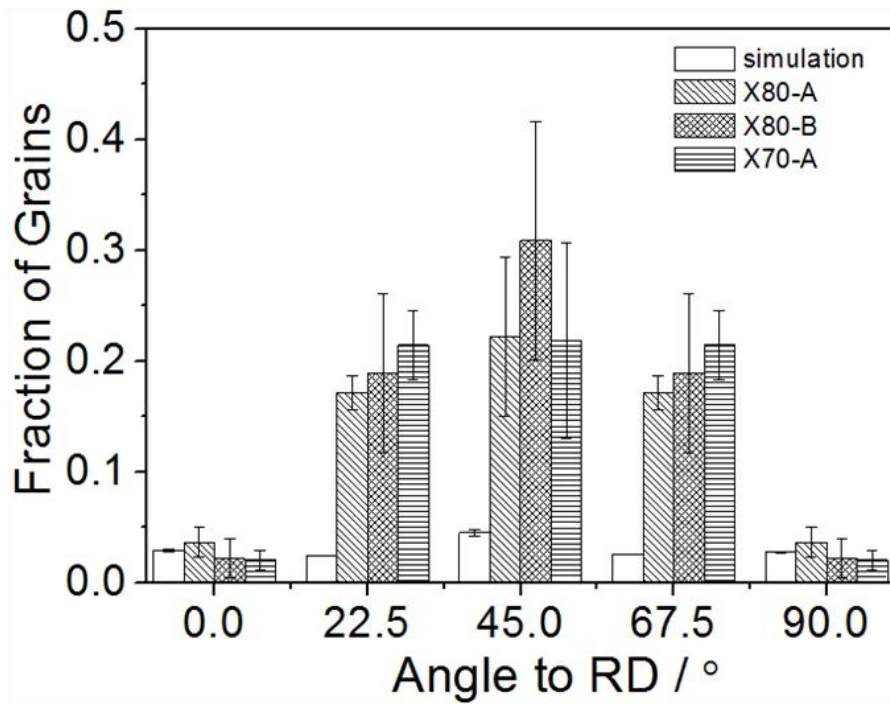


Figure 4.41. The fraction of grain as a function of angle between the $\{100\}$ plane normal and the rolling direction in the investigated steels and simulation, the tolerance angle was 11.25° to capture all the proper grains.

It should be noted that the fractions of grains having $\{100\}$ plane-normal at 45° to the rolling direction, are relatively large while those parallel to the rolling direction in the investigated steels, are comparable to randomly distributed grains. This implies that the crystallographic texture in the hot-rolled steel makes it vulnerable to brittle fracture in the D-D orientation because there is a preponderance of $\{100\}$ planes which are parallel to the fracture surface. Such an interaction between texture and properties would be most pronounced at low temperatures where cleavage occurs, as is observed experimentally.

4.7. Summary

Investigation of the anisotropy of Charpy toughness in three kinds of API linepipe steels has been carried out. The Charpy energies in the upper and lower shelf regimes exhibited isotropy in all the steels. However, it has been appeared that the steels have a similar orientation–dependence of Charpy toughness in the DBTT region. The presence of inclusions does not seem to be related to the phenomena since they have been shown to be spherical in shape. The concept of the density of grain boundaries was introduced because cleavage cracks are deflected at high angle grain boundaries, but the measured densities could not explain the anisotropy. On the other hand, it is revealed that delamination is associated with microstructural banding and strongly influences the orientation dependence of Charpy toughness in the DBTT region in all the investigated steels. In addition, it is implied that the crystallographic texture is related to the anisotropy. Further studies on delamination and crystallographic texture will be discussed in Chapter 5.

V. Delamination and Crystallographic Texture

5.1. Additional Orientation of Charpy Specimen

As discussed in the previous section, delamination is related to the presence of banding in X80_A, X80_B and X70_A steels (Tables 3.1 and 3.2), and the additional plasticity it entails during the process of fracture leads to an effective increase in toughness. As a consequence, the toughness of the D–D orientation of Charpy specimens is worst because the extent of delamination at that orientation is minimal.

Additional tests were conducted to add weight to the argument that delamination is the prime cause of toughness anisotropy in X80_A and X70_A steels. The orientation of the test coupon was prepared as shown in Fig. 3.2b and it was designed to eliminate the effect of delamination on orientation–dependence of impact toughness. Fig. 5.1ab shows the stress states near the notch [Knott, 1973].

The stress distribution at the notch determines the extent of fracture toughness. There the initiation and propagation stresses for delamination are given by σ_z and σ_y for the conventional case or σ_x and σ_y for the additional case because the specimen is sufficiently thick to incur the plane strain condition (Fig. 5.1). When delamination occurs, the effective thickness of the specimen is reduced, and eventually σ_z decreases about to zero at each delamination and a plane stress condition prevails. In this case, the initiation stress for delamination, σ_z for the conventional case is nearly zero but σ_x remains, so that it is still possible to

promote delamination in the additional notch orientation (Fig. 5.1).

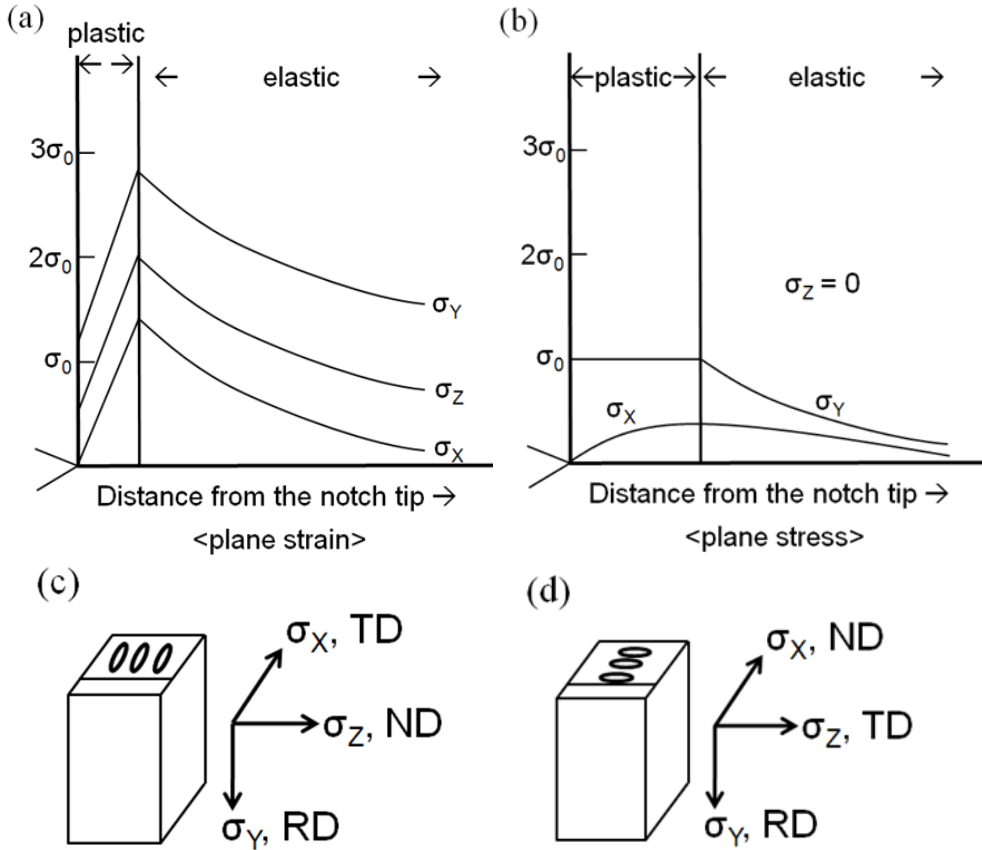


Figure 5.1. Schematic elastic/plastic stress distribution near a notch: (a) in plane strain ($\epsilon_z = 0$), (b) in plane stress ($\sigma_z = 0$), adapted from [Knott, 1973], and schematic diagram for the directions of the stresses: (c) in L-T conventional notch type and (d) L-S additional notch type specimens. Ellipsoid represents delamination.

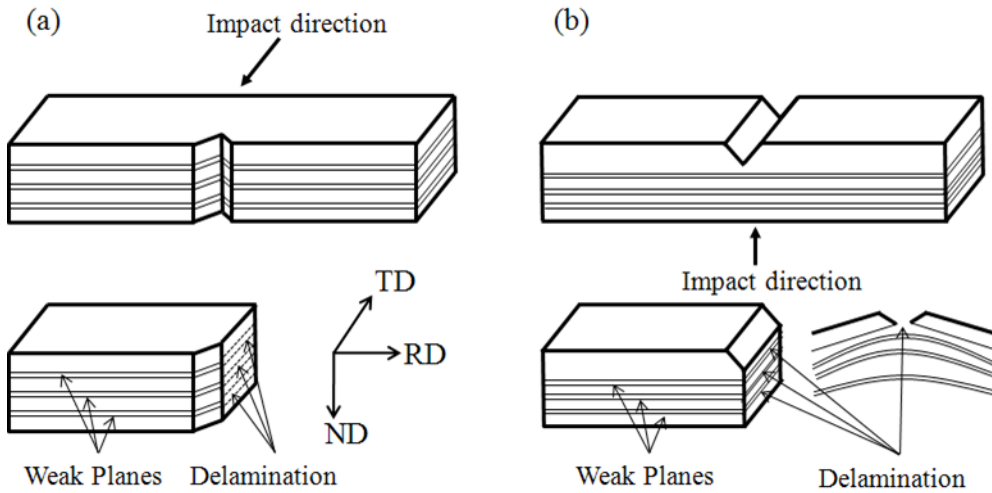


Figure 5.2. Two basic geometries of laminates with impact direction: (a) crack divider type or L–T conventional notch orientation and (b) crack arrester type or L–S additional notch orientation [American Society for Testing, 1969].

The conventional and additional notch orientations actually correspond to the “crack divider” and “crack arrester” types in two basic geometries of laminates, as shown in Fig. 5.2. With a crack divider (Fig. 5.2a), the fracture is split into several parallel cracks propagating independently in distinct layers due to the existence of σ_z (Fig. 5.1c) and triaxial stress conditions cannot be sustained so the brittle mode of fracture is suppressed. This means that the condition for stress distribution is changed from plane strain to plane stress as discussed before. With a crack arrester, when the main crack approaches the weak interface between hard and soft phases, it is likely to delaminate due to the tensile stresses acting parallel to the plane of the

crack (Fig. 5.2b). And the energy is used in delamination when the main crack is completely blunted [American Society for Metals, 1967; American Society for Testing, 1969; Carreño *et al.*, 2003; Pook, 1972]. Eventually, if X80_A or X70_A have well-developed banded microstructures consisting of hard and soft phases which act like the weak interface in the laminate, delamination will be promoted in the additional notch orientation [Almond, 1970; Lum *et al.*, 1975].

Fig. 5.3 shows clearly that all the specimens tested in -20 °C and -60 °C show a large, single split in X80_A steel. At -20 °C, the delaminations occur in a deep and narrow manner, and they become wider at -40 °C and -60 °C because probably the main crack is blunted as pointed out before. It is evident from Fig. 5.4 that the anisotropy is much reduced in the ductile–brittle transition region.

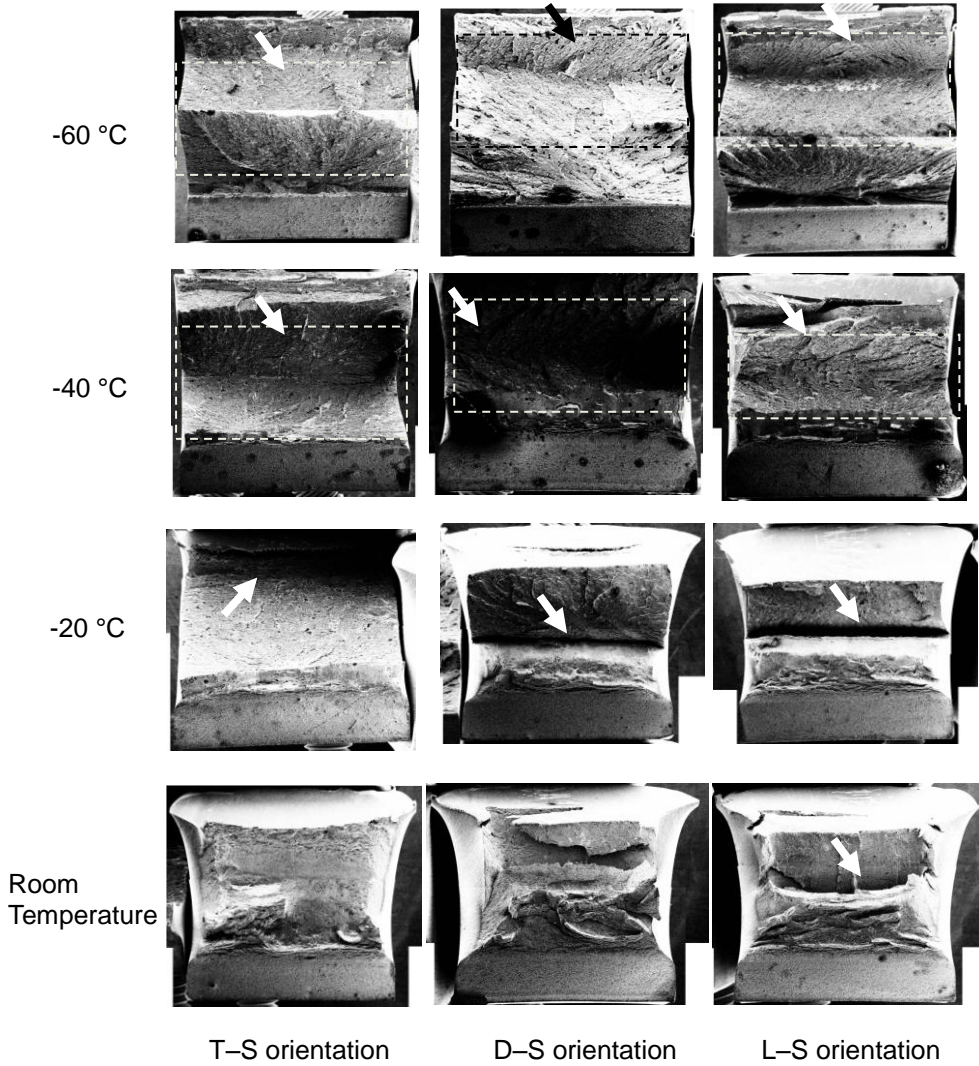


Figure 5.3. The fracture surfaces of additional Charpy specimens from room temperature to -60 °C of T-S, D-S and L-S orientations in X80_A steel.

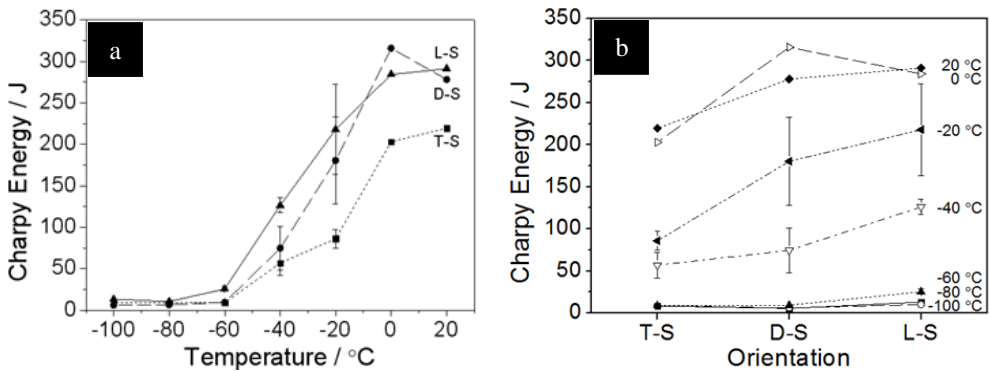


Figure 5.4. Charpy properties of X80_A steel: (a) The impact transition curve and (b) the anisotropy curve (additional notch type specimens, Fig. 3.2b).

Fig. 5.5 shows the fracture surfaces of the additional orientation of Charpy specimen in X70_A steel. In this case, delamination is not well-developed, probably due to the high fraction of allotriomorphic ferrite corresponding to suppression of the evolution of banding between the fine and coarse grained bainite, as with the conventional case as shown in Fig. 4.33. Thus, the anisotropy has not been relieved. However, a toughening effect of delamination was observed for the samples tested at -100 °C. T-S and L-S have delamination and show the higher Charpy energy than D-S (Fig. 5.6) when all the orientations were governed by fully brittle fracture as shown in Fig. 5.7. On the other hand, T-S interestingly shows the lowest absorbed energy in -80 °C. This is because all the orientations were governed by a ductile fracture mechanism (Fig. 5.8) and the delamination decreased the absorbed energy for T-S as discussed in section 2.3.5.

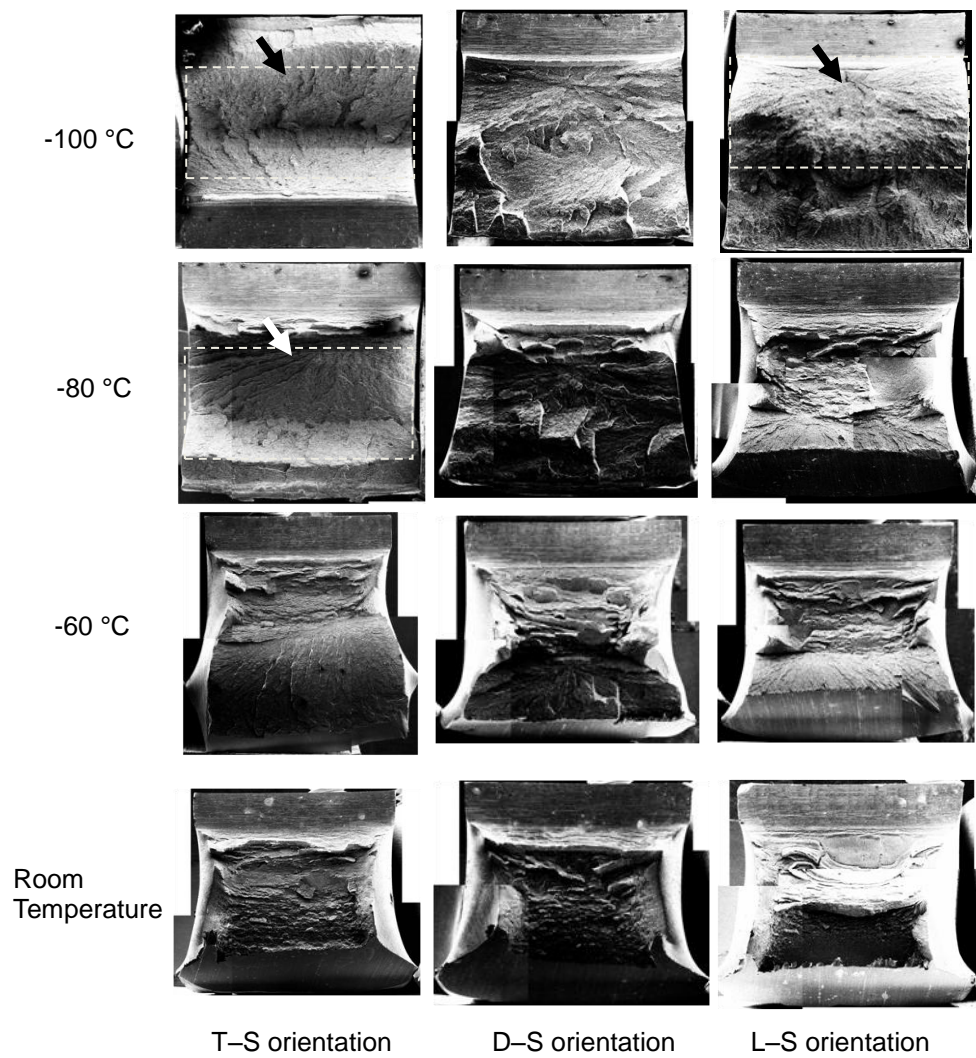


Figure 5.5. The fracture surfaces of additional Charpy specimens from room temperature to -100 °C of T-S, D-S and L-S orientations in X70_A steel.

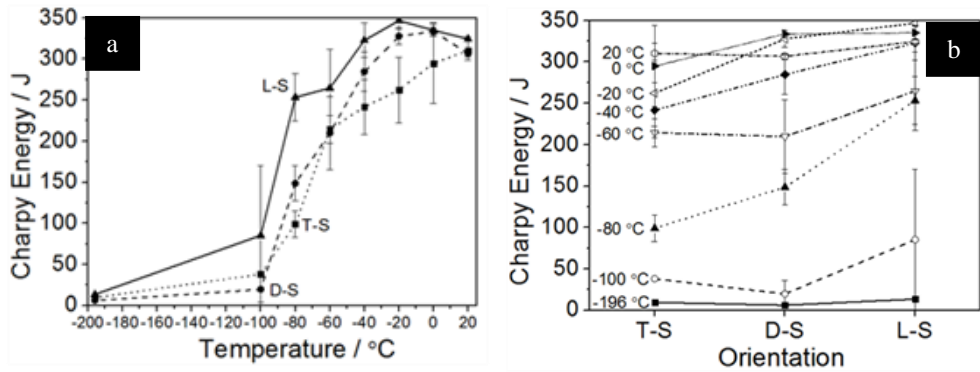


Figure 5.6. Charpy properties of X70_A steel: (a) The impact transition curve and (b) the anisotropy curve (additional notch type specimens, Fig. 3.2b).

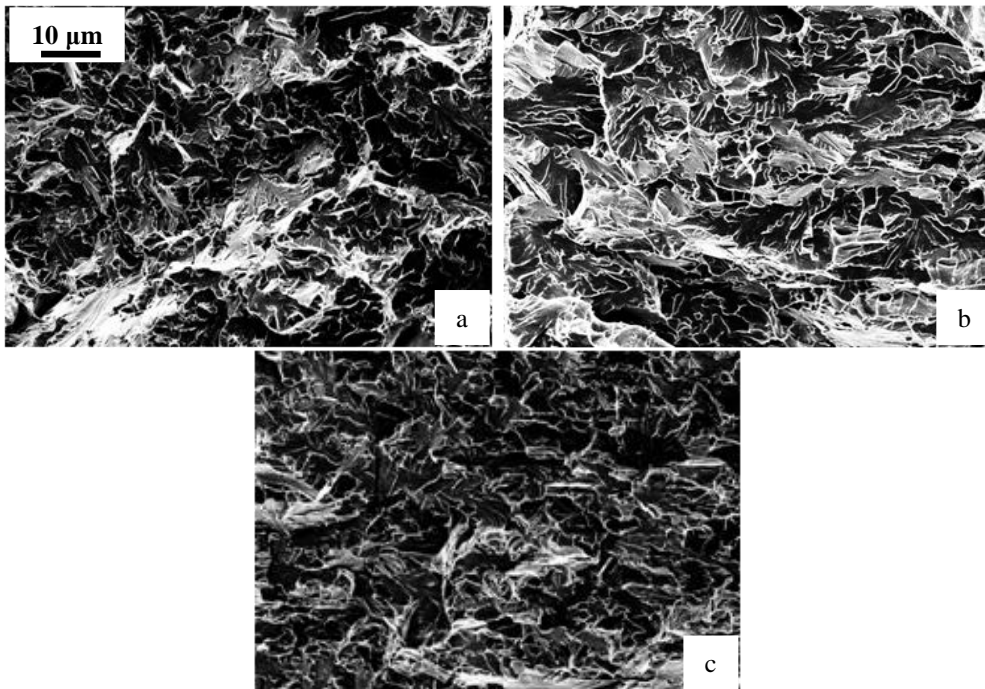


Figure 5.7. Higher magnification of fracture surfaces for the samples tested at -100 °C of X70_A steel: (a) L-S, (b) D-S and (c) T-S (additional notch type specimens, Fig. 3.2b).

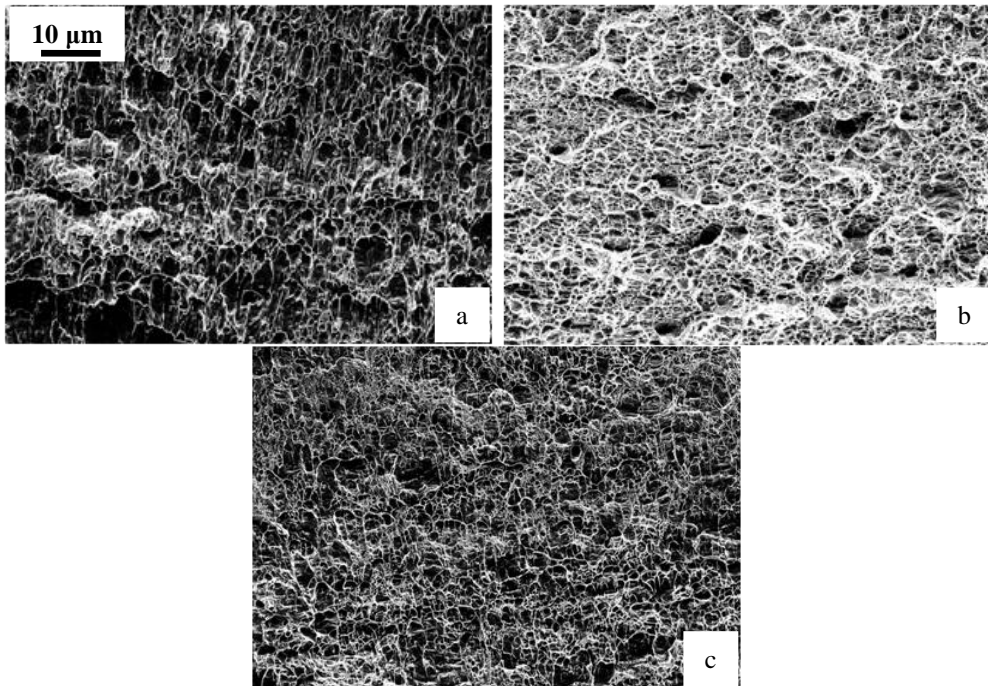


Figure 5.8. Higher magnification of fracture surfaces for the samples tested at -80 °C of X70_A steel: (a) L-S, (b) D-S and (c) T-S (additional notch type specimens, Fig. 3.2b).

5.2. Quenching Heat Treatment

The purpose of the experiments reported here was to dramatically change the microstructure but retain the crystallographic texture within the steel in an attempt to isolate its contribution to anisotropy.

Since the A_{c3} temperature of X80_A steel was calculated as 840 °C using MTDATA and the TCFE4 database [NPL, 2006], and the A_{c3} temperature was approximately 860 °C during dilatometric experiments (Appendix D), the annealing temperature was chosen as 890 °C to minimize the prior austenite grain size and to suppress austenite grain growth in order to retain texture memory effect [Demura *et al.*, 2007; Lischewski *et al.*, 2008] as discussed in section 3.4.1.

After the heat treatment, the microstructure was totally changed due to the quenching process, as shown in Figs 5.9 and 5.10. The banding was eliminated when martensite was formed without pearlite and M/A constituents. Some grains have no sign of martensite of plate-like morphology, appearing white in the optical micrographs. Fig. 5.11 also pointed out that some of grains have little spread less than 1.5°. The hardness values in the martensitic structure and the white area in the optical micrographs are 323 ± 13 and 281 ± 9 HV, respectively, with a macroscopic hardness of 296 ± 6 HV.

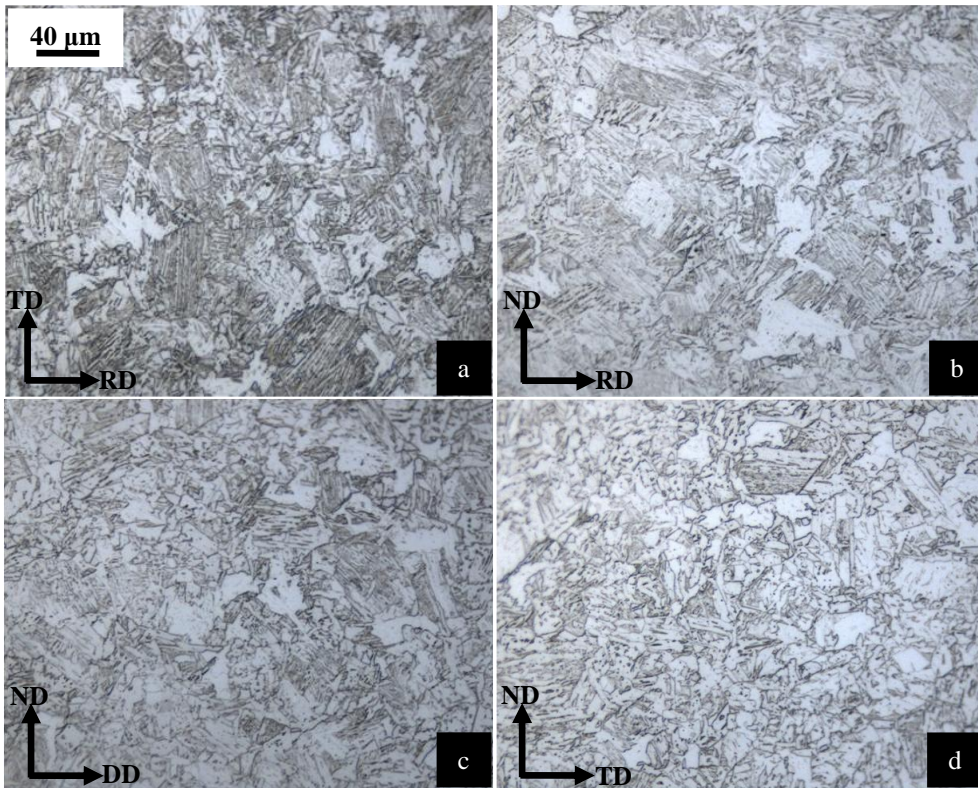


Figure 5.9. Optical micrographs after the heat treatment: Surface normal to (a) ND, (b) TD, (c) DD and (d) RD. 2% nital etched.

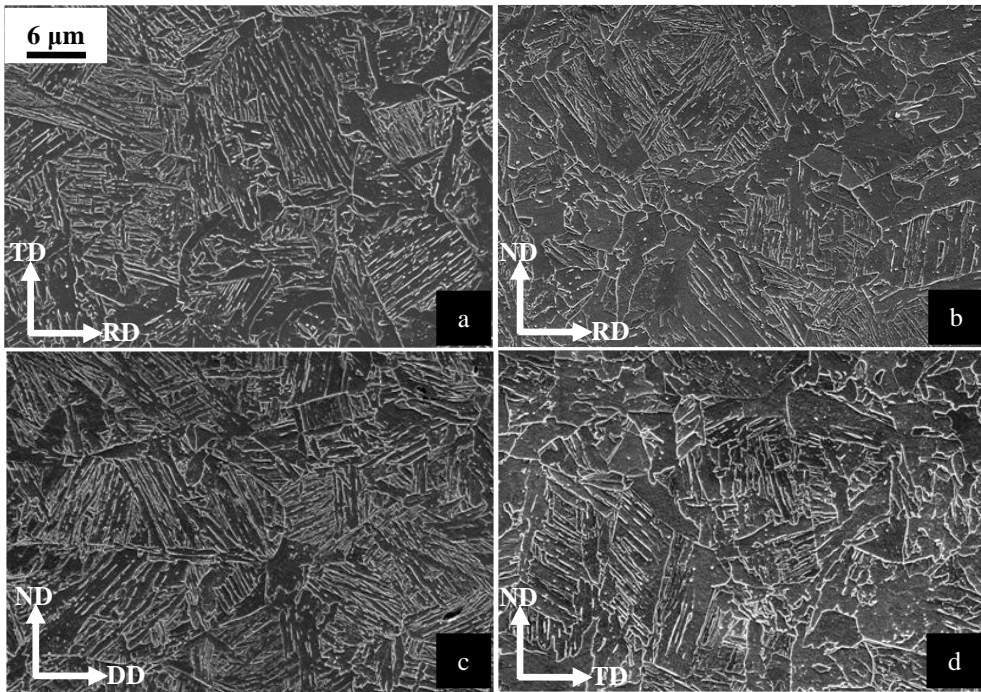


Figure 5.10. SEM micrographs after the heat treatment: Surface normal to (a) ND, (b) TD, (c) DD and (d) RD. 2% nital etched.

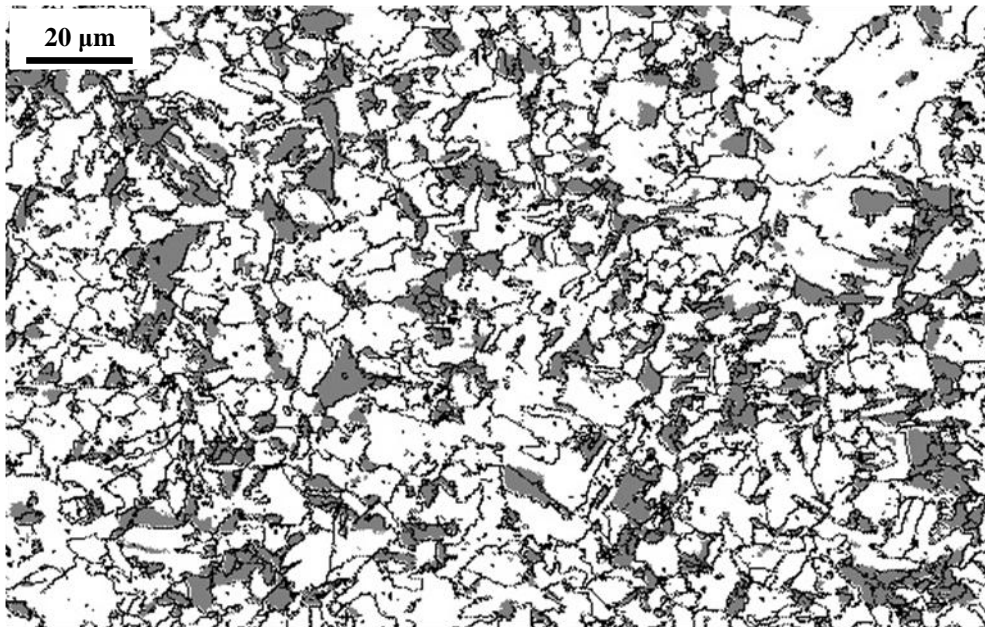


Figure 5.11. Map of grain orientation spread after the heat treatment with the value less than 1.5° in a grain with boundaries identified using the criterion that the orientation difference is greater than 15° .

As discussed previously, the orientation–dependence of Charpy toughness in the linepipe steels studied comes primarily from delamination phenomena associated with a banded microstructure. Therefore, if the banding is eliminated then delamination might also be avoided, and finally the anisotropy mitigated. As shown in Figs 5.9 and 5.10, the microstructure of surfaces normal to RD, TD and DD after the heat treatments shows no banding. Fig. 5.12 shows the fracture surfaces; there is no delamination at any orientation or temperature because the microstructure has no elongated grains or banding. It is expected that the anisotropy decreases in the DBTT region due to the lack of toughening as a

result of delamination in the L–T and T–L orientations at $-40\text{ }^{\circ}\text{C}$ and $-60\text{ }^{\circ}\text{C}$, as shown in Fig. 4.24 [Song *et al.*, 2005].

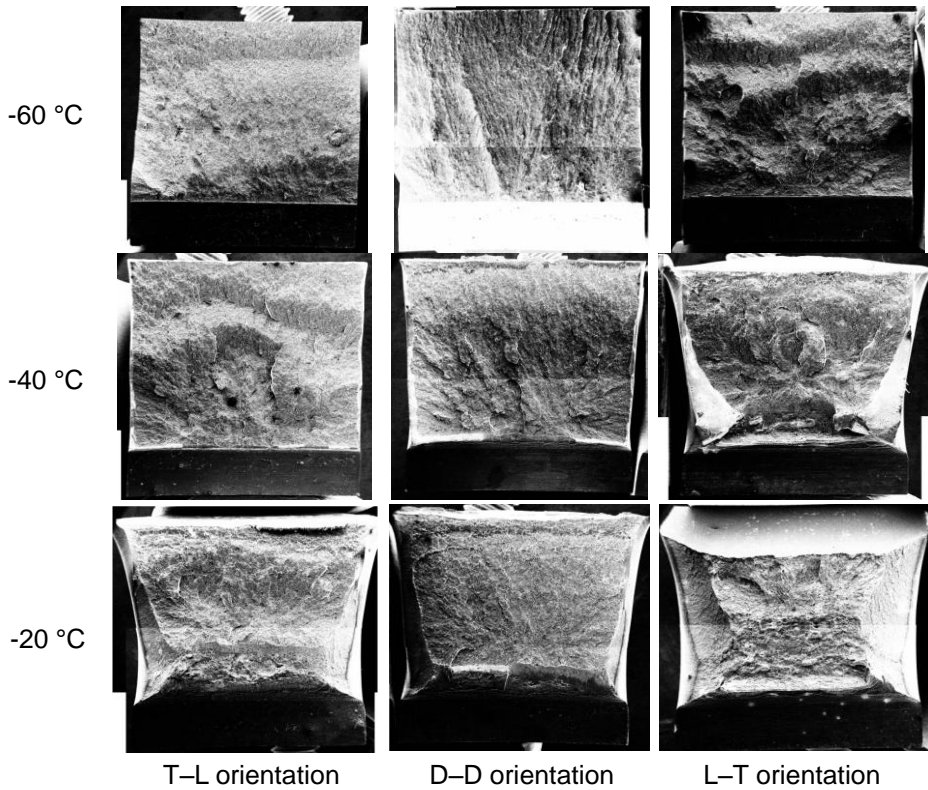


Figure 5.12. The fracture surfaces of Charpy specimens after the heat treatment from $-20\text{ }^{\circ}\text{C}$ to $-60\text{ }^{\circ}\text{C}$ of T–L, D–D and L–T orientations.

Fig. 5.13 shows the impact energy and the anisotropy curves of X80_A steel after a quenching heat treatment for full-sized specimens. The degree of anisotropy decreases in the DBTT region, but the characteristic V-shape persists in the anisotropy curve in the DBTT region even though the microstructure was

totally changed. It is interesting that the D–D orientation always shows the most pronounced ductile–to–brittle transition even after the heat treatment. The density of high–angle grain boundaries still cannot explain the anisotropy in the DBTT region as shown in Fig. 5.14.

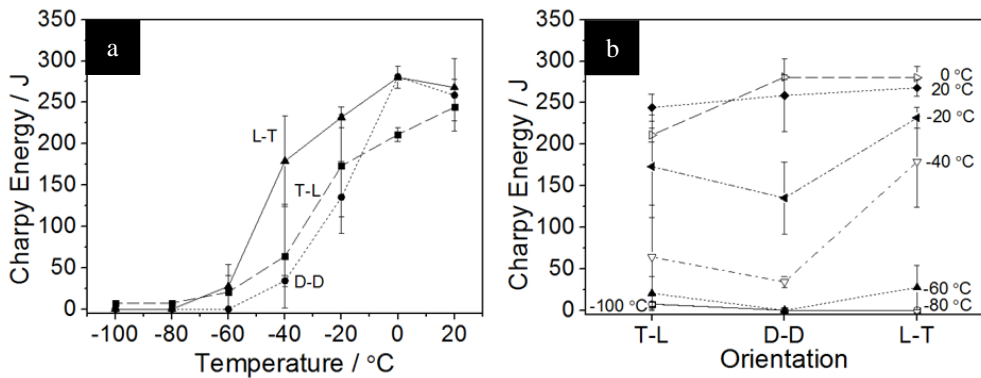


Figure 5.13. Charpy properties after the heat treatment: (a) The impact transition curve and (b) the anisotropy curve.

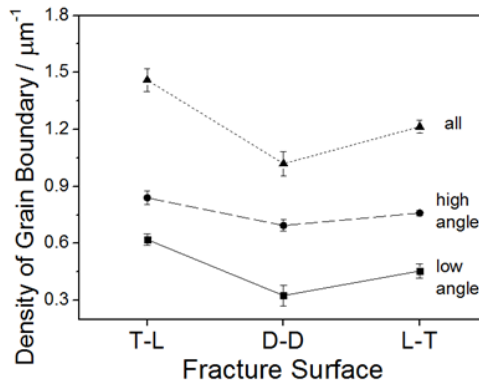


Figure 5.14. Density of grain boundaries after the quenching heat treatment, with low angle (2°~15°), high angle (15°~180°) and all boundaries (2°~180°).

However, it is possible to explain the characteristic V–shape anisotropy with the distribution of the grains having {100} planes parallel to the fracture plane because there is greater propensity of grains having {100} plane parallel to the fracture plane of rolled steel sheet in the D–D orientation [Bourell and Sherby, 1983]. Figs 5.15 and 5.16 show the ODFs and pole figure after the quenching heat treatment. The macroscopic texture is not significantly changed after heat treatment as shown in Figs 4.36 and 5.15. This is believed to be due to the texture memory effects. The measured {200} pole figures show that {112}<110> component was weakened but {100}<011> component was retained as shown in Figs 4.40 and 5.16.

Further analysis has been carried out to support the role of crystallographic texture on the anisotropy of toughness. The fraction of grains having {100} planes parallel to fracture surfaces before and after the quenching heat treatment. Fig. 5.16 shows the fraction of grains as a function of the angles between the {100} plane normal and the rolling direction in X80_A steel, heat–treated sample and hypothetical simulation (Appendix C), achieved from EBSD experiments with a tolerance angle 11.25°. The fractions at intermediate angles (22.5°, 45° and 67.5°) are much greater than that at 0° and 90°. It implies that the toughness anisotropy in the DBTT region was induced by crystallographic texture. In conclusion, the uneven distribution of {100} plane is related to the rapid ductile–to–brittle transition in D–D orientation, and it is the factor for the orientation dependence of Charpy toughness in the DBTT.

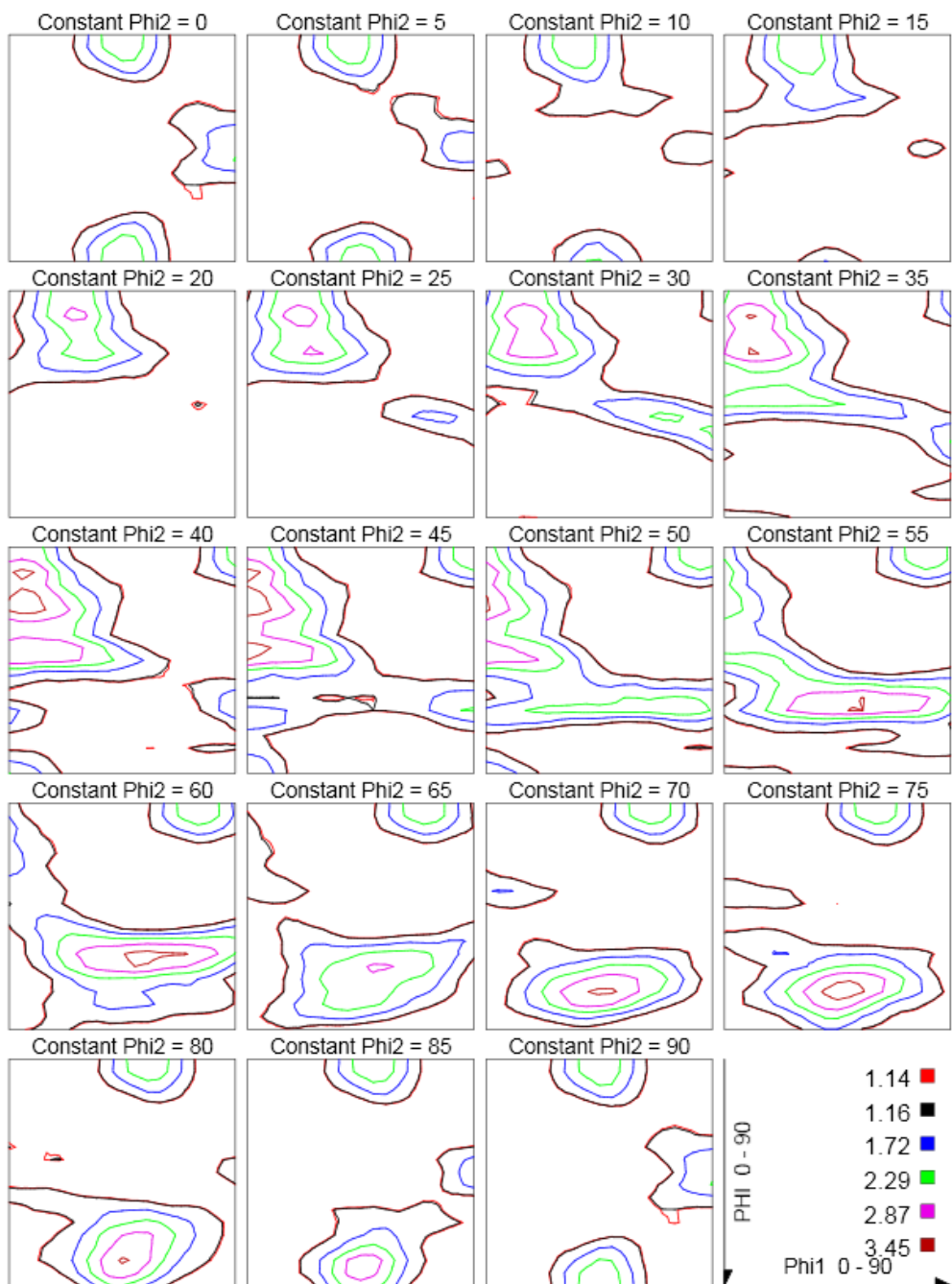


Figure 5.15. ODFs (ϕ_2 sections 0° to 45° , 5° intervals) after the quenching heat treatment.

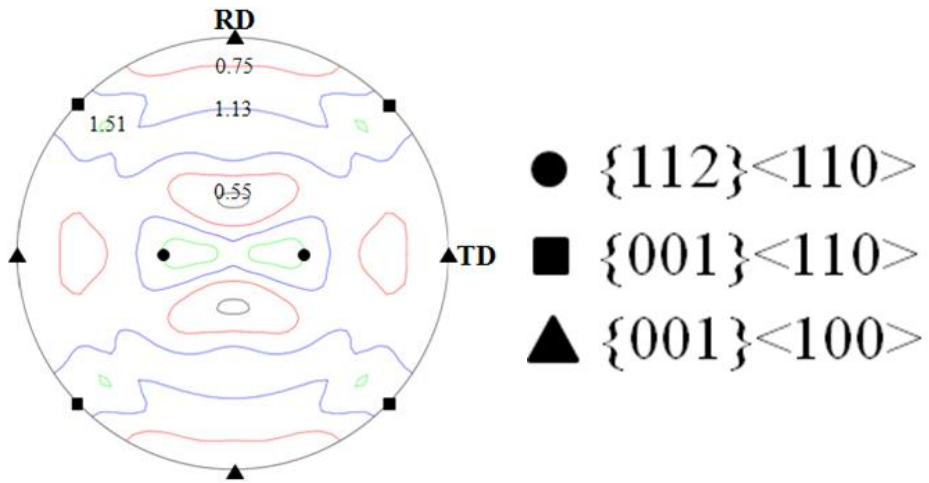


Figure 5.16. $\{200\}$ pole figure with intensity and some important texture components ($\{112\}\langle 110\rangle$, $\{001\}\langle 110\rangle$ and $\{001\}\langle 100\rangle$) after the quenching heat treatment.

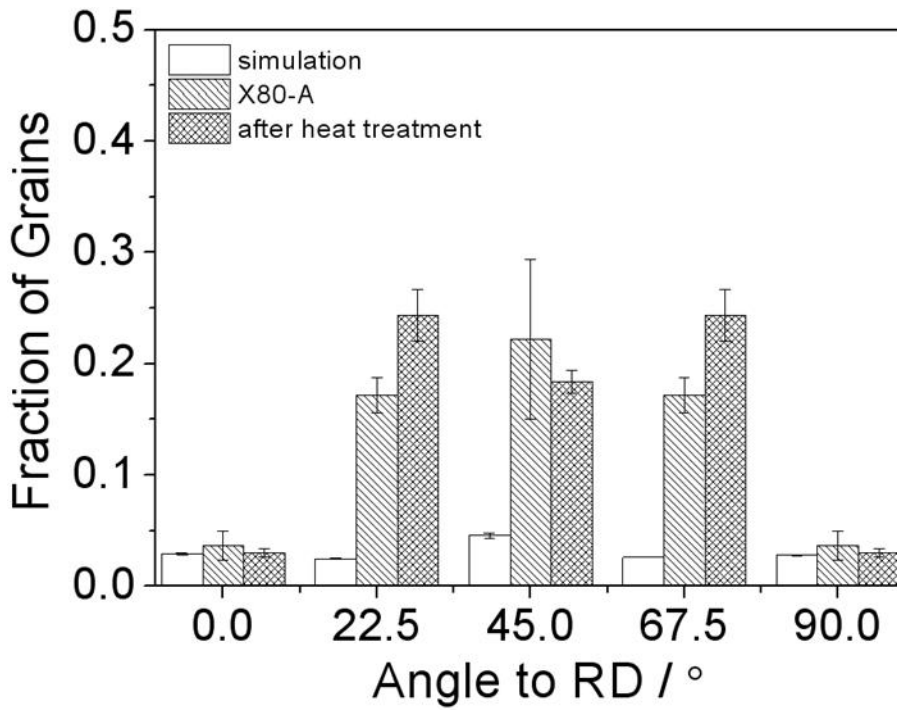


Figure 5.17. The fraction of grain as a function of angle between the {100} plane normal and the rolling direction in X80_A steel, heat-treated sample and simulation, the tolerance angle was 11.25°.

VI. Different Rolling Processes in API_X70 Steels

As listed in Tables 3.1 and 3.2, X70_B, X70_C and X70_D steels having same chemical composition but different finish rolling temperature (FRT) and start cooling temperature (SCT) were prepared in order to investigate the effect of processing variables on orientation-dependence of Charpy properties. Rolling had not conducted severely relative to X80_A, X80_B and X70_A thus the final thickness was bigger than those of X80_A, X80_B and X70_A steels. Charpy specimens were typical full-sized V-notch with the conventional notch orientation as shown in Fig. 3.2a.

6.1. Microstructures

Fig. 6.1 shows optical micrographs of the X70_B steel etched with a 2% nital solution. The microstructure appears to consist of allotriomorphic and bainitic ferrite, with some indication of banding in Fig. 6.1d. Because of the lower carbon contents than X70_A steel, a larger amount of allotriomorphic ferrite was confirmed using scanning electron microscopy with diffraction facilities as shown in Fig. 6.2.

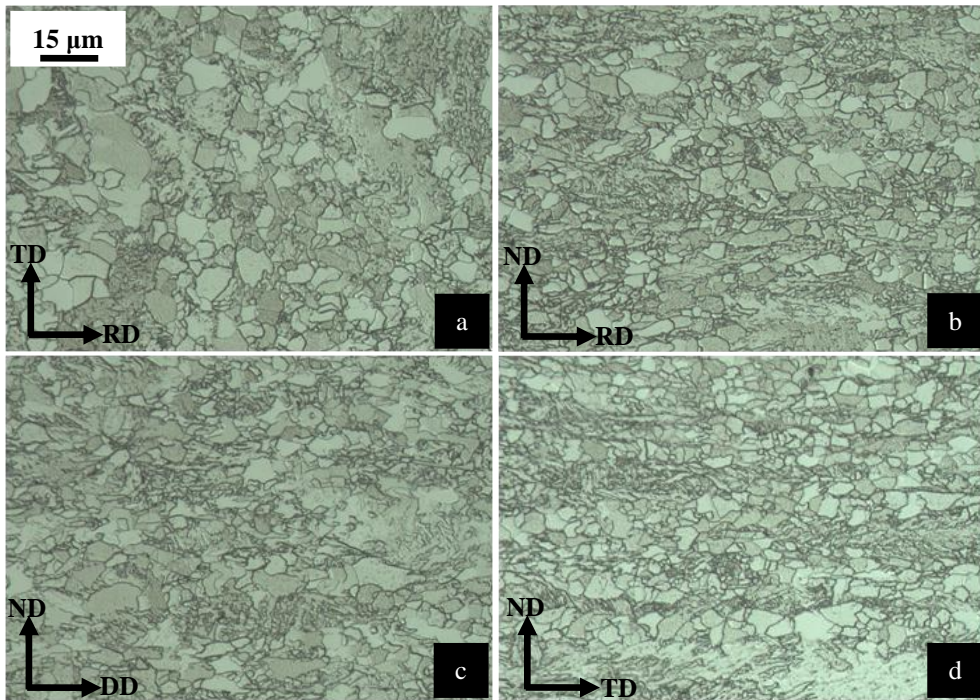


Figure 6.1. Optical micrographs in X70_B steel: Surface normal to (a) ND, (b) TD, (c) DD and RD. 2% nital etched.

Except for allotriomorphic ferrite, fine and coarse grained regions are also found but since the fine grained region is very small, banding is not apparent. SEM micrographs of high magnification revealed a small portion of pearlite and confirm the banded microstructure between allotriomorphic and bainitic ferrite as shown in Fig. 6.3. Austenite was also detected in EBSD experiment but the fraction was approximately 0.01. The volume fraction of allotriomorphic ferrite was calculated as 0.40 ± 0.06 using EBSD. The macroscopic hardness was 192 ± 5 HV.

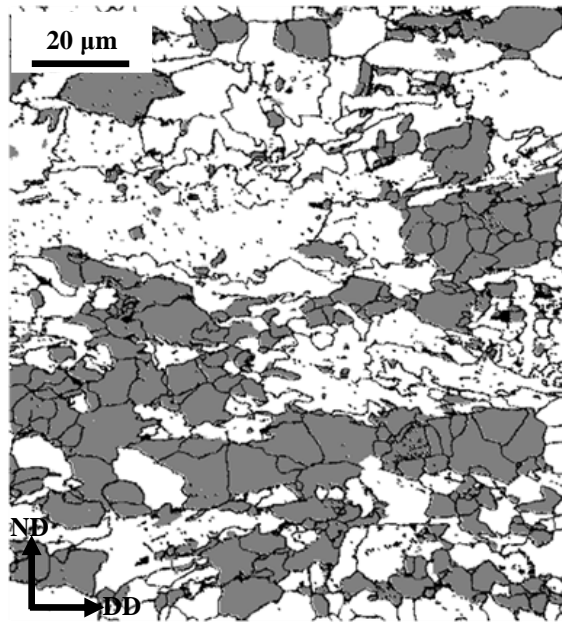


Figure 6.2. Map of grain orientation spread in X70_B with the value less than 1.5° in a grain with boundaries identified using the criterion that the orientation difference is greater than 15° .

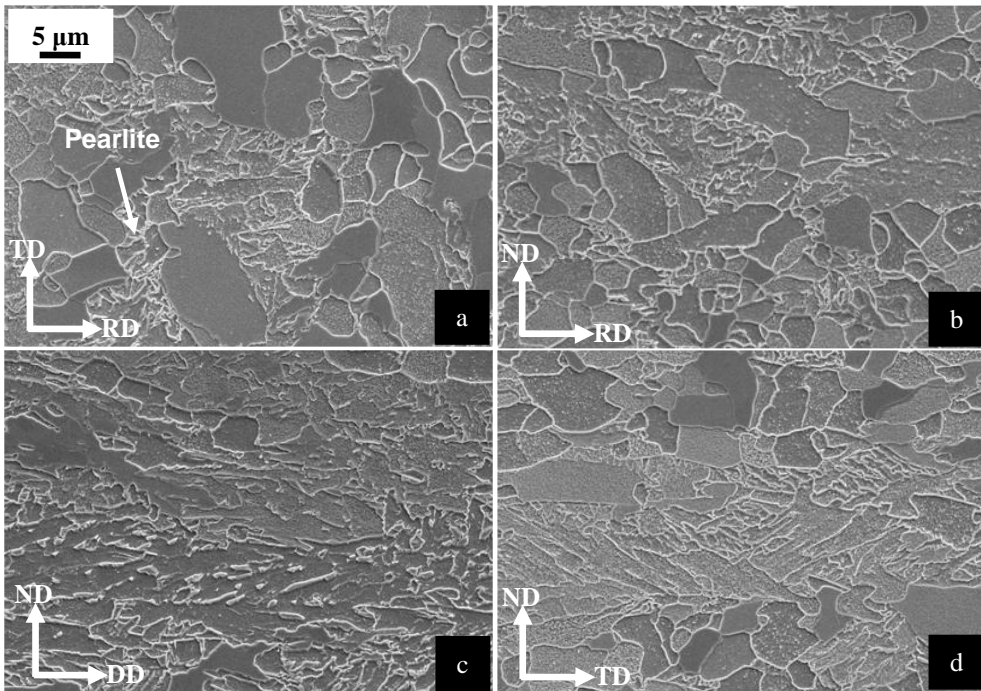


Figure 6.3. SEM micrographs in X70_B steel: Surface normal to (a) ND, (b) TD, (c) DD and RD. 2% nital etched.

Fig. 6.4 shows the optical micrographs of the X70_C steel. The microstructure is similar to X70_B steel. The grain orientation spread (GOS) map clearly shows the banding between allotriomorphic and bainitic ferrite (Fig. 6.5). SEM micrographs indicate presence of pearlite as shown in Fig. 6.6a. Austenite was also detected and the fraction was approximately 0.01. The volume fraction of allotriomorphic ferrite was 0.35 ± 0.09 . The macroscopic hardness value was 179 ± 4 HV.

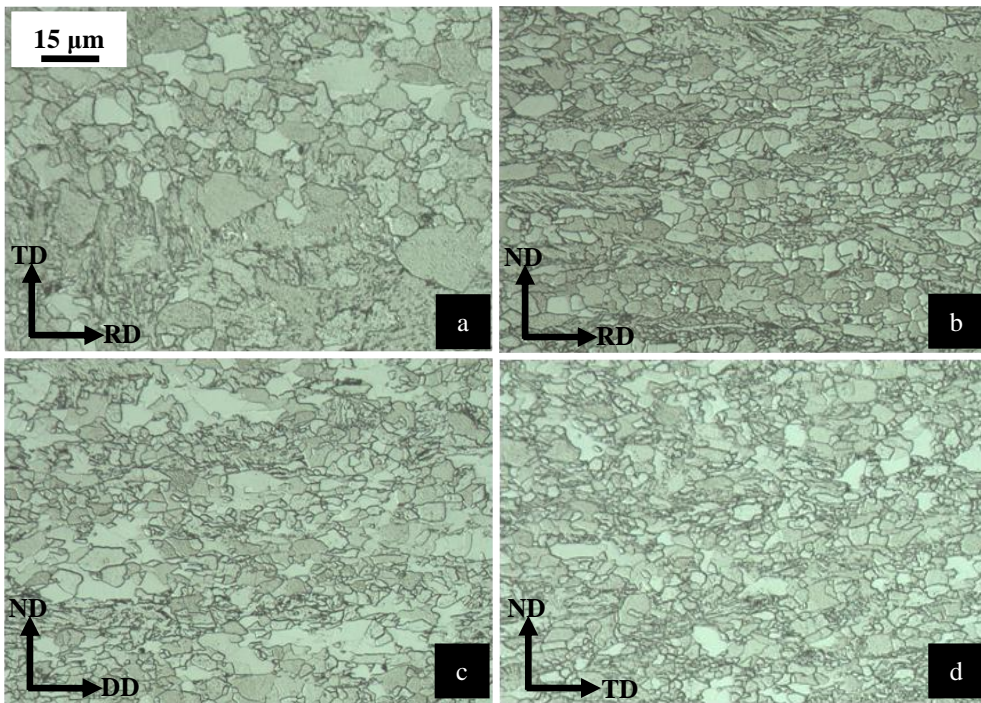


Figure 6.4. Optical micrographs in X70_C steel: Surface normal to (a) ND, (b) TD, (c) DD and RD. 2% nital etched.

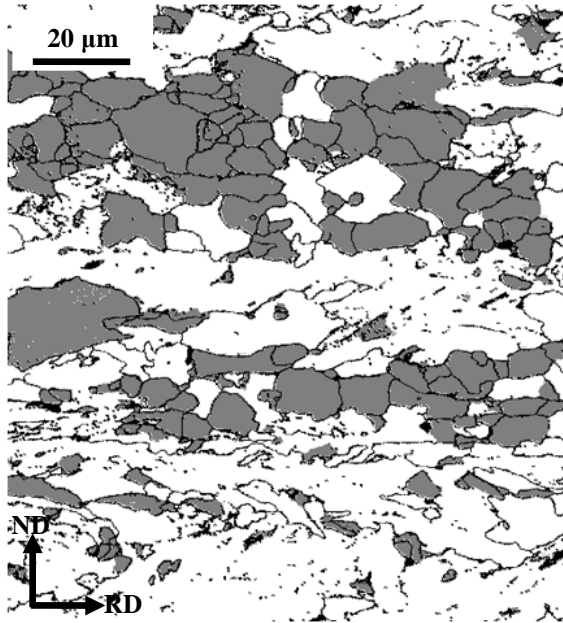


Figure 6.5. Map of grain orientation spread in X70_C with the value less than 1.5° in a grain with boundaries identified using the criterion that the orientation difference is greater than 15° .

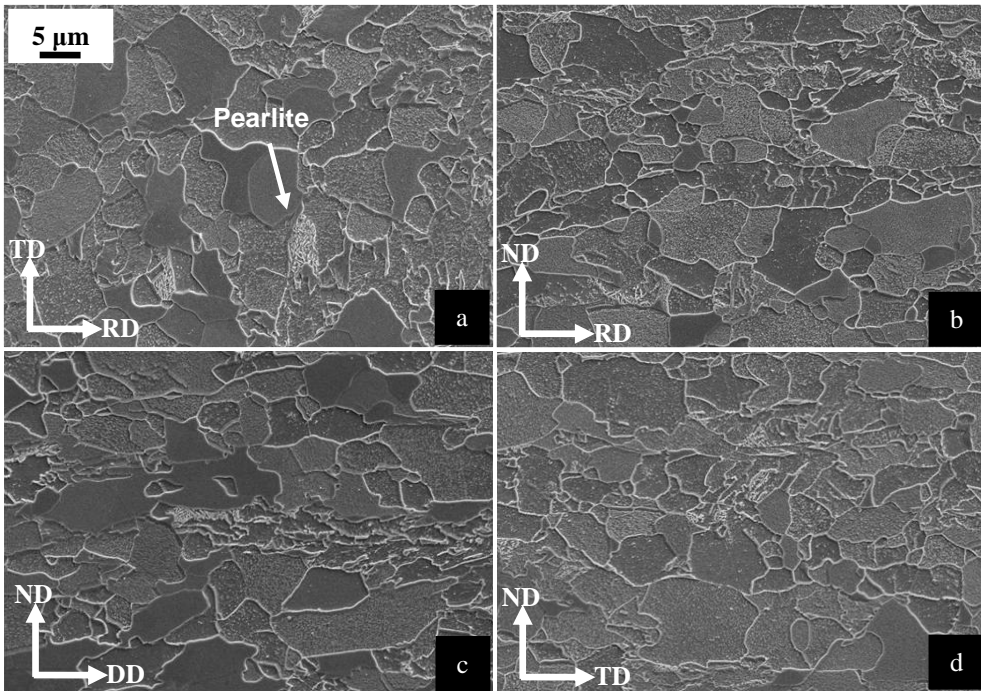


Figure 6.6. SEM micrographs in X70_C steel: Surface normal to (a) ND, (b) TD, (c) DD and RD. 2% nital etched.

Figs 6.7 and 6.9 represent X70_D steel. The microstructure is similar to X70_B and X70_C steels. The grain orientation spread map also shows the banding between allotriomorphic and bainitic ferrite (Fig. 6.8). Austenite was also detected and the fraction was less than 0.01. The volume fraction of allotriomorphic ferrite was 0.34 ± 0.02 . The macroscopic hardness was 189 ± 5 HV.

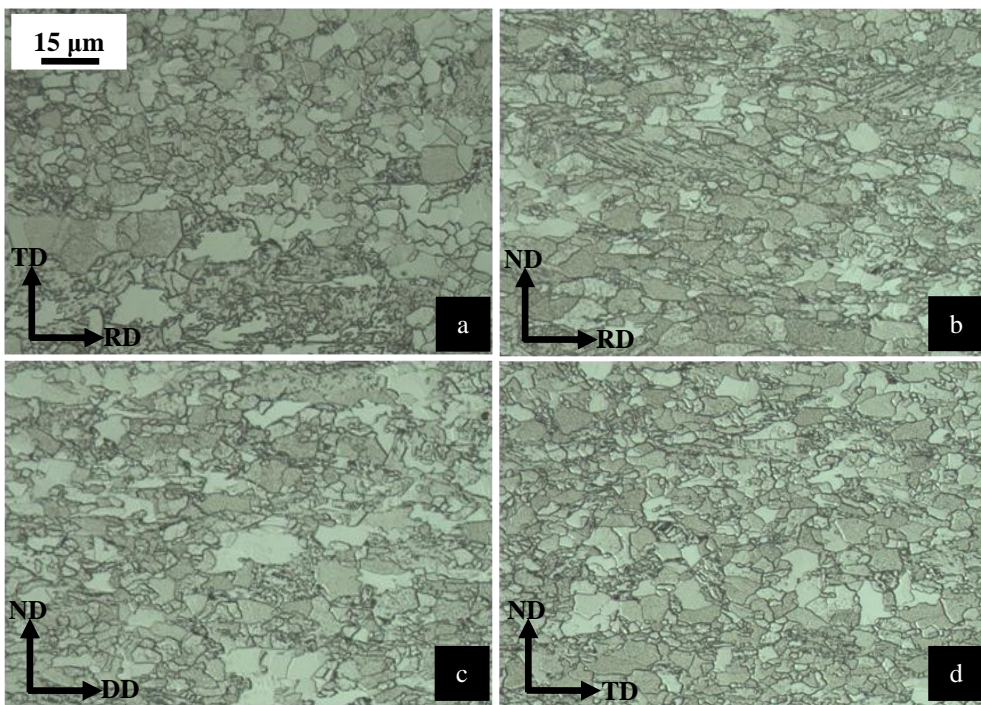


Figure 6.7. Optical micrographs in X70_D steel: Surface normal to (a) ND, (b) TD, (c) DD and RD. 2% nital etched.

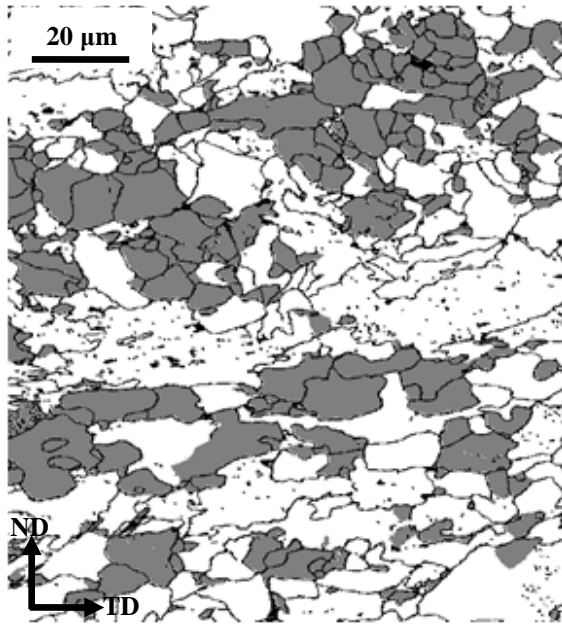


Figure 6.8. Map of grain orientation spread in X70_D with the value less than 1.5° in a grain with boundaries identified using the criterion that the orientation difference is greater than 15° .

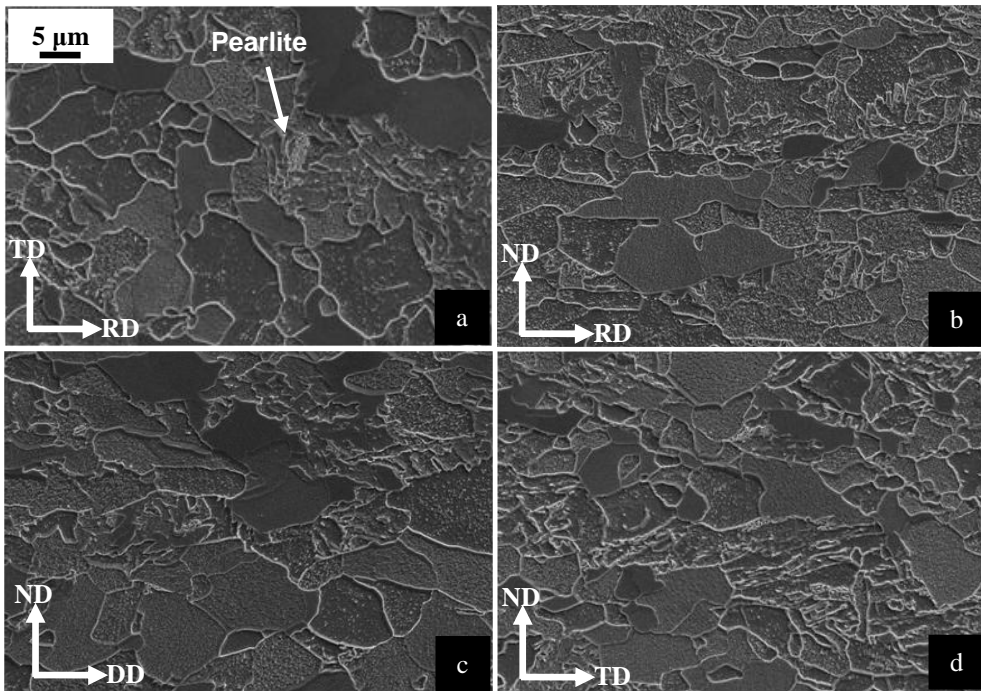


Figure 6.9. SEM micrographs in X70_D steel: Surface normal to (a) ND, (b) TD, (c) DD and RD. 2% nital etched.

In summary, the microstructures, hardness and the grain sizes of X70_B, X70_C and X70_D are similar and the differences are within the scatter as listed in Tables 6.1, 6.2 and 6.3.

Table 6.1. Volume fractions of phases.

Steels	Volume fractions of phases		
	Allotriomorphic	Bainitic	Others
	ferrite	ferrite	
X70_B	0.40 ± 0.06	0.60 ± 0.06	pearlite, retained austenite
X70_C	0.35 ± 0.09	0.65 ± 0.09	pearlite, retained austenite
X70_D	0.34 ± 0.02	0.66 ± 0.02	pearlite, retained austenite

Table 6.2. Macroscopic hardness data (HV)

X70_B	X70_C	X70_D
192 ± 5	179 ± 4	189 ± 5

Table 6.3. Grain size data.

Steels	Metallographic grain size* (µm)	Crystallographic grain size* (µm)
X70_B	1.99 ± 2.04	9.66 ± 3.51
X70_C	2.11 ± 2.34	10.87 ± 3.54
X70_D	1.85 ± 1.98	9.50 ± 2.47

* Metallographic and crystallographic grain size with grain boundary misorientation $\geq 2^\circ$ and 15° respectively.

6.2. Charpy Properties

Fig. 6.10 shows the changes of Charpy energy with temperature and test orientation for the conventional notch orientation (Fig. 3.2a) in X70_B steel. There is isotropy when failure is in the ductile regime, or when the sample fails in a completely brittle manner during testing at $-100\text{ }^{\circ}\text{C}$. In contrast, the orientation dependence of Charpy energy is marked in the ductile–brittle transition temperature range especially for $-60\text{ }^{\circ}\text{C}$, with the D–D orientation being worst as observed for X80_A, X80_B and X70_A steel. X70_C and X70_D steels show similar tendencies as shown in Figs 6.11 and 6.12.

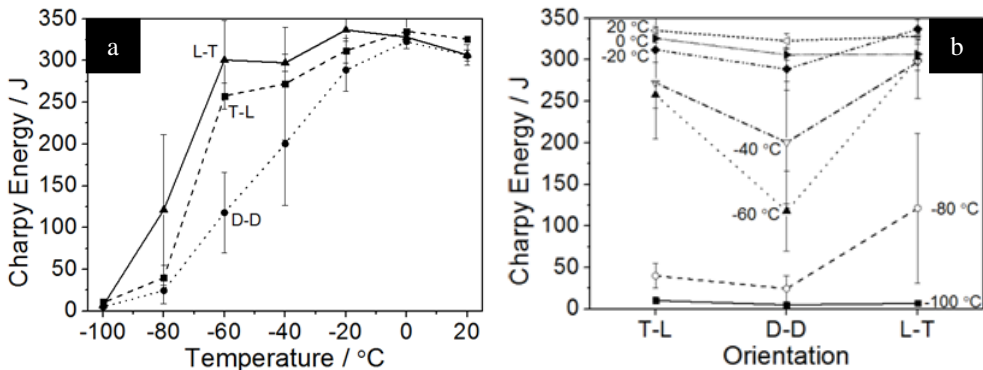


Figure 6.10. Charpy properties of X70_B: (a) The impact transition curve and (b) the anisotropy curve, the specimen has conventional notch orientation.

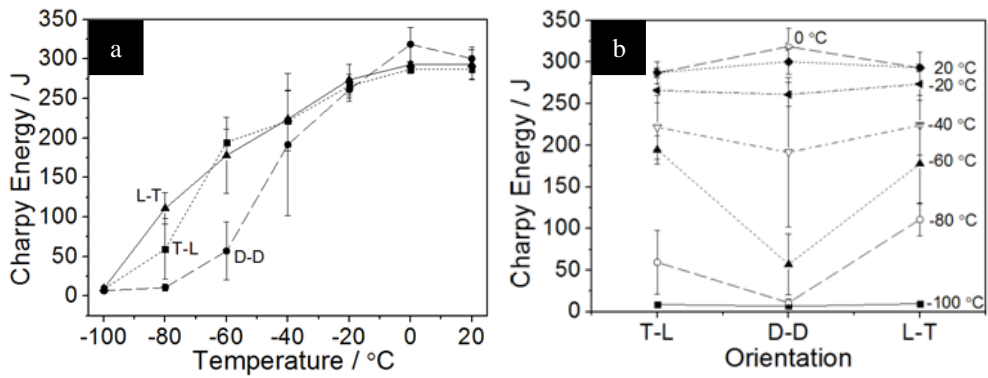


Figure 6.11. Charpy properties of X70_C: (a) The impact transition curve and (b) the anisotropy curve, the specimen has conventional notch orientation.

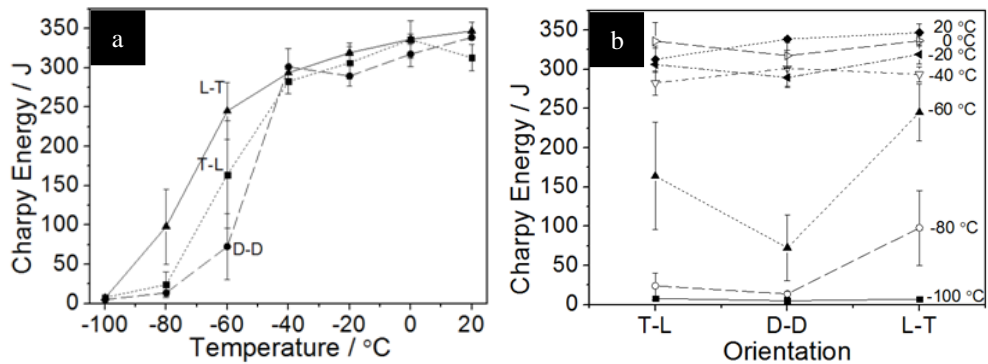


Figure 6.12. Charpy properties of X70_D: (a) The impact transition curve and (b) the anisotropy curve, the specimen has conventional notch orientation.

6.3. Grain Boundary Density

Fig. 6.13 shows the density of grain boundaries ρ_{GB} for each fracture surface with low angle ($2^\circ\sim 15^\circ$), high angle ($15^\circ\sim 180^\circ$) and all boundaries ($2^\circ\sim 180^\circ$) in the X70_B, X70_C and X70_D steels. Differences in the densities of high angle grain boundaries on each surface are small and cannot explain the Charpy results.

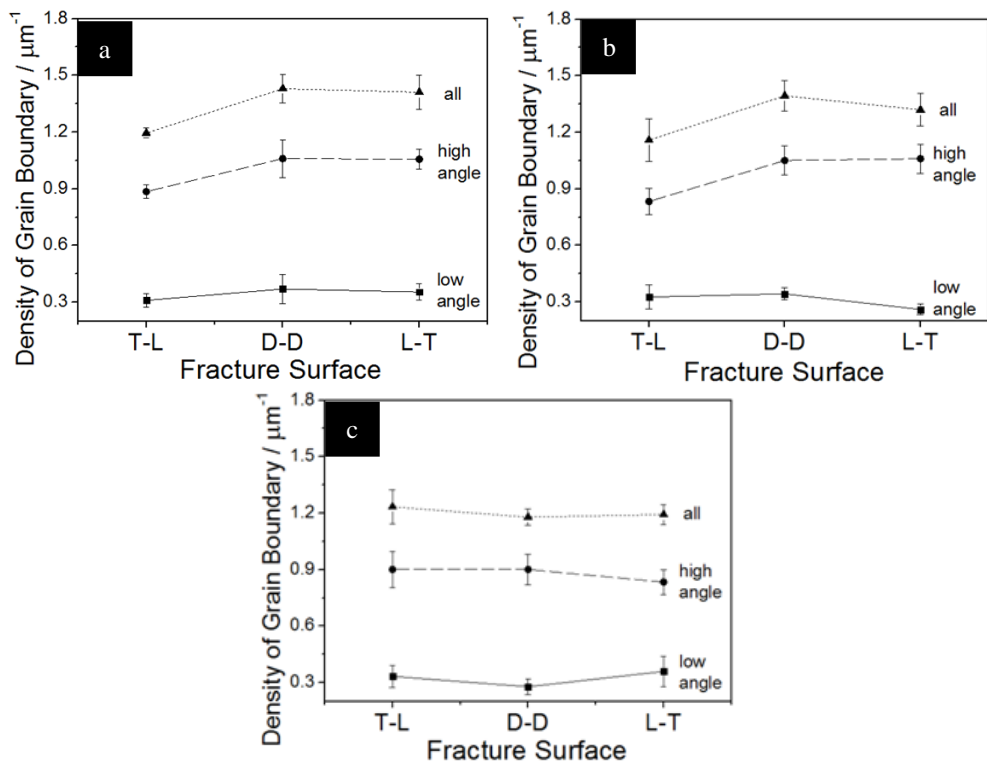


Figure 6.13. Density of grain boundaries: (a) X70_B, (b) X70_C and (c) X70_D, with low angle ($2^\circ\sim 15^\circ$), high angle ($15^\circ\sim 180^\circ$) and all boundaries ($2^\circ\sim 180^\circ$).

6.4. Fracture Surfaces

Fig. 6.14 shows the fracture surfaces of Charpy specimens from X70_B steel. For the -60 °C tests, the D–D orientation has no delamination, unlike the other orientation, consistent with the Charpy results (Fig. 6.10b). Same observation applies for -80 °C but the T–L orientation has weaker delamination than the L–T orientation, thus the Charpy energy of T–L orientation was less than that of L–T orientation. However, the D–D orientation still has no delamination and shows the lowest impact energy (Fig. 6.10a). Interestingly, all the specimens have delamination but anisotropy exists at -40 °C (Fig. 6.10b). This comes from the crystallographic texture as pointed out in chapter 5.

Fig. 6.15 shows the fracture surfaces of Charpy specimens from X70_C steel. For tests done at -20 °C and -40 °C, all the specimens have delamination and show isotropic Charpy properties. The -60 °C samples, the D–D orientation have no delamination and yet show remarkable anisotropy in absorbed energy. The T–L orientation has weak delamination and D–D orientation has no delamination, thus L–T orientation shows the highest impact toughness (Fig. 6.11) due to the toughening effect of delamination in -80 °C.

Fig. 6.16 shows the fracture surfaces of Charpy specimens in X70_D steel. All the specimens are without delamination at -20 °C and with minimal delamination for -40 °C, thus showing relatively isotropic behaviour (Fig. 6.12). Also, D–D orientation has no delamination and shows strong anisotropy in absorbed energy at -60 °C. In -80 °C, L–T only has delamination and shows the highest

impact toughness. These clearly indicate a relationship between the observed Charpy–energy anisotropy and the occurrence of delamination at fracture surface.

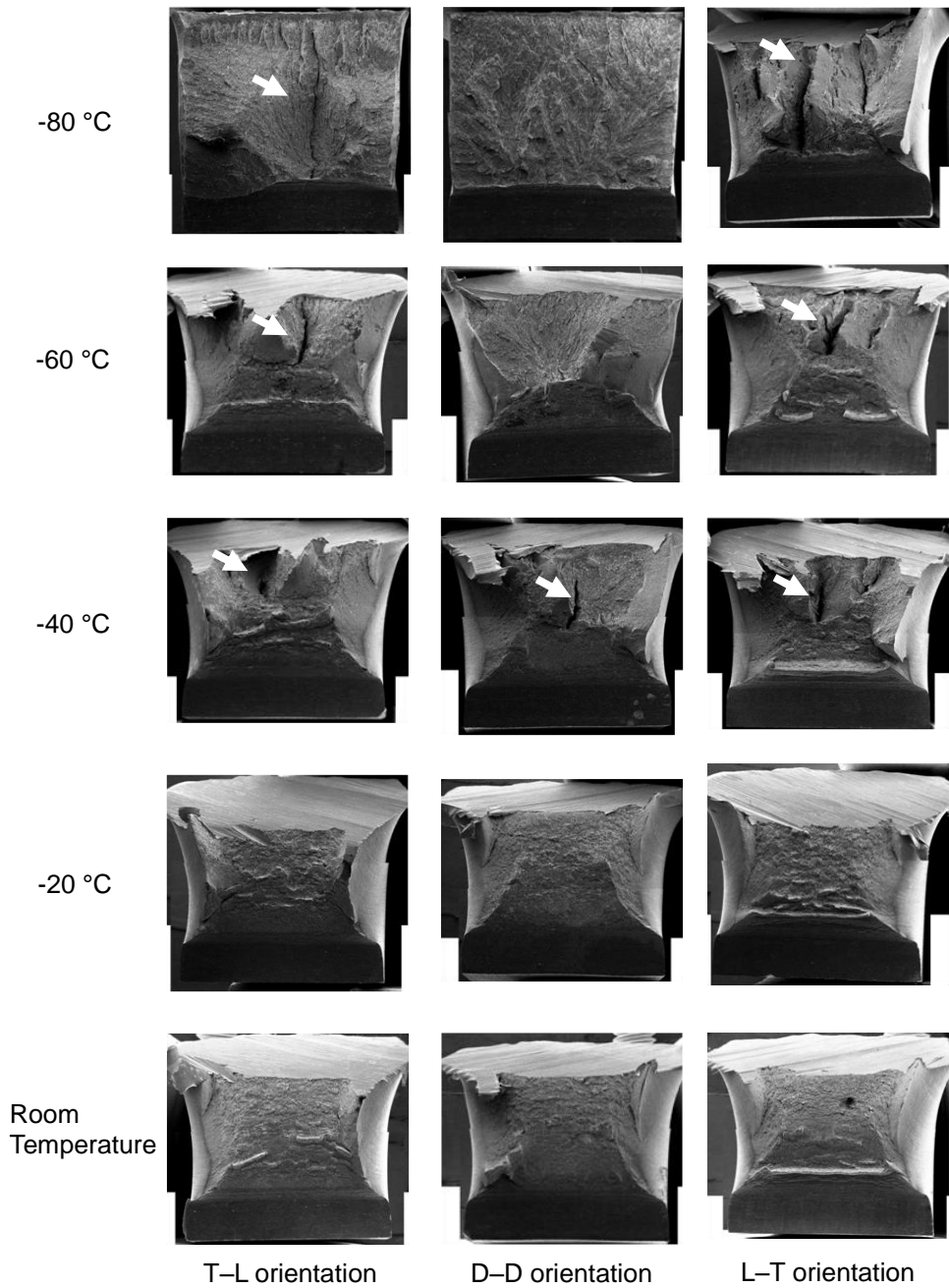


Figure 6.14. Fracture surfaces of Charpy specimens from room temperature to -80 °C of T-L, D-D and L-T orientations with delaminations indicated by white arrows in X70_B steel.

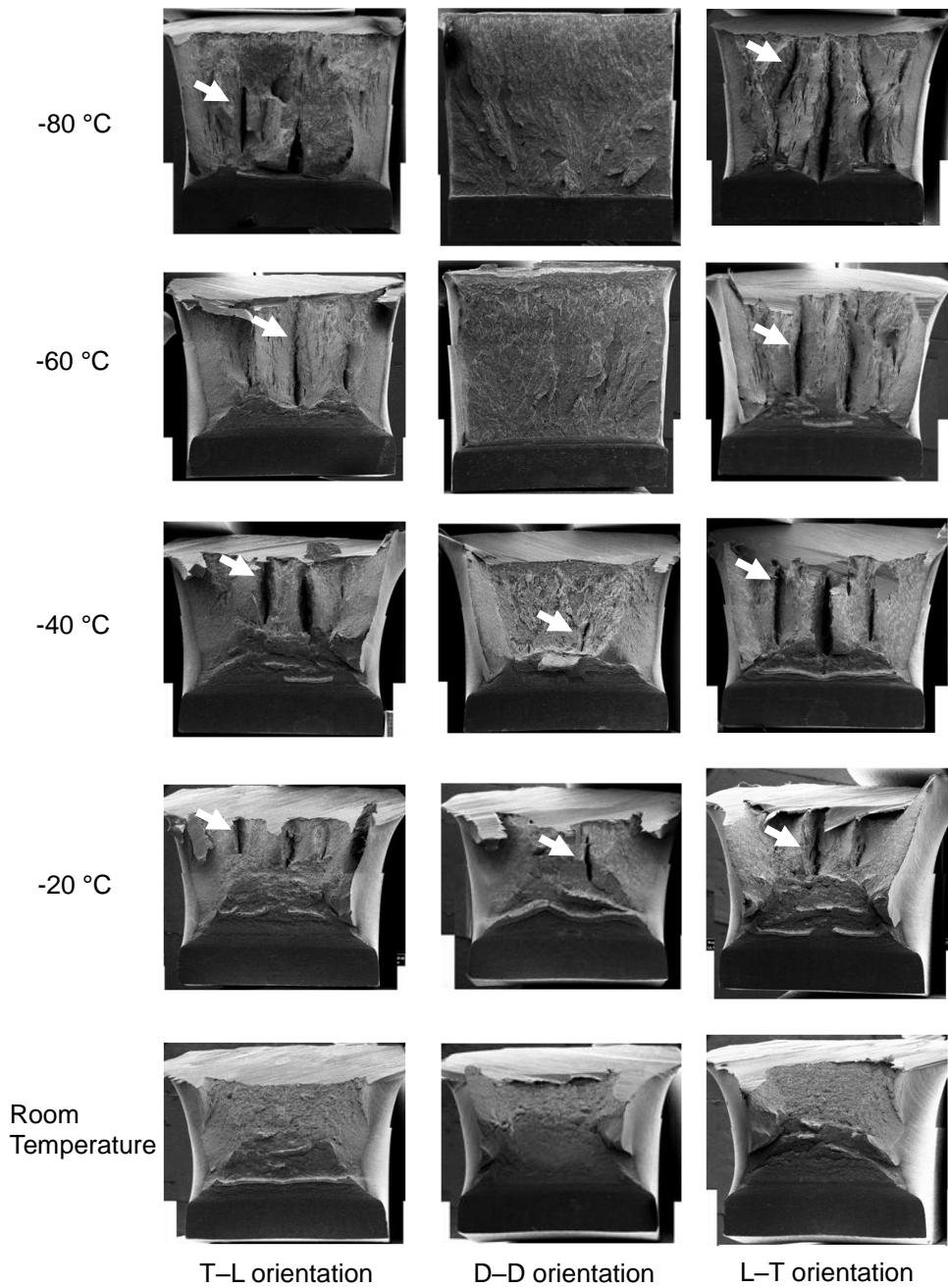


Figure 6.15. Fracture surfaces of Charpy specimens from room temperature to -80 °C of T-L, D-D and L-T orientations with delaminations indicated by white arrows in X70_C steel.

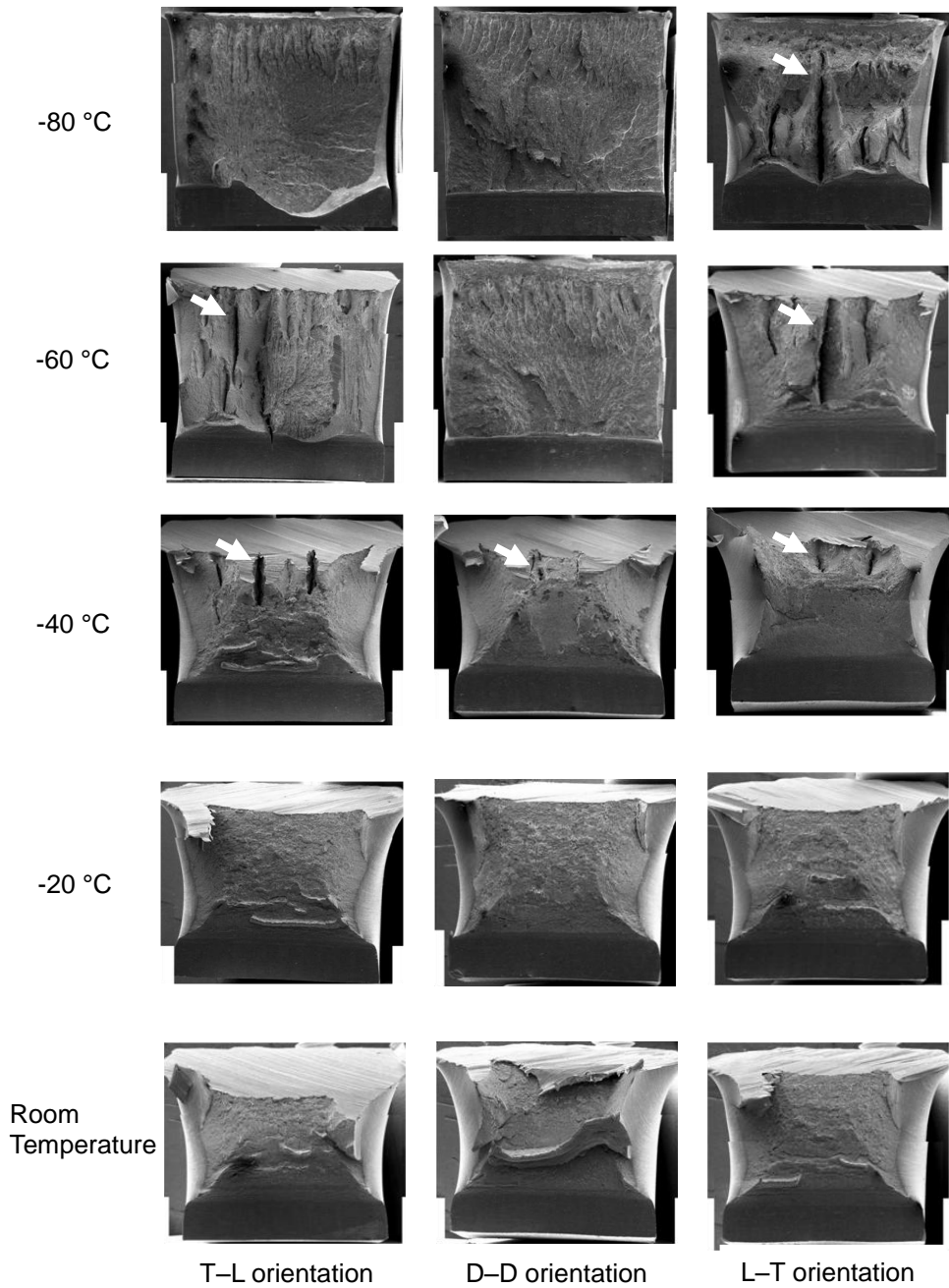


Figure 6.16. Fracture surfaces of Charpy specimens from room temperature to -80 °C of T-L, D-D and L-T orientations with delaminations indicated by white arrows in X70_D steel.

6.5. Crystallographic Texture

Figs 6.17 ~ 6.20 show the textures of X70_B, X70_C and X70_D steels. The macroscopic textures for all the steels are similar. As expected, the steels have a propensity for {100} planes to be parallel to the specific fracture plane as shown in Fig. 6.21, and this should cause the anisotropy of Charpy toughness in low temperatures.

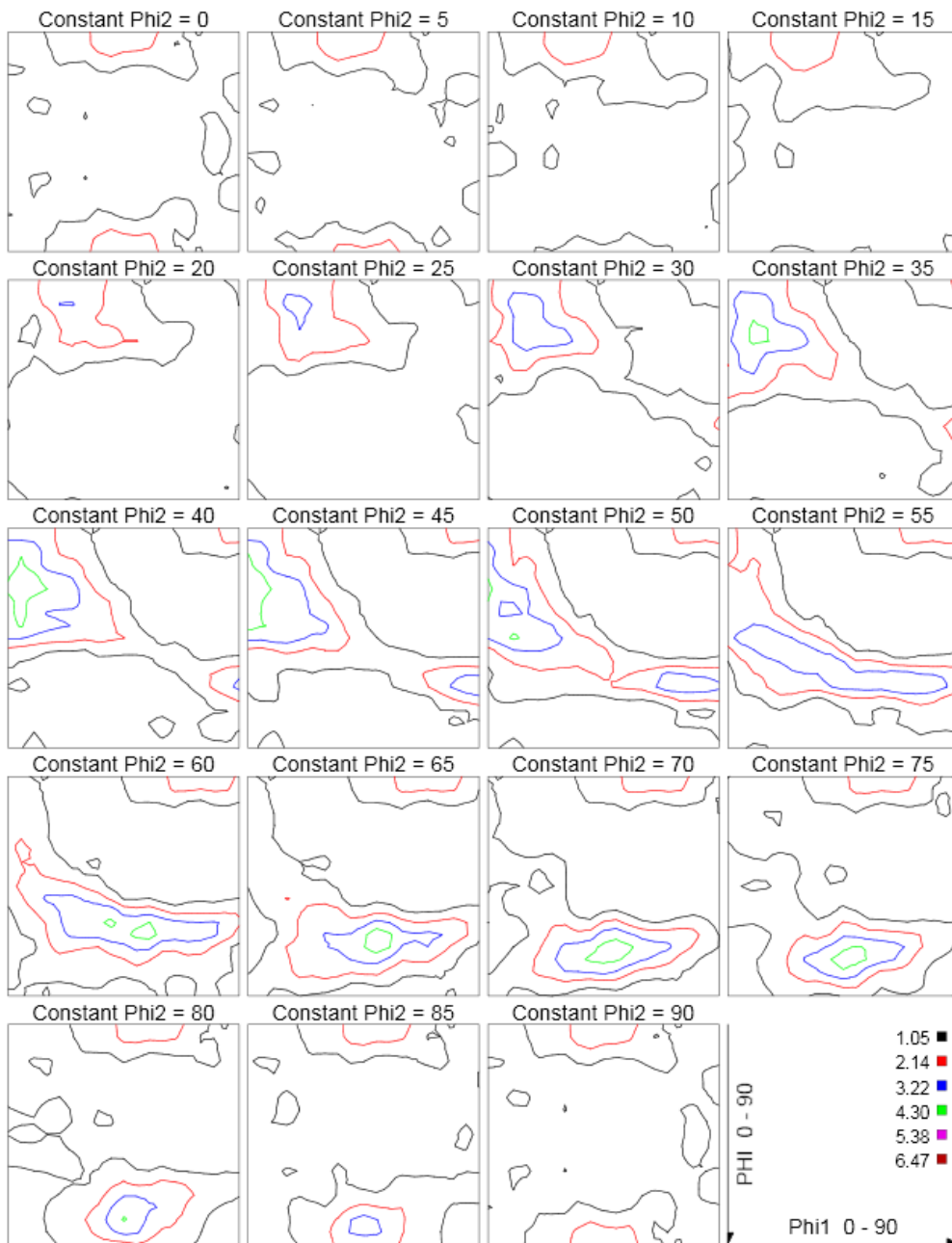


Figure 6.17. ODFs (ϕ_2 sections 0° to 45° , 5° intervals) of X70_B steel.

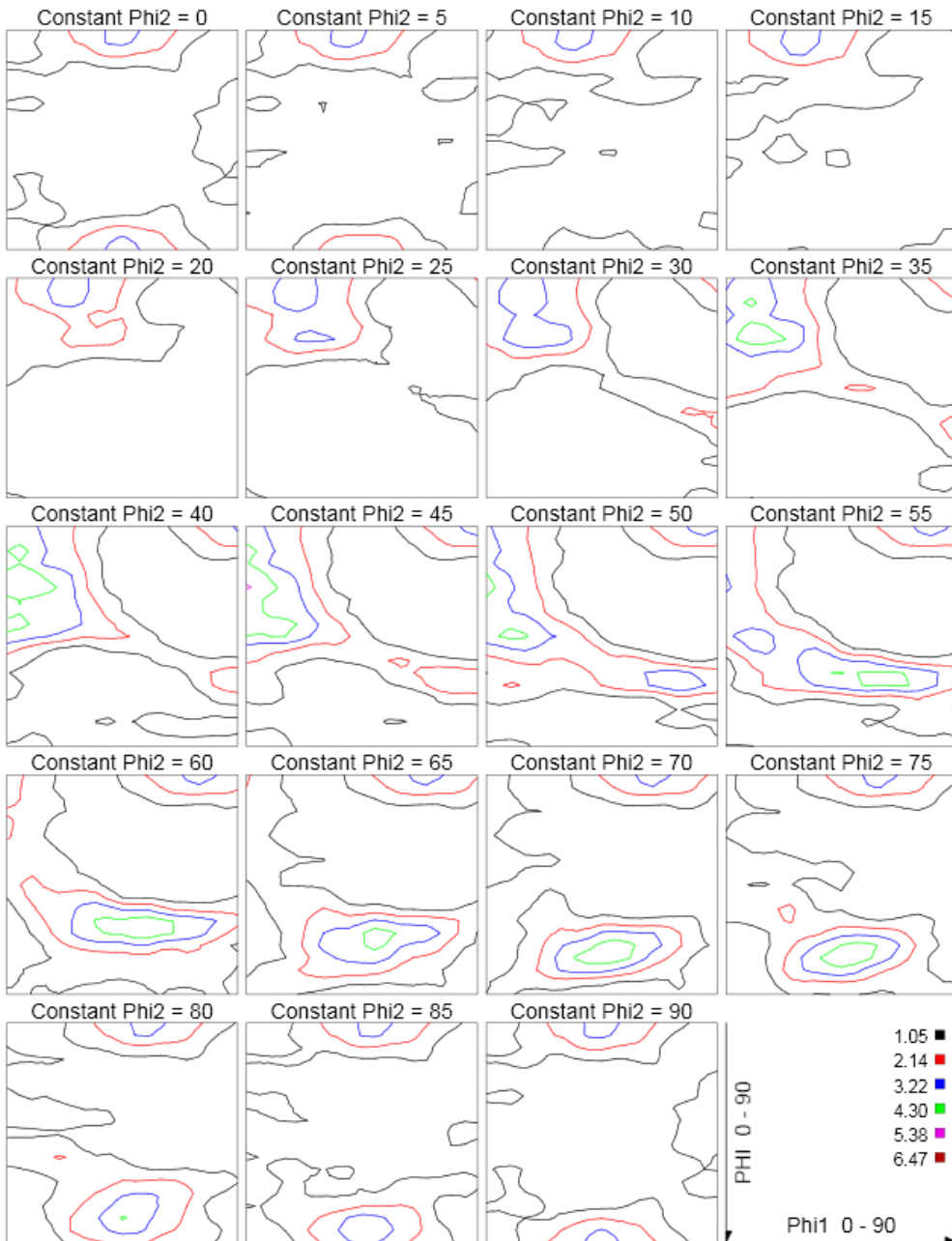


Figure 6.18. ODFs (ϕ_2 sections 0° to 45°, 5° intervals) of X70_C steel.

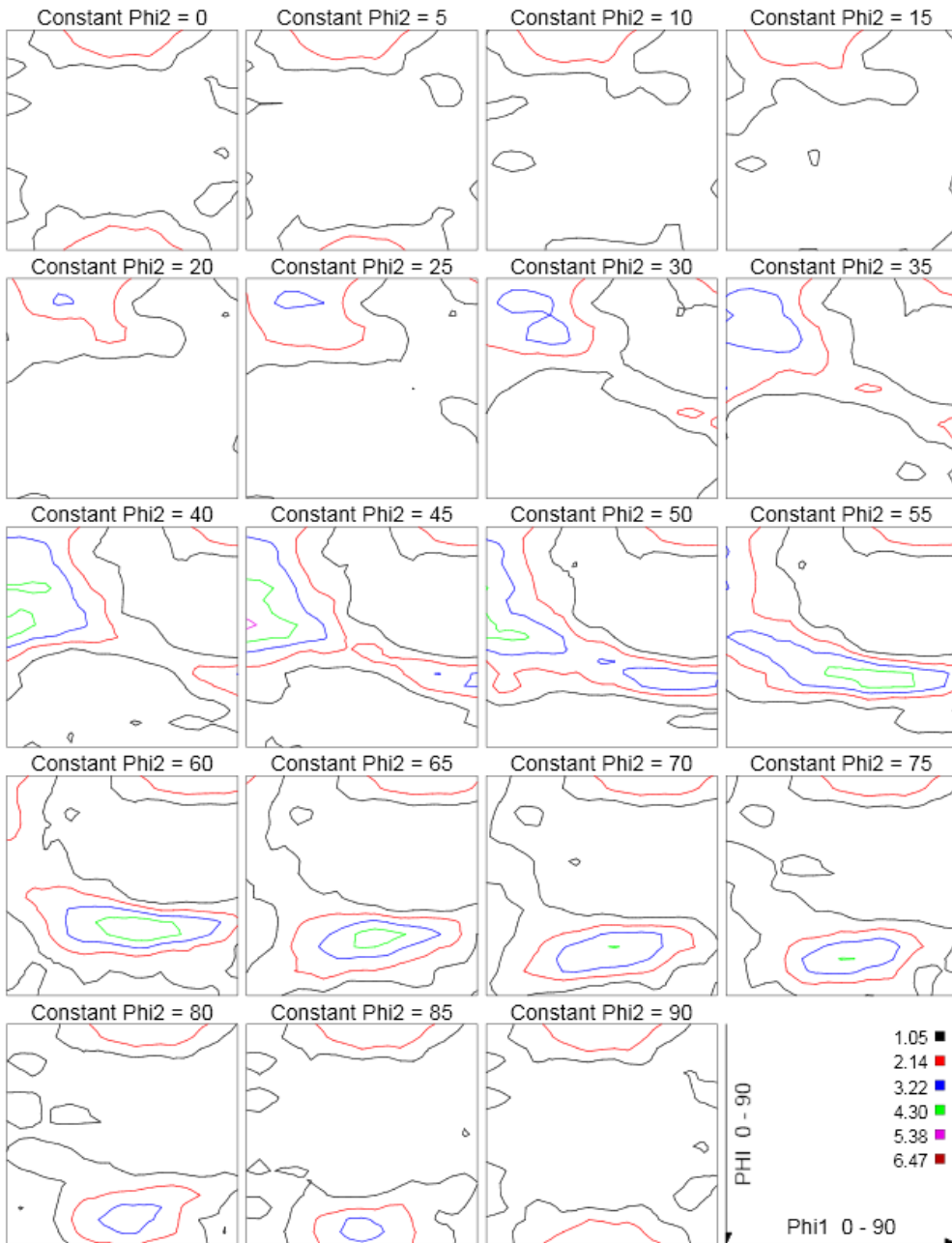


Figure 6.19. ODFs (ϕ_2 sections 0° to 45°, 5° intervals) of X70_D steel.

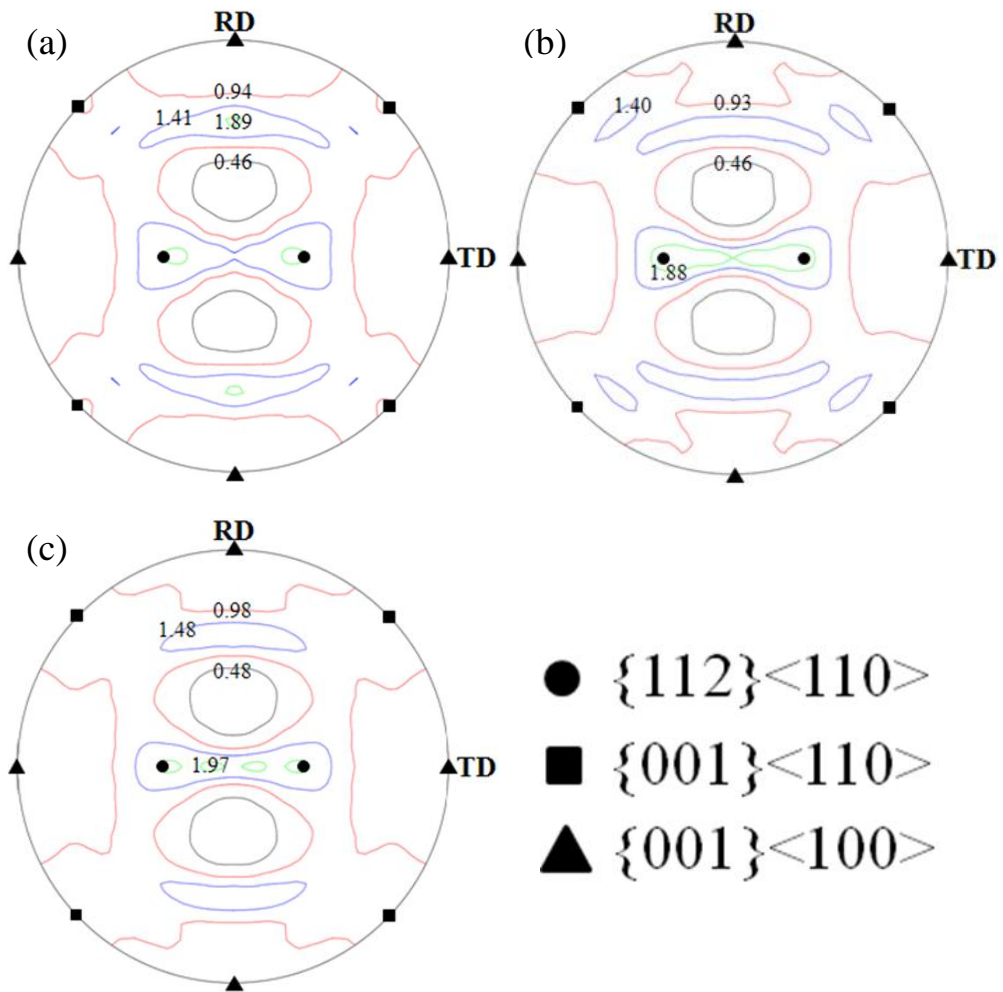


Figure 6.20. $\{200\}$ pole figure with intensity and some important texture components ($\{112\}\langle 110\rangle$, $\{001\}\langle 110\rangle$ and $\{001\}\langle 100\rangle$): (a) X70_B, (b) X70_C and (c) X70_D.

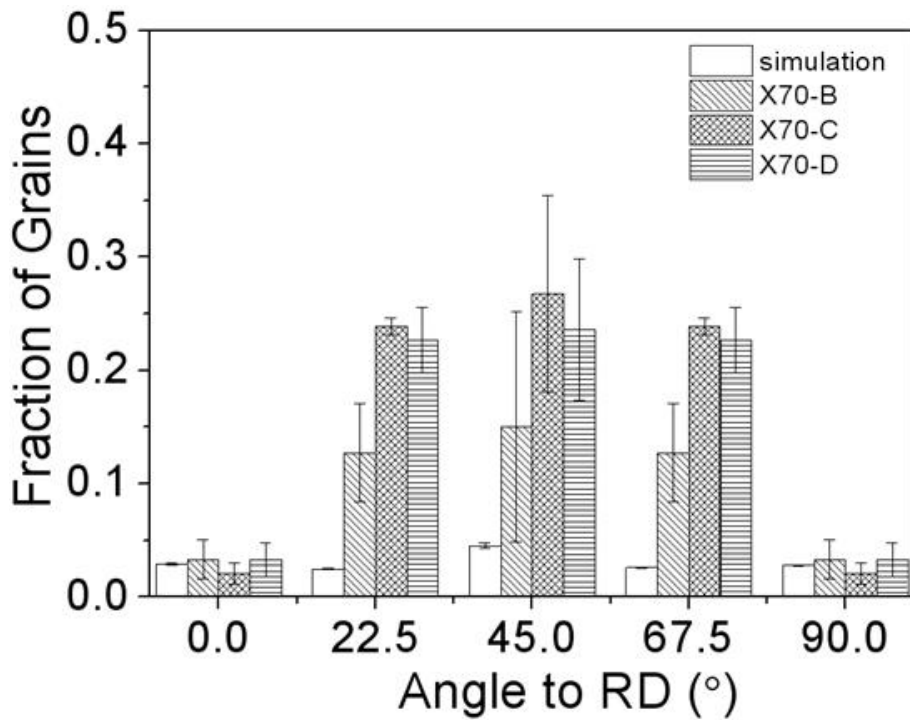


Figure 6.21. The fraction of grain as a function of angle between the {100} plane normal and the rolling direction in the investigated steels and simulation, the tolerance angle was 11.25° to capture all the proper grains.

6.6. Summary

Three kinds of API-X70 linepipe steels have been investigated. The steels have different finish rolling temperature (FRT) and start cooling temperature (SCT) in order to investigate the effect of processing variables on the orientation dependence of Charpy toughness. However, the steels have similar microstructure, texture and Charpy properties. This implies that FRT and SCT do not have a critical influence on the anisotropy. It is believed that the important factors for anisotropy of Charpy toughness in the DBTT region are occurrence of delamination and uneven distribution of {100} cleavage planes.

VII. Concluding Remarks

7.1. Anisotropy indices for the steels

All the investigated steels exhibit similar Charpy anisotropy at the DBTT regimes, irrespective of their chemical composition and processing variables. Fig. 7.1 shows the mean Charpy values in conventional, additional notch orientations and after the quenching heat treatment of X80_A steel processed at specified temperatures. The outer quadrant circumferential boundary represents the isotropic case with the Charpy energy proportional to the radial distance from the origin, and test orientation the angle.

All the graphs show that the anisotropy is worst in the transition temperature range between -20 °C and -60 °C. Direct comparisons at identical temperatures should be more helpful to reveal clearly the phenomenon for all the cases as shown in Fig. 7.2. There is isotropic behaviour in all the cases for 20 °C (Fig. 7.2a), but anisotropy sets in at -20 °C (Fig. 7.2b), is worst for -40 °C (Fig. 7.2c), and persists at -60 °C (Fig. 7.2d).

Another comparison involves on “anisotropy index” defined as:

$$\text{Index}_{\text{anisotropy}} = (\text{MAX}_{\text{temp.}} - \text{MIN}_{\text{temp.}}) / \text{MAX}_{\text{overall}} \quad (7-1)$$

where $\text{MAX}_{\text{temp.}}$ and $\text{MIN}_{\text{temp.}}$ are the maximum and minimum Charpy values at the target temperature respectively, and $\text{MAX}_{\text{overall}}$ is the maximum value over all the temperatures studied.

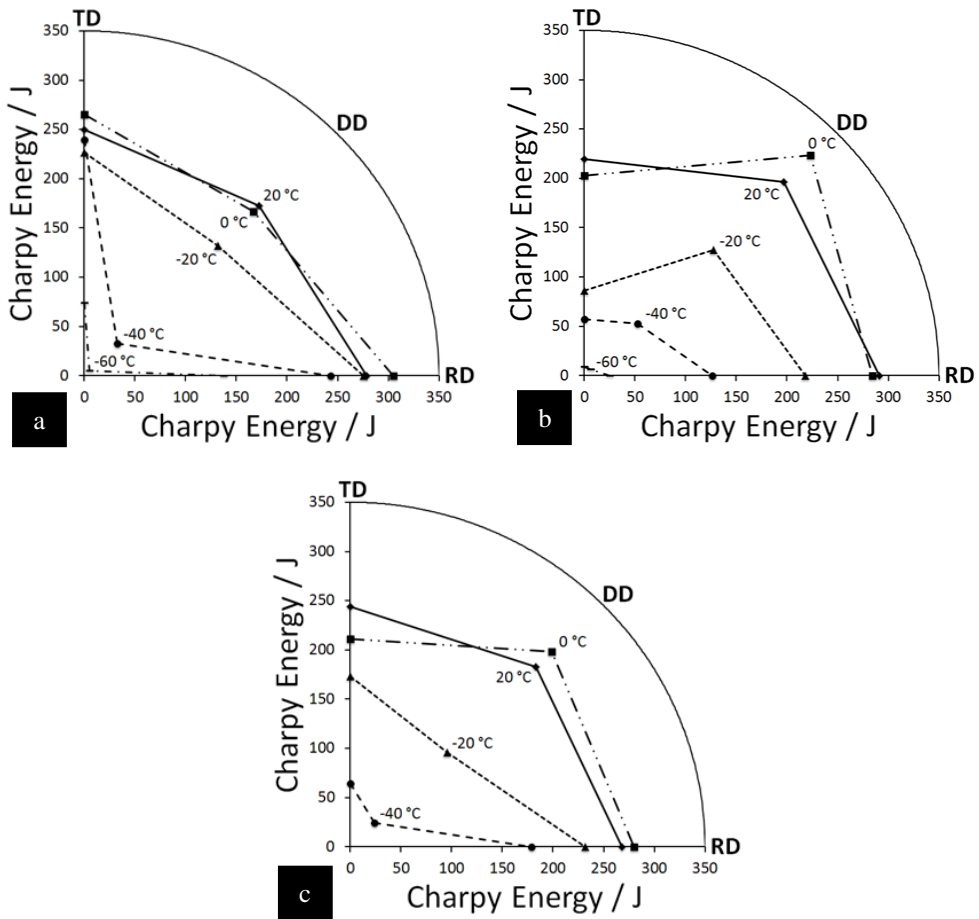


Figure 7.1. Charpy properties of X80_A: (a) the conventional notch orientation (b) the additional notch orientation and (c) the case after the quenching heat treatment.

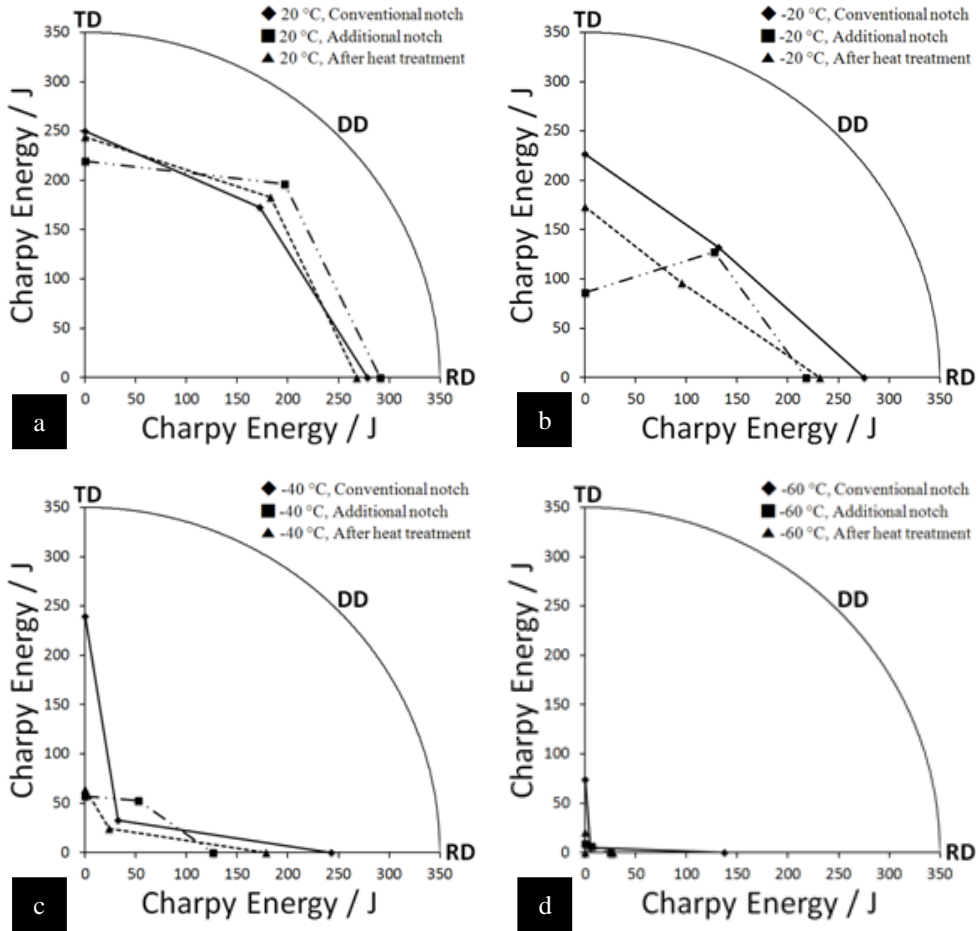


Figure 7.2. Comparisons of Charpy energies of the conventional, additional notch orientations and the case after the quenching heat treatment in X80_A: (a) 20 °C, (b) -20 °C, (c) -40 °C and (d) -60 °C.

Fig. 7.3 shows the anisotropy indices as a function of temperature for the conventional, additional notch orientations and the case after the quenching heat treatment in X80_A steel. This clearly shows that the anisotropy is worst in the transition temperature range.

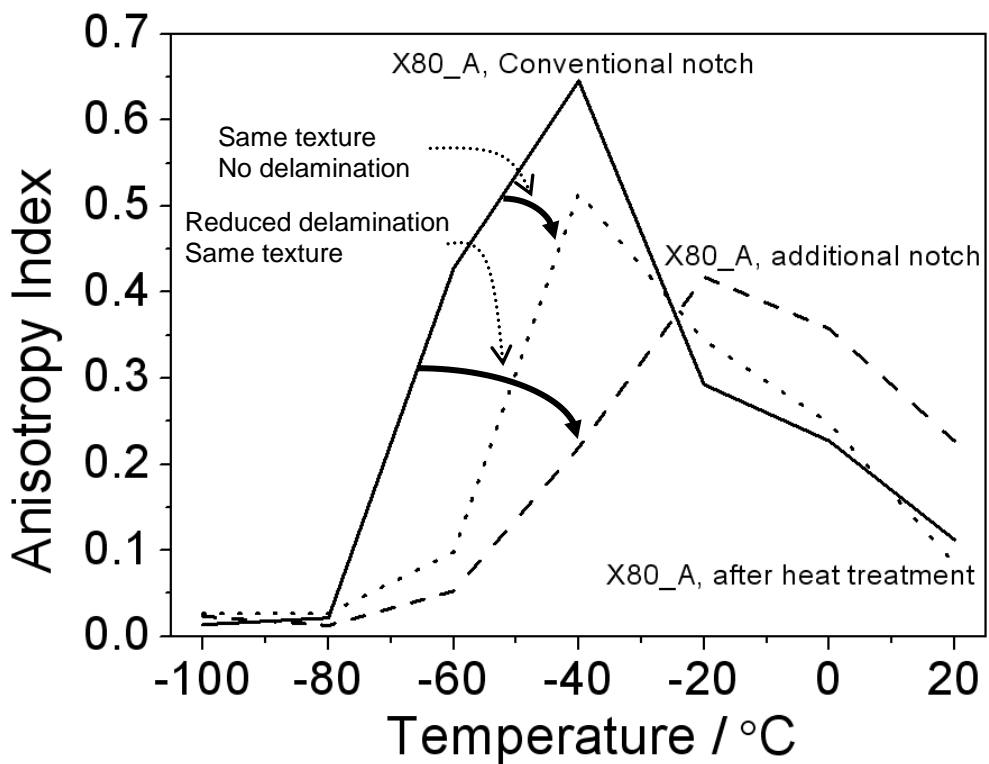


Figure 7.3. Anisotropy indices for cases of the conventional, additional notch orientations and after the quenching heat treatment for X80_A.

The degree of anisotropy is reduced after the heat treatment and proves the role of crystallographic texture. Although the temperature with the maximum anisotropy index is different between the conventional case and additional case due to the absence of effective delamination toughening, the anisotropy index is much less in the additional case than in the conventional case. This establishes the role of delamination. Therefore, there is a combination of texture and delamination which makes the anisotropy greatest in the conventional case.

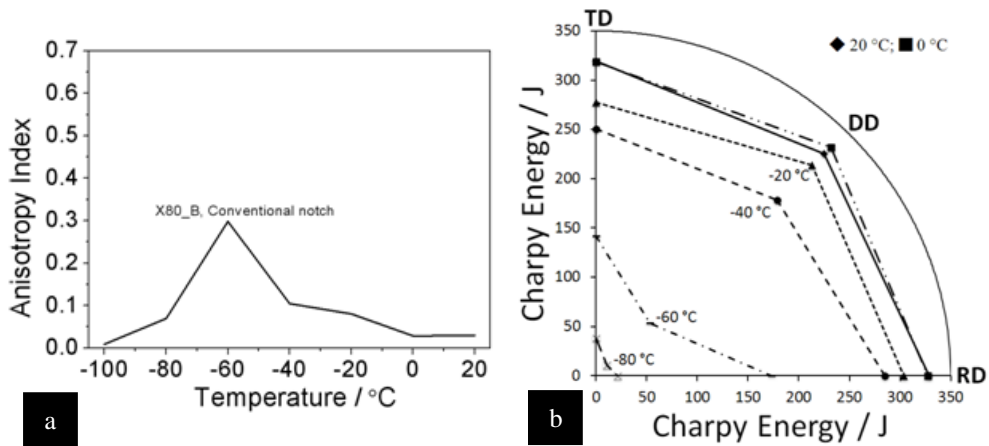


Figure 7.4. (a) Anisotropy index and (b) Charpy properties of the conventional notch orientation in X80_B.

Fig. 7.4 shows the anisotropy index and Charpy energies in X80_B steel. The degree of anisotropy is maximised at -60 °C and this comes from that the delamination is not well developed in the D–D orientation at -60 °C as discussed in the previous section. Fig. 7.5 shows the anisotropy index and Charpy properties in X70_A steel. Anisotropy is not relieved because the delamination was not well–developed after changing the notch orientation.

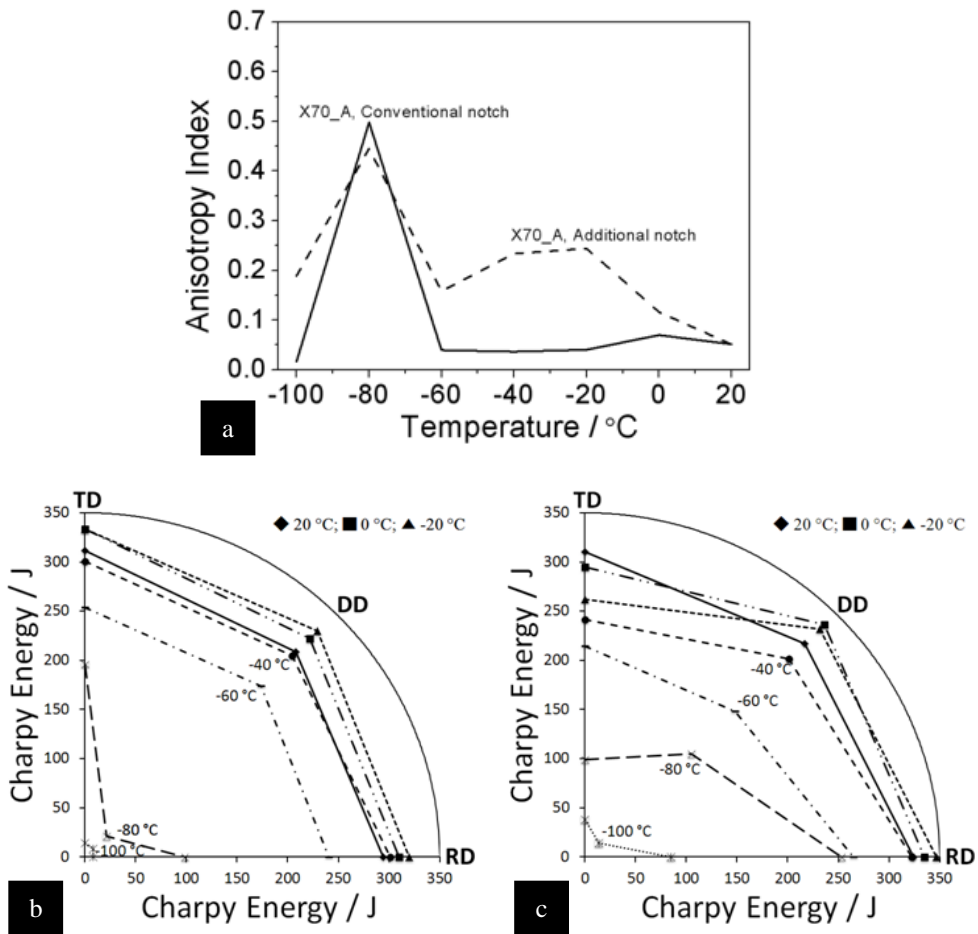


Figure 7.5. (a) Anisotropy index, (b) Charpy properties of the conventional and (c) additional notch orientations in X70_A.

However, it is interesting to mention that the anisotropies in both cases are maximised at -80 °C due to the absence of delamination of D–D orientation in conventional case and the existence of delamination in T–S orientation in ductile fracture as shown in Figs 4.33, 5.5 and 5.7. Moreover, the anisotropy is induced in the additional case at -100 °C due to the absence of delamination of D–S orientation.

Fig. 7.6 shows the direct comparisons of Charpy energies of the conventional and additional notch orientations at same temperatures. The figures show clearly that the anisotropy begins to be incurred in transition temperature regions.

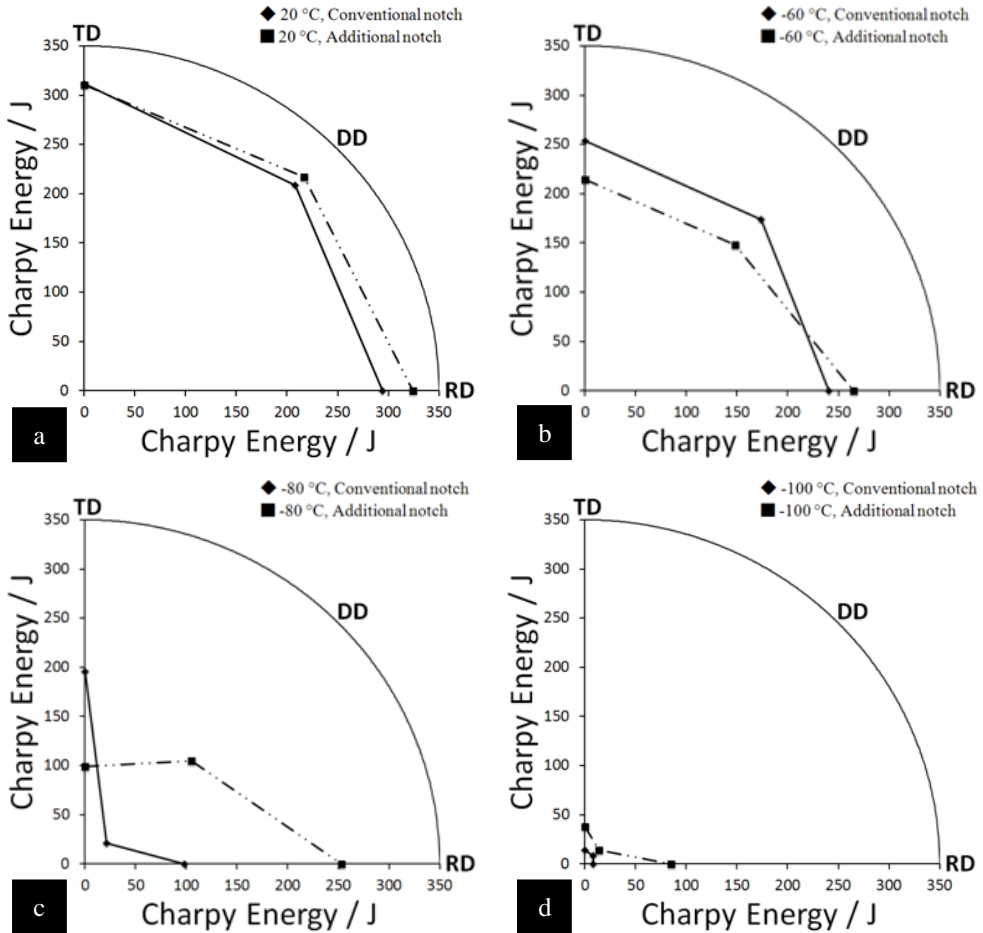


Figure 7.6. Comparisons of Charpy energies of the conventional and additional notch orientations in X70_A: (a) 20 °C, (b) -60 °C, (c) -80 °C and d) -100 °C.

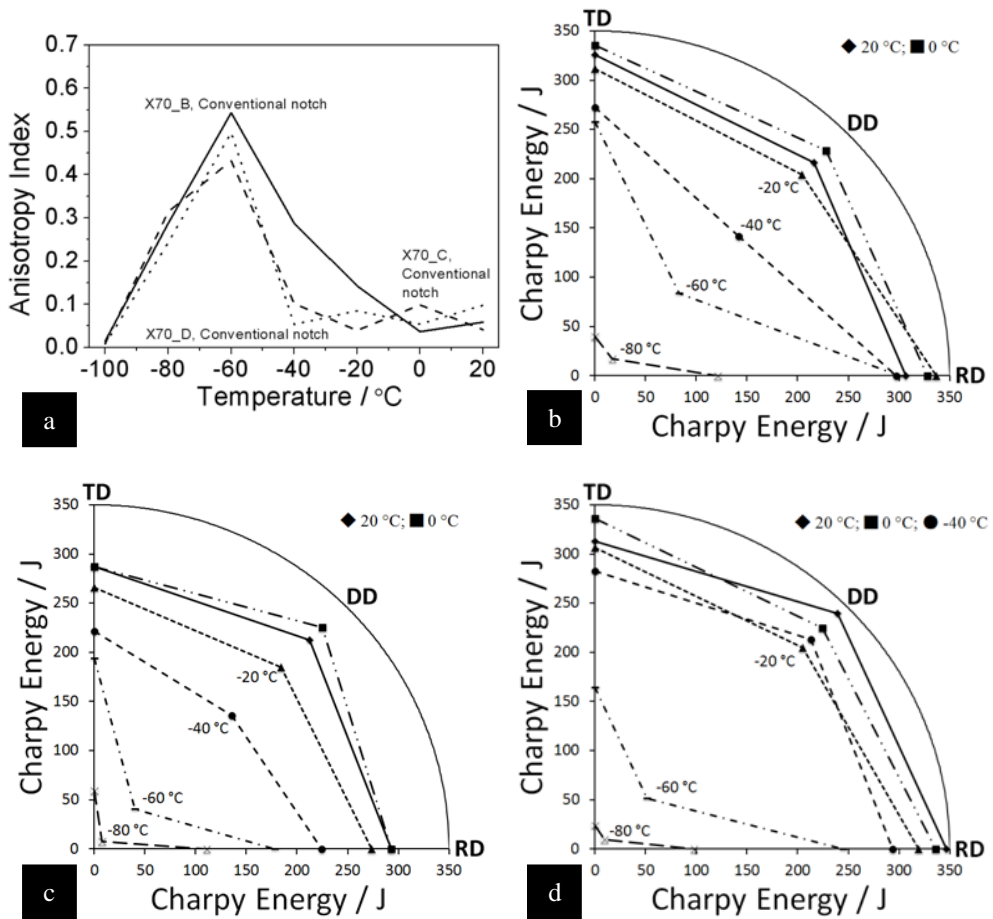


Figure 7.7. (a) Anisotropy indices of X70_B, X70_C and X70_D, (b) Charpy properties of X70_B, (c) X70_C and (d) X70_D.

Fig. 7.7 shows the anisotropy indices and Charpy energies for X70_B, X70_C and X70_D steels. Similarly, they show that anisotropy is worst in the transition temperature range due to the absence of delamination in D–D orientation and a propensity of {100} planes as discussed in previous section.

7.2. Summary and Future Work

The orientation–dependence of Charpy properties in the six alloys of hot–rolled linepipe steels has been studied. All the API linepipe steels of grade X70 and X80 have isotropic features in the upper and lower shelves but severe anisotropic behaviour in the ductile–to–brittle transition temperature region; Charpy specimens machined in diagonally to the rolling direction with a conventional notch orientation always showed the worst toughness. This tendency was always present even though chemical composition and processing variables were varied.

There are many causes to be found in the literature on this topic, and it can be said that the anisotropy of toughness is a complex phenomenon. But, three particular factors can be emphasized: a non–uniform distribution in the size and shape of inclusions, microstructural anisotropy due to banding, and crystallographic texture. In the linepipe steels investigated, some inclusions were discovered, but they probably had no effect on the anisotropy of Charpy–energy due to their spherical shape. It is any inclusions elongated during the rolling process that can contribute to mechanical anisotropy. Moreover, in order to investigate the rapid ductile to brittle transition in the D–D orientation, the concept of the density of grain boundaries of each plane parallel to fracture surface was introduced, but it could not explain the anisotropy.

On the other hand, it has been revealed that the delamination associated with microstructural banding strongly influences the orientation–dependence of Charpy toughness in the ductile–to–brittle transition temperature region in all of

the steels studied. In addition, the role of crystallographic texture on the Charpy anisotropy was examined in terms of the exaggerated alignment of cleavage planes along particular orientations, and such interpretations demonstrated quantitatively that a propensity of grains having cleavage planes parallel to the fracture plane was pronounced. Therefore, a secondary contribution comes from crystallographic texture which in some orientations places a large density of cleavage planes parallel to the fracture plane of the Charpy specimen.

A set of experiments has been performed to add weight to the main cause, delamination, in the case of X80_A and X70_A steels. Charpy specimens were machined with an additional notch orientation as shown in Fig. 3.2b. The results indicated that the occurrence of delamination during Charpy testing makes a meaningful difference in Charpy-energy and can lead to the orientation-dependence of toughness. A quenching heat treatment in X80_A steel confirmed that the delamination is associated with banding and that it deepens the degree of anisotropy. Interestingly, the anisotropic features in the ductile-to-brittle transition temperature region could not be avoided. The characteristic V-shape anisotropy persisted although the microstructure was totally changed after the heat treatment. This is because the rolling and transformation texture was retained after the heat treatment and it comes from the so-called the texture memory effect. As a result, a similar observation of a propensity of grains having cleavage planes parallel to the fracture plane was investigated, and it supports the observation that the anisotropy comes from the delamination and the crystallographic texture in the linepipe steels.

Although the nature of anisotropy in impact toughness of hot-rolled steels due to the microstructural banding and the rolling and transformation texture could not be averted, the ability to predict the orientation-dependence of Charpy toughness in steels is of great interest. The difficulties in prediction can be incurred from the fact that the toughness itself is already complex due to the many influencing factors and is additionally complicated by orientation and temperature. Fortunately, those difficulties can be averted using powerful empirical methods such as neural network modelling. Any variables such as chemical composition, processing variables, texture, work of fracture, target temperature and orientation, can be utilised directly and the modelling can express a full complexity of the relationships quantitatively. However, it is still necessary to conduct a series of experiments, so that the modelling can identify the domains requiring further results to predict the anisotropy of Charpy properties in steels properly since only few data exist that are relevant to the present study.

References

Abson, D. J. and Pargeter, R. J.: Factors influencing the as-deposited strength, microstructure and toughness of manual metal arc welds suitable for C–Mn steel fabrications. *International Materials Reviews*, vol. 31, pp. 141–196, 1986.

Alé, R. M., Rebello, J. M. A. and Charlier, J.: A metallographic Technique for Detecting Martensite–Austenite Constituents in the Weld Heat–Affected Zone of a Micro–alloyed Steel. *Materials Characterization*, vol. 37, pp. 89–93, 1996.

Almond, E. A.: Delamination in Banded Steels. *Metallurgical Transactions*, vol. 1, pp. 2038–2041, 1970.

American Society for Metals: *Ductility: papers presented at a seminar of the American Society for Metals*, pp. 250–252, Taylor & Francis, USA, 1967.

American Society for Testing: *Interfaces in Composites*. pp. 109–110, ASTM International, York, PA, USA, 1969.

Anderson, T. L.: *Fracture Mechanics*. CRC Press, Boca Raton, FL, 1995.

API Recommended Practice 5L3. *API*, 1996.

ASTM Handbook. *ASM International*, vol. 11, p. 695, 1987.

Babu, S. S.: Acicular Ferrite and Bainite in Fe–Cr–C Weld Deposits. *Ph.D. Thesis*, University of Cambridge, 1991

Babu, S. S. and Bhadeshia, H. K. D. H.: Stress and the acicular ferrite transformations, *Materials Science and Engineering A*, vol. A156, pp. 1–9, 1992.

Baker, T. J. and Charles, J. A.: Deformation of MnS inclusions in steel. *Journal of the Iron and Steel Institute*, vol. 210, pp. 680–690, 1972.

Baker, T. J., Kavishe, F. P. L. and Wilson, J.: Effect of non-metallic inclusions on cleavage fracture. *Materials Science and Technology*, vol. 2, pp. 576–582, 1986.

Baldi, G. and Buzzichelli, G.: Critical stress for delamination fracture in HSLA steels. *Metal Science*, vol. 12, pp. 459–472, 1978.

Bastien, P. G.: The mechanism of formation of banded structures. *Journal of the Iron and Steel Institute*, vol. 187, pp. 281–291, 1957.

Baczynski, G. J., Jonas, J. J. and Collins, L. E.: The Influence of Rolling Practice on Notch Toughness and Texture Development in High-Strength Linepipe. *Met. Mater. Trans. A*, vol. 30A, pp. 3045–54, 1999.

Beidokhti, B., Koukabi, A. H. and Dolati, A.: Effect of titanium addition on the microstructure and inclusion formation in submerged arc welded HSLA pipeline steel. *Journal of Materials Processing Technology*, vol. 209, pp. 4027–4035, 2009.

Benzerga, A. A., Besson, J. and Pineau, A.: Anisotropic ductile fracture part i: experiments. *Acta Materialia*, vol. 52, pp. 4623–4638, 2004.

Beremin, F. M.: A local criterion for cleavage fracture of a nuclear pressure vessel steel. *Metall. Trans. A*, vol. 14A, pp. 2277–2287, 1983.

Bhadeshia, H. K. D. H.: The theory and significance of retained austenite in steels. *Ph.D. Thesis*, University of Cambridge, 1979.

Bhadeshia, H. K. D. H.: Diffusional formation of ferrite in iron and its alloys, *Progress in Materials Science*, vol. 29, pp. 321–385, 1985.

Bhadeshia, H. K. D. H.: Models for Acicular Ferrite. In *International Trends in Welding Research*, pp. 213–222, edited by S. A. David and J. M. Vitek, ASM International, Ohio, USA, 1992.

Bhadeshia, H. K. D. H.: *Bainite in Steels*. 2nd ed., The Institute of Materials, London, 2001.

Bhadeshia, H. K. D. H.: Phase Transformation Contributing to the Properties of Modern Steels. *Bulletin of the Polish Academy of Sciences*, vol. 58, pp. 255–265, 2010.

Bhadeshia, H. K. D. H.: Mechanical Anisotropy in Steels for Pipelines. In Private Communication to Joo, M. S., 2011.

Bhadeshia, H. K. D. H. and Honeycombe, R. W. K.: *Steels*. 3rd ed., Elsevier Ltd., 2006.

Bhattacharjee, D., Knott, J. F. and Davis, C. L.: Predictability of Charpy impact toughness in thermomechanically control rolled microalloyed steels. *Ironmaking and Steelmaking*, vol. 30, pp. 249–256, 2003.

Bhattacharjee, D., Knott, J. F. and Davis, C. L.: Charpy–impact–toughness prediction using an ‘effective’ grain size for thermomechanically controlled rolled microalloyed steels. *Met. Mater. Trans. A*, vol. 35A, pp. 121–130, 2004.

Bourell, D. L.: Cleavage Delamination in Impact Tested Warm–Rolled Steel. *Metallurgical Transactions A*, vol. 14A, pp. 2487–2496, 1983.

Bourell, D. L. and Sherby, O. D.: Texture Induced Cleavage Delamination of Warm-Rolled Low Carbon Steel. *Metallurgical Transactions A*, vol. 14A, pp. 2563–2566, 1983.

Bowles, J. S. and MacKenzie, J. K.: The crystallography of martensite transformations, part I. *Acta Metallurgica*, vol. 2, pp. 129–137, 1954.

Bramfitt, B. L. and Marder, A. R.: A study of the delamination behaviour of a very low-carbon steel. *Metallurgical transactions A*, vol. 8, pp. 1263–1273, 1977.

Broek, D.: *Elementary Engineering Fracture Mechanics*. Kluwer Academic Publishers Group, 1982.

Brozzo, P. and Buzzichelli, G.: Effect of plastic anisotropy on the occurrence of “separations” on fracture surfaces of hot-rolled steel specimens. *Scripta Metallurgica*, vol. 10, pp. 235–240, 1976.

Burnos, V. A., Vaschilo, T. P. and Balandina, L. E.: Evaluation of the quality of the metal of pipes according to impact toughness with anisotropy taken into account. *Industrial Laboratory (USSR)*, vol. 54, pp. 548–550, 1988.

Carreño, F., Chao, J., Pozuelo, M. and Ruano, O. A.: Microstructure and fracture properties of an ultrahigh carbon steel–mild steel laminated composite. *Scripta Materialia*, vol. 48, pp. 1135–1140, 2003.

Chae, D., Koss, D. A., Wilson, A. L. and Howell, P. R.: Effect of microstructural banding on failure initiation of HY–100 steel. *Metallurgical and Materials Transactions A*, vol. 31A, pp. 995–1005, 2000.

Chao, H. C.: Mechanism of anisotropic lamellar fractures. *Metallurgical transactions A*, vol. 9, pp. 509–514, 1978.

Chen, M.–Y, Linkens, D. A. and Bannister, A.: Numerical analysis of factors influencing Charpy impact properties of TMCR structural steels using fuzzy modelling. *Mat. Sci. and Tech.*, vol. 20, pp. 627–633, 2004.

Clegg, W. J., Kendall, K., Alford, N. M., Birchall, J. D. and Button, T. W.: A simple way to make tough ceramics, *Nature*, vol. 347, pp. 455–457, 1990.

Corbett, K. T., Bowen, R. R. and Petersen, C. W.: High–strength steel pipeline economics. *Journal of Offshore and Polar Engineering*, vol. 14, pp. 75–80, 2004.

Cottrell, A. H.: Theory of Brittle Fracture in Steel and Similar Metals. *Trans. TMS–AIME*, pp. 192–203, 1958.

Courbon, J., Lormand, G., Dudragne, G., Daguler, P. and Vincent, A.: Influence of inclusion pairs, clusters and stringers on the lower bound of the endurance limit of bearing steels. *Tribology International*, vol. 36, pp. 921–928, 2003.

Dabkowski, D. S., Konkol, P. J. and Baldy, M. F.: An investigation of splitting–type fractures in high–strength line–pipe steels. *Metals Engineering Quarterly*, vol. 16, pp. 22–32, 1976.

Dieter, G. E.: *Mechanical Metallurgy*. McGraw–Hill, London, 1988.

De, A. K., Speer, J. G. and Matlock, D. K.: Colour tint–etching for multiphase steels. *Advanced Materials and Processes*, vol. 161(2), pp. 27–30, 2003.

DeArdo, A. J.: An investigation of the mechanism of splitting which occurs in

tensile specimens of high–strength low–alloy steels. *Metallurgical transactions A*, vol. 8A, pp. 473–485, 1977.

Demura, M., Xu, Y., Kishida, K. and Hirano, T.: Texture memory effect in heavily cold–rolled Ni₃Al single crystals. *Acta Materialia*, vol. 55, pp. 1779–1789, 2007.

Denys, R.: *Pipeline Technology*. Vol. I & II, Elsevier, Amsterdam, Netherlands, 2000.

Dubé, C. A., Aaronson, H. I. and Mehl, R. F.: La formation de la ferrite proeutectoïde dans les aciers au carbone, *Revue de Metallurgie*, vol. 55, pp. 201–210, 1958.

Eckel, J. A., Glaws, P. C., Wolfe, J. O. and Zorc, B. J.: Clean Engineered Steels – Progress at the End of the Twentieth Century. In *Advances in the Production and Use of Steel with Improved Internal Cleanliness, ASTM STP 1361*, pp. 1–10, edited by J. K. Mahoney, Jr., American Society for Testing and Materials, West Conshohocken, PA, USA, 1999.

Fairchild, D. P., Macia, M. L., Papka, S. D., Petersen, C. W., Stevens, J. H., Barbas, S. T., Bangaru, N. V., Koo, J. Y. and Luton, M. J.: High Strength Steels – Beyond X80. In *Proceedings of the Int'l Pipe Dreamer's Conference*, pp. 307–321, edited by M. Toyoda and R. Denys, Yokohama, Japan, 7–8 Nov. 2002.

Fegredo., D. M.: Effect of rolling at different temperatures on fracture toughness anisotropy of a C–Mn structural–steel. *Canadian Metallurgical Quarterly*, vol. 14, pp. 243–255, 1975.

François, D. and Pineau, A.: *From Charpy to present impact testing*. Elsevier, 2002.

Fegredo, D. M., Faucher, B. and Shehata, M. T.: Influence of inclusion content, texture and microstructure on the toughness anisotropy of low carbon steels. In *Strength of Metals and Alloys*, vol. 2, pp. 1127–1132, Pergamon Press, Oxford, UK, 1985.

Garcia, O. L., Petrov, R., Bae, J.-H., Kestens, L. and Kang, K. B.: Microstructure – Texture Related Toughness Anisotropy of API-X80 Pipeline Steel. *Advanced Materials Research*, vols. 15–17, pp. 840–845, 2007.

Garwood, S. J.: The effect of temperature, orientation and constraint on the toughness of A533 B Class I steel. In *Application of Fracture Mechanics to Materials and Structures*, pp. 939–950, Martinus Nijhoff Publishers, Leiden, Holland, 1984.

Gerberich, W. W., Chen, Y. T., Atteridge, D. G. and Johnson, T.: Plastic flow of Fe–BINARY alloys–II. Application of the description to the ductile–brittle transition, *Acta Metallurgica*, vol. 29, pp. 1187–1201, 1981.

Gourgues, A. F., Flower, H. M. and Lindley, T. C.: Electron backscattering diffraction study of acicular ferrite, bainite, and martensite steel microstructures. *Mater. Sci. Technol.*, vol. 16(1), pp. 26–40, 2000.

Greninger, A. B. and Troiano, A. R.: Kinetics of the austenite to martensite transformation in steel. *Trans. ASM*, vol. 28, p. 537, 1940

Griffith, A. A.: The phenomena of rupture and flow in solids. *Phil. Trans. Roy. Soc.*, London, vol. 22, pp. 163–198, 1921.

Grimpe, F., Heyer, J., Dahl, W.: Influence of temperature, strain rate and specimen geometry on the microscopic cleavage fracture stress. *Nuclear Engineering and*

Design, vol. 188, pp. 155–160, 1999.

Guillén, M. P. B.: Transformation Textures in Hot Rolled Steels. *Ph.D. Thesis*, McGill University, 1995.

Guo, W., Dong, H., Lu, M. and Zhao, X.: The coupled effects of thickness and delamination on cracking resistance of X70 pipeline steel. *International Journal of Pressure Vessels and Piping*, vol. 79, pp.403–412, 2002.

Gurson, A. L.: Plastic Flow and Fracture Behaviour of Ductile Materials Incorporating Void Nucleation, Growth and Interaction. *Ph.D. Thesis*, Brown University, 1975.

Gurson, A. L.: Continuum theory of ductile rupture by void nucleation and growth: Part I – Yield criteria and flow rules for porous ductile media. *J. Eng. Mater. Technol.*, vol. 99(2), pp. 2–15, 1977.

Güngör, Ö. E., Yan, P., Thibaux, P., Liebeherr, M., Bhadeshia, H. K. D. H. and D. Quidort: Investigations into microstructure–toughness relation in high frequency induction welded pipes. In *Proceedings of the 8th international pipeline conference, IPC2010–31372*, Calgary, Alberta, Canada, 27 Sep.–1 Oct. 2010.

Hahn, G. T., Averbach, B. L., Owen, W. S. and Cohen, M.: In *Fracture*. p. 91, edited by B. L. Averbach, D. K. Felbeck, G. T. Hahn and D. A. Thomas, MIT Press, Cambridge, MA, USA, 1959.

Hall, E. O.: The deformation and ageing of mild steel: III Discussion of results. *Proc. Phys. Soc. London*, vol. B64, pp. 747–753, 1951.

Harada, S., Endo, T. and Kaseda, M.: Effects of forging ratio and specimen

orientation on elastic–plastic fracture toughness of thick forged steel plates. In *Role of Fracture Mechanics in Modern Technology*, pp. 485–496, edited by H. Nisitani, G. C. Sih and T. Ishihara, Amsterdam, Holland, 1987.

Hillert, M.: On the theory of normal and abnormal grain growth. *Acta Metall.*, vol. 13, pp. 227–239, 1965.

Hodge, J. M., Frazier, R. H. and Boulger, F. W.: The effect of sulphur on the notch toughness of heat–treated steels. *Trans. Metall. Soc. AIME*, vol. 215, pp. 745–753, 1959.

Howell, P.: The Pearlite Reaction in Steels Mechanisms and Crystallography* 1:: Part I. From HC Sorby to RF Mehl. *Materials Characterization*, vol. 40(4–5), pp. 227–260, 1998.

Hyzak, J. M. and Bernstein, I. M.: The role of microstructure on the strength and toughness of fully pearlitic steels. *Metall. Trans. A*, vol. 7A, pp. 1217–1224, 1976.

Ikawa, H., Oshige, H. and Tanoue, T.: Effect of Martensite–Austenite Constituent on the HAZ Toughness of a High Strength Steel. IIW Doc. IX–1156–80, *International Institute of Welding*, London, 1980.

Imai, T., Nishida, Y. and Kogiso, S.: Anisotropy of the Charpy impact value of carbon steels and corrective heat treatment. *Journal of Mechanical Working Technology*, vol. 7, pp. 147–161, 1982.

Imai, T., Nishida, Y. and Kogiso, S.: Anisotropy of the Charpy impact value of carbon steels. I. elimination of the anisotropy by heat treatment. *Reports of Government Industrial Research Institute, Nagoya*, vol. 34, pp. 123–133, 1985.

Inagaki, H., Kurihara, K. and Kozasu, I.: Influence of Crystallographic Texture on the Strength and Toughness of the Controlled Rolled High Tensile Strength Steel. *The Iron and Steel Institute of Japan*, vol. 7, pp. 991–1011, 1975.

Inoue, T., Yin, F., Kimura, Y., Tsuzaki, K. and Ochiai, S.: Delamination Effect on Impact Properties of Ultrafine-Grained Low-Carbon Steel Processed by Warm Caliber Rolling. *Metallurgical and Materials Transactions A*, vol. 41, pp. 341–355, 2010.

Ito, Y. and Nakanishi, M.: Study on Charpy impact properties of weld metal with submerged arc welding. *Sumitomo Search*, issue 15, pp. 42–62, 1976.

Jatczak, C. F., Girardi, D. J. and Rowland, E. S.: On banding in steel. *Trans. ASM*, vol. 48, pp. 279–305, 1956.

Ju., J.-B., Lee, J.-S. and Jang, J.-I.: Fracture toughness anisotropy in a API steel line-pipe. *Materials Letters*, vol. 61, pp. 5178–5180, 2007.

Kameda, J.: A kinetic model for ductile-brittle fracture mode transition behaviour. *Acta metall.*, vol. 34(12), pp. 2391–2398, 1986.

Kang, K.-B., Bae, J. H. and Choo, W.-Y.: Effect of thermomechanical processing parameters on mechanical properties and microstructure of API-X80 grade hot rolled strips. In *4th Int. Conf. on Pipeline Technology*, vol. 4, pp. 1689–1699, Ostend, Belgium, 9–13 May 2004.

Kapp, J. A. and Underwood, J. H.: Correlation between fracture toughness, Charpy V-notch impact energy, and yield strength for ASTM A723 steel. Memorandum report ARCCB-MR-92008, Final Report, AD-A249142, 1992.

Kasada, R., Lee, S. G., Isselin, J., Lee, J. H., Omura, T., Kimura, A., Okuda, T., Inoue, M., Ukai, S., Ohnuki, S., Fujisawa, T. and Abe, F.: Anisotropy in tensile and ductile–brittle transition behaviour of ODS ferritic steels. *Journal of Nuclear Materials*, 2011, doi:10.1016/j.jnucmat.2010.12.069.

Kichkina, A. A., Matrosoy, M. Yu., Efron, L. I., Klyukvin, M. B. and Golovanov, A. V.: Effect of structural anisotropy of ferrite–bainite pipe steel on mechanical properties in tensile and impact bending tests. *Metallurgist*, vol. 54, pp. 808–816, 2011.

Kim, K. and Bae, J.–H.: Metallurgical and process parameters for commercial production of high toughness API–X80 grade hot rolled strips. In *Proceedings of the Biennial International Pipeline Conference, IPC*, vol. 3, pp. 167–173, 2008.

Kim, M.–C., Oh, Y. J. and Hong, J. H.: Characterisation of boundaries and determination of effective grain size in Mn–Mo–Ni low alloy steel from the view of misorientation. *Scripta Mater.*, vol. 43, pp. 205–211, 2000.

Kim, N. J.: The physical metallurgy of HSLA linepipe steels – a review. *Journal of Metals*, vol. 35, pp. 21–27, 1983.

Kim, S. K.: Effect of Microstructure on Yield Ratio and Toughness of High Strength API Steels. *Ph.D. Thesis*, POSTECH, 2002.

Kimura, Y., Inoue, T. Yin, F. and Tsuzaki, K.: Inverse Temperature Dependence of Toughness in an Ultrafine Grain–Structure Steel. *Science*, vol. 320, pp. 1057–1060, 2008.

Kimura, Y., Inoue, T. Yin, F. and Tsuzaki, K.: Delamination Toughening of Ultrafine Grain Structure Steels Processed through Tempforming at Elevated

Temperatures. *ISIJ International*, vol. 50, pp. 152–161, 2010.

Kirkaldy, J. S., Brigham, R. J., Domian, H. A. and Ward, R. G.: A study of banding in Skelp by electron–probe microanalysis. *Canadian Metallurgical Quarterly*, vol. 2, pp. 233–241, 1963.

Kirkaldy, J. S., von Destinon–Forstmann, J., and Brigham, R. J.: Simulation of banding in steels. *Canadian Metallurgical Quarterly*, vol. 59, pp. 59–81, 1962.

Klassen, R. J., Bassim, M. N., Bayoumi, M. R. and Wilsdorf, H. G. F.: Characterisation of the effect of alloying elements on the fracture toughness of high strength, low alloy steels. *Mat. Sci. and Eng.*, vol. 80(1), pp. 25–35, 1986.

Knott, J. F.: *Fundamentals of Fracture Mechanics*. pp. 114–149, John Wiley & Sons, New York, 1973.

Ko, T. and Cottrell, S. A.: The formation of bainite. *Journal of the Iron and Steel Institute*, vol. 172, pp. 307–313, 1952.

Korda, A. A., Mutoh, Y., Miyashita, Y., Sadasue, T. and Manan, S. L.: In situ observation of fatigue crack retardation in banded ferrite–pearlite microstructure due to crack branching. *Scripta Materialia*, vol. 8, pp. 1835–1840, June 2006.

Kotrechko, S., Stetsenko, N. and Shevchenko, S.: Effect of texture smearing on the anisotropy of cleavage–stress of metals and alloys. *Theoretical and Applied Fracture Mechanics*, vol. 42, pp. 89–98, 2004.

Kramer, G. S., Wilkowski, G. M. and Maxey, W. A.: Flaw tolerance of spiral–welded line pipe. Technical Report L51514, American Gas Association, Washington, D. C., USA, 1987.

Liessem, A., Schröder, J., Pant, M., Erdelen–Peppier, M., Liedtke, M., Höhler, S. and Stallybrass, C.: Manufacturing challenges of high strength line pipes. In *New Developments on Metallurgy and Applications of High Strength Steels*, pp. 543–555, edited by T. Perez, TMS–AIME, Materials Park, Ohio, USA, 2008.

Lischewski, I., Kirch, D. M., Ziemons, A. and Gottstein, G.: Investigation of the α – γ – α Phase Transformation in Steel: High–Temperature In Situ EBSD Measurements. *Texture, Stress, and Microstructure*, 2008, doi: 10.1155/2008/294508.

Low, J. R.: Relation of Properties to Microstructure. *American Society for Metals*, Metals Park, Ohio, 1954.

Lum, P. T., Chait, R. and Hickey, JR., C. F.: The Toughness of High Hardness Laminar Composite Steel as Influenced by Specimen and Crack Orientation. *Metallurgical Transactions A*, vol. 6A, pp. 1093–1100, 1975

Lyons, W. C. and Plisga, G. J.: *Standard handbook of petroleum and natural gas engineering*. 2nd ed., Gulf Professional Publishing, 2005.

Mackenzie, J. K.: Second Paper on the Statistics Associated with the Random Disorientation of Cubes. *Biometrika*, vol. 45, p. 229, 1958.

Maina, E., Crowther, D. N., Banerjee, J. R. and Mintz, B.: Influence of directionality on strength and impact behaviour of high strength steels. *Materials Science and Technology*, 2012,
<http://dx.doi.org/10.1179/1743284711Y.0000000061>.

Materials Algorithms Project (MAP), University of Cambridge and National Physical Laboratory, UK, <http://www.msm.cam.ac.uk/map/mapmain.html>.

Matrosov, Yu. I. and Polyakov, I. E.: Increasing the toughness and ductility and decreasing the property anisotropy of low-alloy steels. *Stal*, vol. 2, pp. 162–167, 1976.

McEvily, A. J. and Bush, R. H.: An investigation of the notch-impact strength of an ausformed steel. *Trans. ASM*, vol. 55, pp. 654–666, 1962.

Medinskaya, I. P., Rubenchik, Yu I., Pisarenko, T. A. and Afanasenko, E. A.: The influence of property anisotropy on the technological effectiveness of weldable steels, *Chemical and Petroleum Engineering*, vol. 16, pp. 658–661, 1981.

Meguid, S. A.: *Engineering Fracture Mechanics*. Elsevier, New York, USA, 1989.

Mintz, B., Morrison, W. B., Morris, P. P. and Davies, G. J.: The influence of texture on the tensile and impact properties of controlled-rolled steels. In *Texture and properties of materials*, pp. 224–234, edited by G. J. Davies, The Metals Society, London, UK, 1976.

Mintz, B., Morrison, W. B., Welch, P. I. and Davies, G. J.: The relative contributions of texture and grain shape to the properties of warm-rolled Fe-Mn alloys. In *Texture of Materials*, vol. 2, pp. 465–474, edited by G. Gottstein and K. Lucke, Springer-Verlag, Berlin, Germany, 1978.

Mintz, B., Morrison, W. B. and Jones, A.: Influence of carbide thickness on impact transition temperature of ferritic steels. *Met. Technol.*, vol. 6, pp. 252–260, 1979.

Mintz, B.: Influence of grain boundaries on fissure formation during impact testing of ferritic stainless steels. *Metals Technology*, vol. 7, pp. 127–129, 1980.

Mintz, B., Maina, E. and Morrison, W. B.: Origin of fissures on fracture surfaces of impact samples of HSLA steel with ferrite/pearlite microstructures. *Materials Science and Technology*, vol. 23, pp. 347–354, 2007.

Mintz, B., Maina, E. and Morrison, W. B.: Influence of dislocation hardening, precipitation hardening, grain elongation and sulphides on fissure formation in HSLA steels having a ferrite/pearlite microstructure. *Materials Science and Technology*, vol. 24, pp. 177–188, 2008.

Mitsche, S., Polt, P. and Sommitsch, C.: Quantitative Metallography, *Imaging & Microscopy*, vol. 8, pp. 38–39 2006.

Mohan, R., Marshall, C., Krishnaswamy, P., Brust, F., Ghadiali, N. and Wilkowski, G.: Fracture behaviour of short circumferentially surface-cracked pipe, short cracks in piping and piping welds. Technical Report NUREG/CR-6298, BMI-2183, Nuclear Regulatory Commission, Ohio, USA, 1995a.

Mohan, R., Marschall, C., Krishnaswamy, P., Brust, F., Ghadiali, N. and Wilkowski, G.: Effects of toughness anisotropy and combined tension, torsion and bending loads on fracture behaviour of ferritic nuclear pipe. Technical Report NUREG/CR-6299 BMI-2184, Nuclear Regulatory Commission, Washington, D. C., USA, 1995b.

Morrison, W. B.: In *Controlled Processing of HSLA Steels*. Sheffield: British Steel Corporation, 1976.

Moskovic, R., Windle, P. L. and Smith, A. F.: Modelling Charpy impact energy property changes using a Bayesian method. *Metall. and Mater. Trans. A*, vol. 28A(5), pp. 1181–1193, 1997.

Naylor, J. P.: The Influence of the Lath Morphology on the Yield Stress and

Transition Temperature of Martensitic–Bainitic Steels. *Metall. Trans. A*, vol. 10A, pp. 861–873, 1979.

Naylor, J. P. and Krahe, P. R.: Cleavage Planes in Lath Type Bainite and Martensite. *Metall. Trans.*, vol. 6A, p. 595, 1975.

NPL: MTDATA. Software, National Physical Laboratory, Teddington, UK, 2006.

Okuda, N., Kasada, R. and Kimura, A.: Statistical evaluation of anisotropic fracture behaviour of ODS ferritic steels by using small punch tests. *Journal of Nuclear Materials*, vols. 386–388, pp. 974–978, 2009.

Oldfield, W.: Curve fitting impact test data: A statistical procedure. *ASTM Standardisation News*, vol. 3(11), pp. 24–29, Nov. 1975.

Orowan, E.: Energy criteria of fracture. *Welding J.*, vol. 34, pp. 1575–1605, 1955.

Parton, V. Z.: *Fracture Mechanics From Theory to Practice*. p. 66, Gordon and Breach Science Publishers, 1992.

Petch, N. J.: The cleavage strength of polycrystals. *J. of Iron Steel Institute*, vol. 173, pp. 25–28, 1953.

Petrov, R., Garcia, O. L., Mulders, J. J. L., Reis, A. C. C., Bae, J.–H., Kestens, L. and Houbaert, Y.: Three dimensional microstructure–microtexture characterization of pipeline steel. *Materials Science Forum*, vol. 550, pp. 625–630, 2007a.

Petrov, R., Garcia, O. L., Mouriño, N. S., Kestens, L., Bae, J. H., and Kang, K. B.: Microstructure–texture related toughness anisotropy of API–X80 pipeline steel characterised by means of 3D–EBSD technique. *Materials Science Forum*, vols.

558–559, pp. 1429–1434, 2007b.

Pickering, F. B.: In *Proc. Symp. Transformation and hardenability in steels*. pp. 109–129, Ann Arbor, MI, Climax Molybdenum Co. and the University of Michigan, 1967.

Pickering, F. B. and Gladman, T.: Metallurgical development in carbon steels. *ISI Spec. Rep.*, vol. 81, p. 10, 1963.

Pook, L. P.: The effect of notch angle on the behaviour of Charpy testpieces. *Engineering Fracture Mechanics*, vol.4, pp. 483–486, 1972.

Pyshmintsev, I., Gervasyev, A., Petrov, R. H., Olalla, V. C. and Kestens, L.: Crystallographic texture as a factor enabling ductile fracture arrest in high strength pipeline steel. *Materials Science Forum*, vols. 702–703, pp. 770–773, 2012.

Qiao, Y. and Argon, A. S.: Cleavage cracking resistance of high angle grain boundaries in Fe–3%Si alloy. *Mech. Mater.*, vol. 35, pp. 313–331, 2003.

Ray, A., Paul, S. K., and Jha., S.: Effect of inclusions and microstructural characteristics on the mechanical properties and fracture behaviour of a high–strength low–alloy steel. *Journal of Materials Engineering and Performance*, vol. 4, pp. 679–688, 1995.

Ray, R. K. and Basu, S.: Mechanism of splitting of a few Fe–Mn–Ni–base alloys subjected to thermomechanical treatment. *Mat. Techn. Steel Research*, vol. 56, pp. 341–345, 1985.

Ridley, N.: A Review of the Data on the Interlamellar Spacing of Pearlite. *Metallurgical and Materials Transactions A*, vol. 15(6), pp. 1019–1036, 1984.

Rinebolt, J. A. and Harris, W. J.: Effect of Alloying Elements on Notch Toughness of Pearlitic Steels. *Trans. Am. Soc. Met.*, vol. 43, p. 1197, 1951.

Ritchie, R. O., Knott, J. F. and Rice, J. R.: On the relationship between critical tensile stress and fracture toughness in mild steel. *Journal of Mechanics and Physics of Solids*, vol. 21, pp. 395–410, 1973.

Sakai, M., Bradt, R. C. and Fischbach, D. B.: Fracture toughness anisotropy of a pyrolytic carbon. *Journal of Materials Science*, vol. 21, pp. 1491–1501, 1986.

Sage, A. M.: A Review of the Physical Metallurgy of High–Strength, Low–Alloy Line–Pipe and Pipe–Fitting Steels. In *Proc. of an International Conference on Steels for Pipeline and Fittings*, p. 39, The Metal Society, London, UK, 1981,

Seo, D. H., Song, W. H., Ahn, S. S., Kim, C. M. and Yoo, J. Y.: Microstructure and Mechanical Properties of API–X80/X100 Grade Plates and Pipes. *POSCO 研究論文*, vol. 12(1), pp. 20–27, 2007.

Schofield, R., Rowntree, G., Sarma, N. V. and Weiner, R. T.: Arrow–head fractures in controlled–rolled pipeline steels. *Metals Technology*, vol. 1, pp. 325–331, 1974.

Shackelford, J. F. and Doremus, R. H.: *Ceramic and glass materials: structure, properties and processing*. pp. 1–24, Springer, New York, 2008.

Shin, S. Y., Han, S., Y., Hwang, B. C., Lee, C., G. and Lee, S. H.: Effects of Cu and B addition on microstructure and mechanical properties of high–strength bainitic steels. *Materials Science and Engineering A*, vol. 517, pp. 212–218, 2009a.

Shin, S. Y., Hong, S. M., Bae, J. H., Kim, K. S. and Lee, S. H.: Separation

phenomenon occurring during the Charpy impact test of API X80 pipeline steels. *Metallurgical & Materials Transactions A*, vol. 40, pp. 2333–2349, 2009b.

Sims, C. E.: The nonmetallic constituents of steel. *Trans. Met. Soc. AIME*, vol. 215, pp. 367–393, 1959.

Song, R., Ponge, D. and Raabe, D.: Mechanical properties of an ultrafine grained C–Mn steel processed by warm deformation and annealing. *Acta Materialia*, vol. 53, pp. 4881–4892, 2005.

Sorby, H. C.: On the application of very high powers to the study of microscopic structure of steel. *J. Iron Steel Inst.*, vol. 1, pp. 140–147, 1886.

Spitzig, W. A. and Leslie, W. C.: Solid–solution softening and thermally activated flow in alloys of Fe with 3 at.% Co, Ni or Si. *Acta Metallurgica*, vol. 19(11), pp. 1143–1152, 1971.

Srinivasan, G. R. and Wayman, C. M.: The crystallography of the bainite transformation. *Acta Metallurgica*, vol. 16, pp. 621–636, 1968.

Stalheim, D., Barnes, K. and McCutcheon, D.: Alloy designs for high strength oil and gas transmission linepipe steels. In *Proc. Int. Symp. on Microalloyed Steels for the Oil and Gas Industry*, pp. 73–108, The Minerals, Metals & Materials Society (TMS), Araxa, MG, Brazil, January 23–26, 2006.

Stoloff, N. S.: *Fracture, volume VI: fracture of metals, chapter 1: effects of alloying on fracture Characteristics*. Academic Press, New York, 1969.

Strangwood, M. and Bhadeshia, H. K. D. H.: Mechanism of acicular ferrite formation in steel weld deposits. In *Advances in Welding Technology and Science*,

pp. 209–213, edited by S. A. David, ASM International, Materials Park, Ohio, USA, 1987.

Suh, D.-W., Oh, C. S. and Kim, S. J.: Dilatometric analysis of austenite formation during intercritical annealing. *Met. Mater. Int.*, vol. 14, pp. 275–282, 2008.

Sun, J. and Boyd, J. D.: Effect of thermomechanical processing on anisotropy of cleavage fracture stress in microalloyed linepipe steel. *International Journal of Pressure Vessels and Piping*, vol. 77, pp. 369–377, 2000.

Swallow, E. and Bhadeshia, H. K. D. H.: High resolution observations of displacements caused by bainitic transformation. *Materials Science and Technology*, vol. 12, pp. 121–125, 1996.

Tamura, I., Sekine, H., Tanaka, T. and Ouchi, C.: In *Thermomechanical Processing of High-strength Low-alloy Steels*. Butterworth & Co. Ltd., 1988.

Tanaka T.: Controlled rolling of Steel Plate and Strip. *International Metals Reviews*, vol. 4, pp. 185–212, 1981.

Tau, L., Chan, S. L. and Shin, C. S.: Effects of anisotropy on the hydrogen induced fatigue crack propagation of a banded ferrite–pearlite steel. *Journal of Marine Science and Technology*, vol. 1, pp. 19–22, 1993.

Thompson, S. W. and Howell, P. R.: Factors influencing ferrite/pearlite banding and origin of large pearlite nodules in a hypoeutectoid plate steel. *Materials Science and Technology*, vol. 8, pp. 777–784, 1992.

Tomita, Y.: Effect of decreased hot-rolling reduction treatment on fracture toughness of low alloy structural steels. *Metallurgical and Materials Transactions A*,

vol. 21, pp. 2555–2563, 1990.

Tsunekage, N., Kobayashi, K. and Tsubakino, H.: Influence of sulphur and vanadium additions on toughness of bainitic steels. *Mater. Sci. Technol.*, vol. 17, pp. 847–855., 2001

Tvergaard, V. and Needleman, A.: Analysis of the cup and con fracture in a round tensile bar. *Acta Metall.*, vol. 32, pp. 157–169, 1984.

Tvergaard, V. and Needleman, A.: Numerical modelling of the ductile–brittle transition, *International Journal of Fracture*, vol. 101, pp. 73–97, 2000.

Todinov, M.T.: Fitting impact fracture toughness data in the transition region. *Mater. Sci. Eng.*, Vol. A265, pp. 1–6, 1999.

Tyson, W. R., Ayres, R. A. and Stein, D. F.: Anisotropy of cleavage in B.C.C. transition metals. *Acta Metallurgica*, vol. 21(5), pp. 621–627, 1973.

Verdeja, J. I., Asensio, J. and Pero–Sanz, J. A.: Texture, formability, lamellar tearing and HIC susceptibility of ferritic and low–carbon HSLA steels. *Materials Characterization*, vol. 50, pp. 81–86, 2003.

Wilson, P. C., Murty, Y. V., Kattamis, T. Z. and Mehrabian, R.: Effect of homogenization on sulphide morphology and mechanical properties of rolled AISI 4340 steel. *Metals Technology*, vol. 2, pp. 241–244, 1975.

Yan, P., Güngör, Ö. E., Thibaux, P., Bhadeshia, H. K. D. H.: Crystallographic Texture of Induction–welded and Heat–treated Pipeline Steel. *Advanced Materials Research*, vols. 89–91, pp. 651–656, 2010.

Yi, H. L.: Full Pearlite Obtained by Slow Cooling in Medium Carbon Steel. *Materials Science and Engineering A*, vol. 527, pp. 7600–7604, 2010.

Watson, J. D. and McDougall, P. G.: The crystallography of Widmanstätten ferrite. *Acta Metallurgica*, vol. 21, pp. 961–973, 1973.

Wechsler, M. S., Lieberman, D. S. and Read, T. A.: On the theory of the formation of martensite, *Trans. AIME Journal of Metals*, vol. 197, pp. 1503–1515, 1953.

Wilkowski, G. M., Ahmad, J., Brust, F., Ghadiali, N., Krishnaswamy, P., Landow, M., Marschall, C. W., Scott, P. and Vieth, P.: Short cracks in piping and piping welds. Technical Report NUREG/CR-599-Vol.1-No.1; BMI.2173-Vol.1-No.1, Nuclear Regulatory Commission, Ohio, USA, 1991.

Wilson, D. V.: Reversible work hardening in alloys of cubic metals. *Acta Metallurgica*, vol. 13, pp. 807–814, 1965.

Zhu, Q., Sellars, C. M. and Bhadeshia, H. K. D. H.: Quantitative metallography of deformed grains. *Materials Science and Technology*, vol. 23, pp. 757–766, 2007.

Appendix A. Chemical Compositions for Linepipe Steels

The actual chemical compositions of linepipe steels are listed here from the literatures. Unit is wt%.

A.1. API X65

C	Mn	Si	Cu	Mo	Ni	Nb	V	Al	Sn	Ti	Cr	P	S	N	Ca	B	Others	References
≤0.26	≤1.40					≥0.005	≥0.005					≤0.04	≤0.05					API Recommended Practice, 1996
0.061	1.42	0.199	0.144	0.132		0.0538		0.0417	0.0167	0.0142	0.0126	0.01						Rabizadeh <i>et al.</i> , 2011
0.08	1.45	0.31										0.019	0.003					Ju <i>et al.</i> , 2007
0.041	1.1	0.18						0.32						0.0053				Yan <i>et al.</i> , 2010
0.061	1.42	0.199	0.144	0.132							0.012							Zarebidaki <i>et al.</i> , 2011
0.17	1.32	0.02	0.02	0.01	0.10		0.21				0.08	0.01	0.029					Jeglic <i>et al.</i> , 1978
0.12	1.68	0.29		0.01	0.03	0.04	0.06				0.04	0.007	0.009					Vosikovsky <i>et al.</i> , 1981
0.089	1.15											0.013	0.011					Hinton <i>et al.</i> , 1983
0.09	1.51	0.3		0.003	0.019	0.06	0.057			0.048	0.031	0.024	0.002					Kim <i>et al.</i> , 2011

C	Mn	Si	Cu	Mo	Ni	Nb	V	Al	Sn	Ti	Cr	P	S	N	Ca	B	Others	References
0.09	0.85	0.29										0.007	0.001				Nb, V, Ca	Kobayashi <i>et al.</i> , 1987
0.04	1.55	0.28										0.004	0.001				Cu, Ni, Nb, V, Ca	
0.044	1.22	0.29		0.14	0.27	0.048		0.022		0.011		0.004	0.0003		0.0021			Takahashi <i>et al.</i> , 1996
	1.3												0.003				Cu, Ni, Nb, V, Ca	Hyodo <i>et al.</i> , 1987
	1.3												0.001				Cu, Ni, Nb	
0.11	1.05	0.29	0.31		0.15	0.032	0.055	0.035		0.01		0.014	0.005		0.0074			Fassini <i>et al.</i> , 1993
0.11	1.05	0.29	0.31		0.15	0.032	0.055	0.035		0.01		0.014	0.005		0.0074			Zampronio <i>et al.</i> , 1995
0.088	1.46	0.379	0.01	0.005	0.022	0.033	0.054	0.033		0.003	0.021	0.013	0.001	0.004				Hu <i>et al.</i> , 1998
0.11	1.05	0.29	0.31		0.015	0.032	0.0055	0.035		0.01		0.014	0.005		0.0074			Lesage <i>et al.</i> , 2000
0.098	1.63	0.33			0.02	0.04	< 0.01	0.051		0.022	0.01	0.02	0.002					Abbade <i>et al.</i> , 2000
0.1	1.49	0.25	0.024		0.25	0.024	0.05					0.014	0.001					Tsay <i>et al.</i> , 2001
0.1	1.5	0.26				0.046	0.053			0.016								Choi <i>et al.</i> , 2001
0.08	1.45	0.31										0.019	0.003					Lee <i>et al.</i> , 2004
0.08	1.07	0.25	0.07	0.21	0.03	0.027		0.018			0.03	0.012	0.003	0.006	0.0027			Murtagian <i>et al.</i> , 2005
0.11	1.27	0.25	0.08	0.02	0.04	0.028	0.05	0.03	0.005		0.05	0.008	0.002	0.0115	0.003			
0.1	1.30	0.25										0.018	0.010					Kawaguchi <i>et al.</i> , 2004
0.09	0.30	1.39										0.019	0.006					
0.07	1.36	0.19	< 0.01	< 0.01	0.01	0.04	< 0.01	0.011		< 0.01	0.2	0.013	0.002					Arafin <i>et al.</i> , 2010
0.07	1.47	0.14	0.04	0.01	0.02	0.03	0.04			0.01	0.03	< 0.02	0.005					Baek <i>et al.</i> , 2010
0.073	1.366	0.208				0.041				0.002		0.014	0.001					Chung <i>et al.</i> , 2011

C	Mn	Si	Cu	Mo	Ni	Nb	V	Al	Sn	Ti	Cr	P	S	N	Ca	B	Others	References
0.07	1.34	0.3			0.005	0.048	0.05	0.036				0.015	0.002					Dey <i>et al.</i> , 2006
0.07	1.48	0.25	0.09		0.8	0.042	0.064	0.04		0.017	0.02	0.013	0.002					Fragiel <i>et al.</i> , 2007
0.071	1.515	0.209	0.018	0.003	0.011	0.044	0.042			0.017	0.157							Hashemi, 2011
0.11	1.12	0.28	0.14	0.11	0.099	0.018	0.058			0.002	0.082	0.01	0.003			0.0003		Holtam <i>et al.</i> , 2010
0.12	1.27	0.18	0.12	0.17	0.07	0.054	0.057	0.022	0.008	0.001	0.11	0.008	0.002			0.0005		Hu <i>et al.</i> , 2011
0.14	1.47	0.3	0.1		0.017	0.045	0.047			0.011	0.023	0.021	0.0057					Lemos <i>et al.</i> , 2011
0.04	1.48	0.34	0.20	0.01	0.03						0.17	0.006	0.001					Rethmeier <i>et al.</i> , 2009
0.08	1.67	0.28	0.19	0.01	0.01						0.01	0.012	0.001					
0.08	1.45	0.31										0.019	0.03					Oh <i>et al.</i> , 2007
0.08	1.45	0.31										0.019	0.03					Oh <i>et al.</i> , 2011
0.05	1.25	0.2		≤ 0.1				0.1		≤ 0.1	0.005	0.002			0.002		Nb+Ti+V ≤ 0.1 Cu+Ni ≤ 0.4	Park <i>et al.</i> , 2008
0.04	1.5	0.2		0.02								0.011	0.003					Zhang <i>et al.</i> , 2007
0.08	1.45	0.31										0.019	0.003					Lee <i>et al.</i> , 2006
0.07	1.46	0.25	0.1		0.1	0.051	0.07	0.042		0.018	0.02	0.012	0.002					Natividad <i>et al.</i> , 2007
0.11	1.3	0.26		< 0.01	< 0.01	0.05		0.026			< 0.01	0.017	0.009					Villalba <i>et al.</i> , 2009
0.04	1.5	0.2		0.02								0.011	0.003					Zhang <i>et al.</i> , 2009a
0.15		0.22		1.6	0.09		0.06					0.025	0.015					Neville <i>et al.</i> , 2009
0.09	1.56	0.28	0.02	0.01	0.03	0.04	0.05				0.05	0.014	0.001					Kittel <i>et al.</i> , 2010
0.11	1.18			0.15	0.42	0.023	0.06			< 0.01	0.17							Fassina <i>et al.</i> , 2011
0.065	1.54	0.25	0.04	0.007	0.04			0.041			0.05	0.013	0.001					Choi <i>et al.</i> , 2011

A.2. API X70

C	Mn	Si	Cu	Mo	Ni	Nb	V	Al	Sn	Ti	Cr	Co	P	S	N	Ca	O	Mg	Others	References	
≤ 0.23	≤ 1.60												≤ 0.04	≤ 0.05						API Recommended Practice, 1996	
0.02	1.91	0.25											0.021	0.001					Nb, B, Ca	Kobayashi <i>et al.</i> , 1987	
0.05	1.5	0.24		0.15	0.01	0.06		0.029			0.01		0.012	0.009						Villalba <i>et al.</i> , 2009	
0.063	1.97	0.2											< 0.008	< 0.002			< 0.005		Ni+Mo+Nb : 0.4	Shin <i>et al.</i> , 2009b	
0.057	1.77	0.2											< 0.002	< 0.002			< 0.005	0.001	Al+Ti : 0.02		
0.09	1.56	0.28	0.12	0.07	0.07	0.031	0.07	0.029~0.038	0.012		0.08		0.015	0.005	0.0059	0.0012				Korczak, 2004	
0.05	1.6	0.3						0.04					0.008	0.002	0.005				Ni+Cu : 0.4	Kichkina <i>et al.</i> , 2011	
0.04	1.76	0.281	0.193	0.194		0.067	0.001			0.023	0.058		0.016	0.001					Nb, V, Ti		
0.04~0.07	1.0~1.7	0.1~0.3		≤ 0.5																Nb+V+Ti ≤ 0.15	Bae <i>et al.</i> , 2002
0.10	1.55	0.33				0.025	0.096			0.02			0.020	0.004						Pluvinage <i>et al.</i> , 1992	
0.08	1.56	0.44	0.05		0.02			0.02			0.02		0.013	0.003							
0.055	1.62	0.22				0.07	0.03			0.009			0.013	0.002						Zhang <i>et al.</i> , 2009b	
0.064	1.48	0.39	0.16		0.08	0.05	0.045	0.031		0.02	0.03		0.013	0.01						Ilker Yelbay <i>et al.</i> , 2010	
0.05	1.55	0.2		0.17	0.18	0.058				0.021			0.011	0.0013	0.0045	0.002				Li <i>et al.</i> , 2011a	

C	Mn	Si	Cu	Mo	Ni	Nb	V	Al	Sn	Ti	Cr	Co	P	S	N	Ca	O	Mg	Others	References	
0.05	1.7	0.22		0.198	0.196	0.052	0.04			0.012	0.018		0.024							Kim <i>et al.</i> , 2011	
0.08	1.55	0.23	0.006	0.01	0.02	0.03	0.005	0.02		0.03	0.17		0.025	0.011						Beidokhti <i>et al.</i> , 2009	
0.08	1.73	0.25	0.016	0.003	0.194	0.064	0.045	0.028		0.027	0.02		0.017	0.002	0.0067					Beltrão <i>et al.</i> , 2010	
0.125	1.68	0.27	0.045	0.021	0.04	0.033		0.038		0.003	0.051			0.005						Capelle <i>et al.</i> , 2010	
0.116	1.67	0.26	0.04	0.02	0.04	0.03		0.03			0.05		0.012	< 0.01	0.009					Chatzidouros <i>et al.</i> , 2011	
0.069	1.62	0.18				0.056	0.044			0.032			0.016	0.002	0.0041					Choi <i>et al.</i> , 2000	
0.077	1.50	0.19		0.3		0.051	0.028			0.001			0.013	0.002	0.0039						
0.05	1.5	0.2		0.24	0.187	0.05	0.04	0.03		0.018	0.01		0.008	0.015						Hashemi <i>et al.</i> , 2009	
0.05	1.24	0.27																	Cu+Ni+Mo : 0.5	Hwang <i>et al.</i> , 2008	
																			Nb+V+Ti : 0.1		
0.05	1.5	0.21		0.24	0.187	0.05				0.019	0.01	0.003	0.08	0.015						Hashemi, 2008	
0.075	1.54	0.26																		Cu+Ni+Mo : 0.63	
																				0.095 ≤ Nb+V+Ti ≤ 0.105	
0.07	1.55	0.25																		Cu+Ni+Mo : 0.48	
																				0.095 ≤ Nb+V+Ti ≤ 0.105	Hwang <i>et al.</i> , 2005
0.046	1.51	0.26																		Cu+Ni+Mo : 0.55	
																				0.095 ≤ Nb+V+Ti ≤ 0.105	
0.09	1.63	0.32	0.01			0.04	0.05			0.01			0.009	0.003	0.002					Khoddam <i>et al.</i> , 2010	
0.066	1.56	0.223	0.011	0.236	0.172		0.039	0.042		0.028	0.007		0.013	0.006						Kiarasi <i>et al.</i> , 2010	
0.05	1.48	0.26	0.22	0.17	0.15	0.05	0.052			0.016	0.027		0.012	0.003						Li <i>et al.</i> , 2011b	

C	Mn	Si	Cu	Mo	Ni	Nb	V	Al	Sn	Ti	Cr	Co	P	S	N	Ca	O	Mg	Others	References	
0.142	1.44	0.34				0.044	0.095						0.013	0.009	0.009					Mirzakhani <i>et al.</i> , 2009	
0.09	1.63	0.32				0.04	0.05			0.01			0.009	0.003	0.002					Mirzakhani <i>et al.</i> , 2010	
0.1	1.51	0.3				0.036	0.042	0.024					0.014	0.002	0.0046					Shimizu <i>et al.</i> , 1986	
0.1	1.57	0.3				0.034	0.058	0.018					0.016	0.003	0.0044						
0.075	1.54	0.26	0.16	0.24	0.23	0.056	0.03			0.017					0.0052					Shin <i>et al.</i> , 2006	
																			P+N < 0.01		
0.062	1.56	0.311						0.023											Nb+Ti : 0.06		
																			Ni+Mo : 0.2	Shin <i>et al.</i> , 2007	
																			P+N < 0.01		
0.045	1.56	0.297						0.031											Nb+Ti : 0.06		
																			Ni+Mo : 0.37		
0.037	1.5	0.14	0.27		0.16	0.09		0.03		0.01	0.26		< 0.015	< 0.003	0.004	0.0025				Mendoza <i>et al.</i> , 2002	
																			P+S < 0.01		
0.05~0.06	1.5~1.6	0.2~0.3																		0.2 ≤ Ni+Mo ≤ 0.3	Hong <i>et al.</i> , 2011
																				0.08 ≤ Nb+Ti+Al ≤ 0.1	
0.037	1.51	0.14	0.27		0.157	0.092		0.032		0.01	0.266		0.014	0.002	0.004						Mendoza <i>et al.</i> , 1999
																				P+S < 0.01	
0.062	1.56	0.311		0.05~0.1	0.1~0.15			0.023												Nb+Ti : 0.06	Kim <i>et al.</i> , 2010
																				P+S < 0.01	
0.045	1.56	0.297		0.2~0.25	0.1~0.15			0.031												Nb+Ti : 0.06	

A.3. API X80

C	Mn	Si	Cu	Mo	Ni	Nb	V	Al	Sn	Ti	Cr	P	S	N	B	Others	References
≤ 0.18	≤ 1.80											≤ 0.03	≤ 0.0018				API Recommended Practice, 1996
0.05	1.90	0.19										0.011	0.001			Mo, Nb, B, Ca	Kobayashi <i>et al.</i> , 1987
0.06	1.50	0.30	0.015	0.26	0.75	0.067	0.002			0.007	0.12	0.008	0.003				Sun <i>et al.</i> , 2000
0.076	1.87	0.24										0.011	0.003			Mo+Ni : 0.51, Al+Ti : 0.04, Nb+V : 0.06, Cr+Cu : 0.3	
0.075	1.82	0.25										0.011	0.003			Mo+Ni : 0.3, Al+Ti : 0.03, Nb+V : 0.12, Cr+Cu : 0.29	
0.075	1.83	0.26										0.011	0.003			Mo+Ni : 0.3, Al+Ti : 0.04, Nb+V : 0.06, Cr+Cu : 0.29	
0.074	1.85	0.24										0.011	0.003			Mo+Ni : 0.39, Al+Ti : 0.04, Nb+V : 0.09, Cr+Cu : 0.15	Shin <i>et al.</i> , 2009a
0.051	1.85	0.26										0.011	0.003			Mo+Ni : 0.61, Al+Ti : 0.04, Nb+V : 0.11, Cr+Cu : 0.25	
0.075	1.85	0.3										0.011	0.003			Mo+Ni : 0.45, Al+Ti : 0.22, Nb+V : 0.12, Cr+Cu : 0.23	
0.06	1.87	0.14										0.02	0.002			Mo+Ni : 0.39, Al+Ti : 0.04, Nb+V : 0.04, Cr+Cu : 0.15	
0.058	1.87	0.22										0.009	0.001			Mo+Ni : 0.41, Al+Ti : 0.01, Nb+V : 0.05, Cr+Cu : 0.15	
0.05	1.76	0.17		0.20	0.02	0.066	0.025	0.035		0.016	0.015	0.016	0.002	0.0059	0.0003		Santos <i>et al.</i> , 2010
0.06	1.82	0.23		0.26	0.28	0.039	0.01			0.01	0.01	0.004	0.001				Kim <i>et al.</i> , 2011
0.028	1.7	0.31		0.3				0.041	0.013							S+P+N : 0.019, Cu+Ni+Cr : 0.46, Ti+V : 0.018	Arafin <i>et al.</i> , 2011
0.08	1.9	0.24		0.3			0.06				0.3	0.011	0.003				Han <i>et al.</i> , 2009
0.08	1.9	0.3		0.2	0.25	0.06	0.06			0.02							Han <i>et al.</i> , 2010
0.073	1.76	0.23						0.033								P+N < 0.01, Nb+Ti : 0.05, Mo+Ni : 0.56	Shin <i>et al.</i> , 2007

C	Mn	Si	Cu	Mo	Ni	Nb	V	Al	Sn	Ti	Cr	P	S	N	B	Others	References
0.4	2.00	0.40										0.020	0.010			Nb+V+Ti < 0.15	
0.05	1.74	0.26	0.19	0.29	0.21							0.007	0.004	0.0042		Nb+V+Ti : 0.108	Deng <i>et al.</i> , 2010
0.05	1.58	0.26	0.20	0.25	0.20							0.008	0.003	0.0041		Nb+V+Ti : 0.073	
0.082	1.84	0.25	0.01	0.09	0.19	0.043	0.008	0.023		0.014		0.011	0.001				Ichiyama <i>et al.</i> , 2003
0.07~0.08	1.7~1.8	0.2~0.3														P+S ≤ 0.01, 0.5 ≤ Mo+Ni ≤ 0.6, 0.08 ≤ Nb+Ti+Al ≤ 0.1	Hong <i>et al.</i> , 2011
0.13	1.52	0.2		0.05	0.21	0.038	0.1	0.028		0.005	0.11	0.007	0.009				López <i>et al.</i> , 1996
0.073	1.76	0.23		0.25~0.30	0.25~0.3			0.033								P+S ≤ 0.01, Nb+Ti : 0.05	Kim <i>et al.</i> , 2010
0.038	1.77	0.27		0.25		0.090				0.022		0.009	0.002			Ni+Cr+Cu : 0.59	
0.030	1.80	0.28		0.24		0.088				0.024		0.010	0.003			Ni+Cr+Cu : 0.45	Baczynski <i>et al.</i> , 1999

References

Abbade, N. P. and Crnkovic, S. J.: Sand–water slurry erosion of API 5L X65 pipe steel as quenched from intercritical temperature. *Tribology International*, vol. 33, pp. 811–816, 2000.

API Recommended Practice 5L3, API, 1996.

Arafin, M. A. and Szpunar, J. A.: A novel microstructure – Grain boundary character based integrated modelling approach of intergranular stress corrosion crack propagation in polycrystalline materials. *Computational Materials Science*, vol. 47, pp. 890–900, 2010.

Arafin, M. A. and Szpunar, J. A.: Effect of bainitic microstructure on the susceptibility of pipeline steels to hydrogen induced cracking. *Materials Science and Engineering A*, vol. 528, pp. 4927–4940, 2011.

Bae, J.–H., Choi, S.–H. and Kang, K. B.: Effect of Thermomechanical Processing Parameters upon Texture Development and Yield Strength Anisotropy in High Strength Linepipe Steels. *Materials Science Forum*, vols. 408–412, pp. 1179–1184, 2002.

Baek, J.–H., Kim, Y.–P., Kim, C.–M., Kim, W.–S. and Seok, C.–S.: Effects of pre–strain on the mechanical properties of API 5L X65 pipe. *Material Science and Engineering A*, vol. 527, pp. 1473–1479, 2010.

Baczynski, G. J., Jonas, J. J. and Collins, L. E.: The Influence of Rolling Practice on Notch Toughness and Texture Development in High–

Strength Linepipe. *Met. Mater. Trans. A*, vol. 30A, pp. 3045–54, 1999.

Beidokhti, B., Koukabi, A. H. and Dolati, A.: Effect of titanium addition on the microstructure and inclusion formation in submerged arc welded HSLA pipeline steel. *Journal of Materials Processing Technology*, vol. 209, pp. 4027–4035, 2009.

Beltrão, M. A. N., Castrodeza, E. M. and Bastian, F. L.: Fatigue crack propagation in API 5L X–70 pipeline steel longitudinal welded joints under constant and variable amplitudes. *Fatigue Fract. Engng. Mater. Struct.*, vol. 34, pp. 321–328, 2010

Capelle, J., Dmytrakh, I. and Pluvinage, G.: Comparative assessment of electrochemical hydrogen absorption by pipeline steels with different strength. *Corrosion Science*, vol. 52, pp. 1554–1559, 2010.

Chatzidouros, E. V., Papazoglou, V. J., Tsiourva, T. E. and Pantelis, D. I.: Hydrogen effect on fracture toughness of pipeline steel welds, with in situ hydrogen charging. *International Journal of Hydrogen Energy*, 2011, doi:10.1016/j.ijhydene.2011.06.140.

Choi, C. W., Koh, H. J. and Lee, S.: Analysis and Prevention of Yield Strength Drop during Spiral Piping of Two High–Strength API–X70 Steels. *Metallurgical and Materials Transactions A*, vol. 31A, pp. 2669–2674, 2000.

Choi, Y., Choo, W. Y. and Kwon, D.: Analysis of mechanical property distribution in multiphase ultra–fine–grained steels by nanoindentation. *Scripta Materialia*, vol. 45, pp. 1401–1406, 2001.

Choi, Y.-S. and Nešić, S.: Determining the corrosive potential of CO₂ transport pipeline in high pCO₂-water environments. *International Journal of Greenhouse Gas Control*, vol. 5, pp. 788–797, 2011.

Chung, P. C., Ham, Y., Kim, S., Lim, J. and Lee, C.: Effects of post-weld heat treatment cycles on microstructure and mechanical properties of electric resistance welded pipe welds. *Materials and Design*, 2011, doi:10.1016/j.matdes.2011.05.027.

Deng, W., Gao, X., Zhao, D., Du, L., Wu, D. and Wang, G.: Effect of Ti-enriched Carbonitride on Microstructure and Mechanical Properties of X80 Pipeline Steel. *J. Mater. Sci. Technol.*, vol. 26(9), pp. 803–809, 2010.

Dey, S., Mandhyan, A. K., Sondhi, S. K. and Chattoraj, I.: Hydrogen entry into pipeline steel under freely corroding conditions in two corroding media. *Corrosion Science*, vol. 48, pp. 2676–2688, 2006.

Fassina, P., Bolzoni, F., Fumagalli, G., Lazzari, L., Vergani, L. and Sciuccati, A.: Influence of Hydrogen and Low Temperature on Pipeline Steels Mechanical Behaviour. *Procedia Engineering*, vol. 10, pp. 3226–3234, 2011

Fassini, F. D., Zampronio, M. A. and de Miranda, P. E. V.: Design of ion-implanted coatings to impede hydrogen contamination of steel. *Corrosion Science*, vol. 35(1–4), pp. 549–556, 1993.

- Fragiel, A., Serna, S., Campillo, B. and Cota, L.: Dissimilar mechanical properties–microstructures microalloyed pipeline steels cracking performance under sour environment. *Materials Science and Engineering A*, vol. 467, pp. 1–7, 2007.
- Han, S. Y., Shin, S. Y., Lee, S., Kim, N. J., Bae, J.–H. and Kim, K.: Effects of Cooling Conditions on Tensile and Charpy Impact Properties of API X80 Linepipe Steels. *Metallurgical and Materials Transactions A*, vol. 41A, pp. 329–340, 2010.
- Han, S. Y., Shin, S. Y., Seo, C.–H., Lee, H., Bae, J.–H., Kim, K., Lee, S. and Kim, N. J.: Effects of Mo, Cr, and V Additions on Tensile and Charpy Impact Properties of API X80 Pipeline Steels. *Metallurgical and Materials Transactions A*, vol. 40A, pp. 1851–1862, 2009.
- Hashemi, S. H.: Apportion of Charpy energy in API 5L grade X70 pipeline steel. *International Journal of Pressure Vessels and Piping*, vol. 85, pp. 879–884, 2008.
- Hashemi, S. H.: Strength–hardness statistical correlation in API X65 steel. *Materials Science and Engineering A*, vol. 528, pp. 1648–1655, 2011.
- Hashemi, S. H., Mohammadyani, D., Pouranvari, M. and Mousavizadeh, S. M.: On the relation of microstructure and impact toughness characteristics of DSAW steel of grade API X70. *Fatigue Fract. Engng. Mater. Struct.*, vol. 32, pp. 33–40, 2009.
- Hinton, B. R. W. and Procter, R. P. M.: The effect of strain–rate and cathodic potential on the tensile ductility of X–65 pipeline steel. *Corrosion Science*, vol. 23(2), pp. 101–123, 1983.

Holtam, C. M., Baxter, D. P., Ashcroft, I. A. and Thomson, R. C.: Effect of crack depth on fatigue crack growth rates for a C–Mn pipeline steel in a sour environment. *International Journal of Fatigue*, vol. 32, pp. 288–296, 2010.

Hong, S., Shiing, S. Y., Lee, S. and Kim, N. J.: Effects of Specimen Thickness and Notch Shape on Fracture Modes in the Drop Weight Tear Test of API X70 and X80 Linepipe Steels. *Metallurgical and Materials Transactions A*, vol. 42A, pp. 2619–2632, 2011.

Hu, R. P., Manolatos, P., Jerome, M., Meyer, M., and Galland, J.: Hydrogen absorption by cathodically protected underground steel piping in thiosulfate containing media. *Corrosion Science*, vol. 40(4/5), pp. 619–629, 1998.

Hu, X., Alzawai, K., Gnanavelu, A., Neville, A., Wang, C., Crossland, A. and Martin, J.: Assessing the effect of corrosion inhibitor on erosion–corrosion of API–5L–X65 in multi–phase jet impingement conditions. *Wear*, vol. 271, pp. 1432–1437, 2011.

Hwang, B., Kim, Y. M., Lee, S., Kim, N. J. and Ahn, S. S.: Correlation of Microstructure and Fracture Properties of API X70 Pipeline Steels. *Metallurgical and Materials Transactions A*, vol. 36A, pp. 725–739, 2005

Hwang, B., Shin, S. Y., Lee, S., Kim, N. J. and Ahn, S. S.: Effect of microstructure on drop weight tear properties and inverse fracture occurring in hammer impacted region of high toughness X70 pipeline steels. *Materials Science and Technology*, vol. 24(8), pp. 945–956, 2008.

Hyodo, T., Iino, M., Ikeda, A., Kimura, M. and Shimizu, M.: The hydrogen permeation and hydrogen-induced cracking behaviour of linepipe in dynamic full scale tests. *Corrosion Science*, vol. 27(10/11), pp. 1077–1098, 1987.

Ichiyama, Y. and Saito, T.: Factors affecting flash weldability in high strength steel – Study on toughness improvement of flash welded joint in high strength steel (Report 1) –. *Yosetsu Gakkai Ronbunshu/Quarterly Journal of the Japan Welding Society*, vol. 21(2), pp. 219–226, 2003.

Ilker Yelbay, H., Cam, I. and Hakan Gür, C.: Non-destructive determination of residual stress state in steel weldments by Magnetic Barkhausen Noise technique. *NDT&E International*, vol. 43, pp. 29–33, 2010.

Jeglic, F. S. and Packwood, R. H.: Impact-Deposited White Layer on X65 Steel. *Metallography*, vol. 11, pp. 43–50, 1978.

Ju, J.-B., Lee, J.-S. and Jang, J.-I.: Fracture toughness anisotropy in a API steel line-pipe. *Materials Letters*, vol. 61, pp. 5178–5180, 2007.

Kawaguchi, S., Ohata, M., Oki, Y., Ogita, G., Hagiwara, N. and Toyoda, M.: Applicability of the Critical Condition for Ductile Cracking of Linepipe Steel to the Evaluation of Ductile Cracking of an Axially Notched Linepipe. *Yosetsu Gakkai Ronbunshu/Quarterly Journal of the Japan Welding Society*, vol. 22(2), pp. 282–290, 2004.

Khoddam, S. and Hodgson, P. D.: Post processing of the hot torsion test results using a multi-dimensional modelling approach. *Materials and Design*, vol. 31, pp. 2578–2584, 2010.

Kiarasi, R., Shahrabi, T., Neshati, J. and Aliofkhazrei, M.: Optimization of CO₂ Corrosion for API X70 Steel on Acetic Acid Contained Environment. *Protection of Metals and Physical Chemistry of Surfaces*, vol. 46(3), pp. 350–353, 2010.

Kichkina, A. A., Matrosov, M. Yu., Efron, L. I., Klyukvin, M. B. and Golovanov, A. V.: Effect of structural anisotropy of ferrite–bainite pipe steel on mechanical properties in tensile and impact bending tests. *Metallurgist*, vol. 54, pp. 808–816, 2011.

Kim, Y.–P., Kim, C.–M, Kim, W.–S., Song, K.–S. and Shin, K.–S.: Near–threshold Fatigue Crack Growth Behaviour and Crack Closure of Natural Gas Pipeline Steels. *Procedia Engineering*, vol. 10, pp. 813–820, 2011.

Kim, Y., Shin, S. Y., Kim, Y. G., Kim, N. J. and Lee, S.: Effects of Strain Rate and Test Temperature on Torsional Deformation Behaviour of API X70 and X80 Linepipe Steels. *Metallurgical and Materials Transactions A*, vol. 41A, pp. 1961–1972, 2010.

Kittel, J., Smanio, V., Fregonese, M., Garnier, L. and Lefebvre, X.: Hydrogen induced cracking (HIC) testing of low alloy steel in sour environment: Impact of time exposure on the extent of damage. *Corrosion Science*, vol. 52, pp. 1386–1392, 2010.

Korczak, P.: Modeling of steel microstructure evolution during thermo–mechanical rolling of plate for conveying pipes. *Journal of Materials Processing Technology*, vols. 153–154, pp. 432–435, 2004.

- Kobayashi, Y., Ume, K., Hyodo, T. and Taira, T.: The resistance of welded linepipes to sulphide stress cracking. *Corrosion Science*, vol. 27(10–11), pp. 1117–1135, 1987.
- Lee, J.–S., Jang, J.–I., Lee, B.–W., Choi, Y., Lee, S. G. and Kwon, D.: An instrumented indentation technique, for estimating fracture toughness of ductile materials: A critical indentation energy model based on continuum damage mechanics. *Acta Materialia*, vol. 54, pp. 1101–1109, 2006.
- Lee, Y.–H. and Kwon, D.: Estimation of biaxial surface stress by instrumented indentation with sharp indenters. *Acta Materialia*, vol. 52, pp. 1555–1563, 2004.
- Lemos, M., Kwietniewski, C., Clarke, T., Joia, C. J. B. and Altenhofen, A.: Evaluation of the Fatigue Life of High–Strength Low–Alloy Steel Girth Welds in Aqueous Saline Environments with Varying Carbon Dioxide Partial Pressures. *Journal of Materials Engineering and Performance*, 2011, doi: 10.1007/s11665–011–0018–x.
- Lesage, J., Chicot, D., Bartier, O., Zampronio, M. A. and de Miranda, P. E. V.: Influence of hydrogen contamination on the tensile behaviour of a plasma ion nitride steel. *Materials Science and Engineering A*, vol. 282, pp. 203–212, 2000.
- Li, C., Wang, Y. and Chen, Y.: Influence of peak temperature during in–service welding of API X70 pipeline steels on microstructure and fracture energy of the reheated coarse grain heat–affected zones. *J. Mater. Sci.*, vol. 46, pp. 6424–6431, 2011b.

Li, R., Zuo, X., Hu, Y., Wang, Z. and Hu, D.: Microstructure and properties of pipeline steel with a ferrite/martensite dual-phase microstructure. *Materials Characterization*, vol. 62, pp. 801–806, 2011a.

López, H. F., Raghunath, R., Albarran, J. L. and Martinez, L.: Microstructural Aspects of Sulphide Stress Cracking in an API X–80 Pipeline Steel. *Metallurgical and Materials Transactions A*, vol. 27A, pp. 3601–3611, 1996.

Mendoza, R., Alanis, M., Perez, R., Alvarez, O., Gonzalez, C. and Juarez–Islas, J. A.: On the processing of Fe–C–Mn–Nb steels to produce plates for pipelines with sour gas resistance. *Materials Science and Engineering A*, vol. 337, pp. 115–120, 2002.

Mendoza, R., Huante, J., Alanis, M., Gonzalez–Rivera, C. and Juarez–Islas, J. A.: Slab cracking after continuous casting of API 5L X–70 grade steel for pipeline sour gas application. *Ironmaking and Steelmaking*, vol. 26(3), pp. 205–209, 1999

Mirzakhani, B., Khoddam, S., Arabi, H., Salehi, M. T., Seyedein, S. H. and Aboutalebi, M. R.: Influence of Specimen Geometry of Hot Torsion Test on Temperature Distribution During Reheating Treatment of API–X70. *Journal of Iron and Steel Research International*, vol. 17(3), pp. 34–39, 2010.

Mirzakhani, B., Salehi, M. T., Khoddam, S., Seyedein, S. H. and Aboutalebi, M. R.: Investigation of Dynamic and Static Recrystallisation Behaviour During Thermomechanical Processing in a API–X70 Microalloyed Steel. *Journal of Materials Engineering and Performance*, vol. 18(8), pp. 1029–1034, 2009.

Murtagian, G. R., John, D. H. and Ernst, H. A.: Dynamic crack propagation in steel line pipes. Part I: Experimental investigation. *Engineering Fracture Mechanics*, vol. 72, pp. 2519–2534, 2005.

Natividad, C., Salazar, M., Espinosa–Medina, M. A. and Pérez, R.: A comparative study of the SSC resistance of a novel welding process IEA with SAW and MIG. *Materials Characterization*, vol. 58, pp. 786–793, 2007.

Neville, A. and Wang, C.: Erosion–corrosion of engineering steels–Can it be managed by use of chemicals?. *Wear*, vol. 267, pp. 2018–2026, 2009.

Oh, C.–K., Kim, Y.–J., Back, J.–H. and Kim, W.–S.: Development of stress–modified fracture strain for ductile failure of API X65 steel. *Int. J. Fract.*, vol. 143, pp. 119–133, 2007.

Oh, C.–S., Kim, N.–H., Kim, Y.–J., Baek, J.–H., Kim, Y.–P. and Kim, W.–S.: A finite element ductile failure simulation method using stress–modified fracture strain model. *Engineering Fracture Mechanics*, vol. 78, pp. 124–137, 2011.

Park, G. T., Koh, S. U., Jung, H. G. and Kim, K., Y.: Effect of microstructure on the hydrogen trapping efficiency and hydrogen induced cracking of linepipe steel. *Corrosion Science*, vol. 50, pp. 1865–1871, 2008.

Pluvinage, G., Krasowsky, A. J. and Krassiko, V. W.: Dynamic fracture toughness at crack initiation, propagation and arrest for two pipe–line

steels. *Engineering Fracture Mechanics*, vol. 43(6), pp. 1063–1084, 1992.

Rabizadeh, T. and Allahkaram, S. R.: Corrosion resistance enhancement of Ni–P electroless coatings by incorporation of nano–SiO₂ particles. *Materials and Design*, vol. 32, pp. 133–138, 2011.

Rethmeier, M., Gook, S., Lammers, M. and Gumenyuk, A.: Laser–Hybrid Welding of Thick Plates up to 32 mm Using a 20 kW Fibre Laser. *Yosetsu Gakkai Ronbunshu/Quarterly Journal of the Japan Welding Society*, vol. 27(2), pp. 74s–79s, 2009.

Santos, T. F. A., Hermenegildo, T. F. C., Afonso, C. R. M., Marinho, R. R., Paes, M. T. P. and Ramirez, A. J.: Fracture toughness of ISO 3183 X80M (API 5L X80) steel friction stir welds. *Engineering Fracture Mechanics*, vol. 77, pp. 2937–2945, 2010.

Shimizu, M., Hiromatsu, M. and Kaji, H.: Mill Trial for Application of Accelerated Cooling Combined with Controlled Rolling to X70 Linepipe Steel Plates. *Transactions ISIJ*, vol. 26, pp. 790–797, 1986.

Shin, S. Y., Hong, S., Bae, J.–H., Kim, K. and Lee, S.: Separation Phenomenon Occurring during the Charpy Impact Test of API X80 Pipeline Steels. *Metallurgical and Materials Transactions A*, vol. 40A, pp. 2333–2349, 2009a.

Shin, S. Y., Hwang, B., Kim, S. and Lee, S.: Fracture toughness analysis in transition temperature region of API X70 pipeline steels. *Materials Science and Engineering A*, vol. 429, pp. 196–204, 2006.

Shin, S. Y., Hwang, B., Lee, S., Kim, N. J. and Ahn, S. S.: Correlation of microstructure and Charpy impact properties in API X70 and X80 line-pipe steels. *Materials Science and Engineering A*, vol. 458, pp. 281–289, 2007.

Shin, S. Y., Oh, K., Kang, K. B. and Lee, S.: Effects of Complex Oxides on Charpy Impact Properties of Heat Affected Zones of Two API X70 Linepipe Steels. *ISIJ International*, vol. 49(8), pp. 1191–1199, 2009b.

Sun, J. and Boyd, J. D.: Effect of thermomechanical processing on anisotropy cleavage fracture stress in microalloyed linepipe steel. *International Journal of Pressure Vessels and Piping*, vol. 77, pp. 369–377, 2000.

Takahashi, A. and Ogawa, H.: Influence of Microhardness and Inclusion on Stress oriented Hydrogen Induced Cracking of Line Pipe Steels. *ISIJ International*, vol. 36(3), pp. 334–340, 1996.

Tsay, L. W., Chen, T. C. and Chan, S. L. I.: Sulphide stress corrosion cracking and fatigue crack growth of welded TMCP API 5L X65 pipe-line steel. *International Journal of Fatigue*, vol. 23, pp. 103–113, 2001.

Villalba, E. and Atrens, A.: Hydrogen embrittlement and rock bold stress corrosion cracking. *Engineering Failure Analysis*, vol. 116, pp. 164–175, 2009.

- Vosikovsky, O. and Ravard, A.: Growth of surface fatigue cracks in a steel plate. *International Journal of Fatigue*, vol. 3(3), pp. 111–115, 1981.
- Yan, P., Güngör, Ö. E., Thibaux, P. and Bhadeshia, H. K. D. H.: Induction welding and heat treatment of steel pipes: evolution of crystallographic texture detrimental to toughness. *Science and Technology of Welding and Joining*, vol. 15(2), pp. 137–141, 2010.
- Zampronio, M. A., Fassini, F. D. and de Miranda, P. E. V.: Design of ion-implanted hydrogen contamination barrier layers for steel. *Surface and Coating Technology*, vol. 70, pp. 203–209, 1995.
- Zarebidaki, A. and Allahkaram, S.-R.: Effect of surfactant on the fabrication and characterization of Ni-P-CNT composite coatings. *Journal of Alloys and Compounds*, vol. 509, pp. 1836–1840, 2011.
- Zhang, G., Chen, C., Lu, M., Chai, C. and Wu, Y.: Evaluation of inhibition efficiency of an imidazoline derivative in CO₂-containing aqueous solution. *Materials Chemistry and Physics*, vol. 105, pp. 331–340, 2007.
- Zhang, G. A. and Cheng, Y. F.: Corrosion of X65 steel in CO₂-saturated oilfield formation water in the absence and presence of acetic acid. *Corrosion Science*, vol. 51, pp. 1589–1595, 2009a.
- Zhang, L., Li, X., Du, C. and Huang, Y.: Effect of applied potentials on stress corrosion cracking of X70 pipeline steel in alkali solution. *Materials and Design*, vol. 30, pp. 2259–2263, 2009b.

Appendix B. Fundamentals of Crystallography and Texture

This is the documentation for the fundamentals of crystallography and texture to help the understanding for the present study.

The properties of single crystal are anisotropic, which means that they vary with direction, because the crystalline state is characterized by a regular arrangement of atoms over large distances. Similarly, the properties of polycrystalline, non-randomly oriented aggregates of the many crystals of varying sizes and shapes, can be anisotropic. They are governed by not only the properties of the individual single crystals, but also the aggregate properties such as the size and shape distributions of the single crystals, and the orientation relationships among the individual crystals. Moreover, deformation strains and changes of texture, preferred orientation of the crystals, are related to the changes of the lengths and orientations of vectors in the aggregates during the mechanical works. Thus, crystallography can influence the deformation behaviour of polycrystalline aggregate.

B.1. Orientation of crystallites

In order to describe the orientation of crystallites in a polycrystalline sample, it is necessary to specify the crystal reference frame within that of the sample. Therefore, there will be two bases, one defined with respect to the crystal structure and a second to represent the sample.

B.1.1. Definition of a basis

Figure B.1a shows the face-centred cubic (FCC) unit cell, three vectors parallel to the unit cell edges and they form crystallographic basis as shown in Figure B.1b. The set of vectors \mathbf{a}_i ($i = 1, 2, 3$) are called the basis vectors and the basis itself can be identified by a basis symbol ‘A’. Any vector \mathbf{u} can be represented as a linear combination of the basis \mathbf{a}_i ($i = 1, 2, 3$) of the unit cell.

$$\mathbf{u} = u_1\mathbf{a}_1 + u_2\mathbf{a}_2 + u_3\mathbf{a}_3 \quad (\text{B-1})$$

where the scalar quantities u_1 , u_2 and u_3 are the components of the vector \mathbf{u} with respect to the basis vectors \mathbf{a}_1 , \mathbf{a}_2 and \mathbf{a}_3 .

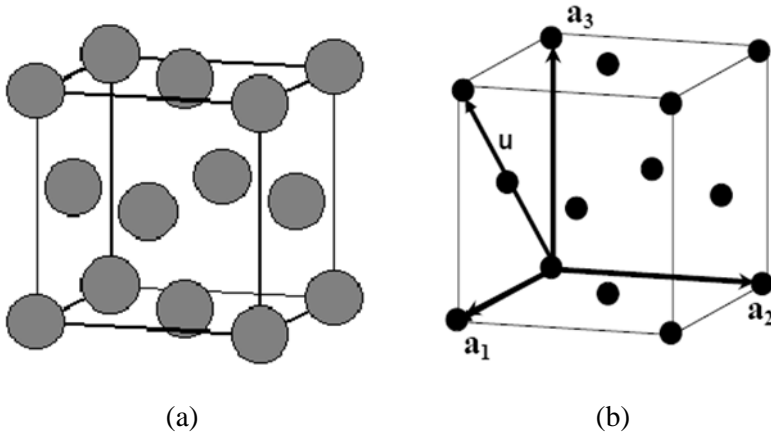


Figure B.1. (a) Conventional FCC unit cell, (b) Crystallographic basis of FCC.

These components of line vector can conveniently be written as a single-column matrix:

$$\begin{bmatrix} u_1 \\ u_2 \\ u_3 \end{bmatrix} \quad (\text{B-2})$$

However, this can also be written using square brackets for the convenience:

$$[u_1 \quad u_2 \quad u_3] \quad (\text{B-3})$$

The matrix representation of the vector \mathbf{u} with respect to the basis A is:

$$(\mathbf{u}; A) = (u_1 \quad u_2 \quad u_3) \quad (\text{B-4})$$

where \mathbf{u} is represented as a row vector. \mathbf{u} can be represented as a column vector alternatively:

$$[A; \mathbf{u}] = [u_1 \quad u_2 \quad u_3] \quad (\text{B-5})$$

For instance, in Fig. B.1b,

$$(\mathbf{u}; A) = (1 \ 0 \ 1) \quad (\text{B-6})$$

$$[A; \mathbf{u}] = [1 \ 0 \ 1] \quad (\text{B-7})$$

The row matrix $(\mathbf{u}; A)$ is the transpose of the column matrix $[A; \mathbf{u}]$, and vice versa.

The external shape of the specimen determines a specific coordinate system. Now,

in the case of rolled sheet steel, consider a sample reference frame with basis

symbol 'S' consisting of basis vector \mathbf{s}_1 // RD (rolling direction) // $[1 \ 0 \ 0]_{\mathbf{s}}$, \mathbf{s}_2 //

TD (transverse direction) // $[0 \ 1 \ 0]_{\mathbf{s}}$, and \mathbf{s}_3 // ND (normal direction) // $[0 \ 0 \ 1]_{\mathbf{s}}$.

The sample contains i grains of ferrite (α), each of which has a crystallographic

frame of ' X_i ', consisting of basis vector $[1 \ 0 \ 0]_{\alpha i}$, $[0 \ 1 \ 0]_{\alpha i}$ and $[0 \ 0 \ 1]_{\alpha i}$ as

shown in Fig. B.2.

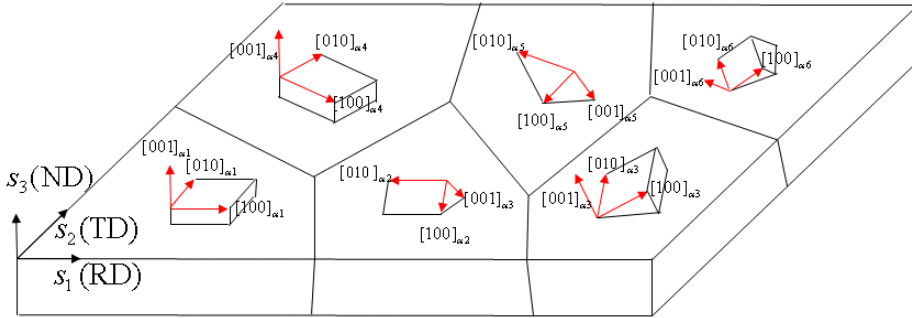


Figure B.2. Coordinate systems for polycrystalline sheet specimen and its crystallites.

B.1.2. Representation of rotation matrix

The components $[u_1 \ u_2 \ u_3]$ of any vector \mathbf{u} together with the basis vectors have its direction and magnitude. For an orthonormal basis, a new unit vector parallel to \mathbf{u} can be obtained by normalizing the vector as:

$$\left[\frac{u_1}{\sqrt{u_1^2 + u_2^2 + u_3^2}} \quad \frac{u_2}{\sqrt{u_1^2 + u_2^2 + u_3^2}} \quad \frac{u_3}{\sqrt{u_1^2 + u_2^2 + u_3^2}} \right] \quad (\text{B-8})$$

or

$$[\cos\alpha \ \cos\beta \ \cos\gamma] \quad (\text{B-9})$$

where α , β and γ are the angles between \mathbf{u} and \mathbf{a}_1 , \mathbf{a}_2 and \mathbf{a}_3 of basis A, which are the basis vectors, respectively and $\cos\alpha$, $\cos\beta$ and $\cos\gamma$ are called the direction cosines of \mathbf{u} . The basis vectors \mathbf{a}_i can be selected arbitrarily.

In the case of orthonormal bases, the orientation of a second basis 'B' can be

specified by the direction cosines of its three axes \mathbf{b}_1 , \mathbf{b}_2 and \mathbf{b}_3 in basis A, that is:

$$\begin{aligned}\mathbf{b}_1 &= \cos\alpha_1 \times \mathbf{a}_1 + \cos\beta_1 \times \mathbf{a}_2 + \cos\gamma_1 \times \mathbf{a}_3 \\ \mathbf{b}_2 &= \cos\alpha_2 \times \mathbf{a}_1 + \cos\beta_2 \times \mathbf{a}_2 + \cos\gamma_2 \times \mathbf{a}_3 \\ \mathbf{b}_3 &= \cos\alpha_3 \times \mathbf{a}_1 + \cos\beta_3 \times \mathbf{a}_2 + \cos\gamma_3 \times \mathbf{a}_3\end{aligned}\quad (\text{B-10})$$

where α_i , β_i and γ_i ($i = 1, 2, 3$) are the angles between basis axes \mathbf{a}_i and \mathbf{b}_1 , \mathbf{a}_i and \mathbf{b}_2 , \mathbf{a}_i and \mathbf{b}_3 , respectively.

The matrix relating this transform from basis A to basis B is denoted as a rotation matrix (A J B):

$$(\text{A J B}) = \begin{pmatrix} \cos\alpha_1 & \cos\alpha_2 & \cos\alpha_3 \\ \cos\beta_1 & \cos\beta_2 & \cos\beta_3 \\ \cos\gamma_1 & \cos\gamma_2 & \cos\gamma_3 \end{pmatrix}\quad (\text{B-11})$$

The transformation of components of any vector \mathbf{u} then follows the straightforward rule,

$$[\text{A}; \mathbf{u}] = (\text{A J B})[\text{B}; \mathbf{u}]\quad (\text{B-12})$$

or

$$[\text{B}; \mathbf{u}] = (\text{B J A})[\text{A}; \mathbf{u}]\quad (\text{B-13})$$

where (B J A) is the inverse of (A J B).

B.1.3. The reciprocal basis

If considering a lattice, represented by a basis symbol A and an arbitrary set of basis vectors \mathbf{a}_1 , \mathbf{a}_2 and \mathbf{a}_3 , then the corresponding reciprocal basis A^* has basis vectors \mathbf{a}_1^* , \mathbf{a}_2^* and \mathbf{a}_3^* , defined by the following equations:

$$\begin{aligned}
\mathbf{a}_1^* &= (\mathbf{a}_2 \wedge \mathbf{a}_3) / (\mathbf{a}_1 \cdot \mathbf{a}_2 \wedge \mathbf{a}_3) \\
\mathbf{a}_2^* &= (\mathbf{a}_3 \wedge \mathbf{a}_1) / (\mathbf{a}_1 \cdot \mathbf{a}_2 \wedge \mathbf{a}_3) \\
\mathbf{a}_3^* &= (\mathbf{a}_1 \wedge \mathbf{a}_2) / (\mathbf{a}_1 \cdot \mathbf{a}_2 \wedge \mathbf{a}_3)
\end{aligned}
\tag{B-14}$$

In the above first equation, the term $(\mathbf{a}_1 \cdot \mathbf{a}_2 \wedge \mathbf{a}_3)$ represents the volume of the unit cell formed by \mathbf{a}_i , while the magnitude of the vector $(\mathbf{a}_2 \wedge \mathbf{a}_3)$ represents the area of the $(1\ 0\ 0)_A$ plane. Since $(\mathbf{a}_2 \wedge \mathbf{a}_3)$ points along the normal to the $(1\ 0\ 0)_A$ plane, it follows that \mathbf{a}_1^* also points along the normal to $(1\ 0\ 0)_A$ and that its magnitude $|\mathbf{a}_1^*|$ is the reciprocal of the spacing of the $(1\ 0\ 0)_A$ planes. The components of any vector referred to the reciprocal basis represent the Miller indices of a plane whose normal is along that vector, with the spacing of the plane given by the inverse of the magnitude of that vector.

The scalar product between the components of any vector and the components of its reciprocal vector is:

$$\mathbf{a}_i \cdot \mathbf{a}_i^* = \delta_{ij} \tag{B-15}$$

where δ_{ij} is the Kronecker delta, which has a value of unity when $i = j$ and is zero when $i \neq j$.

B.1.4. Rotation axis–angle pairs

The rotation matrix (A J B) can also be represented by a pair of rotation axis \mathbf{u} and a right handed rotation angle θ . Supposing $\mathbf{u} = [u_1\ u_2\ u_3]$ in basis B, if \mathbf{u} happens to lie along the rotation axis relating bases A and B, then not only the

components of \mathbf{u} in both bases remain the same, but also their directions remain invariant to the rotation operation so that $[\mathbf{B}; \mathbf{u}] = [\mathbf{A}; \mathbf{u}]$. Substituting it into equation B–12, then:

$$[\mathbf{B}; \mathbf{u}] = (\mathbf{A} \mathbf{J} \mathbf{B})[\mathbf{B}; \mathbf{u}] \quad (\text{B-16})$$

that is,

$$\{(\mathbf{A} \mathbf{J} \mathbf{B}) - \mathbf{I}\}[\mathbf{B}; \mathbf{u}] = 0 \quad (\text{B-17})$$

where \mathbf{I} is a 3×3 identity matrix.

Equation B–15 always has non–zero solution as long as the matrix $(\mathbf{A} \mathbf{J} \mathbf{B})$ is not an identity matrix which represents a null rotation. Naturally, if the rotation axis and angle are known, then the rotation matrix can be derived as [Bunge, 1982]:

$$\begin{aligned} & (\mathbf{A} \mathbf{J} \mathbf{B}) \\ &= \begin{pmatrix} u_1 u_1 (1 - \cos \theta) + \cos \theta & u_1 u_2 (1 - \cos \theta) + u_3 n & u_1 u_3 (1 - \cos \theta) - u_2 n \\ u_1 u_2 (1 - \cos \theta) - u_3 n & u_2 u_2 (1 - \cos \theta) + \cos \theta & u_2 u_3 (1 - \cos \theta) + u_1 n \\ u_1 u_3 (1 - \cos \theta) + u_2 n & u_2 u_3 (1 - \cos \theta) - u_1 n & u_3 u_3 (1 - \cos \theta) + \cos \theta \end{pmatrix} \end{aligned} \quad (\text{B-18})$$

where u_1 , u_2 and u_3 are the components of a unit rotation axis and θ is the corresponding right–handed rotation angle. By this way only three independent values are needed to define the rotation matrix, *i.e.* any two components of the unit rotation axis and one rotation angle.

B.1.5. The metric

Consider any arbitrary crystal system, defined by a basis \mathbf{A} with basis vectors \mathbf{a}_i , and by the corresponding reciprocal basis \mathbf{A}^* with basis vectors \mathbf{a}_i^* . To find the angle between the direction \mathbf{u} and the plane normal \mathbf{h} , it would be useful to have a

matrix $(A^* G A)$, which allows the transformation of the components of a vector referred to the basis A , to those referred to its reciprocal basis A^* . Each column of $(A^* G A)$ thus consists of the components of one of the basis vectors of A , when referred to the basis A^* . For example,

$$\mathbf{a}_1 = G_{11}\mathbf{a}_1^* + G_{21}\mathbf{a}_2^* + G_{31}\mathbf{a}_3^* \quad (\text{B-19})$$

Taking successive scalar dot products with \mathbf{a}_1 , \mathbf{a}_2 and \mathbf{a}_3 respectively on both sides of equation B-19, then:

$$G_{11} = \mathbf{a}_1 \cdot \mathbf{a}_1, \quad G_{21} = \mathbf{a}_1 \cdot \mathbf{a}_2, \quad G_{31} = \mathbf{a}_1 \cdot \mathbf{a}_3 \quad (\text{B-20})$$

since $\mathbf{a}_i \cdot \mathbf{a}_j^* = 0$ when $i \neq j$. The rest of the elements of $(A^* G A)$ can be determined in a similar way, so that:

$$(A^* G A) = \begin{pmatrix} \mathbf{a}_1 \cdot \mathbf{a}_1 & \mathbf{a}_2 \cdot \mathbf{a}_1 & \mathbf{a}_3 \cdot \mathbf{a}_1 \\ \mathbf{a}_1 \cdot \mathbf{a}_2 & \mathbf{a}_2 \cdot \mathbf{a}_2 & \mathbf{a}_3 \cdot \mathbf{a}_2 \\ \mathbf{a}_1 \cdot \mathbf{a}_3 & \mathbf{a}_2 \cdot \mathbf{a}_3 & \mathbf{a}_3 \cdot \mathbf{a}_3 \end{pmatrix} \quad (\text{B-21})$$

This matrix is called the metric. The determinant of $(A^* G A)$ equals the square of the volume of the cell formed by the basis vectors of A .

B.2. Texture

Although less appreciated and understood, anisotropy also exists in crystalline materials. This anisotropy is a one of the major factors influencing macroscopic property. Just as in the use of rolled steel to build a structure, the knowledge of anisotropy of steel (crystalline material) is needed to optimize its performance. Related to the anisotropy, the texture which means that crystals or grains show some preferred orientation, need to be analysed.

B.2.1. Euler angles

“Euler angles” describe the rotation of two bases (coordinate systems which represent the crystal and specimen) with respect to each other and thereby can represent the crystal orientation. It has three rotation angles φ , θ and ψ as shown in Fig. B.3a.

Initially, the orientations of the two coordinate systems are parallel to each other. The first rotation (Fig. B.3b) by a right-handed angle φ about \mathbf{a}_3 axis gives a rotation matrix:

$$R_\varphi = \begin{pmatrix} \cos\varphi & -\sin\varphi & 0 \\ \sin\varphi & \cos\varphi & 0 \\ 0 & 0 & 1 \end{pmatrix} \quad (\text{B-22})$$

and then, the second rotation by θ about \mathbf{a}_1 gives (Fig. B.3c):

$$R_\theta = \begin{pmatrix} 1 & 0 & 0 \\ 0 & \cos\theta & -\sin\theta \\ 0 & \sin\theta & \cos\theta \end{pmatrix} \quad (\text{B-23})$$

finally, the third rotation by ψ about \mathbf{a}_3 gives (Fig. B.3d):

$$R_\psi = \begin{pmatrix} \cos\psi & -\sin\psi & 0 \\ \sin\psi & \cos\psi & 0 \\ 0 & 0 & 1 \end{pmatrix} \quad (\text{B-24})$$

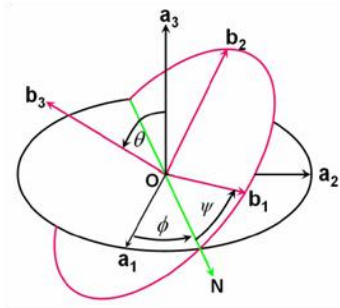
Thus, the multiplication of the above three matrices yields:

$$(A \mid B) = R_\psi \cdot R_\theta \cdot R_\varphi \quad (\text{B-25})$$

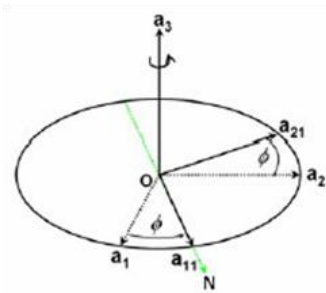
$$= \begin{pmatrix} \cos\psi\cos\varphi - \cos\theta\sin\varphi\sin\psi & \cos\psi\sin\varphi + \cos\theta\cos\varphi\sin\psi & \sin\psi\sin\theta \\ -\sin\psi\cos\varphi - \cos\theta\sin\varphi\cos\psi & -\sin\psi\sin\varphi + \cos\theta\cos\varphi\cos\psi & \cos\psi\sin\theta \\ \sin\theta\sin\varphi & -\sin\theta\cos\varphi & \cos\theta \end{pmatrix} \quad (\text{B-26})$$

Therefore, any orthonormal rotation matrix is given as:

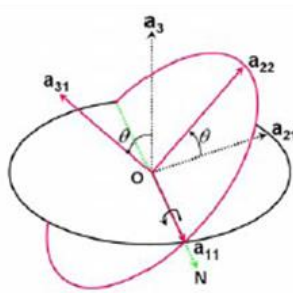
$$(A \mid B) = \begin{pmatrix} J_{11} & J_{12} & J_{13} \\ J_{21} & J_{22} & J_{23} \\ J_{31} & J_{32} & J_{33} \end{pmatrix} \quad (\text{B-27})$$



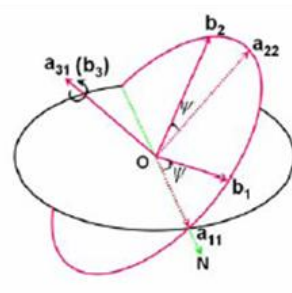
(a)



(b)



(c)



(d)

Figure B.3. The process of Euler angles (a) complete rotation, (b) first rotation, (c) second rotation and (d) third rotation.

And the corresponding “Euler angles” are:

$$\begin{aligned}
 \varphi &= \arctan(J_{31}/J_{32}) \\
 \theta &= \arccos(J_{33}) \\
 \psi &= -\arctan(J_{13}/J_{23})
 \end{aligned}
 \tag{B-28}$$

B.2.2. Other representations

Miller indices

Crystal orientations are often specified by the Miller indices of the crystal plane (hkl) which is parallel to the plane of the sheet, as well as the indices of the crystal

direction $[uvw]$ parallel to the rolling direction:

$$g = (hkl)[uvw] \quad (\text{B-29})$$

Pole figures

The pole figure is a representation of the orientation in which the poles of a specific crystal direction $[hkl]$ is specified with respect to the polycrystalline specimen coordinates in stereographic projection. It can show two dimensional graphical representation of the distribution of crystal orientations. Fig. B.4 shows the process of the stereographic projection of the $\{100\}$ planes.

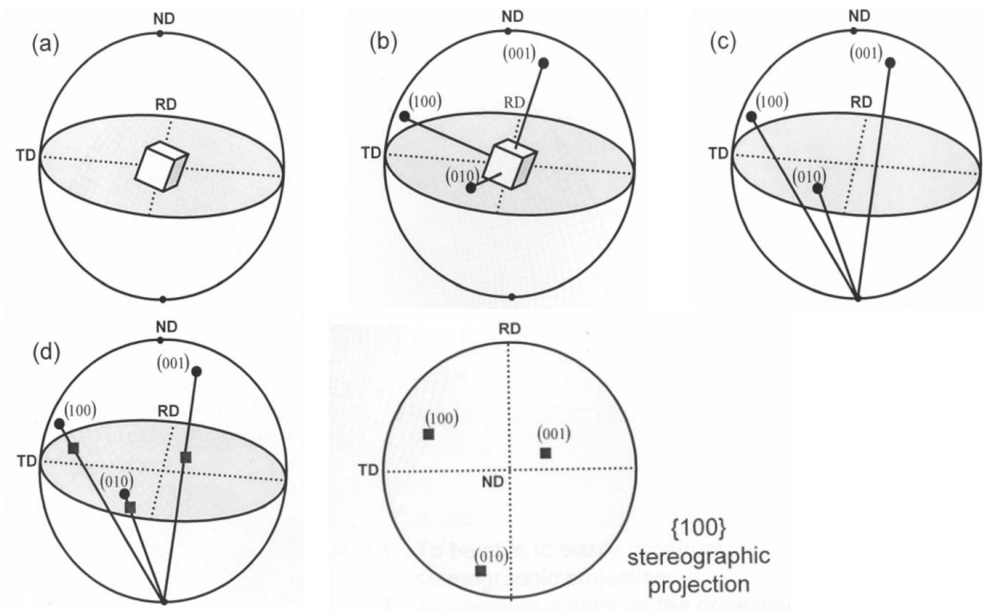


Figure B.4. Pole figure of $\{100\}$ plane

Inverse pole figures

Similar to the pole figures, the orientation can be described by specifying the poles of the specimen coordinate system with respect to those of the crystal coordinate system in stereographic projection.

B.2.3. Orientation distribution function (ODF)

Any crystal can be described using three independent Euler angles $(\varphi \theta \psi)$ with respect to sample basis A. In materials science, as a convention, these angles are generally written as $(\varphi_1 \Phi \varphi_2)$. The set of the orientation of each grain is gathered and makes “Euler space”. Fig. B.5 shows the orientation of 500 textured grains in Euler space.

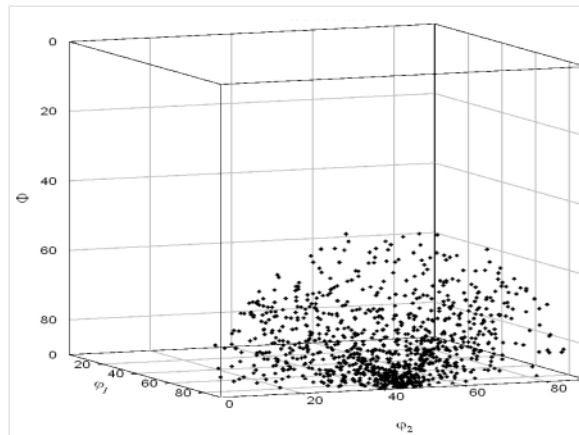


Figure B.5. Euler space of a textured material. Each dot represents the orientation of grain relative to a reference frame.

However, three-dimensional graphs are not always easy to interpret, so intersections of Euler space are frequently plotted. In this method, the Euler space is divided into “slices” at $\varphi_2 = 5^\circ$ intervals. Then these slices are arranged in a grid, putting all the dots in the interval to the nearest slice, and this is called an orientation distribution function as shown in Figure B.6.

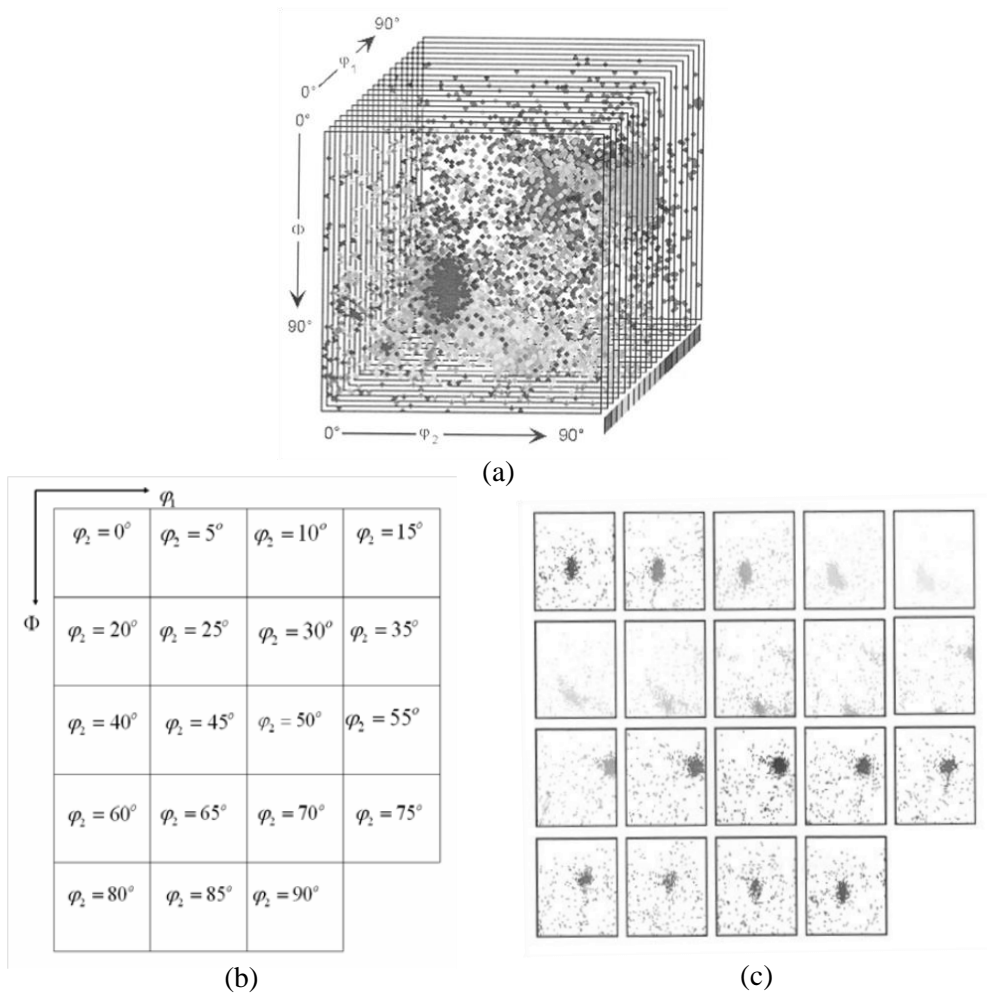


Figure B.6. (a) Euler space as a example, (b) orientation distribution function with $\varphi_2 = 5^\circ$ (c) all sections of (a) with varying φ_2 .

B.3. Summary

Crystalline is anisotropic by nature because it has periodically regularity in the structure; different direction can make different properties. The crystallographic texture, preferred orientation of polycrystalline grains, can be a clue for the anisotropy.

References

Bhadeshia, H. K. D. H.: *Worked examples in the Geometry of Crystals*. 2nd ed., The Institute of Metals, London, 2001.

Bunge, H. J.: *Texture Analysis in Materials Science*. Butterworths–Heinemann, London, 1982.

Lee, D. N.: *TEXTURE AND RELATED PHENOMENA*. The Korean Institute of Metals and Materials, 2006.

Appendix C. RANDOM_ORIENTATION

This is the documentation for the computer program to investigate the number of grains having specific orientation, as used in chapter 5. The result is the hypothetical fraction of the grains. This program is only for cubic crystal system.

Program MAP_STEEL_RANDOM_ORIENTATION

1. Provenance of code.
2. Purpose of code.
3. Specification.
4. Description.
5. References.
6. Parameter descriptions.
7. Error indicators.
8. Accuracy estimate.
9. Any additional information.
10. Example.
11. Auxiliary subroutines required.
12. Keywords.
13. Sources.

1. Provenance of source code.

Min Sung Joo

Graduate Institute of Ferrous Technology (GIFT)

Pohang University of Science and Technology

Pohang, Kyungbuk, Republic of Korea

athpimo@postech.ac.kr

2. Purpose of code.

Consider a polycrystalline material containing a random distribution of 10,000 grains, each with a cubic lattice. This program permits the calculation of the fraction of grains which have a specific orientation relative to an external frame of reference.

3. Specification.

Language: C

Product form: Source code for UNIX/Linux machines.

Complete program.

4. Description.

The computer program to investigate the number of grains having specific orientation. The result is the hypothetical fraction of the grains. This program is

only for crystals with a cubic lattice.

Only ‘*random_orientation.c*’ file exists.

- C program used to get the fraction of grains having specific orientation among 10,000 randomly generated grains.

5. References.

Bhadeshia, H. K. D. H.: *Worked examples in the Geometry of Crystals*. 2nd ed., The Institute of Metals, London, 2001.

Mackenzie, J. K.: Second Paper on the Statistics Associated with the Random Disorientation of Cubes. *Biometrika*, vol. 45, p. 229, 1958.

Lee, D. N.: *TEXTURE AND RELATED PHENOMENA*. The Korean Institute of Metals and Materials, 2006.

6. Parameter descriptions.

Input parameters

After executing the program, the user needs to input four numbers.

pi1	pi1 value for the specific orientation.
cp1	cp1 value for the specific orientation.
pi2	pi2 value for the specific orientation.
tolerance angle	tolerance angle for the specific orientation.

The following definition in the source code can be changed if user needs to control the number of grains in the simulation.

#define NUM_CRYSTAL	the number of randomly generated grains.
---------------------	------------------------------------------

(Optional)

When executing the program, if user inputs any character followed the program then the user can get the 'random.out' file which has counts for each disorientations in the range of $0^\circ \sim 360^\circ$ from randomly generated grains. Therefore, the user can check the randomness of the grains and make a graph so called the Mackenzie plot. For example,

Executable any_charater_or_parameter

Output parameters

The user can see the results from the screen.

Total number of grains

Simply prints out the total number of grains in the simulation.

Total number of grains within misorientation

Print the number of grains having specific orientation within used tolerance angle.

Fraction

The fraction of grains having specific orientation.

(Optional)

random.out

The output file which contains the counts for each disorientations in the range of 0° ~ 360° from randomly generated grains.

7. Error indicators.

If the user has input the wrong value for pi1, cpi, pi2 and tolerance angle, then the program will exit.

8. Accuracy estimate.

None.

9. Any additional information.

None.

10. Example.

1. Program text

Executable

2. Program data

pi1: 0

cpi: 0

pi2: 15

tolerance angle: 11.25

3. Program results

(Case 1)

\$ executable

WELCOME!

Please input the Euler angles to investigate.

pi1: 0

The input value was: 0.000000

cpi: 0

The input value was: 0.000000

pi2: 15

The input value was: 15.000000

Please input the tolerance angle for the Euler angles.

Tolerance angle: 11.25

The input value was: 11.250000

Total number of grains : 10000

Total number of grains within misorientation : 269

Fraction : 0.026900

(Case 2)

\$ executable disorientation

WELCOME!

Please input the Euler angles to investigate.

pi1: 0

The input value was: 0.000000

phi: 0

The input value was: 0.000000

pi2: 15

The input value was: 15.000000

Please input the tolerance angle for the Euler angles.

Tolerance angle: 11.25

The input value was: 11.250000

Total number of grains : 10000

Total number of grains within misorientation : 269

Fraction : 0.026900

random.out file was generated.

11. Auxiliary subroutines required.

None.

12. Keywords.

Mackenzie plot, Disorientation, Misorientation

13. Sources.

random_orientation.c

```
#include <stdio.h>
#include <stdlib.h>
#include <string.h>
#include <math.h>

#define PI 3.141592654
#define TORADIAN 0.017453
#define TOANGLE 57.29579

#ifndef NUM_CRYSTAL
#define NUM_CRYSTAL 10000
#endif

/* Crystal coordinate */
typedef struct _crystal_coordinate {
    /* for miller indices */
    double x1[3];
    double x2[3];
    double x3[3];

    /* for Euler angles */
    double pi1;
    double cpi;
    double pi2;
} c_coordinate;

void make_euler_crystal_coor(c_coordinate *crystal_coor){
    double pi1 = 0, cpi = 0, pi2 = 0;
    double h = 0, k = 0, l = 0;
    double u = 0, v = 0, w = 0;
    double a = 0, b = 0, c = 0;

    /* Get x2 components of Miller index */
    a = crystal_coor->x3[0];
    b = crystal_coor->x3[1];
    c = crystal_coor->x3[2];

    h = a / sqrt (a*a + b*b + c*c);
    k = b / sqrt (a*a + b*b + c*c);
    l = c / sqrt (a*a + b*b + c*c);

    a = crystal_coor->x1[0];
    b = crystal_coor->x1[1];
    c = crystal_coor->x1[2];
    v = b / sqrt (a*a + b*b + c*c);
    w = c / sqrt (a*a + b*b + c*c);

    crystal_coor->x2[0] = l*v - k*w;
    crystal_coor->x2[1] = 0 - (l*u - h*w);
    crystal_coor->x2[2] = k*u - h*v;

    /* Get Euler angles */
    if (l == 1) {
        pi1 = atan(0 - v/u) * TOANGLE;
        cpi = 0;
        pi2 = 0;
    } else if (l == -1) {
        pi1 = atan(v/u) * TOANGLE;
        cpi = 180.0;
        pi2 = 0;
    } else {
        pi1
        asin((w/sqrt((u*u+v*v+w*w))*sqrt((h*h+k*k+l*l)/(h*h+k*k)))
        TOANGLE;
        cpi = acos(l/sqrt(h*h+k*k+l*l)) * TOANGLE;
        pi2 = asin(h/sqrt(h*h+k*k)) * TOANGLE;
    }

    crystal_coor->pi1 = pi1;
    crystal_coor->cpi = cpi;
    crystal_coor->pi2 = pi2;
    return;
}

void make_miller_crystal_coor(c_coordinate *crystal_coor) {
    double pi1 = 0, cpi = 0, pi2 = 0;

    double t1 = 0, t2 = 0, t3 = 0;
    int it1 = 0, it2 = 0, it3 = 0, it4 = 0;

    pi1 = crystal_coor->pi1 * TORADIAN;
    cpi = crystal_coor->cpi * TORADIAN;
    pi2 = crystal_coor->pi2 * TORADIAN;

    /* for [100] */
    t1 = cos(pi1) * cos(pi2) - sin(pi1) * sin(pi2) * cos(cpi);
    t2 = 0 - cos(pi1) * sin(pi2) - sin(pi1) * cos(pi2) * cos(cpi);
    t3 = sin(pi1) * sin(cpi);

    crystal_coor->x1[0] = t1;
    crystal_coor->x1[1] = t2;
    crystal_coor->x1[2] = t3;

    /* for [010] */
    t1 = sin(pi1) * cos(pi2) + cos(pi1) * sin(pi2) * cos(cpi);
    t2 = 0 - sin(pi1) * sin(pi2) + cos(pi1) * cos(pi2) * cos(cpi);
    t3 = 0 - cos(pi1) * sin(cpi);

    crystal_coor->x2[0] = t1;
    crystal_coor->x2[1] = t2;
    crystal_coor->x2[2] = t3;

    /* for [001] */
    t1 = sin(pi2) * sin(cpi);
    t2 = cos(pi2) * sin(cpi);
    t3 = cos(cpi);

    crystal_coor->x3[0] = t1;
    crystal_coor->x3[1] = t2;
    crystal_coor->x3[2] = t3;

    return;
}

void get_nth_symmetry(c_coordinate *sym_crystal, c_coordinate
crystal_coor, int nth) {
    double c[3][3] = {'\0'};

    if (nth == 0) {
        c[0][0] = 1.0, c[0][1] = 0.0, c[0][2] = 0.0;
        c[1][0] = 0.0, c[1][1] = 1.0, c[1][2] = 0.0;
        c[2][0] = 0.0, c[2][1] = 0.0, c[2][2] = 1.0;
    }
}
```

```

} else if (nth == 1) {
    c[0][0] = 0.0, c[0][1] = 0.0, c[0][2] = -1.0;
    c[1][0] = 0.0, c[1][1] = -1.0, c[1][2] = 0.0;
    c[2][0] = -1.0, c[2][1] = 0.0, c[2][2] = 0.0;
} else if (nth == 2) {
    c[0][0] = 0.0, c[0][1] = 0.0, c[0][2] = -1.0;
    c[1][0] = 0.0, c[1][1] = 1.0, c[1][2] = 0.0;
    c[2][0] = 1.0, c[2][1] = 0.0, c[2][2] = 0.0;
} else if (nth == 3) {
    c[0][0] = -1.0, c[0][1] = 0.0, c[0][2] = 0.0;
    c[1][0] = 0.0, c[1][1] = 1.0, c[1][2] = 0.0;
    c[2][0] = 0.0, c[2][1] = 0.0, c[2][2] = -1.0;
} else if (nth == 4) {
    c[0][0] = 0.0, c[0][1] = 0.0, c[0][2] = 1.0;
    c[1][0] = 0.0, c[1][1] = 1.0, c[1][2] = 0.0;
    c[2][0] = -1.0, c[2][1] = 0.0, c[2][2] = 0.0;
} else if (nth == 5) {
    c[0][0] = 1.0, c[0][1] = 0.0, c[0][2] = 0.0;
    c[1][0] = 0.0, c[1][1] = 0.0, c[1][2] = -1.0;
    c[2][0] = 0.0, c[2][1] = 1.0, c[2][2] = 0.0;
} else if (nth == 6) {
    c[0][0] = 1.0, c[0][1] = 0.0, c[0][2] = 0.0;
    c[1][0] = 0.0, c[1][1] = -1.0, c[1][2] = 0.0;
    c[2][0] = 0.0, c[2][1] = 0.0, c[2][2] = -1.0;
} else if (nth == 7) {
    c[0][0] = 1.0, c[0][1] = 0.0, c[0][2] = 0.0;
    c[1][0] = 0.0, c[1][1] = 0.0, c[1][2] = 1.0;
    c[2][0] = 0.0, c[2][1] = -1.0, c[2][2] = 0.0;
} else if (nth == 8) {
    c[0][0] = 0.0, c[0][1] = -1.0, c[0][2] = 0.0;
    c[1][0] = 1.0, c[1][1] = 0.0, c[1][2] = 0.0;
    c[2][0] = 0.0, c[2][1] = 0.0, c[2][2] = 1.0;
} else if (nth == 9) {
    c[0][0] = -1.0, c[0][1] = 0.0, c[0][2] = 0.0;
    c[1][0] = 0.0, c[1][1] = -1.0, c[1][2] = 0.0;
    c[2][0] = 0.0, c[2][1] = 0.0, c[2][2] = 1.0;
} else if (nth == 10) {
    c[0][0] = 0.0, c[0][1] = 1.0, c[0][2] = 0.0;
    c[1][0] = -1.0, c[1][1] = 0.0, c[1][2] = 0.0;
    c[2][0] = 0.0, c[2][1] = 0.0, c[2][2] = 1.0;
} else if (nth == 11) {
    c[0][0] = 0.0, c[0][1] = 0.0, c[0][2] = 1.0;
    c[1][0] = 1.0, c[1][1] = 0.0, c[1][2] = 0.0;
    c[2][0] = 0.0, c[2][1] = 1.0, c[2][2] = 0.0;
} else if (nth == 12) {
    c[0][0] = 0.0, c[0][1] = 1.0, c[0][2] = 0.0;
    c[1][0] = 0.0, c[1][1] = 0.0, c[1][2] = 1.0;
    c[2][0] = 1.0, c[2][1] = 0.0, c[2][2] = 0.0;
} else if (nth == 13) {
    c[0][0] = 0.0, c[0][1] = 0.0, c[0][2] = -1.0;
    c[1][0] = -1.0, c[1][1] = 0.0, c[1][2] = 0.0;
    c[2][0] = 0.0, c[2][1] = 1.0, c[2][2] = 0.0;
} else if (nth == 14) {
    c[0][0] = 0.0, c[0][1] = -1.0, c[0][2] = 0.0;
    c[1][0] = 0.0, c[1][1] = 0.0, c[1][2] = 1.0;
    c[2][0] = -1.0, c[2][1] = 0.0, c[2][2] = 0.0;
} else if (nth == 15) {
    c[0][0] = 0.0, c[0][1] = 1.0, c[0][2] = 0.0;
    c[1][0] = 0.0, c[1][1] = 0.0, c[1][2] = -1.0;
    c[2][0] = -1.0, c[2][1] = 0.0, c[2][2] = 0.0;
} else if (nth == 16) {
    c[0][0] = 0.0, c[0][1] = 0.0, c[0][2] = -1.0;
    c[1][0] = 1.0, c[1][1] = 0.0, c[1][2] = 0.0;
    c[2][0] = 0.0, c[2][1] = -1.0, c[2][2] = 0.0;
} else if (nth == 17) {
    c[0][0] = 0.0, c[0][1] = 0.0, c[0][2] = 1.0;
    c[1][0] = -1.0, c[1][1] = 0.0, c[1][2] = 0.0;
    c[2][0] = 0.0, c[2][1] = -1.0, c[2][2] = 0.0;
} else if (nth == 18) {
    c[0][0] = 0.0, c[0][1] = -1.0, c[0][2] = 0.0;
    c[1][0] = 0.0, c[1][1] = 0.0, c[1][2] = -1.0;
    c[2][0] = 1.0, c[2][1] = 0.0, c[2][2] = 0.0;
} else if (nth == 19) {
    c[0][0] = 0.0, c[0][1] = 1.0, c[0][2] = 0.0;
    c[1][0] = 1.0, c[1][1] = 0.0, c[1][2] = 0.0;
    c[2][0] = 0.0, c[2][1] = 0.0, c[2][2] = -1.0;
} else if (nth == 20) {
    c[0][0] = -1.0, c[0][1] = 0.0, c[0][2] = 0.0;
    c[1][0] = 0.0, c[1][1] = 0.0, c[1][2] = 1.0;
    c[2][0] = 0.0, c[2][1] = 1.0, c[2][2] = 0.0;
} else if (nth == 21) {
    c[0][0] = 0.0, c[0][1] = 0.0, c[0][2] = 1.0;
    c[1][0] = 0.0, c[1][1] = -1.0, c[1][2] = 0.0;
    c[2][0] = 1.0, c[2][1] = 0.0, c[2][2] = 0.0;
} else if (nth == 22) {
    c[0][0] = 0.0, c[0][1] = -1.0, c[0][2] = 0.0;
    c[1][0] = -1.0, c[1][1] = 0.0, c[1][2] = 0.0;
    c[2][0] = 0.0, c[2][1] = 0.0, c[2][2] = -1.0;
} else if (nth == 23) {
    c[0][0] = -1.0, c[0][1] = 0.0, c[0][2] = 0.0;
    c[1][0] = 0.0, c[1][1] = 0.0, c[1][2] = -1.0;
    c[2][0] = 0.0, c[2][1] = -1.0, c[2][2] = 0.0;
} else {
    c[0][0] = 1.0, c[0][1] = 0.0, c[0][2] = 0.0;
    c[1][0] = 0.0, c[1][1] = 1.0, c[1][2] = 0.0;
    c[2][0] = 0.0, c[2][1] = 0.0, c[2][2] = 1.0;
}

sym_crystal->x1[0] = c[0][0] * crystal_coor.x1[0]
    + c[0][1] * crystal_coor.x1[1]
    + c[0][2] * crystal_coor.x1[2];

sym_crystal->x1[1] = c[1][0] * crystal_coor.x1[0]
    + c[1][1] * crystal_coor.x1[1]
    + c[1][2] * crystal_coor.x1[2];

sym_crystal->x1[2] = c[2][0] * crystal_coor.x1[0]
    + c[2][1] * crystal_coor.x1[1]
    + c[2][2] * crystal_coor.x1[2];

sym_crystal->x2[0] = c[0][0] * crystal_coor.x2[0]
    + c[0][1] * crystal_coor.x2[1]
    + c[0][2] * crystal_coor.x2[2];

sym_crystal->x2[1] = c[1][0] * crystal_coor.x2[0]
    + c[1][1] * crystal_coor.x2[1]
    + c[1][2] * crystal_coor.x2[2];

sym_crystal->x2[2] = c[2][0] * crystal_coor.x2[0]
    + c[2][1] * crystal_coor.x2[1]
    + c[2][2] * crystal_coor.x2[2];

sym_crystal->x3[0] = c[0][0] * crystal_coor.x3[0]
    + c[0][1] * crystal_coor.x3[1]
    + c[0][2] * crystal_coor.x3[2];

sym_crystal->x3[1] = c[1][0] * crystal_coor.x3[0]
    + c[1][1] * crystal_coor.x3[1]
    + c[1][2] * crystal_coor.x3[2];

sym_crystal->x3[2] = c[2][0] * crystal_coor.x3[0]
    + c[2][1] * crystal_coor.x3[1]
    + c[2][2] * crystal_coor.x3[2];

make_euler_crystal_coor(sym_crystal);
return;
}

double get_misorientation(c_coordinate A, c_coordinate B) {
    double a, b, c, d, e, f, g, h, i;
    c_coordinate result, B_inv;
    double determinant = 0.0;
    double ret = 0.0, u1 = 0.0, u2 = 0.0, u3 = 0.0;

    a = B.x1[0], b = B.x2[0], c = B.x3[0];
    d = B.x1[1], e = B.x2[1], f = B.x3[1];
    g = B.x1[2], h = B.x2[2], i = B.x3[2];

    determinant = a*e*i + b*f*g + c*d*h - c*e*g - b*d*i - a*f*h;

    if (determinant == 0) return 360;

#ifdef __U_DEBUG__
    printf("Determinant: %f\n", determinant);
#endif
}

```

```

B_inv.x1[0] = (1.0/determinant) * (e*i - f*h);
B_inv.x1[1] = (1.0/determinant) * (f*g - d*i);
B_inv.x1[2] = (1.0/determinant) * (d*h - e*g);
B_inv.x2[0] = (1.0/determinant) * (c*h - b*i);
B_inv.x2[1] = (1.0/determinant) * (a*i - c*g);
B_inv.x2[2] = (1.0/determinant) * (b*g - a*h);
B_inv.x3[0] = (1.0/determinant) * (b*f - c*e);
B_inv.x3[1] = (1.0/determinant) * (c*d - a*f);
B_inv.x3[2] = (1.0/determinant) * (a*e - b*d);

result.x1[0] = A.x1[0]*B_inv.x1[0] + A.x2[0]*B_inv.x1[1] +
A.x3[0]*B_inv.x1[2];
result.x1[1] = A.x1[1]*B_inv.x1[0] + A.x2[1]*B_inv.x1[1] +
A.x3[1]*B_inv.x1[2];
result.x1[2] = A.x1[2]*B_inv.x1[0] + A.x2[2]*B_inv.x1[1] +
A.x3[2]*B_inv.x1[2];

result.x2[0] = A.x1[0]*B_inv.x2[0] + A.x2[0]*B_inv.x2[1] +
A.x3[0]*B_inv.x2[2];
result.x2[1] = A.x1[1]*B_inv.x2[0] + A.x2[1]*B_inv.x2[1] +
A.x3[1]*B_inv.x2[2];
result.x2[2] = A.x1[2]*B_inv.x2[0] + A.x2[2]*B_inv.x2[1] +
A.x3[2]*B_inv.x2[2];

result.x3[0] = A.x1[0]*B_inv.x3[0] + A.x2[0]*B_inv.x3[1] +
A.x3[0]*B_inv.x3[2];
result.x3[1] = A.x1[1]*B_inv.x3[0] + A.x2[1]*B_inv.x3[1] +
A.x3[1]*B_inv.x3[2];
result.x3[2] = A.x1[2]*B_inv.x3[0] + A.x2[2]*B_inv.x3[1] +
A.x3[2]*B_inv.x3[2];

ret = acos((result.x1[0] + result.x2[1] + result.x3[2] - 1.0) /
2.0) * TOANGLE;

u1 = (result.x3[1] - result.x2[2]);
u2 = (result.x1[2] - result.x3[0]);
u3 = (result.x2[0] - result.x1[1]);

#ifdef __U_DEBUG__
printf("Product matrix\n");
printf("x1 : %f %f %f\n",
result.x1[0],
result.x1[1],
result.x1[2]);
printf("x2 : %f %f %f\n",
result.x2[0],
result.x2[1],
result.x2[2]);
printf("x3 : %f %f %f\n",
result.x3[0],
result.x3[1],
result.x3[2]);
#endif

#ifdef __U_DEBUG__
printf("Miss orientation: %f\n", ret);
printf("Axis %f, %f %f\n", u1, u2, u3);
#endif

/* TEST the axis is on FZ */
if (u1 >= 0 && u2 >= 0 && u3 >= 0) {
return ret;
}
return 360;
}

int main (int argc, char ** argv) {
int i = 0, j = 0, k = 0;
int nRet = 0;
float tempf = 0;

c_coordinate crystal_coor[NUM_CRYSTAL] = {'\0'};
c_coordinate target_coor;
double tolerance_angle = 0;

c_coordinate sym_crystal, sym_target_crystal;
double temp_misorientation = 0, misorientation = 0;

int count = 0;

FILE * fp = NULL;
int l = 0, plot[360] = {'\0'};

/* Now, Make the grains */
/* give the random orientations using Euler angles {0-359,
0-359, 0-359} */
/* 1. get the 3 random integers (angles) (0-359) for each grains
*/
/* 2. Euler angles -> miller indices */

system("clear");
printf("WELCOME!\n");

#ifdef __U_DEBUG__
printf("Randomly generated crystals (Euler angles)\n");
#endif

/* 1. get the 3 angles for each grains */
srand(time(0));
for(i = 0; i < NUM_CRYSTAL; i++) {

#if 1
crystal_coor[i].pi1 = (rand() % 36000)/100.0;
crystal_coor[i].cpi = (rand() % 36000)/100.0;
crystal_coor[i].pi2 = (rand() % 36000)/100.0;

#elif 0
crystal_coor[i].pi1 = 100.0;
crystal_coor[i].cpi = 35.2599983;
crystal_coor[i].pi2 = 45.0;

#else
#endif
#ifdef __U_DEBUG__
printf("Crystal # : %d\n", i+1);
printf("Euler angles : %f %f %f\n",
crystal_coor[i].pi1,
crystal_coor[i].cpi,
crystal_coor[i].pi2);
#endif

}

/* 2. Euler angles -> miller indices */
/* matrix for Euler rotations
[
[ cos(pi1)cos(pi2) - sin(pi1)sin(pi2)cos(cpi)
sin(pi1)cos(pi2) + cos(pi1)sin(pi2)cos(cpi)
sin(pi2)sin(cpi) ]
[
[ -cos(pi1)sin(pi2) - sin(pi1)cos(pi2)cos(cpi) -
sin(pi1)sin(pi2) + cos(pi1)cos(pi2)cos(cpi) cos(pi2)sin(cpi) ]
[
[ -cos(pi1)sin(cpi)
cos(cpi) ]
]
]
*/

#ifdef __U_DEBUG__
printf("Randomly generated crystals (Miller indices)\n");
#endif

for(i = 0; i < NUM_CRYSTAL; i++) {
make_miller_crystal_coor(&crystal_coor[i]);

#ifdef __U_DEBUG__
printf("Crystal # : %d\n", i+1);
printf("x1 : %f %f %f\n",
crystal_coor[i].x1[0],
crystal_coor[i].x1[1],
crystal_coor[i].x1[2]);
printf("x2 : %f %f %f\n",
crystal_coor[i].x2[0],
crystal_coor[i].x2[1],
crystal_coor[i].x2[2]);

printf("x3 : %f %f %f\n",
crystal_coor[i].x3[0],
crystal_coor[i].x3[1],
crystal_coor[i].x3[2]);
#endif

}

/* find the grains which have {100}<001> texture components
*/
/* The the degree of tolerance is 11.25 */
printf("Please input the Euler angles to investigate.\n");

```

<pre> printf("pi1: "); if(scanf("%f", &tempf)) { printf("The input value was: %f\n", tempf); target_coor.pi1 = tempf; } else { fprintf(stderr, "Error reading the value from user\n"); goto err; } printf("cpi: "); if(scanf("%f", &tempf)) { printf("The input value was: %f\n", tempf); target_coor.cpi = tempf; } else { fprintf(stderr, "Error reading the value from user\n"); goto err; } printf("pi2: "); if(scanf("%f", &tempf)) { printf("The input value was: %f\n", tempf); target_coor.pi2 = tempf; } else { fprintf(stderr, "Error reading the value from user\n"); goto err; } printf("Please input the tolerance angle for the Euler angles.\n"); printf("Tolerance angle: "); if(scanf("%f", &tempf)) { printf("The input value was: %f\n", tempf); tolerance_angle = tempf; } else { fprintf(stderr, "Error reading the value from user\n"); goto err; } make_miller_crystal_coor(&target_coor); #ifdef __U_DEBUG__ printf("Target Crystal, tolerance_angle : %f\n", tolerance_angle); printf("x1 : % .6f % .6f % .6f\n", target_coor.x1[0], target_coor.x1[1], target_coor.x1[2]); printf("x2 : % .6f % .6f % .6f\n", target_coor.x2[0], target_coor.x2[1], target_coor.x2[2]); printf("x3 : % .6f % .6f % .6f\n", target_coor.x3[0], target_coor.x3[1], target_coor.x3[2]); printf("pi1, cpi, pi2: % .6f % .6f % .6f\n", target_coor.pi1, target_coor.cpi, target_coor.pi2); #endif if (argc == 1) { i = j = k = count = 0; for(i=0; i < NUM_CRYSTAL; i++) { misorientation = 360; /* Maximum misorientation */ for(j=0; j < 24; j++) { /* get nth symmetry for crystal */ get_nth_symmetry(&sym_crystal, crystal_coor[i], j); /* get nth symmetry for target */ for(k=0; k < 24; k++) { get_nth_symmetry(&sym_target_crystal, target_coor, k); temp_misorientation = get_misorientation(sym_target_crystal, sym_crystal); #ifdef __U_DEBUG__ printf("!!!! %dth crystal - %dth symmetry with %dthe target symmetry!!!!\n", i, j, k); printf("misorientation : %f, min : %f\n", temp_misorientation, misorientation); #endif } } } } err: return -1; </pre>	<pre> if(temp_misorientation <= misorientation) misorientation = temp_misorientation; memset(&sym_target_crystal, 0x00, sizeof(c_coordinate)); } memset(&sym_crystal, 0x00, sizeof(c_coordinate)); } if (misorientation <= tolerance_angle) count++; } printf("Total number of grains : %d\n", NUM_CRYSTAL); printf("Total number of grains within misorientation : %d\n", count); printf("Fraction : %f\n", (double)count/(double)NUM_CRYSTAL); } else { /* Mackenzie plot */ i = j = k = count = 0; for(i=0; i < NUM_CRYSTAL; i++) { for (l=+1; l < NUM_CRYSTAL; l++) { memcpy(&target_coor, &crystal_coor[l], sizeof(c_coordinate)); misorientation = 360; /* Maximum misorientation */ for(j=0; j < 24; j++) { /* get nth symmetry for crystal */ get_nth_symmetry(&sym_crystal, crystal_coor[i], j); /* get nth symmetry for target */ for(k=0; k < 24; k++) { get_nth_symmetry(&sym_target_crystal, target_coor, k); temp_misorientation = get_misorientation(sym_target_crystal, sym_crystal); #ifdef __U_DEBUG__ printf("!!!! %dth crystal - %dth symmetry with %dthe target symmetry!!!!\n", i, j, k); printf("misorientation : %f, min : %f\n", temp_misorientation, misorientation); #endif } } if(temp_misorientation <= misorientation) misorientation = temp_misorientation; memset(&sym_target_crystal, 0x00, sizeof(c_coordinate)); } memset(&sym_crystal, 0x00, sizeof(c_coordinate)); } plot((int)misorientation)++; } if (misorientation <= tolerance_angle) count++; } printf("Total number of grains : %d\n", NUM_CRYSTAL); printf("Total number of grains within misorientation : %d\n", count); printf("Fraction : %f\n", (double)count/(double)NUM_CRYSTAL); fp = fopen("./random.out", "w+"); fprintf(fp, "Angle of disorientation : Count\n"); for (i=0; i<360; i++) { fprintf(fp, "%d : %d\n", i, plot[i]); } fclose(fp); printf("\nrandom.out file was created.\n"); } return 1; err: return -1; } </pre>
--------------------------------------------------------------------------------------------------------------------------------------------------------------------------------------------------------------------------------------------------------------------------------------------------------------------------------------------------------------------------------------------------------------------------------------------------------------------------------------------------------------------------------------------------------------------------------------------------------------------------------------------------------------------------------------------------------------------------------------------------------------------------------------------------------------------------------------------------------------------------------------------------------------------------------------------------------------------------------------------------------------------------------------------------------------------------------------------------------------------------------------------------------------------------------------------------------------------------------------------------------------------------------------------------------------------------------------------------------------------------------------------------------------------------------------------------------------------------------------------------------------------------------------------------------------------------------------------------------------------------------------------------------------------------------------------------------------------------------------------------------------------------------------------------------------------------------------------------------------------------------------------------------------------------------------------------------------------------------------------------------------------------------------------------------------------------------------------------------------------------------------------------------------------------------------------------------------------------------------------------------------------------------------------------------------------------	--------------------------------------------------------------------------------------------------------------------------------------------------------------------------------------------------------------------------------------------------------------------------------------------------------------------------------------------------------------------------------------------------------------------------------------------------------------------------------------------------------------------------------------------------------------------------------------------------------------------------------------------------------------------------------------------------------------------------------------------------------------------------------------------------------------------------------------------------------------------------------------------------------------------------------------------------------------------------------------------------------------------------------------------------------------------------------------------------------------------------------------------------------------------------------------------------------------------------------------------------------------------------------------------------------------------------------------------------------------------------------------------------------------------------------------------------------------------------------------------------------------------------------------------------------------------------------------------------------------------------------------------------------------------------------------------------------------------------------------------------------------------------------------------------------------------------------------------------------------------------------------------------------------------------------------------------------------------------------------------------------------------------------------------------------------------------------------------------------------------------------------------------------------------------------------------------------------------

Appendix D. Change of Microstructure in X80_A Steel

Several heat treatment and dilatometric experiments were conducted in order to check the possibility of change in microstructure of X80_A steel. Figs D.1 ~ D.3 show the time–temperature profiles and dilatometer curves from three experiments;

- Case 1 – heating at $5\text{ }^{\circ}\text{C s}^{-1}$ and kept for 1 min at $890\text{ }^{\circ}\text{C}$ followed by gas quenching at $20\text{ }^{\circ}\text{C s}^{-1}$
- Case 2 – heating at $5\text{ }^{\circ}\text{C s}^{-1}$ and kept for 1 min at $890\text{ }^{\circ}\text{C}$ followed by gas quenching at $50\text{ }^{\circ}\text{C s}^{-1}$
- Case 3 – heating at $5\text{ }^{\circ}\text{C s}^{-1}$ and kept for 1 min at $950\text{ }^{\circ}\text{C}$ followed by gas quenching at $20\text{ }^{\circ}\text{C s}^{-1}$

The M_s temperatures of cases 1, 2 and 3 were measured as 682 , 649 and $671\text{ }^{\circ}\text{C}$ respectively using offset method [Yang and Bhadeshia, 2007]. All the dilatometer curves show the transformation of ferrite to austenite has been completed by approximately $860\text{ }^{\circ}\text{C}$. Fig. D.4 shows the microstructures after the experiments; microstructures have been changed as shown in Fig. 4.1, but it is difficult to observe martensite with clarity. This probably comes from high–martensite start temperature corresponding to low fraction of martensite [Yang and Bhadeshia, 2009]. Macroscopic hardness was measured as 233 ± 1 , 220 ± 2 and $223 \pm 3\text{ HV}$, for cases 1, 2, and 3 respectively, and the values are similar to the macroscopic hardness ($241 \pm 2\text{ HV}$) of as–received X80_A steel. This implies that the microstructures

were not changed to fully martensitic state.

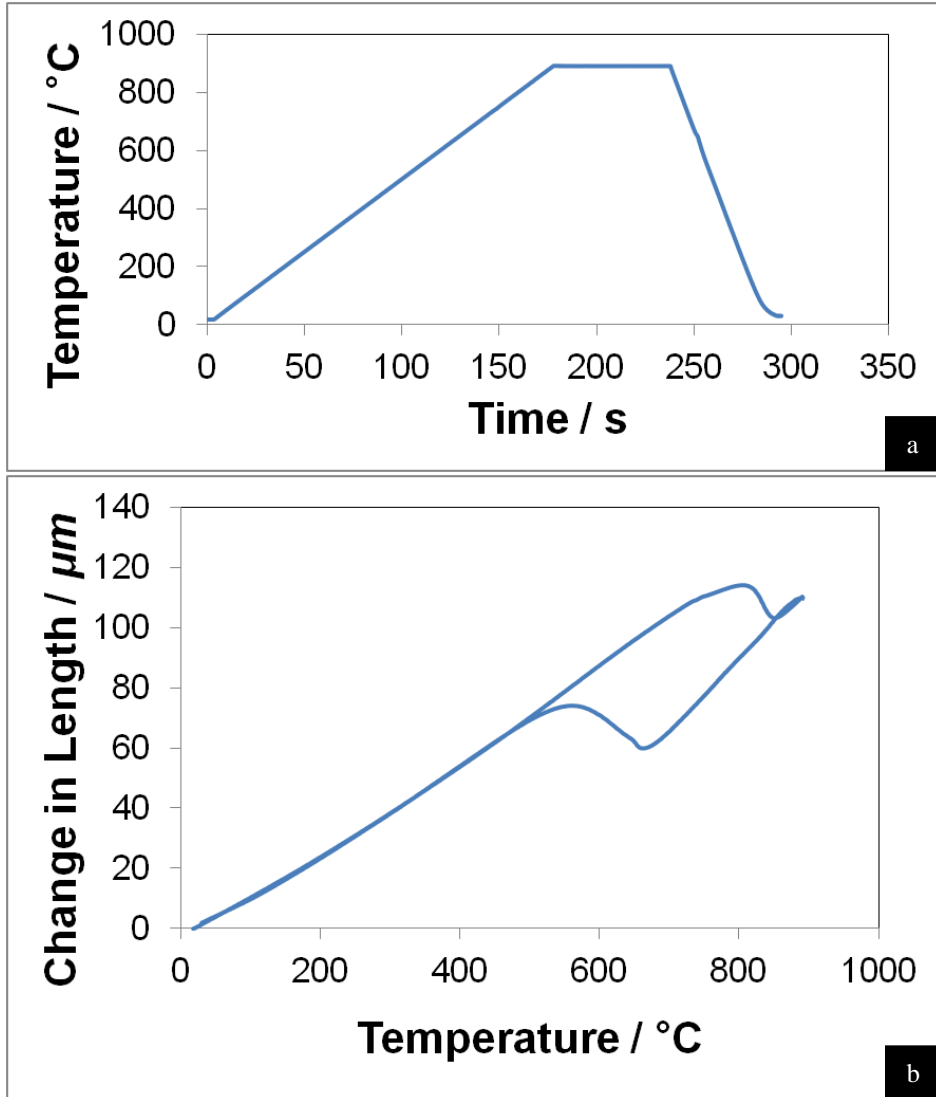


Figure D.1. Time–temperature profile and dilatometer curve of case 1, heating at $5\text{ }^{\circ}\text{C s}^{-1}$ and kept for 1 min at $890\text{ }^{\circ}\text{C}$ followed by gas quenching at $20\text{ }^{\circ}\text{C s}^{-1}$.

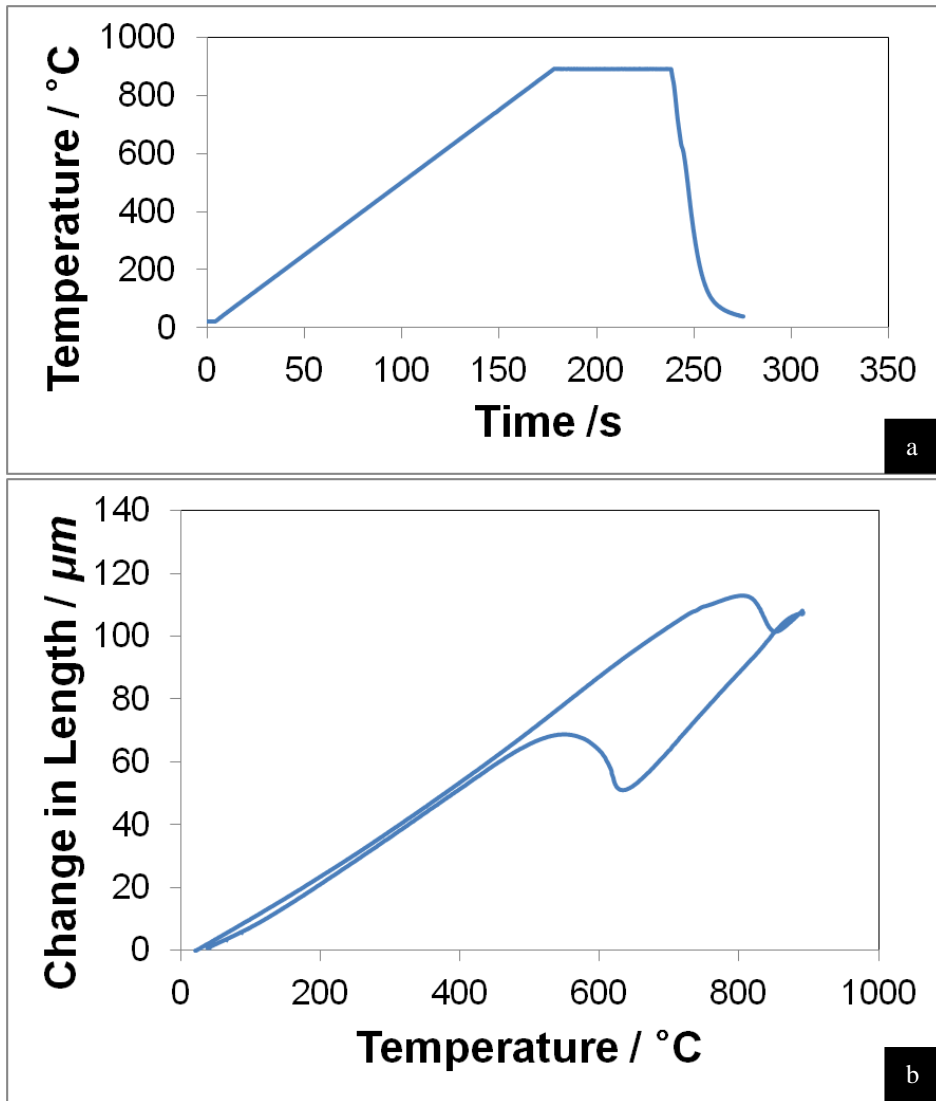


Figure D.2. Time–temperature profile and dilatometer curve of case 2, heating at $5\text{ }^{\circ}\text{C s}^{-1}$ and kept for 1 min at $890\text{ }^{\circ}\text{C}$ followed by gas quenching at $50\text{ }^{\circ}\text{C s}^{-1}$.

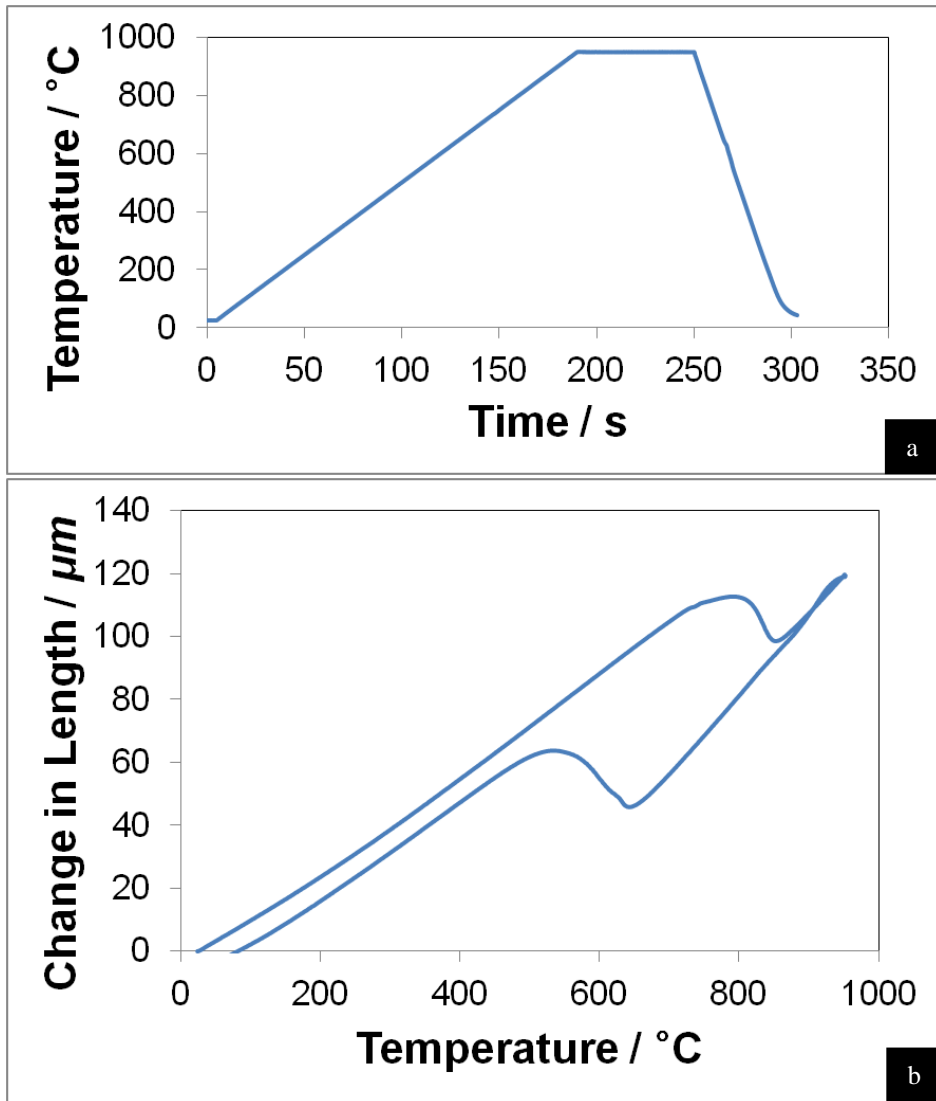


Figure D.3. Time–temperature profile and dilatometer curve of case 3, heating at $5\text{ }^{\circ}\text{C s}^{-1}$ and kept for 1 min at $950\text{ }^{\circ}\text{C}$ followed by gas quenching at $20\text{ }^{\circ}\text{C s}^{-1}$.

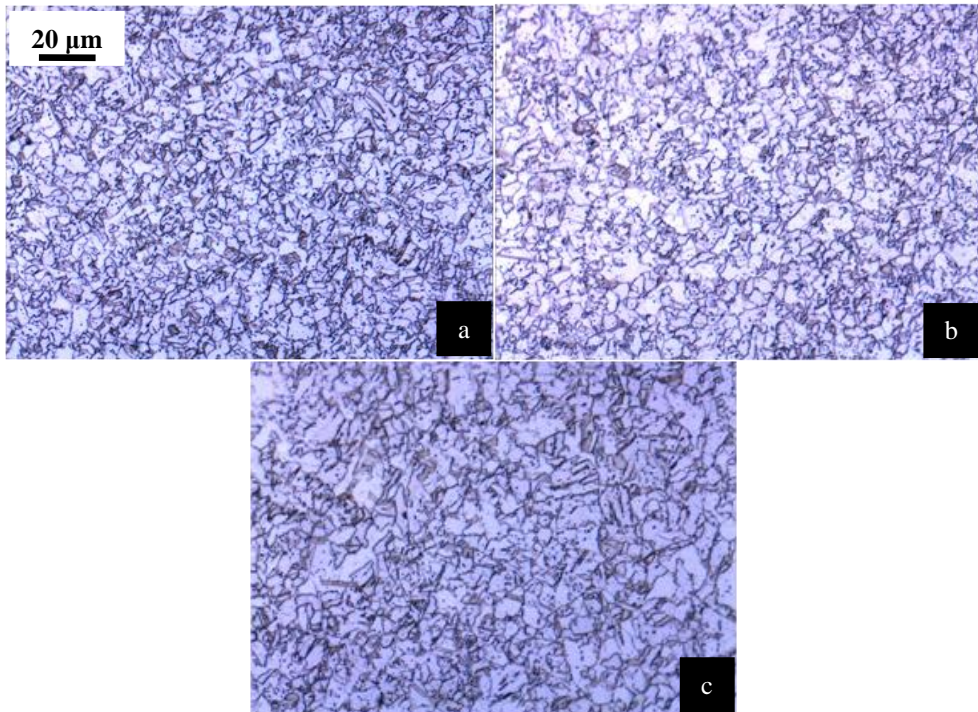


Figure D.4. Optical micrographs in dilatometer specimens: (a) case 1, (b) case 2 and (c) case 3. 2% nital etched.

Therefore, simple heat treatments were conducted in order to induce martensite in the microstructure. Small pieces of X80_A steel were taken and they underwent simple heat treatments;

- Case 1 – the specimen was heated from room temperature in a furnace at $1\text{ }^{\circ}\text{C s}^{-1}$ and kept for 1, 5 and 10 min at $860\text{ }^{\circ}\text{C}$, followed by water quenching to room temperature.
- Case 2 – the specimen was heated from room temperature in a furnace at

1 °C s⁻¹ and kept for 1, 5 and 10 min at 890 °C, followed by water quenching to room temperature.

Case 3 – the specimen was heated from room temperature in a furnace at 1 °C s⁻¹ and kept for 1, 5 and 10 min at 920 °C, followed by water quenching to room temperature.

Case 4 – the specimen was heated from room temperature in a furnace at 1 °C s⁻¹ and kept for 1, 5 and 10 min at 950 °C, followed by water quenching to room temperature.

Fully martensitic state was successfully obtained after 10 min annealing in all the cases. Fig. D.5 shows the microstructures after the simple heat treatments of X80_A steel after annealing for 10 min. All the micrographs have plate-like structures. Macroscopic hardness was measured as 373 ± 6 , 359 ± 8 , 333 ± 1 and 325 ± 6 HV for cases 1, 2, 3 and 4 respectively, and the values are relatively larger than that of X80_A steel. This is because that the martensite fraction is constrained with prior austenite grain size [Yang and Bhadeshia, 2009]. Indeed, it is favourable to pick the case with lowest annealing temperature in order to retain texture successfully [Demura *et al.*, 2007; Lischewski *et al.*, 2008]. However, the case 1 was exempted although martensitic structure was obtained, because 860 °C is close to the A_{c3} temperature from the dilatometric experiments. Thus, the annealing temperature for quenching experiment in section 5.2 was determined as 890 °C although 860 °C is applicable.

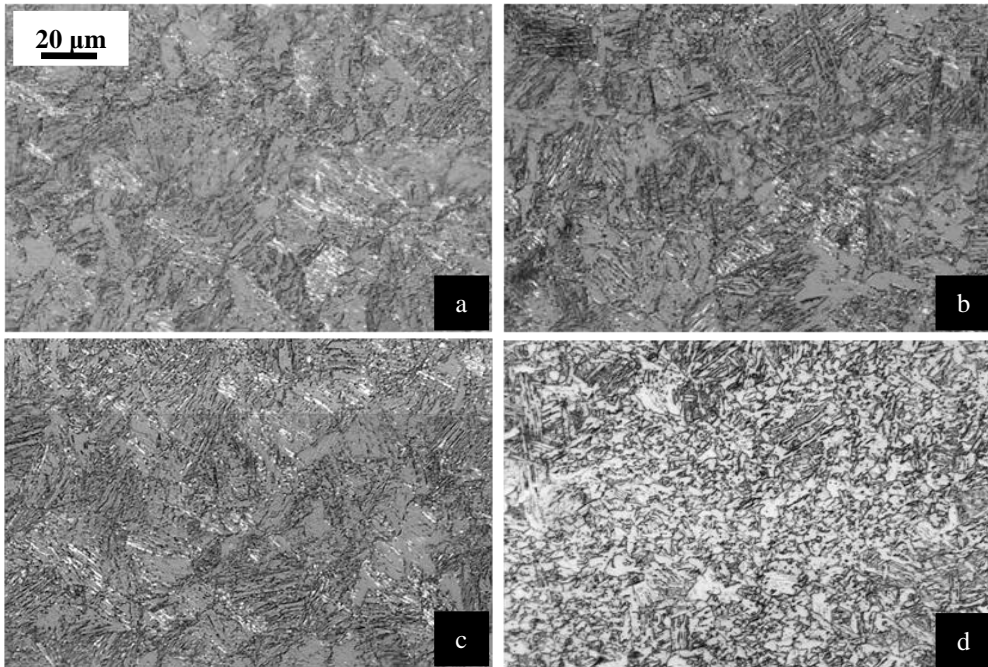


Figure D.5. Optical micrographs in heat-treated specimens with 10 minutes annealing: (a) case 1, (b) case 2 (c) case 3 and (c) case 4. 2% nital etched.

References

Demura, M., Xu, Y., Kishida, K. and Hirano, T.: Texture memory effect in heavily cold-rolled Ni₃Al single crystals. *Acta Materialia*, vol. 55, pp. 1779–1789, 2007.

Lischewski, I., Kirch, D. M., Ziemons, A. and Gottstein, G.: Investigation of the α - γ - α Phase Transformation in Steel: High-Temperature In Situ EBSD Measurements. *Texture, Stress, and Microstructure*, 2008, doi: 10.1155/2008/294508.

Yang, H.-S. and Bhadeshia, H. K. D. H.: Uncertainties in the Dilatometric Determination of the Martensite-Start Temperature. *Materials Science and Technology*, vol. 23, pp. 556–560, 2007.

Yang, H.-S. and Bhadeshia, H. K. D. H.: Austenite Grain Size and the Martensite-Start Temperature. *Scripta Materialia*, vol. 60, pp. 493–495, 2009.

Acknowledgement

I am extremely grateful to my supervisor, Professor H. K. D. H. Bhadeshia for his constant guidance, support, great friendship and for his unique and charming way of teaching the simplicity and beauty of science. I am also thankful to Professor Dong–Woo Suh, my co–advisor, for advice, guidance and support. Also thanks to Professor Hae–Geon Lee, Professor In Gee Kim and Professor Rongshan Qin for their advice, support and friendship.

I acknowledge POSCO for their strong financial support to me and establishment of GIFT. I am also thankful to Dr. Jin–Ho Bae for the preparing test alloys and useful discussion. I thank members in Sheet Products and Process Research Group for discussions.

I would like to express my thanks to all the people in the Graduate Institute of Ferrous Technology (GIFT) in Pohang University of Science and Technology, especially those members in Computational Metallurgy Laboratory (CML), for all their help and for all the memories we have. The life with CML members was quite pleasant and enjoyable.

I thank all the members of Phase Transformations & Complex Properties Research Group, University of Cambridge, for their help and friendship during being my stay in Cambridge.

Finally, I would like to take this opportunity to express my deepest gratitude to my family members, especially my parents, Kang Soon Joo and Bok Soon Jin and my lovely wife, You Young Song, for their love, unfailing encouragement and support.

Curriculum Vitae

Name: Joo, Min Sung (주 민 성)

E-mail: athpimo@postech.ac.kr; minsung.joo@gmail.com

Date of birth: 23th June, 1980

Place of birth: Seoul, South Korea

Education

Ph.D. 2012, POSTECH (Pohang, Korea), Graduate Institute of Ferrous Technology, Computational Metallurgy Group

M. S. 2008, POSTECH (Pohang, Korea), Graduate Institute of Ferrous Technology, Computational Metallurgy Group

B. S. 2006, POSTECH (Pohang, Korea), Department of Computer Science and Engineering

Publications

Joo, M. S., Ryu, J. H. and Bhadeshia, H. K. D. H.: Domains of Steels with Identical Properties. *Materials and Manufacturing Processes*, vol. 24, pp. 53–58, 2009.

Joo, M. S., Suh, D.-W., Bae, J.-H. and Bhadeshia, H. K. D. H.: Influence of Delamination and Crystallography on Anisotropy of Charpy toughness in API-X80 steel. *Materials Science & Engineering A*, vol. 546, pp. 314–322, 2012.

Joo, M. S., Suh, D.-W., Bae, J.-H. and Bhadeshia, H. K. D. H.: An Experiment to Separate the Effect of Texture on Anisotropy of Pipeline Steel. *Submitted*, 2012.

Joo, M. S., Suh, D.-W. and Bhadeshia, H. K. D. H.: Mechanical Anisotropy in Steels for Pipelines. *To be submitted*, 2012.